

# Analysis of Highly Coupled Wideband Antenna Arrays Using Scattering Parameter Network Models

Koichiro Takamizawa

Dissertation submitted to the Faculty of the  
Virginia Polytechnic Institute and State University  
in partial fulfillment of the requirements for the degree of

Doctor of Philosophy  
in  
Electrical and Computer Engineering

Dr. Warren L. Stutzman, Chair

Dr. William A. Davis

Dr. Gary S. Brown

Dr. Ahmad Safaai-Jazi

Dr. Werner Kohler

December 10, 2002

Blacksburg, Virginia

Keywords: Antenna Array, Mutual Coupling, Scattering Parameters, Wideband Array

Copyright 2004, Koichiro Takamizawa

# Analysis of Highly Coupled Wideband Antenna Arrays Using Scattering Parameter Network Models

Koichiro Takamizawa

(ABSTRACT)

Wideband phased arrays require very tight element spacing to permit wide angle scanning of the main beam over the wide bandwidth. The consequence of tight spacing is very high mutual coupling among the elements in the array. Previous efforts by Virginia Tech Antenna Group has shown that the strong coupling can be utilized in arrays to obtain broadband frequency response while maintaining a small element spacing. However, mutual coupling between elements in a tightly coupled array can sometimes dramatically change the operating frequency, bandwidth, and radiation pattern from that of the single isolated element. Thus, there are some fundamental questions that remain regarding the effective operation of highly coupled arrays for beam forming, beam scanning, and aperture reconfiguration. Existing antenna pattern analysis techniques including the active element pattern method are inadequate for the application in highly coupled arrays.

This dissertation focuses on the development of a new antenna array analysis technique. The presented method is based on the scattering parameter network descriptions of the array elements, associated feed network and the active element patterns. The developed model is general. It can be applied to an array of any size and configuration. The model can be utilized to determine directivity, gain and realized gain of arrays as well as their radiation efficiency and impedance mismatch. Using the network model, the relationship between radiation pattern characteristics and the input impedance characteristics of the array antennas becomes clear. Three types of source impedance matching conditions for array antennas are investigated using the model. A numerically simulated array of strip dipole array is used to investigate the effects of various impedance matching methods on the radiation pattern and impedance bandwidth. An application of network analysis is presented on an experimental investigation of  $3 \times 3$  Foursquare array test bed to further verify the concepts.

## Acknowledgments

I would like to thank Dr. Warren L. Stutzman, who has served many years as my adviser and committee chairman for my Masters and Ph. D degrees. Dr. Stutzman provided invaluable advice and support throughout the work on this dissertation and my career development. Without his support and patience, I would not have completed my doctoral degree.

I would like to thank Dr. William A. Davis for the technical assistance on the work presented in this dissertation. Many hours of discussions we have spent on analysis, modeling, measurements, programming, education, and teaching were very enlightening. I would also like to thank other members of my advisory committee, Dr. Gary S. Brown, Dr. Ahmad Safaai-Jazi and Dr. Warner Kohler for their help on completing my work.

The work presented here was made possible by the support of the Navy Collaborative Integrated Information Technology Initiative (NAVCIITI), and Harris Corporation of Melborn, FL.

Lastly, I would like to thank my wife and my best friend, Joan M. Johnson, for being extremely supportive and patient throughout my long graduate work.

## Notice

Figure 3.4 on page 37 reprinted with permission from IEEE Std Std 145-1993, “IEEE Standard Definitions of Terms and Antennas” Copyright 1993 by IEEE. The IEEE disclaims any responsibility or liability resulting from the placement and use in the described manner.

# Contents

<b>1</b>	<b>Introduction</b>	<b>1</b>
1.1	Motivation . . . . .	1
1.2	Overview . . . . .	4
<b>2</b>	<b>Array Antenna Basics</b>	<b>5</b>
2.1	Traditional Array Antenna Analysis Techniques . . . . .	6
2.1.1	Array Analysis based on Maxwell's Equations . . . . .	6
2.1.2	Ideal Array Theory . . . . .	9
2.2	Analysis of Mutual Coupling Effects in Antenna Arrays . . . . .	11
2.2.1	Active Input Impedance Analysis of Arrays . . . . .	12
2.2.2	Active-Element Pattern Method . . . . .	17
2.2.3	Network Descriptions of Arrays including Radiation Ports . . . . .	19
2.3	Infinite Array Analysis . . . . .	22
2.4	Wideband Arrays . . . . .	24
2.5	Summary . . . . .	27
<b>3</b>	<b>Network Description of Single Antenna Elements</b>	<b>28</b>
3.1	Derivation of an S-parameter Network Model . . . . .	29
3.2	Relationship between Antenna Network Model and Antenna Parameters . . . . .	36
3.2.1	Directivity . . . . .	37
3.2.2	Gain . . . . .	39
3.2.3	Realized Gain, Input Impedance, and Impedance Mismatch . . . . .	41
3.2.4	Partial Directivity, Partial Gain, and Polarization Mismatch . . . . .	42
3.3	Summary . . . . .	43

<b>4</b>	<b>Network Description of Array Antennas</b>	<b>45</b>
4.1	Derivation of S-parameter Model for Antenna Arrays . . . . .	45
4.2	Array Network Model and Antenna Parameters . . . . .	52
4.2.1	Array Directivity . . . . .	52
4.2.2	Array Gain . . . . .	55
4.2.3	Array Realized Gain . . . . .	57
4.2.4	Normalized S-parameters . . . . .	59
4.3	Analysis of 2-Element Dipole Antenna . . . . .	61
4.3.1	Sum Pattern Example . . . . .	63
4.3.2	Difference Pattern Example . . . . .	67
4.3.3	Verification of the assumption that S-parameters are probe position independent . . . . .	70
4.4	Summary . . . . .	72
<b>5</b>	<b>Impedance Matching of Array Antennas</b>	<b>73</b>
5.1	Impedance Matching Configurations and Strategies . . . . .	73
5.1.1	Generalized Source Network . . . . .	76
5.1.2	Individually Matched Sources . . . . .	77
5.1.3	Individual Sources with the Same Source Impedance . . . . .	78
5.2	Example of Array Impedance Matching . . . . .	79
5.2.1	Description of Three Element Strip Dipole Array . . . . .	79
5.2.2	Single Element Characteristics . . . . .	80
5.2.3	Array Scattering Parameters and Active-Element Patterns . . . . .	85
5.2.4	Source Impedance Matching . . . . .	93
5.2.5	Array Bandwidth for Broadside Beam . . . . .	103
5.3	Summary . . . . .	108
<b>6</b>	<b>Analysis of Foursquare Array Antenna</b>	<b>110</b>
6.1	Description of Array Hardware . . . . .	112
6.2	Measurement Setup . . . . .	115
6.2.1	S-parameter Measurements . . . . .	116

6.2.2	Foursquare Array S-parameters . . . . .	117
6.2.3	Radiation Pattern Measurements . . . . .	121
6.2.4	Unbalanced-Fed Active-Element Pattern Measurements . . . . .	125
6.3	Measured Results . . . . .	128
6.3.1	Comparison of Indirectly and Directly Measured Active-Element Pat- terns . . . . .	129
6.3.2	Evaluation of Active-Element Patterns . . . . .	136
6.3.3	Comparison of Indirectly and Directly Measured Array Patterns . .	149
6.3.4	Analysis of Foursquare Array with Ideal Hybrid Feed . . . . .	156
6.4	Summary . . . . .	169
<b>7</b>	<b>Conclusions</b>	<b>170</b>
7.1	Summary . . . . .	170
7.2	Contributions . . . . .	172
7.3	Recommendation for Future Work . . . . .	172
	<b>References</b>	<b>174</b>
<b>A</b>	<b>Derivation of Equation (3.9)</b>	<b>182</b>

# List of Figures

2.1	An array of $N$ arbitrarily distributed current densities. . . . .	7
2.2	An antenna element and its current distribution and terminal current. . . .	10
2.3	Mechanisms for coupling between elements of an array. . . . .	11
2.4	Array of $N$ elements. (a) Free excitation array feed model (b) Equivalent circuit model for element $n$ driven by a Thevenin source. The current $I_n$ that appear across the element terminal depend on the source voltage $V_n$ , source impedance $Z_n^s$ , and active input impedance $Z_n$ . . . . .	13
2.5	Definition of active-element pattern for the element $n$ . . . . .	18
2.6	An arbitrary antenna array and distant probe antenna. . . . .	20
2.7	The variation of reflection with scan angle, in the idealized current sheet array with small electric dipole elements computed using (2.33) and (2.34). . . . .	24
2.8	Minimum element spacing normalized to wavelength as a function of normalized frequency for various element types. The right ordinate shows maximum scan angle. . . . .	25
3.1	An arbitrary test antenna fed with a source with internal impedance $Z_s$ and a distant probe antenna with two orthogonal polarization elements. . . . .	29
3.2	Signal flow diagram for an arbitrary test antenna and a probe antenna with two orthogonal polarization ports. . . . .	31
3.3	Simplified signal flow diagram for an arbitrary test antenna and a probe antenna with two orthogonal polarization ports. . . . .	36
3.4	Gain and directivity flow chart. Modified from the chart in IEEE Std. 145-1993	37
4.1	Arbitrary test antenna array fed by sources with internal impedances $\{Z_{s_n}\}$ and a distant probe antenna with two orthogonal polarization elements. . . . .	46

4.2	Block diagram for an arbitrary array of $N$ elements and a probe antenna with two orthogonal polarization ports. . . . .	47
4.3	Signal flow diagram for an arbitrary array of $n$ elements and a probe antenna with two orthogonal polarization ports. . . . .	50
4.4	Two element parallel dipole array and a dipole probe antenna. Dipole length, $L = 50$ mm, diameter, $W = 0.1$ mm, separation distance, $d = 50$ mm, variable probe position $(r, \theta, \phi)$ , frequency $f = 3$ GHz. . . . .	61
4.5	Equivalent circuits for an element in the two dipole array of Fig. 4.4. (a) Equivalent circuit used for the computation of gain pattern in the NEC4 simulation. (b) Equivalent circuit used to determine the available power from the source in the computation of realized gain pattern. . . . .	62
4.6	Realized-gain patterns ( $E_\theta$ polarization) in $\theta = 90^\circ$ plane for an array of two half-wave dipoles of Fig. 4.4 spaced half wavelength apart and parallel to the z-axis. The geometry is shown in the inset. The solid-curve pattern was computed using the indirect method based on the S-parameter network analysis using (4.54) for a half wavelength dipole probe at $r = 10 \lambda$ (Solid curve). The dashed-curve pattern was computed using the direct method from NEC4 gain pattern which is normalized using (4.71) . . . . .	64
4.7	Comparison of realized gain for the array of Fig. 4.6 in the $E_\theta$ polarization as a function of probe antenna distance, $r$ , between the indirect method using the S-parameter network analysis using (4.54) (solid curve), and the direct method from NEC4 gain pattern output normalized using (4.71) (dashed curve). (a) $\theta = 90^\circ$ , $\phi = 90^\circ$ . (In the beam peak region of Fig. 4.6) (b) $\theta = 90^\circ$ , $\phi = 0^\circ$ (In the pattern null region of Fig. 4.6). . . . .	66

4.8	Realized-gain patterns ( $E_\theta$ polarization) in $\theta = 90^\circ$ plane for an array of two half-wave dipoles of Fig. 4.4 spaced a half wavelength apart and parallel to the z-axis. The geometry is shown in the inset. The solid-curve pattern was computed using the indirect method based on the S-parameter network analysis using (4.54) for a half wavelength dipole probe at $r = 10 \lambda$ (Solid curve). The dashed-curve pattern was computed using the direct method from NEC4 gain pattern which is normalized using (4.71) . . . . .	67
4.9	Comparison of array realized gain for the $E_\theta$ polarization as a function of probe antenna distance, $r$ , between the indirect method using the S-parameter network analysis using (4.54) (solid curve), and the direct method from NEC4 gain pattern output normalized using (4.71) (dashed curve). (a) $\theta = 90^\circ, \phi = 90^\circ$ . (In the beam peak region of Fig. 4.6) (b) $\theta = 90^\circ, \phi = 0^\circ$ (In the pattern null region of Fig. 4.6). . . . .	69
4.10	Errors in the values of scattering parameters, $S_{t_1 t_1}$ and $S_{t_1 t_2}$ , for the two-element parallel dipole array of Fig.4.4 as a function of probe antenna position calculated using (4.76). The errors in the magnitude of S-parameters are shown in solid curves, and the errors in the phase of S-parameters are shown in dashed curves. . . . .	71
5.1	Three types of source network configurations: (a) Generalized source with coupled transmitters, $\mathbf{\Gamma}_{ss}$ is a full S-matrix. (b) Individual sources. Each source circuit has an independent source impedance value. (c) Individual sources with the same source impedance. . . . .	75
5.2	Array of three-element parallel strip dipoles with the element length of $L = 38$ mm and strip width of $W = 2$ mm. The elements are printed on an infinite dielectric substrate with a finite thickness of $t = 1$ mm and dielectric constant of $\epsilon_r = 2.33$ . The substrate is suspended over an infinite ground plane at height of $h = 20$ mm. . . . .	79

5.3	A single strip dipole with the element length of $L = 38$ mm and strip width of $W = 2$ mm. The element is printed on a infinite dielectric substrate with a finite thickness of $t = 1$ mm and dielectric constant of $\epsilon_r = 2.33$ . The substrate is suspended over an infinite ground plane at height of $h = 20$ mm.	81
5.4	Scattering parameter as a function of frequency for a single strip dipole with dimensions in Fig. 5.3 simulated by IE3D . . . . .	81
5.5	Input impedance and VSWR computed using IE3D of a single isolated strip dipole with the dimensions in Fig. 5.2. (a) Input impedance of the strip dipole as a function of frequency computed from S-parameter using (5.10), (b) VSWR as a function of frequency computed from S-parameter using (5.13).	83
5.6	Directivity, gain, and realized gain patterns of the isolated strip dipole depicted in Fig. 5.2 at 3 GHz for $E_\theta$ polarization in $\phi = 0^\circ$ plane simulated using IE3D. . . . .	84
5.7	Scattering parameters computed with IE3D as a function of frequency of three-element parallel strip dipole array of Fig. 5.2 printed on a suspended infinite substrate. (a) $S_{t_1t_1}$ and $S_{t_3t_3}$ (b) $S_{t_1t_2}$ , $S_{t_2t_1}$ , $S_{t_2t_3}$ and $S_{t_3t_2}$ , (c) $S_{t_1t_3}$ and $S_{t_3t_1}$ , (d) $S_{t_2t_2}$ . . . . .	86
5.8	Directivity, gain and realized gain active-element patterns of the three element parallel strip dipoles of Fig. 5.2 printed on an infinite substrate computed by IE3D simulations. The patterns are computed at 3 GHz when one element is excited and other two elements are terminated with $50 \Omega$ loads. .	88
5.9	Active-element input impedance as a function of frequency computed using IE3D for the three element array of Fig. 5.2 when one element in the array is excited and all other elements are terminated with reference impedance, $Z_o$ . (a) Element No. 1 or No. 3 active, (b) Element No. 2 active. . . . .	91
5.10	Active-element VSWR for $50 \Omega$ impedance of the three element strip dipole array of Fig. 5.2 computed using IE3D. The VSWR was determined from the active-element S-parameter, $S_{t_n}$ , when element $n$ is excited and all other elements are terminated with reference impedance, $Z_o$ . . . . .	92

5.11	Active input impedance as a function of frequency calculated using IE3D for the three element array of Fig. 5.2 when fully excited with identical excitations. (a) Element No. 1 and No. 3, (b) Element No. 2. . . . .	95
5.12	VSWR as a function of frequency of fully excited array for Case 5 source impedance matching. The array VSWR based on impedance mismatch factor computed using (5.46)(solid curve). The active VSWR for elements 1 and 3 computed using (5.49), (dotted curve). The active VSWR for element 2 computed using (5.49), (dashed curve). . . . .	104
5.13	Array $VSWR_q$ as a function of frequency based on the impedance mismatch factor for fully excited array computed using (5.46) for the six matching cases. The required source impedances and source incident waves are computed at 3 GHz using procedures discussed in Sections 5.2.4.1 to 5.2.4.6, and used as the constants as the frequency is varied. The bandwidth is determined for $VSWR_q \leq 2$ . . . . .	107
6.1	Geometry of hardware test model $3 \times 3$ array of Foursquare elements: (a) Top view. (b) Side view of one element. The array dimensions are summarized in Table 6.1 . . . . .	113
6.2	A block diagram of feed network configuration using two 8-way power dividers and one 180 degree hybrid. . . . .	115
6.3	Representative sample plots of measured S-parameters, $S_{t_{5A}t_{5A}}$ and $S_{t_{5A}t_{5B}}$ , as a function of frequency for the Foursquare array of Fig. 6.1. Solid curves represent the real components, and dashed curves represent the imaginary components. . . . .	119
6.4	Illustration of VTAG anechoic chamber. . . . .	121
6.5	Near-field and far-field measurement configurations used at VTAG chamber. . . . .	123
6.6	Measured amplitude and phase of co-polarization component of the unbalanced-fed active-element patterns (UF-AEP) at 3 GHz for element 5A of the Foursquare test array of Fig. 6.1. Solid curves represent a pattern in $\phi = 0^\circ$ plane. Dashed curves represent a pattern in $\phi = 90^\circ$ plane. These far-field quantities were determined from near-field measurements. . . . .	126

6.7	Measured amplitudes and phases of co-polarization component of the unbalanced-fed active-element patterns (UF-AEP) at 3 GHz for element 5B of the Foursquare test array of Fig. 6.1. Solid curves represent patterns in $\phi = 0^\circ$ plane. Dashed curves represent patterns in $\phi = 90^\circ$ plane. These far-field quantities were determined from near-field measurements. . . . .	127
6.8	Schematic of the array network configuration for measurement of active-element pattern of element 5 in the Foursquare array of Fig. 6.1. . . . .	129
6.9	Comparison of indirectly and directly measured active-element gain patterns for element 1 at 3 GHz in $\phi = 0^\circ$ and $90^\circ$ planes. . . . .	131
6.10	Comparison of indirectly and directly measured active-element gain patterns for element 2 at 3 GHz in $\phi = 0^\circ$ and $90^\circ$ planes. . . . .	132
6.11	Comparison of indirectly and directly measured active-element gain patterns for element 3 at 3 GHz in $\phi = 0^\circ$ and $90^\circ$ planes. . . . .	133
6.12	Comparison of indirectly and directly measured active-element gain patterns for element 5 at 3 GHz in $\phi = 0^\circ$ and $90^\circ$ planes. . . . .	134
6.13	Measured insertion loss as a function of frequency between 1 to 5 GHz of a 180 degree broadband hybrid that is configured as a broadband balun as shown in Fig. 6.2(a). . . . .	135
6.14	Composite plots of indirectly measured active-element patterns of $3 \times 3$ Foursquare array of Fig. 6.1 in $\phi = 0^\circ$ plane at 3 GHz . . . . .	137
6.15	Composite plots of indirectly measured active-element patterns of $3 \times 3$ Foursquare array of Fig. 6.1 in $\phi = 90^\circ$ plane at 3 GHz . . . . .	138
6.16	Variations in the indirectly measured active-element patterns for the element 5 of $3 \times 3$ Foursquare array of Fig. 6.1 in $\phi = 0^\circ$ plane for the frequencies between 2 GHz to 4 GHz in 250 MHz steps. . . . .	140
6.17	Schematics of fully excited Foursquare array feed configurations using two broadband 1:8 power dividers and a broadband $180^\circ$ hybrid. The shaded elements on the Foursquare array illustrations represent excited elements. (a) Configuration 1: elements 1 and 9 are unexcited, (b) Configuration 2: elements 3 and 7 are unexcited. . . . .	150

6.18	Comparison of indirectly and directly measured co-pol and cross-pol patterns of the Foursquare array shown in Fig. 6.1 fed by broadband power dividers and a broadband $180^\circ$ hybrid feed network in Configuration 1 shown Fig. 6.17(a).	152
6.19	Computed co-pol and cross-pol patterns of the Foursquare array shown in Fig. 6.1 fed by broadband power dividers and a broadband $180^\circ$ hybrid feed network in Configuration 2 shown Fig. 6.17(b).	154
6.20	Schematic of fully excited Foursquare array of Fig. 6.20 fed with nine ideal $180^\circ$ hybrids and nine ideal voltage sources with $50\ \Omega$ internal impedance. This model is used for numerical simulation to investigate the array impedance bandwidth.	157
6.21	Port number definitions for an ideal $180^\circ$ hybrid and an ideal balun.	157
6.22	Comparison of three voltage standing wave ratio (VSWR) as a function of frequency over a range between 1 to 5 GHz for Foursquare array of Fig. 6.1 fed with nine idealized baluns shown in Fig. 6.20. Solid curves are active-element $VSWR_{ae}$ referenced to $50\ \Omega$ computed using (6.21). Dashed curves are active $VSWR_a$ referenced to $50\ \Omega$ computed using (6.16). Dotted curves are array $VSWR_q$ computed using (6.6).	162
6.23	Geometry of $3 \times 3$ array of half-wavelength strip dipoles suspended over an infinite ground plane with strip length, $L=48$ mm, strip width, $W=2$ mm, and strip height over ground, $h=25$ mm. The array is designed to operate at center frequency of 3 GHz, ( $\lambda = 100$ mm).	166
6.24	Comparison of three voltage standing wave ratio (VSWR) as a function of frequency over a range between 2 to 4 GHz for a $3 \times 3$ array of strip dipoles of Fig. 6.23 excited with uniform excitation. Solid curves are active-element $VSWR_{ae}$ referenced to $50\ \Omega$ computed using (6.21). Dashed curves are active $VSWR_a$ referenced to $50\ \Omega$ computed using (6.16). Dotted curves are array $VSWR_q$ computed using (6.6).	167
A.1	Signal flow diagram for an arbitrary test antenna and a probe antenna with two orthogonal polarization ports.	183

# List of Tables

3.1	Summary of antenna parameters and their definition in terms of antenna network S-parameters. . . . .	44
4.1	Summary of antenna parameters and their definition in terms of array network S-parameters. . . . .	72
5.1	A summary of electrical performance of the isolated strip dipole of the same dimension as one element in Fig. 5.2 printed on an infinite dielectric substrate over an infinite ground plane simulated using IE3D. . . . .	85
5.2	A summary of electrical performance of the strip dipole array of Fig. 5.2 at 3 GHz computed using IE3D for the active-element pattern condition where one element is excited and all other elements in the array are terminated with reference impedance, $Z_o$ . . . . .	89
5.3	Summary of impedance matching cases investigated for the three-element strip dipole array with the dimensions in Fig. 5.2 simulated by IE3D. . . . .	93
5.4	A summary of broadside directivity, gain and radiation efficiency at 3 GHz for the fully active three element strip dipole array of Fig. 5.2 for the uniform incident waves. . . . .	94
5.5	Summary of impedance matching results for the uniform incident waves requirement, $\mathbf{a}_t = [1 \ 1 \ 1]^T$ at 3 GHz for the three element strip dipole array depicted in Fig. 5.2. . . . .	102
5.6	A summary of the lower and the upper cutoff frequencies determined at VSWR=2 from Fig. 5.12 for the array VSWR based on $q$ and for the active VSWR of fully excited three element strip dipole with Case 5 impedance matching. The percent bandwidths are computed using (5.14). . . . .	105

5.7	Summary of upper and lower cutoff frequencies determined for VSWR=2 for the curves in Fig. 5.12, and percent bandwidth computed using (5.14) for six impedance matching cases. The source impedances and source incident waves were determined at 3 GHz using the procedures discussed in Sections 5.2.4.1 through 5.2.4.6. . . . .	106
6.1	Dimensions of the $3 \times 3$ Foursquare hardware test article array of Fig. 6.1, given both in mils and in mm. . . . .	112
6.2	Electrical specifications for ETI P8D118-8 broadband 8-way power divider.	114
6.3	Electrical specifications for ETI HY118-180 broadband 180 degree hybrid. .	115
6.4	The measurement plan for the 153 two-port measurements of the Foursquare article array of Fig. 6.1. The measurements that include port 5A of the center element are highlighted to illustrate that there are 17 reflection coefficient measurements for this port within the overall measured data sets. . . . .	118
6.5	Summary of resonance frequencies, $f_R$ , and impedance bandwidths, $B_p$ , for $3 \times 3$ Foursquare array of Fig. 6.1 computed based on three definitions of voltage standing wave ratio: $VSWR_q$ , $VSWR_a$ , and $VSWR_{ae}$ . The minimum values for VSWR are used to estimate the resonance frequencies, $f_R$ , of the array and elements. The upper and lower cutoff frequencies which are determined from the plots in Fig. 6.22 are shown in columns $f_U$ and $f_L$ . The center frequencies, $f_C$ , are determined by taking the average of $f_U$ and $f_L$ using (5.15). Impedance bandwidths, $B_p$ , are determined using (5.14). . . .	164

# Chapter 1

## Introduction

### 1.1 Motivation

Phased array antennas are becoming increasingly popular for applications that require radiation pattern control. This popularity exists because the radiation pattern of a phased array can be shaped and steered electronically by proper element excitations. In addition, phased arrays allow for aperture and polarization reconfiguration and shared aperture operations for the spatial processing of signals for propagation impediment mitigation. Until recently, phased arrays were mostly used in government applications where performance requirements are more important than cost. Recent improvements in the performance and in the cost of RFICs have stimulated commercial applications for phased arrays. Many research and development efforts for the next generation of wireless applications will consider the use of multiple antenna elements in their systems, although some of these designs will use multiple antennas not in a phased array configuration, but as a switched-element antenna for antenna, pattern or polarization diversity [1, 2]. Even in fixed-phase arrays, the proximity of the antenna elements require array analysis for the proper prediction of their performance.

The analysis and design of array antennas is complicated due to the fact that array elements are not independent of each other. Instead, the elements interact electromagnetically through what is called mutual coupling. There has been much effort directed toward developing analysis methods that account for the effects of mutual coupling in an array

environment. The knowledge of mutual coupling effects is important in the design of array elements, for array geometry selection to reduce mutual coupling among elements, and also for compensating the mutual coupling effects with feeding circuits.

Tremendous improvements in the accuracy of the numerical evaluation of antenna characteristics have been achieved in the last 50 years. Some of the popular antenna analysis methods utilize numerical techniques to directly solve Maxwell's equations such as the method of moments (MoM), the finite element method (FEM), and the finite-difference time-domain method (FDTD). These methods have evolved to the point where there now are very accurate and reliable commercial numerical analysis tools available. The increase in the computational speeds and the reduction in the computer hardware costs, along with the improvements in the numerical analysis methods and availability of numerous commercial software packages, allow electrical engineers to very easily and rapidly analyze antennas of various geometries. At the same time, these complex simulations codes are often used improperly and code outputs are not interpreted properly.

Analytical antenna array analysis methods have also seen a steady progress. As the complexity of array antennas increased, improved techniques became necessary for the understanding of array behavior. The first order pattern characteristics of antenna arrays can be determined by the principle of pattern multiplication that does not include mutual coupling among the array elements and assumes identical element radiation patterns. Pattern multiplication is a useful tool for understanding the basic principles of antenna arrays, but it is completely inadequate for thorough analysis of arrays. The most popular closed-form pattern analysis that includes mutual coupling effects is the active element pattern method [3]. The active element pattern method is a powerful approach that provides means to calculate fully excited array patterns, including element mutual coupling effects, from a set of element radiation patterns in the fully excited array load termination environment. The active element pattern approach also provides an estimate of the scan capability of large arrays [4]. Unfortunately, it cannot be used to evaluate the pattern of an array including source network coupling and mismatch. However, the network descriptions of array elements and the source network allow computation of fully excited antenna arrays including source network effects. Various forms of network descriptions have been developed since the

1960's, and yet, they are not being utilized by many engineers. Part of this unpopularity may exist due to their formulations which make them difficult to measure and to apply to real antenna arrays.

Since the mid 1990's, Virginia Tech Antenna Group (VTAG) has been investigating a new class of array antennas with very tight element spacings to permit wide angle scan of the main beam over wide bandwidth. The consequence of tight spacing is very high mutual coupling among the elements in the array [5, 6]. The highly coupled array is a fundamentally different type of wideband antenna where the mutual coupling among the array elements is utilized to shift down the center frequency, and at the same time broaden the impedance bandwidth of the array. For example, Buxton [6] showed that the impedance bandwidth of closely packed Foursquare elements will progressively shift the center of the operational frequency down, and at the same time widen the bandwidth as the array size is increased from a single isolated Foursquare element, to a 3x3 array, and then to an infinite planar array of Foursquare elements. The numerical analysis of Foursquare antennas allow us to understand some of the operational characteristics of highly coupled antenna arrays [5, 6]. However, there are still some fundamental questions that remain regarding the effective operation of highly coupled array for beam forming, beam scanning, and aperture reconfiguration.

This dissertation presents a new scattering parameter based network model for the description of antenna arrays. The model includes a description for the mutual coupling between array elements and the coupling through the source network. The expressions for directivity, gain, realized gain, radiation efficiency, impedance mismatch, and polarization mismatch are derived directly from the model. Thus, this model allows a compact description of the impedance characteristics and the radiation characteristics of antenna arrays from the same set of S-parameters. Key concepts such as array impedance matching and array impedance bandwidth are investigated using the S-parameter model.

Numerically simulated printed strip dipole arrays are used to validate the model, and to investigate various source impedance matching conditions. Then, the network-based array model is applied experimentally to investigate a  $3 \times 3$  Foursquare array test bed.

## 1.2 Overview

The second chapter of this dissertation reviews background materials related to the research presented in this dissertation. Specifically, a review of analysis techniques including array mutual coupling effects is presented. The emphasis is placed on analytical array analysis techniques. The advantages and disadvantages of existing techniques will be discussed, enforcing the motivation of the proposed research.

A single-element antenna model and an antenna array model based on the scattering parameter descriptions of the antenna elements and the source network are derived in Chapters 3 and 4. The single-element antenna model in Chapter 3 introduces the notation, and provides a check for consistency with known characteristics. The single-element network model is extended in Chapter 4 to include multiple antenna elements, and a source network that may be coupled. These models allow computation of radiated field and radiated power in terms of waves incident on the antenna element or the array elements. The incident waves and the radiated power can be used to compute antenna design parameters such as directivity, gain and efficiencies.

Chapter 5 presents the development of the source-network impedance-matching concept in the array environment. Three types of source-network configurations will be considered for impedance matching. A three-element strip-dipole array printed on a substrate will be analyzed based on numerically simulated data. Various impedance matching technique will be applied to the array, and the effects will be evaluated.

The next chapter details the analysis of a 3x3 Foursquare test-bed array based on experimentally measured data. The network model analysis is applied to the measured S-parameters of the array elements and their active element patterns. The performance of the array is predicted based on the measured data. Finally, conclusions and recommendations for future work is presented in Chapter 7.

## Chapter 2

# Array Antenna Basics

Many antenna array analysis techniques have been developed in the last 50 years. Current state of the art techniques allow very accurate prediction of the radiation pattern and input impedance of an antenna radiating in free space. The radiation pattern and the input impedance are determined by solving Maxwell's equations for a given antenna geometry in its radiating environment. Depending on the solution technique chosen, either an integral form or differential form of Maxwell's equations in the frequency domain, or the time domain is selected to describe the problem. Sometimes, a combination of equation forms or domains is used to describe complex antenna problems. These equations are solved using one of various numerical methods available. For example, the integral form of Maxwell's equations which are solved using the method of moments (MoM) [7] is one of the most popular techniques used to determine antenna properties. Other popular techniques include the finite element method (FEM) [8] and the finite-difference time-domain method (FDTD) [9]. Overall, the techniques and methods that are commonly used have similar solution accuracies and computational resource requirements [10, 11]

When multiple radiating elements are introduced in antenna systems, the analysis and design of the systems become complicated due to electromagnetic interaction among the elements. This interaction is called mutual coupling. Mutual coupling effects in an antenna array can be analyzed by solving Maxwell's equations for the array geometry. Unfortunately, this solution approach is currently limited to arrays of moderate sizes due to excessive computational resources required to solve Maxwell's equations numerically. Thus,

approximate techniques must be utilized in the analysis and design of large array antennas.

This chapter reviews the existing techniques for the analysis of antenna arrays. We begin the chapter by reviewing the full electromagnetic analysis of array antennas. An ideal array theory which assumes no mutual coupling among array elements is introduced next. Then, analysis techniques including mutual coupling are reviewed. Specifically, we discuss the classical array method, the active-element pattern method, and the network-based method that includes radiation ports. Finally, we will discuss infinite array techniques which can be applied to approximate the performance of large arrays.

## 2.1 Traditional Array Antenna Analysis Techniques

### 2.1.1 Array Analysis based on Maxwell's Equations

This section reviews procedures for finding fields radiated by an antenna array based on Maxwell's equations. Antenna radiation patterns are determined from the impressed current distributions on the antenna elements. When proper boundary conditions in terms of the current distributions on the antenna elements are specified, it is always possible to determine the exact radiated fields by solving the Maxwell's equations. We will assume that these currents on the elements are known. Consider an array of  $N$  arbitrary array elements represented by electric current densities,  $\vec{J}_n(\vec{r}')$ , for  $n = 1 \dots N$  as illustrated in Fig. 2.1. We wish to determine the electric fields radiated by these currents.

The vector magnetic potential of the array of currents is given by

$$\vec{A}(\vec{r}) = \iiint_{v'} \sum_{n=1}^N \mu \vec{J}_n(\vec{r}') \frac{e^{-jk_o R}}{4\pi R} dv' \quad (2.1)$$

where  $\vec{r}$  is the vector from the coordinate origin to an observation point,  $\vec{r}'$  is the vector from the origin to a point on an element and  $R = |\vec{r} - \vec{r}'|$ . The electric field of this array can be determined from

$$\vec{E}(\vec{r}) = \frac{1}{j\omega\mu\epsilon} \left( \nabla \times \nabla \times \vec{A}(\vec{r}) - \sum_{n=1}^N \vec{J}_n(\vec{r}') \right) = \frac{1}{j\omega\mu\epsilon} \left( k^2 \vec{A}(\vec{r}) + \nabla(\nabla \cdot \vec{A}(\vec{r})) \right) \quad (2.2)$$

in the source region and

$$\vec{E}(\vec{r}) = \frac{1}{j\omega\epsilon\mu} \left( \nabla \times \nabla \times \vec{A}(\vec{r}) \right) = -j\omega \left( \vec{A}(\vec{r}) + \frac{1}{k^2} \nabla(\nabla \cdot \vec{A}(\vec{r})) \right) \quad (2.3)$$

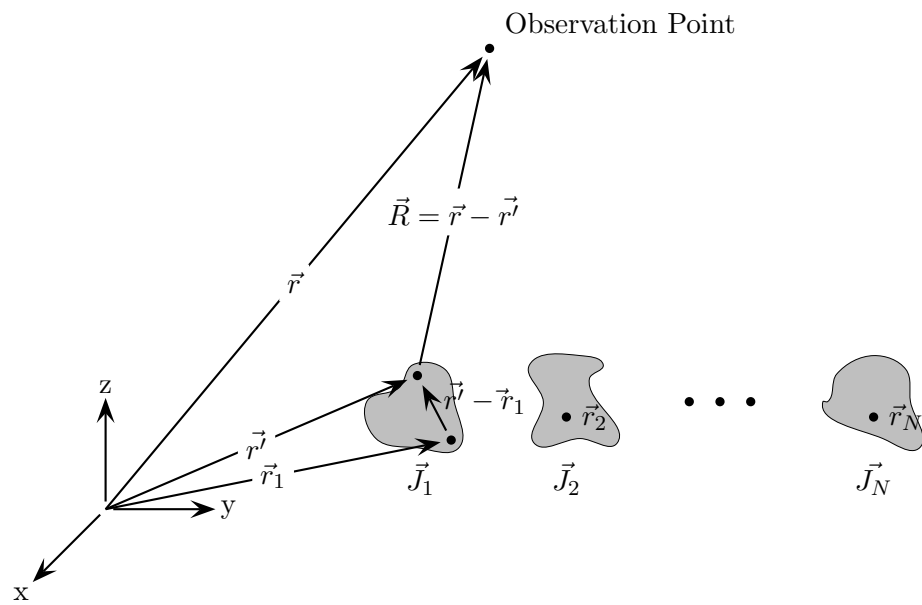


**Figure 2.1** An array of  $N$  arbitrarily distributed current densities.

in the source free region. In general, we are interested in the antenna radiation pattern in a source free region away from the array elements. First, we find the electric field created by the currents and then simplify the form for far-field distances. The general electric field is found by substituting (2.1) into (2.3):

$$\vec{E}(\vec{r}) = \frac{1}{j\omega\epsilon} \nabla \times \nabla \times \iiint_{v'} \sum_{n=1}^N \vec{J}_n(\vec{r}') \frac{e^{-jk_o R}}{4\pi R} dv'. \quad (2.4)$$

Using the superposition, (2.4) can be written as a sum of the electric fields from  $N$  separate currents,

$$\vec{E}(\vec{r}) = \sum_{n=1}^N \left( \frac{1}{j\omega\epsilon} \nabla \times \nabla \times \iiint_{v'} \vec{J}_n(\vec{r}') \frac{e^{-jk_o R}}{4\pi R} dv' \right). \quad (2.5)$$

Thus, the total field is obtained from a sum of fields generated by the  $N$  element current distributions,  $\{\vec{J}_n(\vec{r}')\}$ . The expression (2.5) represents the exact electric fields due to element currents. It can be applied to determine fields at any point  $\vec{r}$  in the source free region.

We are typically interested in the radiated fields in the far-field region of the array. When far-field conditions are satisfied such that

$$\begin{aligned} r &> 2D^2/\lambda \\ r &\gg D \\ r &\gg \lambda \end{aligned} \quad (2.6)$$

where  $D$  is the largest extent of the array dimension, (2.5) simplifies to

$$\vec{E}^{ff}(\vec{r}) = \sum_{n=1}^N \left( \frac{1}{j\omega\epsilon} \frac{e^{-jk_o r}}{4\pi r} \hat{r} \times \hat{r} \times \iiint_{v'} \vec{J}_n(\vec{r}') e^{jk_o \hat{r} \cdot \vec{r}'} dv' \right). \quad (2.7)$$

The approximation  $R \approx r$  was used for the magnitude factor and  $R = r - \hat{r} \cdot \vec{r}'$  was used for the phase factor in the radiation integral in (2.7). A radiation pattern is the variation of radiated fields over a sphere of constant  $r$  centered on the antenna coordinate system [12].

The unnormalized radiation pattern of the fields represented by (2.7) is given by

$$\vec{F}(\theta, \phi) = \sum_{n=1}^N \left( \hat{r} \times \hat{r} \times \iiint_{v'} \vec{J}_n(\vec{r}') e^{jk_o \hat{r} \cdot \vec{r}'} dv' \right). \quad (2.8)$$

The effects of mutual coupling in the radiated field expressions (2.5) and (2.7) and in the radiation pattern (2.8) are contained in the electric current densities,  $\{\vec{J}_n\}$ . The array

element current distributions are different from the isolated element current distributions due to mutual coupling. In general, it is difficult to analytically determine the element current distributions. Typically, we must utilize numerical methods to determine the unknown current distributions. Ideal array theory which will be discussed next allows us to estimate the characteristics of array antennas without the knowledge of exact currents on the elements.

### 2.1.2 Ideal Array Theory

Ideal array theory provides a tool to accomplish analysis of antenna arrays without need for solving exact electromagnetic models. The ideal array theory assumes that there is no mutual coupling among the array elements. This assumption implies that:

- The current distributions in the array elements,  $\{\vec{J}_n(\vec{r}^j)\}$ , are identical to the current distribution of the same elements in an isolated environment,  $\{\vec{J}_n^i(\vec{r}^j)\}$ .
- Terminal currents and terminal voltages are related by the input impedance of the elements in an isolated environment:  $V_n^i = Z_n^i I_n^i$ .
- The current distribution does not change as the main beam of the array radiation pattern is scanned.

Using these assumptions, we can simplify the exact radiation pattern formula (2.8). Let us express the element current distributions as

$$\vec{J}_n^i(\vec{r}^j) = I_n^i \vec{j}_n^i(\vec{r}^j) \quad (2.9)$$

where  $\{I_n^i\}$  are complex valued terminal currents and  $\{\vec{j}_n^i\}$  are normalized current distributions of isolated elements as illustrated in Fig. 2.2. Substituting (2.9) into (2.8) yields

$$\vec{F}^i(\theta, \phi) = \sum_{n=1}^N \left( \hat{r} \times \hat{r} \times \iint \iint_{v'} \vec{j}_n^i(\vec{r}^j) e^{jk_o \hat{r} \cdot \vec{r}^j} dv' \right) I_n^i \quad (2.10)$$

When element radiation patterns due to normalized element currents are referenced to the locations where terminal currents are determined, then (2.10) is modified to

$$\vec{F}^i(\theta, \phi) = \sum_{n=1}^N \left( \hat{r} \times \hat{r} \times \iint \iint_{v'} \vec{j}_n^i(\vec{r}^j) e^{jk_o \hat{r} \cdot (\vec{r}^j - \vec{r}_n)} dv' \right) I_n^i e^{jk_o \hat{r} \cdot \vec{r}_n} \quad (2.11)$$

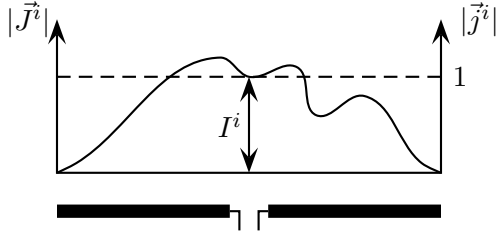


**Figure 2.2** An antenna element and its current distribution and terminal current.

where  $\{\vec{r}_n\}$  are vectors to the element terminal positions. The term inside parenthesis represents the radiation pattern of isolated element  $n$ . Substituting the isolated element pattern by  $\vec{g}_n^i(\theta, \phi)$  yields the generalized pattern of ideal array

$$\vec{F}^i(\theta, \phi) = \sum_{n=1}^N \vec{g}_n^i(\theta, \phi) I_n^i e^{jk_o \hat{r} \cdot \vec{r}_n}. \quad (2.12)$$

In addition to the no mutual coupling assumption, if we assume that the elements in the array are identical, the element patterns  $\{g_n^i(\theta, \phi)\}$  become the same. Thus, we can factor the element pattern out of the summation in (2.12), resulting in

$$\vec{F}^i(\theta, \phi) = \vec{g}^i(\theta, \phi) \sum_{n=1}^N I_n^i e^{jk_o \hat{r} \cdot \vec{r}_n}. \quad (2.13)$$

The summation term of (2.13) represents the far-field radiation pattern of the array geometry when all of the elements are isotropic radiators. This term is referred as the array factor which is represented by  $f^i(\theta, \phi)$ . Thus, the radiation pattern of an ideal antenna array with identical elements is given by a multiplication of the isolated element pattern and the array factor, or

$$\vec{F}^i(\theta, \phi) = \vec{g}^i(\theta, \phi) f^i(\theta, \phi). \quad (2.14)$$

The principle of *pattern multiplication* represented by (2.14) provides a simple but powerful tool to visualize the first order behavior of array antenna patterns. The technique is applicable as long as the mutual coupling effects among array elements are negligible and array elements are identical. The performance of most practical antenna arrays are significantly altered by the coupling effects. These effects are generally considered detrimental to the proper operation of the antenna array. The coupling effects are of extreme significance in phased array antennas since their effects vary with the excitation of the array elements.

Thus, the ideal array analysis is generally inadequate to predict the true performance of practical array antennas. We must account for the mutual coupling effects in the analysis and design of array antennas.

## 2.2 Analysis of Mutual Coupling Effects in Antenna Arrays

Properties of antenna elements can change dramatically when placed in an array environment. Both the radiation pattern and the input impedance of the elements are altered from free space values due to mutual coupling. Mutual coupling occurs due to three mechanisms: direct space coupling among array elements, indirect coupling caused by near-by scatterers, and coupling through feed network [12]. The three mechanisms of mutual coupling are illustrated in Fig. 2.3.

In an array environment the field radiated and scattered by a given element changes the current distributions of the other elements. For an array with aperture type elements, the changes occur in the aperture field distributions. Likewise, the field radiated or scattered by the other elements affects the current distribution or aperture field distribution of the original element. The coupling and mismatches introduced by the feed network complicates the overall effects of mutual coupling.

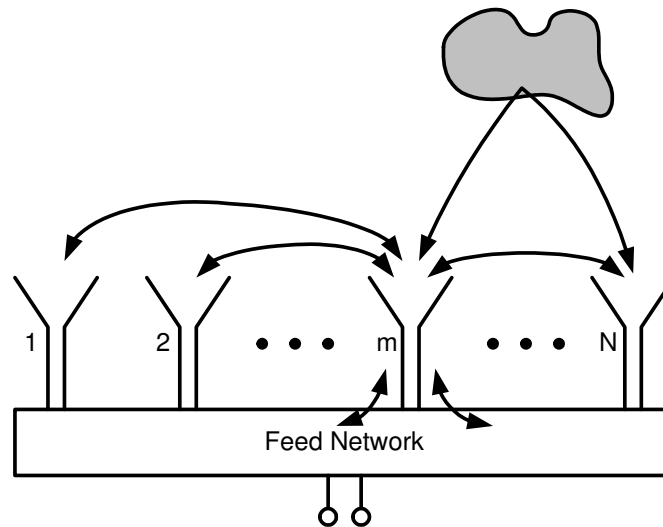


**Figure 2.3** Mechanisms for coupling between elements of an array.

The changes in the current distribution are observed in the changes of total array pattern and in the changes of element input impedances. The effect of altered element current distributions can be modeled in various ways. Several approaches have emerged that address mutual coupling effects in the analysis, including the active input impedance method, the method that employs active-element patterns, the network based array description method including radiation ports, and infinite array based analysis. In this section we review these four array analysis methods.

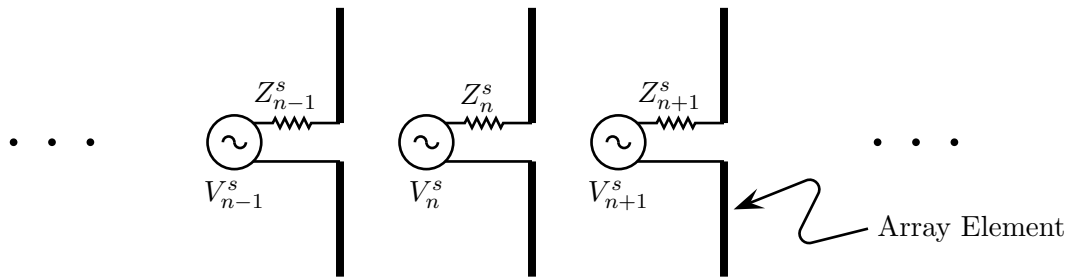
### 2.2.1 Active Input Impedance Analysis of Arrays

If mutual coupling affects the terminal current values, but does not affect the normalized element current distribution then element current can be expressed as

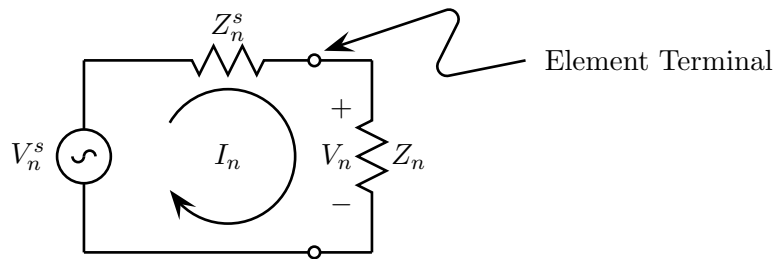
$$\vec{J}_n(\vec{r}') = I_n \vec{j}_n^i(\vec{r}') \quad (2.15)$$

where  $\{I_n\}$  are complex valued terminal currents and  $j_n^i(\vec{r}')$  are the normalized current distributions of isolated elements. This assumption allows us to treat an  $N$  element array as an  $N$ -port network. It follows that the mutual coupling between array elements can be characterized by a conventional multi-port circuit model, such as an impedance matrix, an admittance matrix, or a scattering matrix [13, 14, 15, 16, 17, 18]. Theoretically, the type of matrix used to represent the array network is not important since matrix transforms can be applied to change the type of matrix representation.

The array elements are excited either directly by a set of individual transmitters or indirectly through a feed network. In either case, the array excitation can be modeled as a set of Thevenin equivalent voltage sources with source impedances as shown in Fig. 2.4. This model is defined as the free-excitation model by Oliner and Malech [14]. Once the array elements and feed network are represented in matrix forms, multi-port network analysis techniques are applied to determine the terminal voltages and currents or incident and reflected waves.



(a)



(b)

**Figure 2.4** Array of  $N$  elements. (a) Free excitation array feed model (b) Equivalent circuit model for element  $n$  driven by a Thevenin source. The current  $I_n$  that appear across the element terminal depend on the source voltage  $V_n$ , source impedance  $Z_n^s$ , and active input impedance  $Z_n$ .

Let us assume that an  $N$  element array is represented by an impedance matrix,

$$\mathbf{Z} = \begin{bmatrix} Z_{11} & Z_{12} & \cdots & Z_{1N} \\ Z_{21} & Z_{22} & \cdots & Z_{2N} \\ \vdots & \vdots & \ddots & \vdots \\ Z_{N1} & Z_{N2} & \cdots & Z_{NN} \end{bmatrix} \quad (2.16)$$

The diagonal components of (2.16),  $\{Z_{nn}\}$ , represent the self-impedance of the element  $n$ , and the off-diagonal components,  $\{Z_{nm}\}$ , represent the mutual impedance between two terminal pairs of elements  $n$  and  $m$ . Following the multi-port network definition of impedance matrix, the mutual impedance  $Z_{mn}$  is determined from the ratio of open circuit voltage produced at the terminal  $m$  to the current supplied to the terminal  $n$  when all other terminals are open-circuited,

$$Z_{mn} = \left. \frac{V_m}{I_n} \right|_{I_k=0} \quad \text{for all } k \text{ except } k = n. \quad (2.17)$$

Let us also assume that the array elements are fed by independent Thevenin sources with source impedances as indicated in Fig. 2.4a which are represented by a diagonal matrix,

$$\mathbf{Z}^s = \begin{bmatrix} Z_{11}^s & 0 & \cdots & 0 \\ 0 & Z_{22}^s & \ddots & \vdots \\ \vdots & \ddots & \ddots & 0 \\ 0 & \cdots & 0 & Z_{NN}^s \end{bmatrix}. \quad (2.18)$$

The terminal currents depend on the mutual impedance, source impedance and source voltages and are found by

$$\mathbf{I} = \{\mathbf{Z} + \mathbf{Z}^s\}^{-1} \mathbf{V}^s. \quad (2.19)$$

Similarly, the terminal voltages are given by

$$\begin{aligned} \mathbf{V} &= \mathbf{Z} \mathbf{I} \\ &= \mathbf{Z} \{\mathbf{Z} + \mathbf{Z}^s\}^{-1} \mathbf{V}^s. \end{aligned} \quad (2.20)$$

An active input impedance is the impedance of an element in an array when all of the elements are fully excited. The active input impedance of element  $n$  is determined from terminal voltages (2.20) and terminal currents (2.19) by

$$Z_n = \frac{V_n}{I_n}. \quad (2.21)$$

It is apparent from (2.19)-(2.21) that the active input impedance depends on the mutual impedance of the array. It is also important to note that the source voltages and source impedances affect the active input impedances. The result implies that the active input impedance changes as the array beam is scanned. This scan dependent effect makes it very difficult to compensate for the mutual coupling.

The radiation pattern of the array modeled by an N-port network is determined from

$$\vec{F}(\theta, \phi) = \sum_{n=1}^N \vec{g}_n^i(\theta, \phi) I_n e^{jk_o \hat{r} \cdot \vec{r}_n} \quad (2.22)$$

where isolated element patterns are used since we assumed that array element current distributions are proportional to the isolated element current distribution. Following the terminology of Kelley and Stutzman [3], (2.22) is referred to here as the *classical analysis method* because of its extensive use.

When the array is constructed from identical antenna elements their isolated element patterns are identical. Thus, the element pattern can be factored out of the summation in (2.22) giving

$$\begin{aligned} \vec{F}(\theta, \phi) &= \vec{g}^i(\theta, \phi) \sum_{n=1}^N I_n e^{jk_o \hat{r} \cdot \vec{r}_n} \\ &= \vec{g}^i(\theta, \phi) f(\theta, \phi). \end{aligned} \quad (2.23)$$

This formulation is identified as *classical analysis method with pattern multiplication*. When mutual coupling only affects the terminal current values in an array of identical elements the array radiation pattern can be determined from the multiplication of isolated element pattern and array factor based on the terminal currents given by (2.19).

The classical array pattern analysis approaches of (2.22) and (2.23) have been widely applied for many years in array analysis and synthesis. For example, Lee [15] analyzed numerical model of a  $14 \times 28$  element array of dipoles over a ground plane. Each row of the array consists of 14 co-linear dipoles. There are 28 rows of parallel dipoles in the array. The array is fed by a numerically modeled corporate feed. Each row of the array is fed by a 14:1 equal power reactive power divider. The reactive power dividers are fed by a 28:1 Wilkinson resistive power divider with variable power ratios to produce a Taylor distribution over the array. The scattering parameter descriptions of the array elements and

the feed network were used to determine the terminal currents at the array elements with and without array element mutual coupling. Then these two sets of currents were used to determine the radiation pattern with and without the element mutual coupling using (2.23) and (2.13). The computed results of the radiation patterns show over 15 dB of differences in the side lobe levels for the broadside beam. Also, Lee showed that the gain falls off more rapidly for the pattern including mutual coupling when the main beam is scanned off broadside.

The mutual coupling matrix formulation can be also used for a synthesis of the array feed network to compensate the mutual coupling effects. Smith and Stutzman [16], followed by Takamizawa and Stutzman [17], used scattering matrix descriptions of the array elements and the feed network to analyze the mutual coupling effects in 8-element array of micro-strip patches and 8-element monopole arrays. They also developed techniques to synthesize feed networks to compensate the element mutual coupling effects using attenuators and phase shifters [16] and variable ratio power dividers [17]. Their technique requires the S-parameter matrix of the antenna array and the desired terminal currents or terminal voltages to solve for the S-parameters of compensating feed network. The problem can be represented as a system of nonlinear equations which can be solved using one of many numerical techniques available. The mutual coupling compensation techniques developed by these authors are narrow-band solutions for a fixed beam scan angle.

In the numerical simulations, they showed that the desired terminal currents can be obtained using the mutual coupling compensating circuits between array elements and the feed network [16, 17]. The measured results for an eight element array of closely spaced microstrip patches did not yield the desired effects in the radiation pattern [17]. The discrepancy between the predicted and measured patterns is most likely because the mutual coupling in the experimental array was high enough that the current distribution in the antenna elements differed from the current distribution of an isolated element, and thus, violates the assumption in the derivation of classical array pattern method.

Steyskal and Herd [19] also implemented mutual coupling compensation by applying the inverse of the coupling matrix between the feed network and the array elements. Experimental verification of the mutual coupling compensation technique was accomplished with

an 8-element linear array of X-band rectangular waveguides in a ground plane. They determined the coupling matrix by measurements and Fourier decomposition of active-element patterns. The inverse of the coupling matrix was applied off-line. They demonstrated that a 30-dB Dolph-Chebyshev pattern can be synthesized using the compensation matrix for both the broadside beam and for the beam scanned to 30°.

The Steyskal and Herd [19] approach yields a good approximation to the array pattern if the relative array element current distributions are the same as an isolated element. This assumption is typically met for narrow-band single-mode elements such as dipoles or monopoles with sufficient element-to-element spacing [20]. However, for antenna arrays with small electrical spacing or wideband arrays which are constructed from elements that have multiple radiation modes, the assumption is often not met. Thus, the arrays with high mutual coupling will have radiation patterns that are significantly different from (2.22).

## 2.2.2 Active-Element Pattern Method

In cases where mutual coupling effects are significant such that element current distributions are affected, the active-element pattern method of (2.27) must be employed to evaluate the array pattern [3]. The active-element pattern is also called the scan-element pattern by some authors [21]. The active-element pattern concept was initially employed as an intermediate step in the theoretical analysis of phased array behavior [22, 23, 24]. More recently, the technique has been used as a useful tool for determination of array radiation patterns including mutual coupling effects [3, 4, 25].

The active-element pattern is determined from the radiation pattern of an antenna array when one of the elements is excited with a unit voltage and all other elements are terminated in source impedances as illustrated in Fig. 2.5. Mathematically, the *unit-input active-element pattern* of element  $n$  is determined from

$$\vec{g}_n^{au}(\theta, \phi) = \frac{1}{j\omega\epsilon} \hat{r} \times \hat{r} \times \iint\limits_{v'} \vec{j}_n^a(\vec{r}') e^{jk_o\hat{r}\cdot\vec{r}'} dv' \Big|_{V_n^s=1, V_j^s=0 \text{ for all } j \text{ except } n} \quad (2.24)$$

where  $\vec{j}_n^a$  is the currents that exist on all elements in the array when element  $n$  is excited with a unit voltage. The array pattern using the unit-input active-element pattern is determined

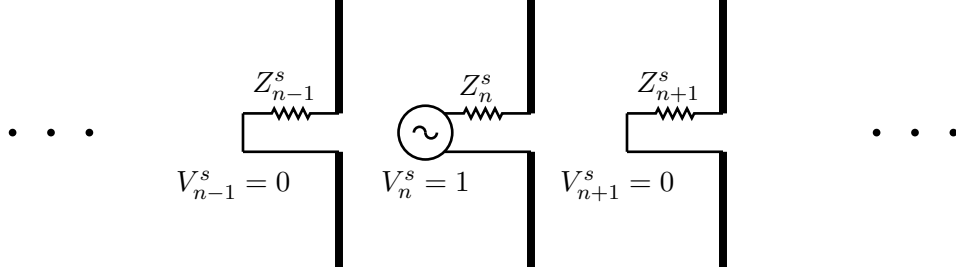


**Figure 2.5** Definition of active-element pattern for the element  $n$ .

from

$$\vec{F}(\theta, \phi) = \sum_{n=1}^N \vec{g}_n^{au}(\theta, \phi) V_n^s \quad (2.25)$$

which is identified here as the *unit-input active-element pattern* [26].

The array pattern expression of (2.25) does not explicitly show the dependence of the pattern on the array. This is in contrast to the ideal array pattern expression of (2.12) or to the classical array pattern expression of (2.22) which contain the spatial phase term  $\exp(jk_o \hat{r} \cdot \vec{r}_n)$ . In (2.24), the spatial phase information related to the element locations is implicitly contained in the active-element patterns. Kelley [26] introduced a different active-element pattern which is referred to as the *phase-adjusted unit input active-element pattern*,  $g_n^{ap}(\theta, \phi)$ . This new element pattern is defined from the unit input active-element pattern by extracting the spatial phase information using

$$g_n^{ap}(\theta, \phi) = g_n^{au}(\theta, \phi) e^{-jk_o \hat{r} \cdot \vec{r}_n}, \quad (2.26)$$

which, after substituting (2.26) into (2.25) yields the array pattern expression

$$\vec{F}(\theta, \phi) = \sum_{n=1}^N \vec{g}_n^{ap}(\theta, \phi) V_n^s e^{jk_o \hat{r} \cdot \vec{r}_n}. \quad (2.27)$$

The array pattern computed from individual active-element patterns using (2.25) or (2.27) is exact as long as the source impedances are used to determine the active-element patterns. If the elements are fed individually by transmitters, then the correct source impedance values are internal impedances of transmitters. These values stay constant as the relative phases of the transmitters are varied to scan the beam. On the other hand, if the

array elements are fed by a reactive power divider feed network, the equivalent Thevenin source impedances will change as the beam is scanned. In this case, the active-element patterns must be determined for each scan angle as the element excitations are changed.

When an array is constructed from a large number of uniformly spaced identical elements and they are fed by identical transmitters, the interior elements in the array see a similar environment surrounding them. It is then possible to approximate the active-element patterns by their average value. Using the average active-element pattern,  $\bar{g}^a(\theta, \phi)$ , the array radiation pattern becomes

$$\begin{aligned}\vec{F}(\theta, \phi) &= \bar{g}^a(\theta, \phi) \sum_{n=1}^N V_n^i e^{jk_o \hat{r} \cdot \vec{r}_n} \\ &= \bar{g}^a(\theta, \phi) f^i(\theta, \phi).\end{aligned}\tag{2.28}$$

which is referred here as the *average active-element pattern*. It should be noted that the array factor  $f^i(\theta, \phi)$  in (2.28) which is based on the terminal voltages is identical to that of ideal array method in (2.14) which is based on the terminal currents. In the active-element pattern methods,

The array factors in two equations are the same because the terminal voltages and currents in both methods are proportional to each other when the mutual coupling is ignored.

It is also possible to apply average active-element patterns only on the internal elements of the array, and retain the individual active-element patterns for the edge elements. Kelley and Stutzman [3] developed such a hybrid active-element pattern method. They have shown that for a 7-element parallel dipole array, the hybrid method results are very close to the full active-element pattern method [3].

### 2.2.3 Network Descriptions of Arrays including Radiation Ports

In Sec. 2.2.1, we discussed the classical array pattern method where the terminal currents and voltages of an  $N$ -element antenna array is determined from an  $N$ -port network matrix. In this  $N$ -port description of the array elements, the power radiated from the array and the power dissipated in the array as ohmic loss are indistinguishable. Although we can compute the radiated power from the radiation pattern expression of (2.22), it is not possible to separate the radiated power and the ohmic loss from  $N$ -port matrix by itself. This deficiency

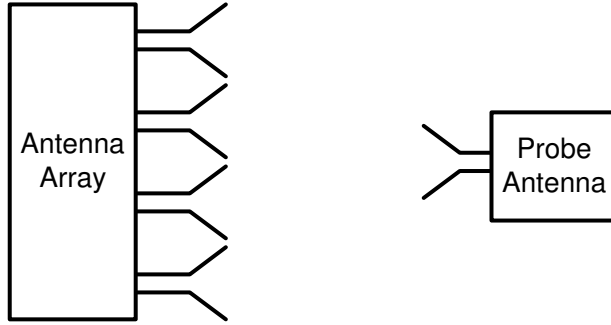


**Figure 2.6** An arbitrary antenna array and distant probe antenna.

in the  $N$ -port description can be over come by introducing a radiation port to the network model to characterize the radiated power [27, 28, 29, 30, 31, 32, 33]. Then, an  $N$  element antenna array is described by an  $N + M$  port network, where  $M$  ports are used to describe the radiated power.

Harrington [27] represented the radiated power of an array with an additional port in the network model. The radiated power is detected as a terminal current and a voltage by a probe antenna at some distance away from the array as illustrated in Fig. 2.6. In his model, the radiation port is a function of the type of probe antenna and its location. The network with the antenna array and the probe antenna is described by a matrix equation of order  $N + 1$ ,

$$\begin{bmatrix} \mathbf{V}_a \\ V_p \end{bmatrix} = \begin{bmatrix} \mathbf{Z}_{aa} & \mathbf{Z}_{ap} \\ \mathbf{Z}_{pa} & Z_{pp} \end{bmatrix} \begin{bmatrix} \mathbf{I}_a \\ I_p \end{bmatrix} \quad (2.29)$$

where  $\mathbf{Z}_{aa}$  is the impedance matrix of the array identical to (2.16),  $Z_{pp}$  is the input impedance of the probe antenna, and  $\mathbf{Z}_{ap}$  and  $\mathbf{Z}_{pa}$  are coupling impedances between the antenna array and the probe antenna. Using this model, Harrington showed that the gain of the array is determined from

$$G = K \frac{\mathbf{I}_a^\dagger \mathbf{Z}_{pa}^\dagger \mathbf{Z}_{pa} \mathbf{I}_a}{\mathbf{I}_a^\dagger [\mathbf{Z}_{aa} + \mathbf{Z}_{aa}^\dagger] \mathbf{I}_a} \quad (2.30)$$

where  $\mathbf{I}_a$  are terminal currents and  $K$  is a constant related to the receiving aperture of the test antenna [27]. By taking the derivatives of (2.30) with respect to terminal currents, we can determine the terminal currents required to maximize the gain of the array. When

element spacings are small, the solution yields required terminal currents for a super-gain array [27].

Instead of representing the radiated field by power detected at the probe antenna port, Kahn and Wasyliwskyj [28], and Gately et al. [29] used an infinite set of orthogonal spherical vector wave functions to directly represent the radiated electric field of the array. Consequently, the resulting S-parameter matrix is an infinite order square matrix.

Gately [29] analyzed the Yagi-Uda antenna using the network formulation. He computed the radiation pattern of a 20-element Yagi-Uda antenna using the network theory and then compared to measured patterns. The results show that computed patterns compared well with the experimental data. Gately also analyzed loading the parasitic elements in Yagi-Uda antenna with active loads. He demonstrated that a 3 dB increase in the simulated directivity of the 20-element Yagi-Uda antenna can be implemented by loading the parasitic elements with active loads with negative resistances or amplifiers [29].

Perhaps the most popular use of the spherical vector expansion of the fields detected by the probe is in spherical near-field antenna measurements [32, 33]. In spherical near-field antenna measurements, the detected power at the probe antenna is represented by a truncated series of vector spherical expansion modes. Then, the near-field to far-field transformation is applied to this series to determine the far-field radiation pattern of the antenna under test.

Wiesbeck and Heindrich [30] extended Harrington's formulation of a  $N+1$  port network by representing the radiated power by two radiation ports for two orthogonal polarizations. They used conventional network scattering parameters to represent radiation ports. However, instead of using the coupling between the test antenna and the probe, they used RCS measurements of the antenna when it is loaded with either an open, short, or matched load to determine the antenna radiation S-parameters. The measurement setup used by Wiesbeck and Heindrich [30] is related to the remote impedance measurement method developed by Caswell and Davis [34].

There are many advantages to including the radiation ports in the network representations of the single element antenna model and the antenna array model. Unfortunately, the formulations derived by previous authors are not well known. Perhaps these techniques

are unknown to typical antenna engineers because it is difficult to directly apply measured data in the forms derived by these authors. The network based analysis method presented in Chapters 3 and 4 are based on the same concept. In this new model, only conventional S-parameters are used to represent antenna arrays which makes it easy to apply on experimental investigations.

## 2.3 Infinite Array Analysis

Large, uniform, periodic, antenna arrays are usually evaluated using one of two methods. In the first method, the performance of the large array is characterized by evaluating a subset of the antenna array using methods discussed in Sections 2.1 and 2.2, and the results are projected for a larger array as the number of elements in the subset array are increased [35]. The analysis of a subset array very quickly becomes impractical as the number of elements is increased due to excessive storage and computational time required. The second method takes advantage of the periodic nature of the array. The large array performance is estimated by evaluating an equivalent infinite array assuming periodic boundary conditions around an element in the array grid [35, 21, 14].

The direct approach to infinite array analysis of a large antenna array uses the periodicity of the array grid to expand the fields in a Fourier series of modes with an additional linear phase taper to account for the beam scanning. The linear phase taper within a grid is determined from the desired beam scan direction in the analysis. This type of expansion is referred as a Floquet series expansion [5]. Many researchers have found Floquet series of increasing complexity to model infinite array structures [36, 37, 38, 39, 39, 40, 41, 42, 43, 44, 45].

The important part of infinite array analysis is the identification of scan blindness in the array. Scan blindness is a condition that results from array mutual coupling such that a complete cancellation of the radiation pattern occur at certain scan angles. The scan blindness can also be identified by a nearly unity reflection coefficient of the fully excited array elements [35]. Since the active-element pattern is also related to the element reflection coefficient of an infinite array, scan blindness can also be identified by nulls in

the active-element pattern [21, 4]. Pozar and Schaubert [36] analyzed scan blindness in an infinite array of strip dipoles printed on a dielectric substrate. Pozar [20] later analyzed a finite strip dipole array of the same geometry to numerically demonstrate the relationship between active-element patterns of  $7 \times 7$  and  $19 \times 19$  arrays and the equivalent infinite array.

The element pattern is also related to the impedance mismatch in the array as the main beam is scanned. Wheeler introduced the concept of an infinite current sheet to study the relationship between beam scan angle and scan impedance of a large array [46, 47]. A current sheet is a hypothetical array consisting of many small dipoles closely spaced in a rectangular grid which is backed by a open circuit boundary condition, or small magnetic dipoles in a rectangular grid backed by a short circuit boundary. Wheeler assumes that the input resistance of ideal current sheet is matched to the intrinsic impedance of free space,  $\eta$ , at broadside. Then, Wheeler [47] showed that the input resistance of an element in the fully active current sheet array is given by

$$R_r(\theta) = \frac{\eta l^2}{A \cos \theta} \{g(\theta)\}^2 \quad (2.31)$$

where  $l$  is the effective length of a small dipole,  $A \cos \theta$  is the projected area of a cell in a square grid array, and  $g(\theta)$  is the isolated element pattern of the small dipole. If the source impedance is matched to the resistance of the current sheet elements at broadside, then the reflection coefficient of the elements as a function of scan angle is given by

$$\rho(\theta) = \frac{R_r(\theta) - R_r(0)}{R_r(\theta) + R_r(0)}. \quad (2.32)$$

Using the facts that the E-plane and H-plane patterns of a short dipole are  $\cos \theta$  and 1, respectively, Wheeler showed that the reflection coefficient of infinite current sheet with short dipoles is given by

$$\rho(\theta) = \frac{\cos \theta - 1}{\cos \theta + 1} = -\tan^2\left(\frac{\theta}{2}\right) \quad (2.33)$$

for the E-plane scan and

$$\rho(\theta) = \frac{1 - \cos \theta}{1 + \cos \theta} = \tan^2\left(\frac{\theta}{2}\right). \quad (2.34)$$

for the H-plane scan. Plots of reflection coefficient values as a function of scan angle in the E-plane and the H-plane by infinite current sheet are shown in Fig. 2.7.

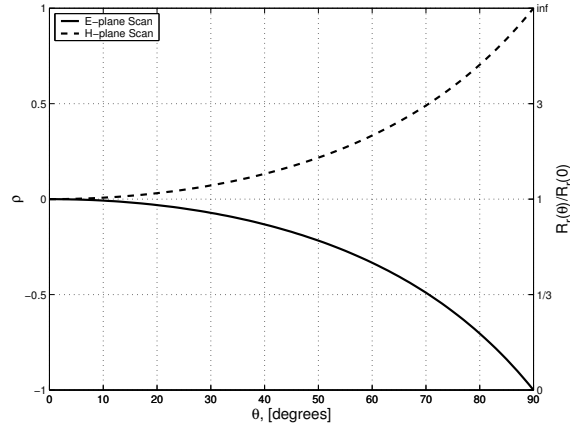


**Figure 2.7** The variation of reflection with scan angle, in the idealized current sheet array with small electric dipole elements computed using (2.33) and (2.34).

Pozar [48] developed models similar to the infinite current sheet model for analysis of printed phased array antennas based on a few low-order Floquet modes for the array geometries. Using this analysis, he evaluated scan characteristics of an infinite dipole array in free space, an infinite dipole array  $1/4\lambda$  above a ground plane, and an infinite dipole array on a grounded dielectric substrate. Also, the properties of the same arrays were evaluated using full Floquet analysis. Pozar [48] found that dominant scanning characteristics of printed phased arrays such as input impedance, scan blindness, and grating lobe effects are controlled by array geometry factors such as element spacing and substrate geometry rather than by a particular type of element used in the array.

## 2.4 Wideband Arrays

Conventional antenna arrays are typically bandwidth limited in two ways; the lower frequency band of operation is limited by the bandwidth of the individual elements in the array, and the higher frequency band is limited by the formation of grating lobes due to increasing inter-element spacing in terms of wavelength. Additional constraint on the high frequency limit arises from the decreasing requirement on the inter-element spacing as the beam scan angle is increased. The effect of inter-element spacing poses conflicting requirement in designing wideband arrays. It is desirable for inter-element spacing to be small to

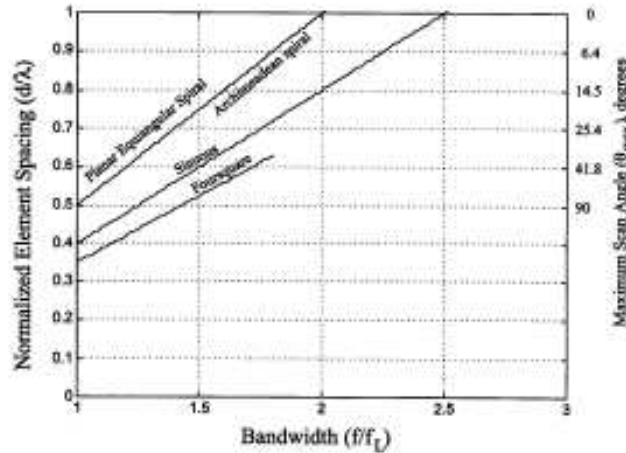


**Figure 2.8** Minimum element spacing normalized to wavelength as a function of normalized frequency for various element types. The right ordinate shows maximum scan angle.

satisfy the high frequency and the beam scan angle requirements. However, the minimum inter-element spacing is limited by the antenna element size and mutual coupling effect.

The relationship between the maximum beam scan angle, the bandwidth, and the element spacing was studied by Stutzman and Buxton [49, 6]. Figure 2.8 shows minimum element spacing normalized to wavelength as a function of normalized frequency for Archimedean and equiangular spirals, sinuous, and Foursquare. These four elements are low-profile wideband radiating elements which produce unidirectional beam when they are operated over a ground plane. The plot shows that sinuous and Archimedean spirals have wider bandwidth than Foursquare as an isolated element. However, in the array environment, Foursquare can be packed more closely with less inter-element spacing than the other elements, allowing higher array bandwidth for a given maximum scan angle. For example, for 40 degree maximum scan angle, Foursquare can achieve over 1.7:1 bandwidth while sinuous can only achieve 1.5:1 maximum bandwidth as shown in Fig. 2.8. Thus, the array bandwidth is very closely related to the physical shape and size of the antenna element used in the array.

Many investigations were conducted on the wideband antenna elements and wideband array configurations. The selection of array element has major effects on the array geometries that can be implemented. A survey of wideband array literature is given by Caswell[50].

Three types of wideband arrays that are reported in recent literature are of particular interest: arrays using flared slot antenna element, wideband array using variable element sizes (WAVES), and Foursquare arrays.

One of the most popular antenna elements that is studied by many researchers for wideband array applications is tapered-slot antenna [51, 52, 53, 54, 55, 56, 57, 58]. There are also many antennas that are derivative of tapered-slot antenna, such as flared-slot, flared-notch, Vivaldi, and double-slot cross-notch antennas. Kragalott, et al. [58], report on a design of a stripline flared-notch array based on FDTD analysis. They used an experimental  $8 \times 8$  array of flared-notch array with 5:1 bandwidth to demonstrate that scan up to  $50^\circ$  in both E-plane and H-plane.

Caswell [50] used simulations and experiments of a unique wideband array with star spiral antenna elements. The star spiral is a type of slow-wave spiral antenna element that has 17% reduction in size compared to a circular Archimedean spiral. The size reduction allows closer packing of the star spiral element to increase the array bandwidth. The star spiral is a suitable element for application in wideband arrays with variable element sizes (WAVES) configuration which was first introduced by Stutzman [59]. A three octave array using 3 different sizes of star spirals in a WAVES configuration was designed, and its performance was experimentally verified [50]. The measured array patterns and input impedances was shown to match well with the computed results.

The Foursquare antenna element, patented by Nealy [60] in 1999, offers several advantages, including wideband bandwidth, low-profile geometry, similar E-plane and H-plane beam widths, nearly equal radiation patterns over the bandwidth, and dual linear polarizations. A detailed description of the Foursquare antenna and the analysis of Foursquare array are discussed in Chapter 6. Buxton [6] analyzed the Foursquare antenna, and an array of closely packed Foursquare elements. The impedance bandwidth of an isolated Foursquare antenna, a  $3 \times 3$  array of Foursquares, and an infinite array of Foursquares were computed based on FDTD analysis. The simulations demonstrated that the percent bandwidth of closely packed Foursquare will progressively increase as the size of the array is increased from a single isolated Foursquare element, to the  $3 \times 3$  array, and then to the infinite array.

## 2.5 Summary

Many array antenna analysis methods have been developed in an effort to predict the effects of mutual coupling on array performance. The techniques reviewed in this chapter can be utilized to investigate highly coupled wideband arrays to some extent. These techniques are inadequate for understanding of the operational principles of highly coupled arrays. In the following two chapters, we develop a new scattering parameter based network model for the analysis of a single antenna and antenna arrays.

## Chapter 3

# Network Description of Single Antenna Elements

Antenna design involves many electrical and mechanical parameters. The most important electrical parameters include radiation patterns, gain, directivity, input impedance, bandwidth, and efficiency. As might be expected, these parameters are not independent. Thus, a typical antenna design involves trade-offs among the parameters. The mutual dependence of the electrical parameters becomes more complex in antenna arrays. In fact, the complex nature of the antenna parameter dependence sometimes causes confusion even among experienced antenna engineers. There is a need for a technique that integrates the treatment of all the antenna parameters in a systematic way during the design process. Network descriptions of antenna systems allow the integration of some of the antenna electrical parameters. Similar ideas have been published in the last 30 years in various forms [27, 28, 29, 32, 30, 31, 61].

This chapter develops a new form of network description of an antenna system based on scattering parameters or S-parameters of an antenna element and its radiation pattern. In this formulation, antenna radiation is considered in terms of electromagnetic coupling between the test antenna and a probe antenna. The radiation pattern is defined by the power received by the probe antenna moved around a constant distance from the antenna under test operating in the transmit mode. The S-parameter model of a single antenna in

a transmitting system will be derived in the next section. The model is general such that it can be applied to any antenna type. The relationship between the antenna S-parameter model and the antenna electrical parameters will be demonstrated. This relationship will aid in understanding the S-parameter network model, providing the foundation for the extension of the formulation to antenna arrays in the following chapter.

### 3.1 Derivation of an S-parameter Network Model

In this section we develop a network description of a single antenna fed by a transmitter. Consider an arbitrary test antenna with an input port and a distant probe antenna with two ports as illustrated in Fig. 3.1. In general, an antenna can be used either for receiving or for transmitting signals. We will consider the transmitting antenna model where the test antenna is connected to a transmitter and the probe antenna is connected to a receiver. Reciprocity guarantees that the receiving antenna pattern of the test antenna will be identical to the transmitting pattern, as long as the antenna is located in a linear, passive, and isotropic propagation medium [12].

The probe antenna is used to detect the radiated fields of the test antenna. We assume

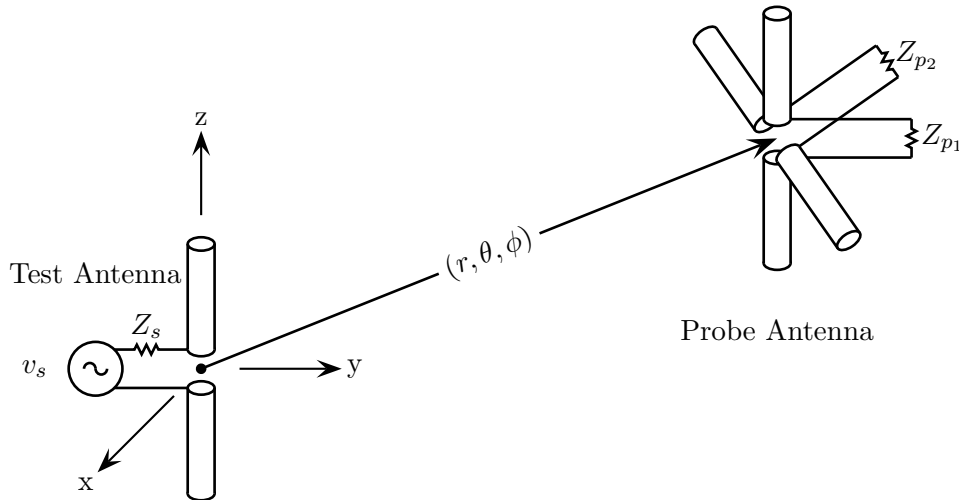


**Figure 3.1** An arbitrary test antenna fed with a source with internal impedance  $Z_s$  and a distant probe antenna with two orthogonal polarization elements.

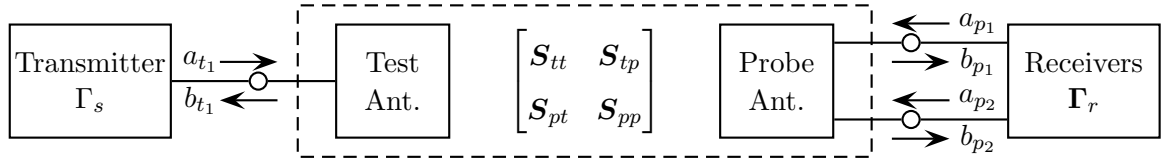
that the probe antenna is a linear passive device with a radiation pattern having a peak realized gain of  $G_{R_p}$ . The probe antenna is located at variable angles  $(\theta, \phi)$  and a constant distance  $r$ , which is sufficiently away from the test antenna that the interaction between the AUT and the probe antenna is negligible. It is oriented such that the probe pattern peak always points toward the test antenna at the center of probing sphere as the  $(\theta, \phi)$  angles are varied. The probe antenna has two ports which are used to detect two orthogonal polarizations. In the illustration in Fig. 3.1, an ideal crossed dipole is used to detect the vertical and horizontal polarizations. However, the choice of polarization pair is arbitrary as long as they are orthogonal to each other. Any other polarization can be determined from a linear combination of a pair of orthogonal polarizations [62] as long as both amplitude and phase informations are included in the patterns.

The test antenna port and the two probe antenna ports form a three port network whose terminal characteristics can be described by a  $3 \times 3$  matrix. The antenna ports can represent physical terminals of the antenna structure or can represent a reference plane defined somewhere in the feed line of the antenna. The three port network can be characterized using standard network theory. For measurement convenience at microwave frequencies, the scattering parameter  $\mathbf{S}$ , or S-parameter matrix, is chosen to describe the network. Using scattering parameter notation, the three port network at a given frequency is described by

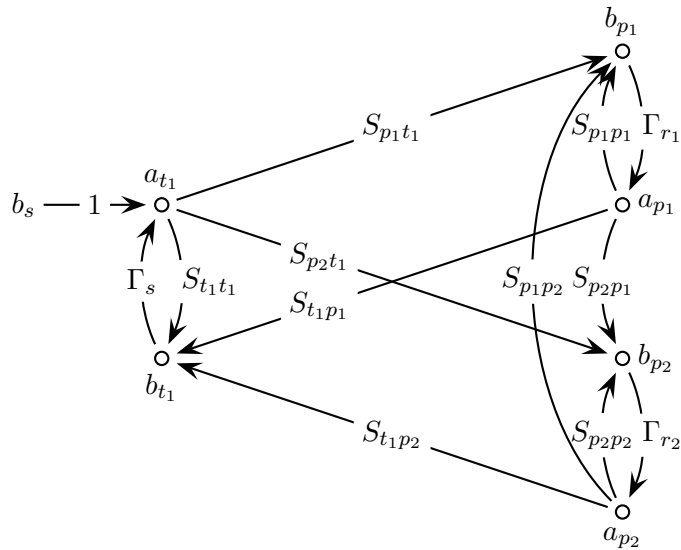
$$\mathbf{b}(r, \theta, \phi) = \mathbf{S}(r, \theta, \phi)\mathbf{a}(r, \theta, \phi) \quad (3.1)$$

where  $\mathbf{a}$  and  $\mathbf{b}$  represent the waves in and out of the network ports, respectively [63]. Bold symbols are used in (3.1) to represent column vectors for  $\mathbf{a}$  and  $\mathbf{b}$  and a square matrix for  $\mathbf{S}$ . The S-matrix equation in (3.1) contains an extension from the usual network S-parameter definition. The arguments  $(r, \theta, \phi)$  for all variables are used to explicitly show that they depend on the distance and the relative angular position of the probe antenna with respect to the test antenna.

The signal flow diagram for the transmit antenna model is shown in Fig. 3.2. The diagram assumes that there is no coupling between two receivers at ports  $p_1$  and  $p_2$ . Using



(a)



(b)

**Figure 3.2** Signal flow diagram for an arbitrary test antenna and a probe antenna with two orthogonal polarization ports.

the signal names defined in Fig. 3.2, the matrix equation (3.1) is expanded to

$$\begin{bmatrix} b_{t_1}(r, \theta, \phi) \\ b_{p_1}(r, \theta, \phi) \\ b_{p_2}(r, \theta, \phi) \end{bmatrix} = \begin{bmatrix} S_{t_1 t_1}(r, \theta, \phi) & S_{t_1 p_1}(r, \theta, \phi) & S_{t_1 p_2}(r, \theta, \phi) \\ S_{p_1 t_1}(r, \theta, \phi) & S_{p_1 p_1}(r, \theta, \phi) & S_{p_1 p_2}(r, \theta, \phi) \\ S_{p_2 t_1}(r, \theta, \phi) & S_{p_2 p_1}(r, \theta, \phi) & S_{p_2 p_2}(r, \theta, \phi) \end{bmatrix} \begin{bmatrix} a_{t_1}(r, \theta, \phi) \\ a_{p_1}(r, \theta, \phi) \\ a_{p_2}(r, \theta, \phi) \end{bmatrix}, \quad (3.2)$$

or in the compressed form as,

$$\begin{bmatrix} \mathbf{b}_t(r, \theta, \phi) \\ \mathbf{b}_p(r, \theta, \phi) \end{bmatrix} = \begin{bmatrix} \mathbf{S}_{tt}(r, \theta, \phi) & \mathbf{S}_{tp}(r, \theta, \phi) \\ \mathbf{S}_{pt}(r, \theta, \phi) & \mathbf{S}_{pp}(r, \theta, \phi) \end{bmatrix} \begin{bmatrix} \mathbf{a}_t(r, \theta, \phi) \\ \mathbf{a}_p(r, \theta, \phi) \end{bmatrix} \quad (3.3)$$

The subscripts  $t$  and  $p$  are used to represent the test antenna and the probe antenna. The S-parameters  $S_{t_1 t_1}(\theta, \phi)$ ,  $S_{p_1 p_1}(\theta, \phi)$  and  $S_{p_2 p_2}(\theta, \phi)$  are the reflection coefficients of the test antenna and probe antenna elements in the modeled environment. When the probe antennas are sufficiently far away from the test antenna, the test antenna reflection coefficient is very close to the corresponding reflection coefficient of the test antenna in an isolated environment. The same characteristics also hold for the probe reflection coefficients. Thus, we model these S-parameters as independent of  $(\theta, \phi)$  angles, and present them without the angular arguments.

The S-parameters,  $S_{p_1 p_2}(\theta, \phi)$  and  $S_{p_2 p_1}(\theta, \phi)$ , represent the forward and reverse mutual coupling between the two probe antenna polarization ports. We will treat the probe antenna to be a reciprocal device and independent of the probe position such that

$$S_{p_2 p_1} = S_{p_1 p_2}. \quad (3.4)$$

When the probe antenna is chosen properly, there should be only a small coupling between two polarization ports. This assumption is usually valid in typical antenna measurement facilities where two polarization measurements are conducted separately using a single probe antenna with good polarization purity.

Finally,  $S_{p_1 t_1}(r, \theta, \phi)$ ,  $S_{p_2 t_1}(r, \theta, \phi)$ ,  $S_{t_1 p_1}(r, \theta, \phi)$  and  $S_{t_1 p_2}(r, \theta, \phi)$  are the coupling coefficients between the test antenna and the probe antenna. We assume a linear, passive, and isotropic propagation medium in the model such that the forward couplings (the first column of the S-matrix) and the corresponding reverse couplings (the first row of the S-matrix) are identical, or

$$S_{p_1 t_1}(r, \theta, \phi) = S_{t_1 p_1}(r, \theta, \phi) \quad (3.5a)$$

$$S_{p_2 t_1}(r, \theta, \phi) = S_{t_1 p_2}(r, \theta, \phi). \quad (3.5b)$$

Based on (3.4) and (3.5), the complex valued S-matrix in (3.2) is a symmetric matrix such that

$$\mathbf{S} = \mathbf{S}^T \quad (3.6)$$

where  $T$  is a simple transpose operator that does not include complex conjugate. The self-transpose relationship for  $S$  is a required condition for a reciprocal network.

In the transmit antenna pattern configuration, a transmitter circuit is connected to the test antenna and two receiver circuits are connected to the probe antenna. The reflection coefficients of the transmitter circuit with source impedance of  $Z_s$ , and the receiver circuit with load impedances of  $Z_{p_1}$  and  $Z_{p_2}$  are determined by [63, 64]

$$\Gamma_s = \frac{Z_s - Z_o}{Z_s + Z_o^*} \quad (3.7a)$$

$$\Gamma_{r_1} = \frac{Z_{p_1} - Z_o}{Z_{p_1} + Z_o^*} \quad (3.7b)$$

$$\Gamma_{r_2} = \frac{Z_{p_2} - Z_o}{Z_{p_2} + Z_o^*} \quad (3.7c)$$

where  $Z_o$  is the reference impedance and  $*$  is the complex conjugate operator. The impedance to S-parameter transforms in (3.7) use the generalized S-parameter form such that the reference impedance can be a complex value. The same reference impedance is used to characterize the antenna element in the analysis. In practice, we generally use a real valued reference impedance of  $Z_o = 50 \Omega$ .

The variables  $\mathbf{b}_p$  and  $\mathbf{a}_p$  in (3.3) represent the output waves that come out of the probe antenna ports and the waves that are reflected from the receivers back to the probe antenna ports. Assuming that  $\mathbf{a}_p$  and  $\mathbf{b}_p$  are in RMS form, the powers delivered from the test antenna to the probe antenna ports are given by

$$P_{del_{p_1}}(r, \theta, \phi) = |b_{p_1}(r, \theta, \phi)|^2 - |a_{p_1}(r, \theta, \phi)|^2 \quad (3.8a)$$

$$P_{del_{p_2}}(r, \theta, \phi) = |b_{p_2}(r, \theta, \phi)|^2 - |a_{p_2}(r, \theta, \phi)|^2 \quad (3.8b)$$

for each polarization component. The delivered powers as functions of angular position of the probe antenna are proportional to the antenna power patterns of the test antenna. The

delivered power is determined by applying Mason's rule [65] on the S-parameters in the signal flow diagram in Fig. 3.2. The resulting output waves from the probe antenna ports are given by

$$\begin{aligned}
b_{p_1}(r, \theta, \phi) = & \left\{ \left[ S_{p_1 t_1}(r, \theta, \phi) \{ 1 - S_{p_2 p_2} \Gamma_{r_2} \} + S_{p_2 t_1}(r, \theta, \phi) \Gamma_{r_2} S_{p_1 p_2} \right] b_s \right\} / \\
& \left\{ 1 - \left[ S_{t_1 t_1} \Gamma_s + S_{p_1 p_1} \Gamma_{r_1} + S_{p_2 p_2} \Gamma_{r_2} + S_{p_1 t_1}(r, \theta, \phi) \Gamma_{r_1} S_{t_1 p_1}(r, \theta, \phi) \Gamma_s \right. \right. \\
& + S_{p_2 t_1}(r, \theta, \phi) \Gamma_{r_2} S_{t_1 p_2}(r, \theta, \phi) \Gamma_s + S_{p_1 t_1}(r, \theta, \phi) \Gamma_{r_1} S_{p_2 p_1} \Gamma_{r_2} S_{t_1 p_2}(r, \theta, \phi) \Gamma_s \\
& + S_{p_2 t_1}(r, \theta, \phi) \Gamma_{r_2} S_{p_1 p_2} \Gamma_{r_1} S_{t_1 p_1}(r, \theta, \phi) \Gamma_s + S_{p_1 p_2} \Gamma_{r_1} S_{p_2 p_1} \Gamma_{r_2} \left. \right] \\
& + \left[ S_{t_1 t_1} \Gamma_s S_{p_1 p_1} \Gamma_{r_1} + S_{t_1 t_1} \Gamma_s S_{p_2 p_2} \Gamma_{r_2} + S_{p_1 p_1} \Gamma_{r_1} S_{p_2 p_2} \Gamma_{r_2} \right. \\
& + S_{p_1 t_1}(r, \theta, \phi) \Gamma_{r_1} S_{t_1 p_1}(r, \theta, \phi) \Gamma_s S_{p_2 p_2} \Gamma_{r_2} \\
& + S_{p_2 t_1}(r, \theta, \phi) \Gamma_{r_2} S_{t_1 p_2}(r, \theta, \phi) \Gamma_s S_{p_1 p_1} \Gamma_{r_1} + S_{p_1 p_2} \Gamma_{r_1} S_{p_2 p_1} \Gamma_{r_2} S_{t_1 t_1} \Gamma_s \left. \right] \\
& \left. - S_{t_1 t_1} \Gamma_s S_{p_1 p_1} \Gamma_{r_1} S_{p_2 p_2} \Gamma_{r_2} \right\} \tag{3.9a}
\end{aligned}$$

$$\begin{aligned}
b_{p_2}(r, \theta, \phi) = & \left\{ \left[ S_{p_2 t_1}(r, \theta, \phi) \{ 1 - S_{p_1 p_1} \Gamma_{r_1} \} + S_{p_1 t_1}(r, \theta, \phi) \Gamma_{r_1} S_{p_2 p_1} \right] b_s \right\} / \\
& \left\{ 1 - \left[ S_{t_1 t_1} \Gamma_s + S_{p_1 p_1} \Gamma_{r_1} + S_{p_2 p_2} \Gamma_{r_2} + S_{p_1 t_1}(r, \theta, \phi) \Gamma_{r_1} S_{t_1 p_1}(r, \theta, \phi) \Gamma_s \right. \right. \\
& + S_{p_2 t_1}(r, \theta, \phi) \Gamma_{r_2} S_{t_1 p_2}(r, \theta, \phi) \Gamma_s + S_{p_1 t_1}(r, \theta, \phi) \Gamma_{r_1} S_{p_2 p_1} \Gamma_{r_2} S_{t_1 p_2}(r, \theta, \phi) \Gamma_s \\
& + S_{p_2 t_1}(r, \theta, \phi) \Gamma_{r_2} S_{p_1 p_2} \Gamma_{r_1} S_{t_1 p_1}(r, \theta, \phi) \Gamma_s + S_{p_1 p_2} \Gamma_{r_1} S_{p_2 p_1} \Gamma_{r_2} \left. \right] \\
& + \left[ S_{t_1 t_1} \Gamma_s S_{p_1 p_1} \Gamma_{r_1} + S_{t_1 t_1} \Gamma_s S_{p_2 p_2} \Gamma_{r_2} + S_{p_1 p_1} \Gamma_{r_1} S_{p_2 p_2} \Gamma_{r_2} \right. \\
& + S_{p_1 t_1}(r, \theta, \phi) \Gamma_{r_1} S_{t_1 p_1}(r, \theta, \phi) \Gamma_s S_{p_2 p_2} \Gamma_{r_2} \\
& + S_{p_2 t_1}(r, \theta, \phi) \Gamma_{r_2} S_{t_1 p_2}(r, \theta, \phi) \Gamma_s S_{p_1 p_1} \Gamma_{r_1} + S_{p_1 p_2} \Gamma_{r_1} S_{p_2 p_1} \Gamma_{r_2} S_{t_1 t_1} \Gamma_s \left. \right] \\
& \left. - S_{t_1 t_1} \Gamma_s S_{p_1 p_1} \Gamma_{r_1} S_{p_2 p_2} \Gamma_{r_2} \right\} \tag{3.9b}
\end{aligned}$$

The derivation of (3.9) is summarized in Appendix A. Using the output waves from (3.9) the waves reflected from the receivers to the probe ports are determined by

$$a_{p_1}(r, \theta, \phi) = \Gamma_{r_1} b_{p_1}(r, \theta, \phi) \tag{3.10a}$$

$$a_{p_2}(r, \theta, \phi) = \Gamma_{r_2} b_{p_2}(r, \theta, \phi). \tag{3.10b}$$

It is clear from equations (3.8), (3.9) and (3.10) that the powers detected at the probe antenna ports are bi-linear functions of forward and reverse couplings between the test antenna and the probe antenna. These detected signals represent radiation patterns in orthogonal polarizations that are measured by a typical uncalibrated antenna range.

When the receiver load impedances are set to the reference impedance,  $Z_{p_1} = Z_{p_2} = Z_o$ , the reflection coefficients of the receivers become zero,  $\Gamma_{r_1} = \Gamma_{r_2} = 0$ . Then, the probe incident waves in (3.10) become

$$a_{p_1}(r, \theta, \phi) = \Gamma_{r_1} b_{p_1}(r, \theta, \phi) = 0 \quad (3.11a)$$

$$a_{p_2}(r, \theta, \phi) = \Gamma_{r_2} b_{p_2}(r, \theta, \phi) = 0. \quad (3.11b)$$

Thus, the delivered powers at the probe ports simplify to

$$P_{del_{p_1}}(r, \theta, \phi) = |b_{p_1}(r, \theta, \phi)|^2 \quad (3.12a)$$

$$P_{del_{p_2}}(r, \theta, \phi) = |b_{p_2}(r, \theta, \phi)|^2 \quad (3.12b)$$

The reflected waves in (3.9) can also be significantly simplified. In the numerator, all but the first term includes  $\Gamma_{r_1}$  or  $\Gamma_{r_2}$ , and thus, they become zero. Similarly, all but the first two terms in the denominator includes  $\Gamma_{r_1}$  or  $\Gamma_{r_2}$ , and thus, they also become zero.

Fig. 3.3 shows the modified signal flow diagram including the assumptions and the simplifications. The negligible signal paths are shown with dotted lines in Fig. 3.3. The output waves from the probes coupled from the test antenna,  $p_1$  and  $p_2$ , become

$$b_{p_1}(r, \theta, \phi) = S_{p_1 t_1}(r, \theta, \phi) a_{t_1}(r, \theta, \phi) = S_{p_1 t_1}(r, \theta, \phi) [1 - \Gamma_s S_{t_1 t_1}]^{-1} b_s \quad (3.13a)$$

$$b_{p_2}(r, \theta, \phi) = S_{p_2 t_1}(r, \theta, \phi) a_{t_1}(r, \theta, \phi) = S_{p_2 t_1}(r, \theta, \phi) [1 - \Gamma_s S_{t_1 t_1}]^{-1} b_s. \quad (3.13b)$$

Finally, the powers delivered to the probe antenna ports are determined by substituting (3.13) into (3.12), giving

$$P_{del_{p_1}}(r, \theta, \phi) = \left| S_{p_1 t_1}(r, \theta, \phi) a_{t_1} \right|^2 = \left| S_{p_1 t_1}(r, \theta, \phi) [1 - \Gamma_s S_{t_1 t_1}]^{-1} b_s \right|^2 \quad (3.14a)$$

$$P_{del_{p_2}}(r, \theta, \phi) = \left| S_{p_2 t_1}(r, \theta, \phi) a_{t_1} \right|^2 = \left| S_{p_2 t_1}(r, \theta, \phi) [1 - \Gamma_s S_{t_1 t_1}]^{-1} b_s \right|^2. \quad (3.14b)$$

Equations (3.13) or (3.14) represent the basic antenna network model for a single antenna. They include the antenna radiation pattern, polarization, input impedance, and

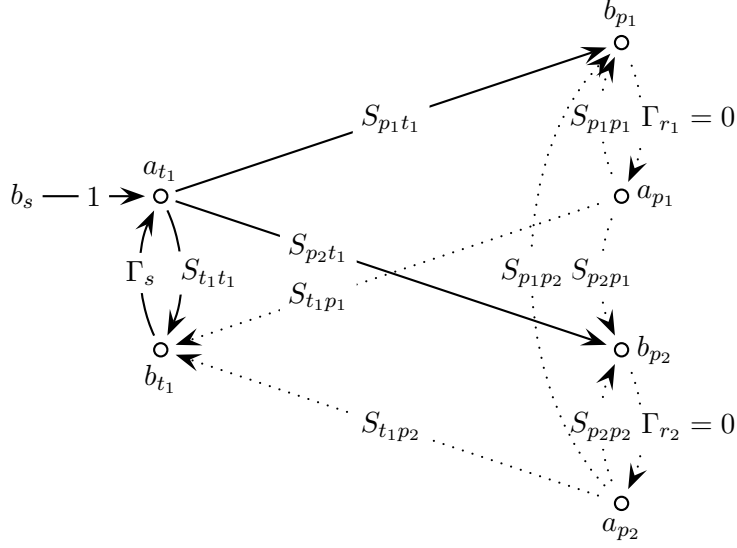
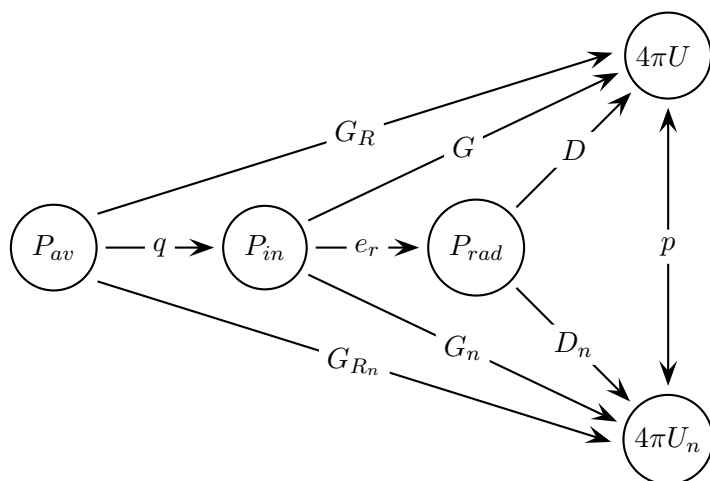


**Figure 3.3** Simplified signal flow diagram for an arbitrary test antenna and a probe antenna with two orthogonal polarization ports.

efficiency in a compact form. In the next section, we develop the specific relationship between these antenna parameters and the antenna network equation.

### 3.2 Relationship between Antenna Network Model and Antenna Parameters

Before we can discuss the relationship between the antenna network model developed in the previous section and the antenna design parameters, it is important that we clearly define the antenna design parameters. Historically, terms such as “Gain” have been used very loosely with various definitions. In this dissertation, we will follow the IEEE Standard 145-1993[66]. The terms that are not well defined by IEEE will be specifically defined. The chart in Fig. 3.4, modified from IEEE Std. 145-1993, aids in the understanding of the definition of various gains, directivities, and efficiencies. The gains and directivity in the upper half of the chart are the total values. The gains and directivity in the lower half of the chart are the partial values for a specific polarization  $p_n$ . For example, the gain of an antenna  $G$  is determined from the ratio of  $4\pi$  times the radiation intensity  $U$  to the input power  $P_{in}$  while the partial gain of the antenna for polarization  $p_1$  is determined from the



$P_{av}$ = power available from source [W]	$G_R$ = realized gain
$P_{in}$ = input power accepted by the antenna[W]	$G$ = gain
$P_{rad}$ = power radiated by the antenna[W]	$D$ = directivity
$U$ = radiation intensity[W/sr]	$G_{Rn}$ = partial realized gain
$U_n$ = partial radiation intensity[W/sr]	$G_n$ = partial gain
$e_r$ = radiation efficiency	$D_n$ = partial directivity
$q$ = impedance mismatch	$p$ = polarization efficiency

**Figure 3.4** Gain and directivity flow chart. Modified from the chart in IEEE Std. 145-1993<sup>1</sup> [66]. Partial quantities denoted with subscript  $n$  correspond to the values for a polarization  $p_n$ .

ratio of  $4\pi U_1$  to  $P_{in}$ .

### 3.2.1 Directivity

Directivity quantifies how the radiated power is concentrated in a given direction compared to the total radiated power. Specifically, the directivity,  $D(\theta, \phi)$ , is defined as  $4\pi$  times the ratio of the radiation intensity in a given direction to the total radiated power, or

$$D(\theta, \phi) = \frac{4\pi U(\theta, \phi)}{P_{rad}}. \quad (3.15)$$

where  $P_{rad}$  is the total radiated power. Radiation intensity,  $U(\theta, \phi)$ , is the power radiated in a given direction per unit solid angle and has the units of watts per square radian (or steradian, sr) [12]. Directivity can be specified as either a function of direction or as the maximum value [66]. We shall use the notation that  $D$  without directional arguments to rep-

<sup>1</sup>From IEEE Std. Std 145-1993, Copyright 1993 IEEE. All rights reserved

resent peak directivity, and  $D(\theta, \phi)$  to represent direction dependent directivity. Formerly, the term *directive gain* was used for the directivity as a function of direction. However, its use has been deprecated by IEEE standard[66]. Thus, we will follow the standard, and use the term directivity to represent both the direction dependent value and the maximum value.

In the previous section, we determined that the power delivered to the probe antenna terminals are given by

$$P_{del_{p_1}}(r, \theta, \phi) = |b_{p_1}(r, \theta, \phi)|^2 = |S_{p_1 t_1}(r, \theta, \phi)|^2 |a_{t_1}|^2 \quad (3.16a)$$

$$P_{del_{p_2}}(r, \theta, \phi) = |b_{p_2}(r, \theta, \phi)|^2 = |S_{p_2 t_1}(r, \theta, \phi)|^2 |a_{t_1}|^2. \quad (3.16b)$$

where subscripts  $p_1$  and  $p_2$  represent orthogonal probe polarizations. These delivered powers are detected by the probe antenna with impedance mismatch factor  $q_p$  and effective aperture area  $A_e$  which is located at distance  $r$  from AUT. Let us define realized effective aperture of probe antenna as

$$A_R = q_p A_e. \quad (3.17)$$

Then, the delivered power densities are determined from  $|b_{p_1}(\theta, \phi)|^2/A_R$  and  $|b_{p_2}(\theta, \phi)|^2/A_R$ . Since two powers densities are in orthogonal polarization states, the total radiated power is determined from the integral of sum of delivered power densities over the sphere of radius  $r$ :

$$P_{rad} = \int_0^{2\pi} \int_0^\pi \frac{|b_{p_1}(r, \theta, \phi)|^2 + |b_{p_2}(r, \theta, \phi)|^2}{A_R} r^2 \sin \theta d\theta d\phi. \quad (3.18)$$

Let us assume that the probe antenna has a peak gain of  $G_p$ . The effective aperture area of the probe antenna is given by [12]

$$A_e = \frac{G_p \lambda^2}{4\pi}. \quad (3.19)$$

Thus, the realized effective aperture is given by

$$A_R = \frac{q_p G_p \lambda^2}{4\pi} = \frac{G_{R_p} \lambda^2}{4\pi} \quad (3.20)$$

where  $G_{R_p}$  is the realized gain of the probe antenna. Substituting (3.16) and (3.20) into (3.18) yields

$$P_{rad} = \frac{4\pi r^2 |a_{t_1}|^2}{G_{R_p} \lambda^2} \iint_{\Omega} \left\{ |S_{p_1 t_1}(r, \theta, \phi)|^2 + |S_{p_2 t_1}(r, \theta, \phi)|^2 \right\} d\Omega \quad (3.21)$$

where the element solid angle is given by  $d\Omega = \sin\theta d\theta d\phi$ . The total radiated power is also related to the radiation intensity by

$$P_{rad} = \iint_{\Omega} U(\theta, \phi) d\Omega \quad (3.22)$$

Thus, comparing (3.21) and (3.22), we can determine that the radiation intensity in terms of the S-parameter model is

$$U(\theta, \phi) = \frac{4\pi r^2 |a_{t1}|^2}{G_{Rp} \lambda^2} \left( |S_{p_1 t_1}(r, \theta, \phi)|^2 + |S_{p_2 t_1}(r, \theta, \phi)|^2 \right). \quad (3.23)$$

Finally, substituting (3.21) and (3.23) into (3.15) yields

$$D(\theta, \phi) = \frac{4\pi (|S_{p_1 t_1}(r, \theta, \phi)|^2 + |S_{p_2 t_1}(r, \theta, \phi)|^2)}{\iint_{\Omega} |S_{p_1 t_1}(r, \theta, \phi)|^2 + |S_{p_2 t_1}(r, \theta, \phi)|^2 d\Omega}. \quad (3.24)$$

It is noted that in (3.24) the radiation pattern is represented by the sum of the amplitudes of two polarization components of the radiated fields. This is consistent with the definition of directivity which assumes polarization matching at every observation angle.

It is also noted that (3.24) is equivalent to the second mathematical form of directivity definition,

$$D(\theta, \phi) = \frac{4\pi |F(r, \theta, \phi)|^2}{\iint_{\Omega} |F(r, \theta, \phi)|^2 d\Omega}. \quad (3.25)$$

Thus, the normalized radiation pattern is determined from the S-parameters by

$$|F(r, \theta, \phi)| = \sqrt{\frac{|S_{p_1 t_1}(r, \theta, \phi)|^2 + |S_{p_2 t_1}(r, \theta, \phi)|^2}{\max(|S_{p_1 t_1}(r, \theta, \phi)|^2 + |S_{p_2 t_1}(r, \theta, \phi)|^2)}}. \quad (3.26)$$

We can conclude from (3.26) that the coupling S-parameters between the test antenna and the probe antenna represent two polarization components of the unnormalized radiation patterns of the test antenna if the probe distance  $r$  is sufficiently large.

### 3.2.2 Gain

Gain is used to quantify how efficiently an antenna transforms the available power at its input terminal to the radiated power in a given direction. So gain is equal to directivity

reduced by losses on the antenna, or radiation efficiency,  $e_r$ . Gain is defined as the ratio of  $4\pi$  times radiation intensity in a given direction to the input power at the antenna terminal, or

$$G(\theta, \phi) = \frac{4\pi U(\theta, \phi)}{P_{in}}. \quad (3.27)$$

Similar to directivity, the gain can be either a function of direction  $G(\theta, \phi)$  or a maximum value  $G$ . The input power at the terminal of the antenna is determined from

$$P_{in} = |a_{t_1}|^2(1 - |\Gamma_{in}|^2) \quad (3.28)$$

where the reflection coefficient looking into the test antenna port for the model in Fig. 3.3 is given by

$$\Gamma_{in} = \frac{b_{t_1}}{a_{t_1}} = \frac{S_{t_1t_1} a_{t_1}}{a_{t_1}} = S_{t_1t_1}. \quad (3.29)$$

Substituting (3.28), (3.29), and (3.23) into (3.27) yields

$$G(\theta, \phi) = \frac{(4\pi r)^2}{G_{R_p} \lambda^2 (1 - |S_{t_1t_1}|^2)} (|S_{p_1t_1}(r, \theta, \phi)|^2 + |S_{p_2t_1}(r, \theta, \phi)|^2). \quad (3.30)$$

At first glance, (3.30) seems to suggest that the gain will increase as the test antenna reflection coefficient,  $S_{t_1t_1}$ , increases. In reality,  $S_{p_1t_1}$  and  $S_{p_2t_1}$  decreases as  $S_{t_1t_1}$  increases. When these S-parameter values are determined with respect to a reference impedance  $Z_o$ , that is a complex conjugate of the the antenna input impedance, the resulting  $S_{t_1t_1}$  will be equal to zero, i.e. when the antenna is matched ( $\Gamma_{in} = 0$ ). Then, the gain becomes purely a function of the transmission coefficients  $S_{p_1t_1}$  and  $S_{p_2t_1}$ . This result is consistent with the definition of gain.

It is useful to define S-parameters that are independent of distance  $r$  and probe realized gain  $G_{R_p}$ . Let us define normalized S-parameters as

$$S'_{p_1t_1}(\theta, \phi) = \frac{r\sqrt{4\pi}}{\lambda\sqrt{G_{R_p}}} S_{p_1t_1}(r, \theta, \phi) \quad (3.31a)$$

$$S'_{p_2t_1}(\theta, \phi) = \frac{r\sqrt{4\pi}}{\lambda\sqrt{G_{R_p}}} S_{p_2t_1}(r, \theta, \phi) \quad (3.31b)$$

. The normalized S-parameters represent the coupling from the test antenna to the probe antenna per unit radian. Using the normalized S-parameters, the gain given by (3.30) simplifies to

$$G(\theta, \phi) = \frac{4\pi}{1 - |S_{t_1t_1}|^2} (|S'_{p_1t_1}(\theta, \phi)|^2 + |S'_{p_2t_1}(\theta, \phi)|^2) \quad (3.32)$$

which is valid when the probe antenna is sufficiently away from the test antenna ( $r \gg 0$ ) such that very little interaction occur between them. We can utilize (3.32) to determine  $S'_{p_1t_1}$  and  $S'_{p_2t_1}$  from a known gain radiation pattern of an antenna evaluated at infinity.

The difference between the directivity in (3.15) and the gain in (3.27) is the reference power quantity in the denominator; the directivity is referenced to the total radiated power,  $P_{rad}$  where as the gain is referenced to the total input power  $P_{in}$ . The difference between the input power and the radiated power defines the power lost in the antenna and its surrounding,

$$P_{loss} = P_{in} - P_{rad}. \quad (3.33)$$

The radiation efficiency of an antenna is determined by the ratio between the input power and the radiated power,

$$e_r = \frac{P_{rad}}{P_{in}}, \quad (3.34)$$

or the ratio between gain and directivity,

$$e_r = \frac{G(\theta, \phi)}{D(\theta, \phi)}. \quad (3.35)$$

Substituting (3.21) and (3.28) into (3.34) results in the radiation efficiency in terms of S-parameters as

$$e_r = \frac{4\pi r^2}{G_{Rp} \lambda^2 (1 - |S_{t_1t_1}|^2)} \iint_{\Omega} |S_{p_1t_1}(r, \theta, \phi)|^2 + |S_{p_2t_1}(r, \theta, \phi)|^2 d\Omega, \quad (3.36)$$

or in terms of the normalized S-parameters as,

$$e_r = \frac{1}{1 - |S_{t_1t_1}|^2} \iint_{\Omega} |S'_{p_1t_1}(\theta, \phi)|^2 + |S'_{p_2t_1}(\theta, \phi)|^2 d\Omega. \quad (3.37)$$

### 3.2.3 Realized Gain, Input Impedance, and Impedance Mismatch

The realized gain of an antenna includes the loss associated with the impedance mismatch between the test antenna and the source impedance. From Fig. 3.4, realized gain is defined as,

$$G_R(\theta, \phi) = \frac{4\pi U(\theta, \phi)}{P_{av}} \quad (3.38)$$

where  $P_{av}$  is the available power from the source. By inspection of Fig. 3.3, the available power from the source is given by

$$P_{av} = \frac{|b_s|^2}{1 - |\Gamma_s|^2}. \quad (3.39)$$

Also by the inspection of the same figure, the incident wave into the test antenna is related to the source by

$$a_{t_1} = \frac{b_s}{1 - S_{t_1 t_1} \Gamma_s} \quad (3.40)$$

Substituting (3.39), (3.40), and (3.23) into (3.38) yields the realized gain as

$$G_R(\theta, \phi) = \frac{(4\pi r)^2 (1 - |\Gamma_s|^2)}{G_{R_p} \lambda^2 |1 - S_{t_1 t_1} \Gamma_s|^2} (|S_{p_1 t_1}(r, \theta, \phi)|^2 + |S_{p_2 t_1}(r, \theta, \phi)|^2). \quad (3.41)$$

Following the same procedure as for gain, we can also write the realized gain using the normalized S-parameters as

$$G_R(\theta, \phi) = \frac{4\pi(1 - |\Gamma_s|^2)}{|1 - S_{t_1 t_1} \Gamma_s|^2} (|S'_{p_1 t_1}(\theta, \phi)|^2 + |S'_{p_2 t_1}(\theta, \phi)|^2). \quad (3.42)$$

The impedance mismatch factor,  $q$ , is determined from the ratio of realized gain to the gain, which yields

$$q = \frac{G_R}{G} = \frac{(1 - |\Gamma_s|^2)(1 - |S_{t_1 t_1}|^2)}{|1 - S_{t_1 t_1} \Gamma_s|^2} \quad (3.43)$$

It is clear from (3.43) that mismatch factor becomes unity ( $q = 1$ ) when the source reflection coefficient is conjugate matched to  $S_{t_1 t_1}$ ,

$$S_{t_1 t_1} = \Gamma_s^*. \quad (3.44)$$

This implies that  $S_{t_1 t_1}$  represents the antenna reflection coefficient. It follows that the antenna input impedance is determined from

$$Z_{in} = \frac{Z_o^* + Z_o S_{t_1 t_1}}{1 - S_{t_1 t_1}} \quad (3.45)$$

### 3.2.4 Partial Directivity, Partial Gain, and Polarization Mismatch

Partial directivity represents the directivity of an antenna in a given polarization component compared to the total radiated power, or

$$D_n(\theta, \phi) = \frac{4\pi U_n(\theta, \phi)}{P_{rad}} \quad (3.46)$$

where subscripts in  $D_n$  and  $U_n$  signify the partial directivity and partial radiation intensity of polarization  $p_n$ . The partial intensity of polarization  $p_1$  is given by

$$U_1(\theta, \phi) = \frac{4\pi r^2 |a_{t1}|^2}{G_{R_p} \lambda^2} |S_{p_1 t_1}(r, \theta, \phi)|^2. \quad (3.47)$$

Substituting (3.47) and (3.21) into (3.46) yields

$$D_1(\theta, \phi) = \frac{4\pi |S_{p_1 t_1}(r, \theta, \phi)|^2}{\iint_{\Omega} |S_{p_1 t_1}(r, \theta, \phi)|^2 + |S_{p_2 t_1}(r, \theta, \phi)|^2 d\Omega}. \quad (3.48)$$

Similarly, the partial directivity of polarization  $p_2$  is given by

$$D_2(\theta, \phi) = \frac{4\pi |S_{p_2 t_1}(r, \theta, \phi)|^2}{\iint_{\Omega} |S_{p_1 t_1}(r, \theta, \phi)|^2 + |S_{p_2 t_1}(r, \theta, \phi)|^2 d\Omega}. \quad (3.49)$$

Partial directivities are related to the total directivity by

$$D(\theta, \phi) = D_1(\theta, \phi) + D_2(\theta, \phi). \quad (3.50)$$

The partial gains,  $G_1$  and  $G_2$ , and the partial realized gains  $G_{R_1}$  and  $G_{R_2}$ , can be determined in similar way as for the partial directivities. The results are summarized in Table 3.1 in the next section.

The ratio between (3.48) and (3.24) is the polarization mismatch factor for the polarization  $p_1$ , which can be simplified as

$$p_1 = \frac{|S_{p_1 t_1}(r, \theta, \phi)|^2}{|S_{p_1 t_1}(r, \theta, \phi)|^2 + |S_{p_2 t_1}(r, \theta, \phi)|^2}. \quad (3.51)$$

As the directivity and gain flow chart in Fig. 3.4 implies, the ratio of partial gain to the total gain, and the ratio of partial realized gain to the total realized gain also yield the same results.

### 3.3 Summary

The derivation of a single antenna description using a three-port, S-parameter, network model was presented in this chapter. The S-parameters in the network were extended to include the spatial dependency to model the coupling from the test antenna to the probe

**Table 3.1** Summary of antenna parameters and their definition in terms of antenna network S-parameters.

Parameter Name	Variables	Definition	S-parameter Definition
Radiation Pattern	$ F(\theta, \phi) $	$\left  \frac{E(r, \theta, \phi)}{\max E(r, \theta, \phi)} \right $	$\sqrt{\frac{ S_{p_1 t_1}(r, \theta, \phi) ^2 +  S_{p_2 t_1}(r, \theta, \phi) ^2}{\max( S_{p_1 t_1}(r, \theta, \phi) ^2 +  S_{p_2 t_1}(r, \theta, \phi) ^2)}}$
Input Reflection	$\Gamma_{in}$	$\frac{Z_{in} - Z_0}{Z_{in} + Z_0}$	$S_{t_1 t_1}$
Directivity	$D(\theta, \phi)$	$\frac{4\pi U(\theta, \phi)}{P_{rad}}$	$\frac{4\pi( S_{p_1 t_1}(r, \theta, \phi) ^2 +  S_{p_2 t_1}(r, \theta, \phi) ^2)}{\iint_{\Omega}  S_{p_1 t_1}(r, \theta, \phi) ^2 +  S_{p_2 t_1}(r, \theta, \phi) ^2 d\Omega}$ $\frac{4\pi( S'_{p_1 t_1}(\theta, \phi) ^2 +  S'_{p_2 t_1}(\theta, \phi) ^2)}{\iint_{\Omega}  S_{p_1 t_1}(\theta, \phi) ^2 +  S_{p_2 t_1}(\theta, \phi) ^2 d\Omega}$
Gain	$G(\theta, \phi)$	$\frac{4\pi U(\theta, \phi)}{P_{in}}$	$\frac{(4\pi r)^2}{\lambda^2(1- S_{t_1 t_1} ^2)}( S_{p_1 t_1}(\theta, \phi) ^2 +  S_{p_2 t_1}(\theta, \phi) ^2)$ , or $\frac{4\pi}{1- S_{t_1 t_1} ^2}( S'_{p_1 t_1}(\theta, \phi) ^2 +  S'_{p_2 t_1}(\theta, \phi) ^2)$
Realized Gain	$G_R(\theta, \phi)$	$\frac{4\pi U(\theta, \phi)}{P_{av}}$	$\frac{(4\pi r)^2(1- S_{t_1 t_1} ^2)}{\lambda^2 1-s_{t_1 t_1}\Gamma_s ^2}( S_{p_1 t_1}(\theta, \phi) ^2 +  S_{p_2 t_1}(\theta, \phi) ^2)$ , or $\frac{4\pi(1- S_{t_1 t_1} ^2)}{ 1-s_{t_1 t_1}\Gamma_s ^2}( S'_{p_1 t_1}(\theta, \phi) ^2 +  S'_{p_2 t_1}(\theta, \phi) ^2)$
Partial Directivity	$D_n(\theta, \phi)$	$\frac{4\pi U_n(\theta, \phi)}{P_{rad}}$	$\frac{4\pi S_{p_n t_1}(\theta, \phi) ^2}{\iint  S_{p_1 t_1}(\theta, \phi) ^2 +  S_{p_2 t_1}(\theta, \phi) ^2 d\Omega}$ , $n = 1$ or $2$
Partial Gain	$G_n(\theta, \phi)$	$\frac{4\pi U_n(\theta, \phi)}{P_{in}}$	$\frac{(4\pi r)^2}{\lambda^2(1- S_{t_1 t_1} ^2)} S_{p_n t_1}(\theta, \phi) ^2$ , $n = 1$ or $2$
Partial Realized Gain	$G_{Rn}(\theta, \phi)$	$\frac{4\pi U_n(\theta, \phi)}{P_{av}}$	$\frac{(4\pi r)^2(1- S_{t_1 t_1} ^2)}{\lambda^2 1-s_{t_1 t_1}\Gamma_s ^2} S_{p_n t_1}(\theta, \phi) ^2$ , $n = 1$ or $2$
Radiation Efficiency	$e_r$	$\frac{G}{D}$	$\frac{4\pi r^2 \iint  S_{p_1 t_1}(\theta, \phi) ^2 +  S_{p_2 t_1}(\theta, \phi) ^2 d\Omega}{\lambda^2(1- S_{t_1 t_1} ^2)}$ , or $\frac{\iint  S'_{p_1 t_1}(\theta, \phi) ^2 +  S'_{p_2 t_1}(\theta, \phi) ^2 d\Omega}{1- S_{t_1 t_1} ^2}$
Impedance Mismatch	$q$	$\frac{G_R}{G}$	$\frac{(1- \Gamma_s ^2)(1- S_{t_1 t_1} ^2)}{ 1-S_{t_1 t_1}\Gamma_s ^2}$
Polarization Mismatch	$p_n(\theta, \phi)$	$\frac{D_n}{D}, \frac{G_n}{G}$ , or $\frac{G_{Rn}}{G_R}$	$\frac{ S_{p_n t_1}(\theta, \phi) ^2}{ S_{p_1 t_1}(\theta, \phi) ^2 +  S_{p_2 t_1}(\theta, \phi) ^2}$ , for $n = 1$ or $2$ , or $\frac{ S'_{p_n t_1}(\theta, \phi) ^2}{ S'_{p_1 t_1}(\theta, \phi) ^2 +  S'_{p_2 t_1}(\theta, \phi) ^2}$

antenna located at  $(r, \theta, \phi)$ . The delivered power to the probe antenna ports when the test antenna is excited with a source was derived. From the delivered powers, the antenna parameters were derived in terms of antenna network S-parameters. A table of derived relationships are shown in Table 3.1.

## Chapter 4

# Network Description of Array

## Antennas

A S-parameter network model of a single antenna system was derived in the last chapter. We also developed the relationship between the antenna S-parameter model and antenna design parameters. In this chapter, the S-parameter antenna model will be extended to include antenna arrays.

### 4.1 Derivation of S-parameter Model for Antenna Arrays

Consider an arbitrary array of  $N$  elements with  $N$  feed ports. We will designate this array as the test array. Similar to the single antenna model of the previous chapter, the array radiated fields will be detected by an ideal probe antenna with two orthogonal polarization ports that is located at position  $(r, \theta, \phi)$  as illustrated in Fig. 4.1. The probe antenna is moved along a spherical surface of constant radius  $r$  to detect the radiated fields. The probe antenna patterns for both polarizations are assumed to have peak realized gain of  $G_{R_p}$ . The pattern peak of the probe is oriented towards center of the sphere as the probe position is varied. The polarization state of the array radiated fields are detected by the two orthogonal polarization elements in the probe antenna. In the Fig. 4.1, an ideal crossed dipole is used to detect the vertical and horizontal polarization. The polarization of the probe antenna is changed as the probe is rotated around the test array to conform with appropriate

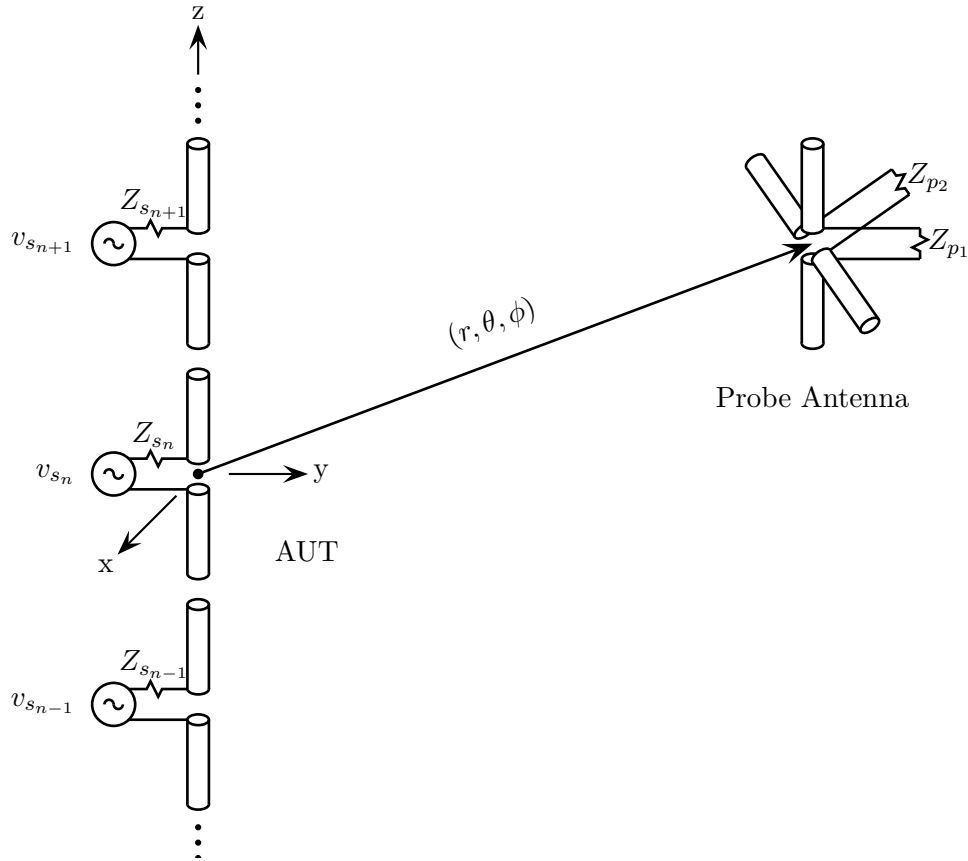


**Figure 4.1** Arbitrary test antenna array fed by sources with internal impedances  $\{Z_{s_n}\}$  and a distant probe antenna with two orthogonal polarization elements.

polarization definition such as Ludwig's second or third polarization definition [67].

The  $N$  ports for the array elements and 2 probe antenna ports form an  $N + 2$  port network which can be described by a scattering matrix equation,

$$\begin{bmatrix} \mathbf{b}_t(r, \theta, \phi) \\ \mathbf{b}_p(r, \theta, \phi) \end{bmatrix} = \begin{bmatrix} \mathbf{S}_{tt}(r, \theta, \phi) & \mathbf{S}_{tp}(r, \theta, \phi) \\ \mathbf{S}_{pt}(r, \theta, \phi) & \mathbf{S}_{pp}(r, \theta, \phi) \end{bmatrix} \begin{bmatrix} \mathbf{a}_t(r, \theta, \phi) \\ \mathbf{a}_p(r, \theta, \phi) \end{bmatrix} \quad (4.1)$$

where variables associated with test array ports and probe antenna ports are designated by subscripts  $t$  and  $p$ , respectively and are illustrated in a block diagram in Fig. 4.2. The elements of the vectors and matrix in (4.1) are also vectors and matrices that are indicated by the use of bold fonts for these variables. Strictly speaking, all of the variables in (4.1) are functions of the position of probe antenna as indicated by the arguments  $(r, \theta, \phi)$ . We will consider each element in the matrix equation (4.1) in detail.

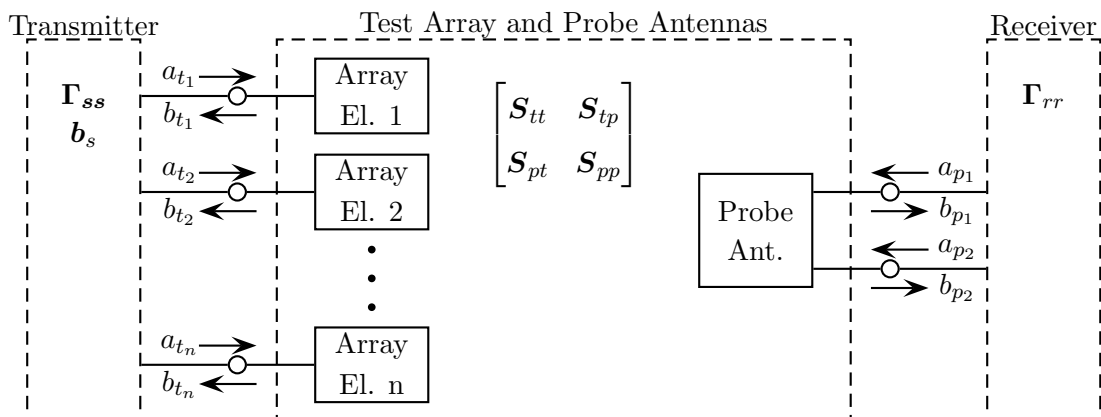


**Figure 4.2** Block diagram for an arbitrary array of  $N$  elements and a probe antenna with two orthogonal polarization ports.

The  $N$ -element array is described by an  $N \times N$  scattering matrix  $\mathbf{S}_{tt}(r, \theta, \phi)$ . The S-parameters in this matrix is dependent on the probe antenna position since the scattered fields by the probe antenna can cause mutual coupling among the array elements. We will assume that the probe antenna is sufficiently far from the test array such that the deviation in the scattering parameters of the array is negligible. Thus, the test array S-matrix is given by probe-position independent S-parameters,

$$\mathbf{S}_{tt} = \begin{bmatrix} S_{t_1 t_1} & \cdots & S_{t_1 t_N} \\ \vdots & \ddots & \vdots \\ S_{t_N t_1} & \cdots & S_{t_N t_N} \end{bmatrix}. \quad (4.2)$$

The S-matrix,  $\mathbf{S}_{tt}$  is implicitly dependent on the frequency of the analysis, as usual.

The array element scattering matrix in (4.2) is related to the mutual impedance matrix discussed in Sec. 2.2.1. We can determine the antenna array S-matrix from its impedance matrix  $\mathbf{Z}_{tt}$  using the transform,

$$\mathbf{S}_{tt} = \left( \sqrt{\mathbf{R}_o} \right)^{-1} \left( \mathbf{Z}_{tt} - \mathbf{Z}_o^\dagger \right) \left( \mathbf{Z}_{tt} + \mathbf{Z}_o \right)^{-1} \sqrt{\mathbf{R}_o} \quad (4.3)$$

where  $\mathbf{Z}_o$  and  $\sqrt{\mathbf{R}_o}$  are diagonal matrices whose diagonal components are given by reference impedances  $Z_{o_n}$  and  $2\sqrt{|\text{Re}Z_{o_n}|}$ , respectively, and the  $\dagger$  operator is the Hermitian transpose of a matrix [63].

The scattering matrix of the probe antenna is given by a  $2 \times 2$  matrix  $\mathbf{S}_{pp}(r, \theta, \phi)$ . Similar to the array scattering parameters, we will also assume that S-parameters of the

probe antenna are independent of its position with respect to the test array. With this assumption, the probe antenna matrix can be written as

$$\mathbf{S}_{pp} = \begin{bmatrix} S_{p_1 p_1} & S_{p_1 p_2} \\ S_{p_2 p_1} & S_{p_2 p_2} \end{bmatrix}. \quad (4.4)$$

The  $2 \times N$  and  $N \times 2$  S-matrices,  $\mathbf{S}_{pt}(r, \theta, \phi)$  and  $\mathbf{S}_{tp}(r, \theta, \phi)$  represent the forward coupling and the reverse coupling between test array elements and the probe antennas which are functions of probe position,

$$\mathbf{S}_{pt}(r, \theta, \phi) = \begin{bmatrix} S_{p_1 t_1}(r, \theta, \phi) & \cdots & S_{p_1 t_N}(r, \theta, \phi) \\ S_{p_2 t_1}(r, \theta, \phi) & \cdots & S_{p_2 t_N}(r, \theta, \phi) \end{bmatrix} \quad (4.5a)$$

$$\mathbf{S}_{tp}(r, \theta, \phi) = \begin{bmatrix} S_{t_1 p_1}(r, \theta, \phi) & S_{t_1 p_2}(r, \theta, \phi) \\ \vdots & \vdots \\ S_{t_N p_1}(r, \theta, \phi) & S_{t_N p_2}(r, \theta, \phi) \end{bmatrix}. \quad (4.5b)$$

Due to reciprocity, the forward couplings and the reverse couplings are related by

$$\mathbf{S}_{tp}(r, \theta, \phi) = \mathbf{S}_{pt}^T(r, \theta, \phi) \quad (4.6)$$

where  $T$  is a matrix transpose operator without complex conjugate. The elements of the matrices are determined from the coupling between a port in the test array to a port in the probe antenna when all other antenna elements are terminated with reference impedances  $\mathbf{Z}_o$ . They are functions of the position of the probe antenna. These S-parameters are un-normalized active-element patterns of the test array when probe antenna is in the far-field region of the array and the source impedances  $\mathbf{Z}_{ss}$  of the array are equal to the reference impedance.

We are interested in the delivered power detected at the probe antenna ports when the array elements are fed with a source network as illustrated in Fig. 4.2. The delivered power is related to the array radiation pattern. We will assume that array is fed by a source network represented by a S-matrix

$$\mathbf{\Gamma}_{ss} = \begin{bmatrix} \Gamma_{s_1 s_1} & \cdots & \Gamma_{s_1 s_N} \\ \vdots & \ddots & \vdots \\ \Gamma_{s_N s_1} & \cdots & \Gamma_{s_N s_N} \end{bmatrix} \quad (4.7)$$

with independent source waves

$$\mathbf{b}_s = \begin{bmatrix} b_{s1} \\ \vdots \\ b_{sN} \end{bmatrix} \quad (4.8)$$

at each port of the array element. Note that source network S-parameters  $\mathbf{\Gamma}_{ss}$  and source waves  $\mathbf{b}_s$  are both independent of the probe antenna position. These two parameters are completely general such that they can represent a corporate feed network, a series feed network, individual transmitters for a phased array, or any other configurations.

A pair of independent receivers are attached to the probe antenna ports to detect the delivered power from the array to the probe antenna as shown in Fig. 4.2. Since the receivers are independent, there is no coupling between receivers, and thus, the off-diagonal components of the receiver S-matrix are zeros. We will also assume that the internal impedances of the receivers are matched to the reference impedance  $Z_o$ . Then, the diagonal components of the receiver s-matrix also become zero. Thus, the S-matrix of the receivers is simply a zero matrix, or

$$\mathbf{\Gamma}_{rr} = \mathbf{0}, \quad (4.9)$$

and the waves reflected from the receiver into the probe antenna becomes

$$\mathbf{a}_p = \mathbf{\Gamma}_{pp}\mathbf{b}_p = \mathbf{0}. \quad (4.10)$$

The matched and independent receivers greatly simplify the array model. The signal flow diagram of an antenna array fed by a source network and detected by the receivers attached to the probe antenna is shown in Fig. 4.3. The matched and independent receivers are depicted in the signal flow diagram by lack of  $a_{p1}$  and  $a_{p2}$ . From the inspection of signal flow diagram, the waves incident on the array elements are obtained from

$$\mathbf{a}_t = \mathbf{\Gamma}_{ss}\mathbf{b}_t + \mathbf{b}_s \quad (4.11)$$

where the waves reflected from the array are given by

$$\mathbf{b}_t = \mathbf{S}_{tt}\mathbf{a}_t. \quad (4.12)$$

Substituting (4.12) into (4.11) and solving for  $\mathbf{a}_t$  yields

$$\mathbf{a}_t = \left[ \mathbf{I} - \mathbf{\Gamma}_{ss}\mathbf{S}_{tt} \right]^{-1} \mathbf{b}_s. \quad (4.13)$$

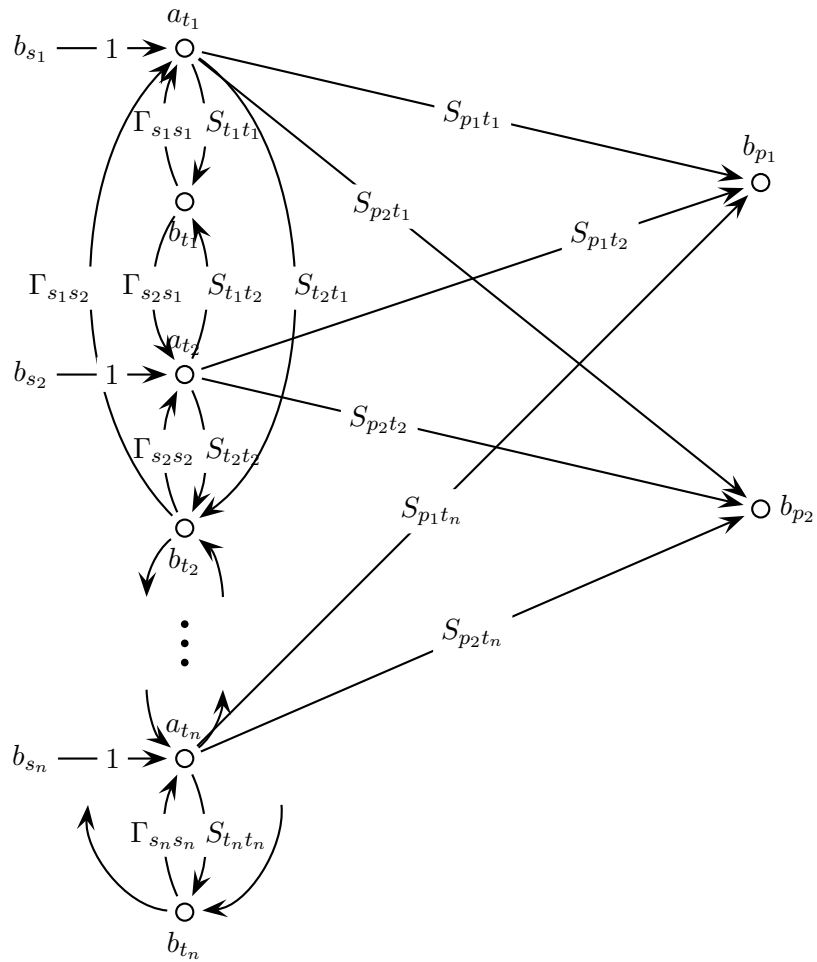


**Figure 4.3** Signal flow diagram for an arbitrary array of  $n$  elements and a probe antenna with two orthogonal polarization ports.

Clearly, the waves incident on the array elements are affected by both the feed network architecture and the array element coupling. In summary, the  $N$ -element antenna array fed by a generalized source network and detected by a probe antenna with two independent receivers for two orthogonal polarizations are described by S-matrix equations

$$\begin{bmatrix} \mathbf{b}_t \\ \mathbf{b}_p(r, \theta, \phi) \end{bmatrix} = \begin{bmatrix} \mathbf{S}_{tt} & \mathbf{S}_{tp}(r, \theta, \phi) \\ \mathbf{S}_{pt}(r, \theta, \phi) & \mathbf{S}_{pp} \end{bmatrix} \begin{bmatrix} \mathbf{a}_t \\ \mathbf{0} \end{bmatrix} \quad (4.14a)$$

$$\mathbf{a}_t = \left[ \mathbf{I} - \mathbf{\Gamma}_{ss} \mathbf{S}_{tt} \right]^{-1} \mathbf{b}_s. \quad (4.14b)$$

We are now ready to determine the total power delivered to the receivers attached to the probe antenna ports. From the definition of S-parameters, the total power delivered is given by

$$P_{del}(r, \theta, \phi) = \mathbf{b}_p^\dagger(r, \theta, \phi) \mathbf{b}_p(r, \theta, \phi) - \mathbf{a}_p^\dagger(r, \theta, \phi) \mathbf{a}_p(r, \theta, \phi). \quad (4.15)$$

Since the reflected waves from the impedance matched receivers are zero based on (4.10), the power delivered to the loads simplifies to

$$P_{del}(r, \theta, \phi) = \mathbf{b}_p^\dagger(r, \theta, \phi) \mathbf{b}_p(r, \theta, \phi). \quad (4.16)$$

Thus, transmitted waves coming out of the probe antenna ports,  $\mathbf{b}_p$ , are proportional to the radiated field quantities of the array in two polarizations. The transmitted waves are related to the waves incident on the antenna array by

$$\mathbf{b}_p(r, \theta, \phi) = \mathbf{S}_{pt}(r, \theta, \phi) \mathbf{a}_t. \quad (4.17)$$

Thus, the total power delivered to the probe antenna is related to the incident waves by

$$P_{del}(r, \theta, \phi) = \mathbf{a}_t^\dagger \mathbf{S}_{pt}^\dagger(r, \theta, \phi) \mathbf{S}_{pt}(r, \theta, \phi) \mathbf{a}_t. \quad (4.18)$$

Alternatively, we can determine the transmitted waves and the delivered power in terms of waves incident from the sources by substituting (4.14b) into (4.17) and (4.18) resulting in the expressions,

$$\mathbf{b}_p(r, \theta, \phi) = \mathbf{S}_{pt}(r, \theta, \phi) \left[ \mathbf{I} - \mathbf{\Gamma}_{ss} \mathbf{S}_{tt} \right]^{-1} \mathbf{b}_s \quad (4.19)$$

for the transmitted waves, and

$$P_{del}(r, \theta, \phi) = \mathbf{b}_s^\dagger \left[ \mathbf{I} - \mathbf{S}_{tt}^\dagger \mathbf{\Gamma}_{ss}^\dagger \right]^{-1} \mathbf{S}_{pt}^\dagger(r, \theta, \phi) \mathbf{S}_{pt}(r, \theta, \phi) \left[ \mathbf{I} - \mathbf{\Gamma}_{ss} \mathbf{S}_{tt} \right]^{-1} \mathbf{b}_s \quad (4.20)$$

for the delivered power. Both transmitted waves and the total power delivered to the probe antenna are functions of forward coupling between array elements and the probe antenna  $\mathbf{S}_{pt}(r, \theta, \phi)$ , the array element mutual coupling  $\mathbf{S}_{tt}$ , source network coupling  $\mathbf{\Gamma}_{ss}$ , and the source excitation  $\mathbf{b}_s$ . Using these expressions for the transmitted waves and the delivered power from the array antenna, we can determine antenna design parameters such as directivity and gain using steps similar to Sec. 3.2.

## 4.2 Array Network Model and Antenna Parameters

In the previous section, we developed expressions for the transmitted waves and power delivered to the receivers attached to the probe antenna ports. Similar to the single antenna network model, these expressions are not useful until their relationships to antenna design parameters are determined. We will develop directivity, gain, and realized gain expressions using S-parameter network model for antenna arrays.

### 4.2.1 Array Directivity

The directivity of an antenna system for an antenna element or for an array of elements is given by

$$D(\theta, \phi) = \frac{4\pi U(\theta, \phi)}{P_{rad}} \quad (4.21)$$

where  $U(\theta, \phi)$  is the radiation intensity in watts per square radian and  $P_{rad}$  is the total radiated power in watts. The total radiated power is determined from an integral over a sphere of radius  $r$  of delivered power per unit area,

$$P_{rad} = \int_0^{2\pi} \int_0^\pi \frac{P_{del}(r, \theta, \phi)}{A_e} r^2 \sin \theta d\theta d\phi \quad (4.22)$$

where  $A_e$  is the effective aperture area probe antenna. For a given probe antenna with peak gain of  $G_{Rp}$ , the effective aperture area is determined by

$$A_e = \frac{G_{Rp} \lambda^2}{4\pi}. \quad (4.23)$$

Substituting the expression for the delivered power (4.18) and the effective aperture (4.23) into (4.22) yields

$$P_{rad} = \frac{4\pi r^2}{G_{Rp} \lambda^2} \int_0^{2\pi} \int_0^\pi \mathbf{a}_t^\dagger \mathbf{S}_{pt}^\dagger(r, \theta, \phi) \mathbf{S}_{pt}(r, \theta, \phi) \mathbf{a}_t d\Omega, \quad (4.24)$$

where element solid angle is given by  $d\Omega = \sin\theta d\theta d\phi$ . The total radiated power is also related to the radiation intensity by

$$P_{rad} = \iint_{\Omega} U(\theta, \phi) d\Omega. \quad (4.25)$$

Comparing (4.24) with (4.25), we can determine that the radiation intensity in terms of S-parameter model is given by

$$U(\theta, \phi) = \frac{4\pi r^2}{G_{Rp}\lambda^2} \mathbf{a}_t^\dagger \mathbf{S}_{pt}^\dagger(r, \theta, \phi) \mathbf{S}_{pt}(r, \theta, \phi) \mathbf{a}_t. \quad (4.26)$$

Finally, substituting (4.24) and (4.26) into (4.21) yields the expression for the array directivity,

$$D(\theta, \phi) = \frac{4\pi \mathbf{a}_t^\dagger \mathbf{S}_{pt}^\dagger(r, \theta, \phi) \mathbf{S}_{pt}(r, \theta, \phi) \mathbf{a}_t}{\iint_{\Omega} \mathbf{a}_t^\dagger \mathbf{S}_{pt}^\dagger(r, \theta, \phi) \mathbf{S}_{pt}(r, \theta, \phi) \mathbf{a}_t d\Omega}. \quad (4.27)$$

Clearly, the array directivity is a function of array element patterns and their excitation coefficients as is evident from (4.27). Thus, the array directivity can be computed with the desired incident waves into the antenna array elements. The feed does not have to be specified to determine the directivity.

Alternatively, we can express the radiation intensity and the directivity of antenna arrays in terms of actual incident source waves resulting in

$$U(\theta, \phi) = \frac{4\pi r^2}{G_{Rp}\lambda^2} \mathbf{b}_s^\dagger \left[ \mathbf{I} - \mathbf{S}_{tt}^\dagger \mathbf{\Gamma}_{ss}^\dagger \right]^{-1} \mathbf{S}_{pt}^\dagger(r, \theta, \phi) \mathbf{S}_{pt}(r, \theta, \phi) \left[ \mathbf{I} - \mathbf{\Gamma}_{ss} \mathbf{S}_{tt} \right]^{-1} \mathbf{b}_s, \quad (4.28)$$

and

$$D(\theta, \phi) = \frac{4\pi \mathbf{b}_s^\dagger \left[ \mathbf{I} - \mathbf{S}_{tt}^\dagger \mathbf{\Gamma}_{ss}^\dagger \right]^{-1} \mathbf{S}_{pt}^\dagger(r, \theta, \phi) \mathbf{S}_{pt}(r, \theta, \phi) \left[ \mathbf{I} - \mathbf{\Gamma}_{ss} \mathbf{S}_{tt} \right]^{-1} \mathbf{b}_s}{\iint_{\Omega} \mathbf{b}_s^\dagger \left[ \mathbf{I} - \mathbf{S}_{tt}^\dagger \mathbf{\Gamma}_{ss}^\dagger \right]^{-1} \mathbf{S}_{pt}^\dagger(r, \theta, \phi) \mathbf{S}_{pt}(r, \theta, \phi) \left[ \mathbf{I} - \mathbf{\Gamma}_{ss} \mathbf{S}_{tt} \right]^{-1} \mathbf{b}_s d\Omega}. \quad (4.29)$$

Thus, the directivity of antenna arrays is a function of array element patterns, excitation, element mutual coupling and feed coupling. All the S-parameter variables in the directivity expression can be determined using standard network analysis or measurement techniques.

Intuitively, the array directivity should not include terms involving feed coupling  $\mathbf{\Gamma}_{ss}$  since the directivity of a single antenna is strictly a function of antenna pattern as shown

in (3.24). However, for the array directivity computation, the mismatch terms  $\mathbf{S}_{tt}\mathbf{\Gamma}_{ss}$  are necessary to determine the proper incident waves into the array elements.

It is simple to show that array directivity expression (4.29) reduces to the directivity of a single antenna (3.24). For a single antenna, the following matrices and vectors become scalars:

$$\begin{aligned} \mathbf{b}_s &\rightarrow b_s \\ \mathbf{\Gamma}_{ss} &\rightarrow \Gamma_{ss} \\ \mathbf{S}_{tt} &\rightarrow S_{tt} \\ \mathbf{I} &\rightarrow 1. \end{aligned} \tag{4.30}$$

Substituting (4.30) into (4.29) yields

$$D(\theta, \phi) = \frac{4\pi \left\{ b_s^* \left[ 1 - S_{tt}^* \Gamma_{ss}^* \right]^{-1} \right\} \mathbf{S}_{pt}^\dagger(r, \theta, \phi) \mathbf{S}_{pt}(r, \theta, \phi) \left\{ \left[ 1 - \Gamma_{ss} S_{tt} \right]^{-1} b_s \right\}}{\iint_{\Omega} \left\{ b_s^* \left[ 1 - S_{tt}^* \Gamma_{ss}^* \right]^{-1} \right\} \mathbf{S}_{pt}^\dagger(r, \theta, \phi) \mathbf{S}_{pt}(r, \theta, \phi) \left\{ \left[ 1 - \Gamma_{ss} S_{tt} \right]^{-1} b_s \right\} d\Omega}. \tag{4.31}$$

Since the terms inside braces in the denominator can be pulled out of the integral and canceled with the terms inside the braces in the numerator, (4.31) simplifies to

$$D(\theta, \phi) = \frac{4\pi \mathbf{S}_{pt}^\dagger(r, \theta, \phi) \mathbf{S}_{pt}(r, \theta, \phi)}{\iint_{\Omega} \mathbf{S}_{pt}^\dagger(r, \theta, \phi) \mathbf{S}_{pt}(r, \theta, \phi) d\Omega}. \tag{4.32}$$

$\mathbf{S}_{pt}(r, \theta, \phi)$  for a single element antenna is a  $2 \times 1$  matrix

$$\mathbf{S}_{pt}(r, \theta, \phi) = \begin{bmatrix} S_{p_1 t_1}(r, \theta, \phi) \\ S_{p_2 t_1}(r, \theta, \phi) \end{bmatrix}. \tag{4.33}$$

Substituting (4.33) into (4.32) results in the directivity for a single element antenna

$$D(\theta, \phi) = \frac{4\pi \left\{ S_{p_1 t_1}^*(r, \theta, \phi) S_{p_1 t_1}(r, \theta, \phi) + S_{p_2 t_1}^*(r, \theta, \phi) S_{p_2 t_1}(r, \theta, \phi) \right\}}{\iint_{\Omega} \left\{ S_{p_1 t_1}^*(r, \theta, \phi) S_{p_1 t_1}(r, \theta, \phi) + S_{p_2 t_1}^*(r, \theta, \phi) S_{p_2 t_1}(r, \theta, \phi) \right\} d\Omega} \tag{4.34}$$

where the Hermitian transpose for the matrices become complex conjugates for the scalars. We can see that (4.34) is identical to the directivity of single element antenna (3.24) derived in the last chapter.

## 4.2.2 Array Gain

Gain is used to quantify how efficiently an array transforms the available powers at its input terminals to the radiated power in a given direction. The gain is defined as

$$G(\theta, \phi) = \frac{4\pi U(\theta, \phi)}{P_{in}} \quad (4.35)$$

for any antenna system. The total power input from the source network to the array is determined from

$$P_{in} = \mathbf{a}_t^\dagger \mathbf{a}_t - \mathbf{b}_t^\dagger \mathbf{b}_t, \quad (4.36)$$

where  $\mathbf{a}_t$  and  $\mathbf{b}_t$  are waves incident on and reflected from the array elements. Since

$$\mathbf{b}_t = \mathbf{S}_{tt} \mathbf{a}_t \quad (4.37)$$

from the definition of S-parameters, (4.36) can be written as

$$P_{in} = \mathbf{a}_t^\dagger \left[ \mathbf{I} - \mathbf{S}_{tt}^\dagger \mathbf{S}_{tt} \right] \mathbf{a}_t. \quad (4.38)$$

Finally, substituting (4.38) and (4.26) into (4.35) yields gain expression in terms of waves incident on the array elements,

$$G(\theta, \phi) = \frac{(4\pi r)^2 \mathbf{a}_t^\dagger \mathbf{S}_{pt}^\dagger(r, \theta, \phi) \mathbf{S}_{pt}(r, \theta, \phi) \mathbf{a}_t}{G_{R_p} \lambda^2 \mathbf{a}_t^\dagger \left[ \mathbf{I} - \mathbf{S}_{tt}^\dagger \mathbf{S}_{tt} \right] \mathbf{a}_t}. \quad (4.39)$$

Alternatively, we can write the gain in terms of incident source waves by substituting (4.14b) into (4.39) which results in the array gain expression

$$G(\theta, \phi) = \frac{(4\pi r)^2 \mathbf{b}_s^\dagger \left[ \mathbf{I} - \mathbf{S}_{tt}^\dagger \mathbf{\Gamma}_{ss} \right]^{-1} \mathbf{S}_{pt}^\dagger(r, \theta, \phi) \mathbf{S}_{pt}(r, \theta, \phi) \left[ \mathbf{I} - \mathbf{\Gamma}_{ss} \mathbf{S}_{tt} \right]^{-1} \mathbf{b}_s}{G_{R_p} \lambda^2 \mathbf{b}_s^\dagger \left[ \mathbf{I} - \mathbf{S}_{tt}^\dagger \mathbf{\Gamma}_{ss} \right]^{-1} \left[ \mathbf{I} - \mathbf{S}_{tt}^\dagger \mathbf{S}_{tt} \right] \left[ \mathbf{I} - \mathbf{\Gamma}_{ss} \mathbf{S}_{tt} \right]^{-1} \mathbf{b}_s}. \quad (4.40)$$

Similar to array directivity, the array gain is a function of array element patterns, excitation, element mutual coupling and feed coupling.

The gain is related to directivity by radiation efficiency. The radiation efficiency of an antenna is determined by the ratio between gain and directivity,

$$e_r = \frac{G(\theta, \phi)}{D(\theta, \phi)}, \quad (4.41)$$

or the ratio between the input power and the radiation power,

$$e_r = \frac{P_{rad}}{P_{in}}. \quad (4.42)$$

Substituting (4.29) and (4.39) into (4.41) results in the array radiation efficiency in terms of network model S-parameters,

$$e_r = \frac{4\pi r^2}{G_{Rp}\lambda^2} \frac{\iint_{\Omega} \mathbf{a}_t^\dagger \mathbf{S}_{pt}^\dagger(r, \theta, \phi) \mathbf{S}_{pt}(r, \theta, \phi) \mathbf{a}_t \, d\Omega}{\mathbf{a}_t^\dagger [\mathbf{I} - \mathbf{S}_{tt}^\dagger \mathbf{S}_{tt}] \mathbf{a}_t}. \quad (4.43)$$

Alternatively, Substituting (4.29) and (4.40) into (4.41) yields the second form of the array radiation efficiency,

$$e_r = \frac{4\pi r^2}{G_{Rp}\lambda^2} \frac{\iint_{\Omega} \mathbf{b}_s^\dagger [\mathbf{I} - \mathbf{S}_{tt}^\dagger \mathbf{\Gamma}_{ss}^\dagger]^{-1} \mathbf{S}_{pt}^\dagger(r, \theta, \phi) \mathbf{S}_{pt}(r, \theta, \phi) [\mathbf{I} - \mathbf{\Gamma}_{ss} \mathbf{S}_{tt}]^{-1} \mathbf{b}_s \, d\Omega}{\mathbf{b}_s^\dagger [\mathbf{I} - \mathbf{S}_{tt}^\dagger \mathbf{\Gamma}_{ss}^\dagger]^{-1} [\mathbf{I} - \mathbf{S}_{tt}^\dagger \mathbf{S}_{tt}] [\mathbf{I} - \mathbf{\Gamma}_{ss} \mathbf{S}_{tt}]^{-1} \mathbf{b}_s}. \quad (4.44)$$

We can show that in the limit of the number of elements in the array becoming one, the array radiation efficiency expression (4.44) reduces to the radiation efficiency of single antenna (3.34). Substituting (4.30) into (4.44) yields

$$e_r = \frac{4\pi r^2}{G_{Rp}\lambda^2} \frac{\iint_{\Omega} \left\{ b_{s_1} [1 - S_{t_1 t_1}^* \Gamma_{s_1 s_1}^*]^{-1} \right\} \mathbf{S}_{pt}^\dagger(r, \theta, \phi) \mathbf{S}_{pt}(r, \theta, \phi) \left\{ [1 - \Gamma_{s_1 s_1} S_{t_1 t_1}]^{-1} b_{s_1} \right\} \, d\Omega}{\left\{ b_{s_1} [1 - S_{t_1 t_1}^* \Gamma_{s_1 s_1}^*]^{-1} \right\} [1 - S_{t_1 t_1}^* S_{t_1 t_1}] \left\{ [1 - \Gamma_{s_1 s_1} S_{t_1 t_1}]^{-1} b_{s_1} \right\}}. \quad (4.45)$$

Since the terms inside braces in the numerator can be pulled out of the integral and canceled with the terms inside the braces in the denominator, (4.45) simplifies to

$$e_r = \frac{4\pi r^2}{G_{Rp}\lambda^2} \frac{\iint_{\Omega} \mathbf{S}_{pt}^\dagger(r, \theta, \phi) \mathbf{S}_{pt}(r, \theta, \phi) \, d\Omega}{1 - S_{t_1 t_1}^* S_{t_1 t_1}}. \quad (4.46)$$

Finally, substituting (4.33) for the two polarization patterns of the single antenna into (4.46) yields the desired expression,

$$e_r = \frac{4\pi r^2}{G_{Rp}\lambda^2} \frac{\iint_{\Omega} S_{p_1 t_1}^*(r, \theta, \phi) S_{p_1 t_1}(r, \theta, \phi) + S_{p_2 t_1}^*(r, \theta, \phi) S_{p_2 t_1}(r, \theta, \phi) \, d\Omega}{1 - S_{t_1 t_1}^* S_{t_1 t_1}}. \quad (4.47)$$

We can see that (4.47) is identical to the radiation efficiency expression for the single element antenna (3.34).

### 4.2.3 Array Realized Gain

The realized gain of an antenna array includes the losses associated with the impedance mismatches between array antenna elements and the sources. The realized gain is defined as

$$G_R(\theta, \phi) = \frac{4\pi U(\theta, \phi)}{P_{av}} \quad (4.48)$$

where  $P_{av}$  is the maximum available power from source network. The maximum available power from the sources are determined from the power incident on a network that is conjugate matched to the source network. For a single port network, the maximum power transfer occurs when the port is fed with a conjugate matched source. The equivalent requirement for a multi-port network requires the source network to be Hermitian transpose of the the network [64], i.e.

$$P_{av} = P_{in} \text{ when } \mathbf{S}_{tt} = \mathbf{\Gamma}_{ss}^\dagger. \quad (4.49)$$

Substituting (4.14b) into (4.38) and replacing  $\mathbf{S}_{tt}$  with  $\mathbf{\Gamma}_{ss}^\dagger$  results in

$$P_{av} = \mathbf{b}_s^\dagger \left[ (\mathbf{I} - \mathbf{\Gamma}_{ss} \mathbf{\Gamma}_{ss}^\dagger)^{-1} \right]^\dagger \left[ \mathbf{I} - \mathbf{\Gamma}_{ss} \mathbf{\Gamma}_{ss}^\dagger \right] \left[ \mathbf{I} - \mathbf{\Gamma}_{ss} \mathbf{\Gamma}_{ss}^\dagger \right]^{-1} \mathbf{b}_s \quad (4.50)$$

which simplifies to

$$P_{av} = \mathbf{b}_s^\dagger \left[ \mathbf{I} - \mathbf{\Gamma}_{ss} \mathbf{\Gamma}_{ss}^\dagger \right]^{-1} \mathbf{b}_s. \quad (4.51)$$

Using the array intensity expression (4.28) and the available power (4.51), the array realized gain is determined as

$$G_R(\theta, \phi) = \frac{(4\pi r)^2 \mathbf{b}_s^\dagger \left[ \mathbf{I} - \mathbf{S}_{tt}^\dagger \mathbf{\Gamma}_{ss}^\dagger \right]^{-1} \mathbf{S}_{pt}^\dagger(r, \theta, \phi) \mathbf{S}_{pt}(r, \theta, \phi) \left[ \mathbf{I} - \mathbf{\Gamma}_{ss} \mathbf{S}_{tt} \right]^{-1} \mathbf{b}_s}{G_{R_p} \lambda^2 \mathbf{b}_s^\dagger \left[ \mathbf{I} - \mathbf{\Gamma}_{ss} \mathbf{\Gamma}_{ss}^\dagger \right]^{-1} \mathbf{b}_s}. \quad (4.52)$$

The equivalent expression in terms of waves incident on the array element is obtained by solving (4.13) for  $\mathbf{b}_s$ ,

$$\mathbf{b}_s = \left[ \mathbf{I} - \mathbf{\Gamma}_{ss} \mathbf{S}_{tt} \right] \mathbf{a}_t \quad (4.53)$$

and substituting (4.53) into (4.52) which gives

$$G_R(\theta, \phi) = \frac{(4\pi r)^2 \mathbf{a}_t^\dagger \mathbf{S}_{pt}^\dagger(r, \theta, \phi) \mathbf{S}_{pt}(r, \theta, \phi) \mathbf{a}_t}{G_{R_p} \lambda^2 \mathbf{a}_t^\dagger \left[ \mathbf{I} - \mathbf{S}_{tt}^\dagger \mathbf{\Gamma}_{ss}^\dagger \right] \left[ \mathbf{I} - \mathbf{\Gamma}_{ss} \mathbf{\Gamma}_{ss}^\dagger \right]^{-1} \left[ \mathbf{I} - \mathbf{\Gamma}_{ss} \mathbf{S}_{tt} \right] \mathbf{a}_t} \quad (4.54)$$

The impedance mismatch factor,  $q$  is determined from the ratio of realized gain to the gain of the array

$$q = \frac{G_R(\theta, \phi)}{G(\theta, \phi)}. \quad (4.55)$$

We can define the impedance mismatching factor in terms of the incident source waves by substituting (4.40) and (4.52) into (4.55) which yields

$$q = \frac{\mathbf{b}_s^\dagger \left[ \mathbf{I} - \mathbf{S}_{tt}^\dagger \boldsymbol{\Gamma}_{ss}^\dagger \right]^{-1} \left[ \mathbf{I} - \mathbf{S}_{tt}^\dagger \mathbf{S}_{tt} \right] \left[ \mathbf{I} - \boldsymbol{\Gamma}_{ss} \mathbf{S}_{tt} \right]^{-1} \mathbf{b}_s}{\mathbf{b}_s^\dagger \left[ \mathbf{I} - \boldsymbol{\Gamma}_{ss} \boldsymbol{\Gamma}_{ss}^\dagger \right]^{-1} \mathbf{b}_s}, \quad (4.56)$$

or define  $q$  in terms of the array incident waves by substituting (4.39) and (4.54) into (4.56) which yields

$$q = \frac{\mathbf{a}_t^\dagger \left[ \mathbf{I} - \mathbf{S}_{tt}^\dagger \mathbf{S}_{tt} \right] \mathbf{a}_t}{\mathbf{a}_t^\dagger \left[ \mathbf{I} - \mathbf{S}_{tt}^\dagger \boldsymbol{\Gamma}_{ss}^\dagger \right] \left[ \mathbf{I} - \boldsymbol{\Gamma}_{ss} \boldsymbol{\Gamma}_{ss}^\dagger \right]^{-1} \left[ \mathbf{I} - \boldsymbol{\Gamma}_{ss} \mathbf{S}_{tt} \right] \mathbf{a}_t}. \quad (4.57)$$

As discussed previously, conjugate matching a multi-port network requires the matching network to have a scattering matrix that is Hermitian transpose of the S-matrix of the multi-port. When the source network is conjugately matched to the array elements such that

$$\boldsymbol{\Gamma}_{ss} = \mathbf{S}_{tt}^\dagger \quad (4.58)$$

the impedance mismatch becomes unity,

$$\begin{aligned} q &= \frac{\mathbf{b}_s^\dagger \left[ \mathbf{I} - \mathbf{S}_{tt}^\dagger \mathbf{S}_{tt} \right]^{-1} \left[ \mathbf{I} - \mathbf{S}_{tt}^\dagger \mathbf{S}_{tt} \right] \left[ \mathbf{I} - \mathbf{S}_{tt}^\dagger \mathbf{S}_{tt} \right]^{-1} \mathbf{b}_s}{\mathbf{b}_s^\dagger \left[ \mathbf{I} - \mathbf{S}_{tt}^\dagger \mathbf{S}_{tt} \right]^{-1} \mathbf{b}_s} \\ &= \frac{\mathbf{b}_s^\dagger \left[ \mathbf{I} - \mathbf{S}_{tt}^\dagger \mathbf{S}_{tt} \right]^{-1} \mathbf{b}_s}{\mathbf{b}_s^\dagger \left[ \mathbf{I} - \mathbf{S}_{tt}^\dagger \mathbf{S}_{tt} \right]^{-1} \mathbf{b}_s} = 1. \end{aligned} \quad (4.59)$$

On the other hand, when there is no mutual coupling in the feed network,  $\boldsymbol{\Gamma}_{ss} = \mathbf{0}$  and the impedance mismatch factor becomes

$$q = \frac{\mathbf{b}_s \left[ \mathbf{I} - \mathbf{S}_{tt}^\dagger \mathbf{S}_{tt} \right] \mathbf{b}_s}{\mathbf{b}_s^\dagger \mathbf{b}_s}. \quad (4.60)$$

Similarly when there is no mutual coupling in the elements,  $\mathbf{S}_{tt} = \mathbf{0}$  and the impedance mismatch factor becomes

$$q = \frac{\mathbf{b}_s^\dagger \mathbf{b}_s}{\mathbf{b}_s \left[ \mathbf{I} - \boldsymbol{\Gamma}_{ss} \boldsymbol{\Gamma}_{ss}^\dagger \right]^{-1} \mathbf{b}_s}. \quad (4.61)$$

In either case, the remaining mutual coupling in the array elements or coupling in the feed network causes the reduction in the array realized gain from the array gain indicated by non-unity  $q$ . When both  $\mathbf{\Gamma}_{ss} = 0$  and  $\mathbf{S}_{tt} = 0$ , the array becomes ideal where there is no mutual coupling anywhere in the system. As expected  $q$  becomes unity for this case.

#### 4.2.4 Normalized S-parameters

It is useful to define S-parameters that are independent of distance  $r$ , and probe antenna gain  $G_{R_p}$  similar to the formulations developed in Chapter 3. Let us define the normalized S-parameters as

$$\mathbf{S}'_{pt}(\theta, \phi) = \frac{r\sqrt{4\pi}}{\lambda\sqrt{G_{R_p}}}\mathbf{S}_{pt}(r, \theta, \phi). \quad (4.62)$$

The normalized S-parameters represent the coupling from the test array to the probe antenna per unit radian. Thus, two elements of the vector  $\mathbf{S}'_{pt}(\theta, \phi)\mathbf{a}_t$  are proportional to two polarization components of the array electric fields in far-field. Using the normalized S-parameters, the directivity expressions (4.27) and (4.29) become

$$D(\theta, \phi) = \frac{4\pi\mathbf{a}_t^\dagger\mathbf{S}'_{pt}{}^\dagger(\theta, \phi)\mathbf{S}'_{pt}(\theta, \phi)\mathbf{a}_t}{\iint_{\Omega}\mathbf{a}_t^\dagger\mathbf{S}'_{pt}{}^\dagger(\theta, \phi)\mathbf{S}'_{pt}(\theta, \phi)\mathbf{a}_t d\Omega} \quad (4.63)$$

$$D(\theta, \phi) = \frac{4\pi\mathbf{b}_s^\dagger\left[\mathbf{I} - \mathbf{S}_{tt}^\dagger\mathbf{\Gamma}_{ss}^\dagger\right]^{-1}\mathbf{S}'_{pt}{}^\dagger(\theta, \phi)\mathbf{S}'_{pt}(\theta, \phi)\left[\mathbf{I} - \mathbf{\Gamma}_{ss}\mathbf{S}_{tt}\right]^{-1}\mathbf{b}_s}{\iint_{\Omega}\mathbf{b}_s^\dagger\left[\mathbf{I} - \mathbf{S}_{tt}^\dagger\mathbf{\Gamma}_{ss}^\dagger\right]^{-1}\mathbf{S}'_{pt}{}^\dagger(\theta, \phi)\mathbf{S}'_{pt}(\theta, \phi)\left[\mathbf{I} - \mathbf{\Gamma}_{ss}\mathbf{S}_{tt}\right]^{-1}\mathbf{b}_s d\Omega}, \quad (4.64)$$

the gain expressions (4.39) and (4.40) become

$$G(\theta, \phi) = \frac{4\pi\mathbf{a}_t^\dagger\mathbf{S}'_{pt}{}^\dagger(r, \theta, \phi)\mathbf{S}_{pt}(r, \theta, \phi)\mathbf{a}_t}{\mathbf{a}_t^\dagger\left[\mathbf{I} - \mathbf{S}_{tt}^\dagger\mathbf{S}_{tt}\right]\mathbf{a}_t} \quad (4.65)$$

$$G(\theta, \phi) = \frac{4\pi\mathbf{b}_s^\dagger\left[\mathbf{I} - \mathbf{S}_{tt}^\dagger\mathbf{\Gamma}_{ss}^\dagger\right]^{-1}\mathbf{S}'_{pt}{}^\dagger(r, \theta, \phi)\mathbf{S}_{pt}(r, \theta, \phi)\left[\mathbf{I} - \mathbf{\Gamma}_{ss}\mathbf{S}_{tt}\right]^{-1}\mathbf{b}_s}{\mathbf{b}_s^\dagger\left[\mathbf{I} - \mathbf{S}_{tt}^\dagger\mathbf{\Gamma}_{ss}^\dagger\right]^{-1}\left[\mathbf{I} - \mathbf{S}_{tt}^\dagger\mathbf{S}_{tt}\right]\left[\mathbf{I} - \mathbf{\Gamma}_{ss}\mathbf{S}_{tt}\right]^{-1}\mathbf{b}_s}, \quad (4.66)$$

and the realized gain expressions (4.52) and (4.54) become

$$G_R(\theta, \phi) = \frac{4\pi\mathbf{a}_t^\dagger\mathbf{S}'_{pt}{}^\dagger(\theta, \phi)\mathbf{S}'_{pt}(\theta, \phi)\mathbf{a}_t}{\mathbf{a}_t^\dagger\left[\mathbf{I} - \mathbf{S}_{tt}^\dagger\mathbf{\Gamma}_{ss}^\dagger\right]\left[\mathbf{I} - \mathbf{\Gamma}_{ss}\mathbf{\Gamma}_{ss}^\dagger\right]^{-1}\left[\mathbf{I} - \mathbf{\Gamma}_{ss}\mathbf{S}_{tt}\right]\mathbf{a}_t} \quad (4.67)$$

$$G_R(\theta, \phi) = \frac{4\pi \mathbf{b}_s^\dagger \left[ \mathbf{I} - \mathbf{S}_{tt}^\dagger \mathbf{\Gamma}_{ss} \right]^{-1} \mathbf{S}'_{pt}{}^\dagger(\theta, \phi) \mathbf{S}'_{pt}(\theta, \phi) \left[ \mathbf{I} - \mathbf{\Gamma}_{ss} \mathbf{S}_{tt} \right]^{-1} \mathbf{b}_s}{\mathbf{b}_s^\dagger \left[ \mathbf{I} - \mathbf{\Gamma}_{ss} \mathbf{\Gamma}_{ss} \right]^{-1} \mathbf{b}_s}. \quad (4.68)$$

The normalized S-parameter forms of the directivity, the gain, and the realized gain expressions are used in the experimental verification discussed in Chapter 6.

### 4.3 Analysis of 2-Element Dipole Antenna

In the previous section, we developed directivity, gain, and realized gain expressions for generalized antenna arrays using the array element coupling, feed coupling, and element patterns. As an example of array antenna network analysis, let us consider a two element array of half-wave dipoles. We will evaluate the array realized gain pattern using the network formulation (4.54) and compare it to the actual realized gain pattern. Fig. 4.4 illustrates the geometry of two element parallel dipole array. It consists of two thin wire dipole elements. Each element has the length of  $L = 50$  mm, wire diameter of  $W = 0.1$  mm, and is fed at the center of dipole. The elements are oriented to be parallel to each other with separation distance of  $d = 50$  mm. In the network analysis, the array radiation pattern is detected using a dipole element of equal geometry at location  $(r, \theta, \phi)$ . The probe dipole orientation is such that its beam maximum is directed towards the center of the array as it is moved around the array.

The Numerical Electromagnetics Code 4 (NEC4) [68] which is a method of moments based wire analysis code was used to simulate the array antenna. The numerical simulations were performed at  $f = 3$  GHz or  $\lambda = 99.93$  mm in wavelength. The two element array realized gain patterns were evaluated using two methods: direct method using the gain pattern output from the NEC4 simulation, and indirect method based on the network S-

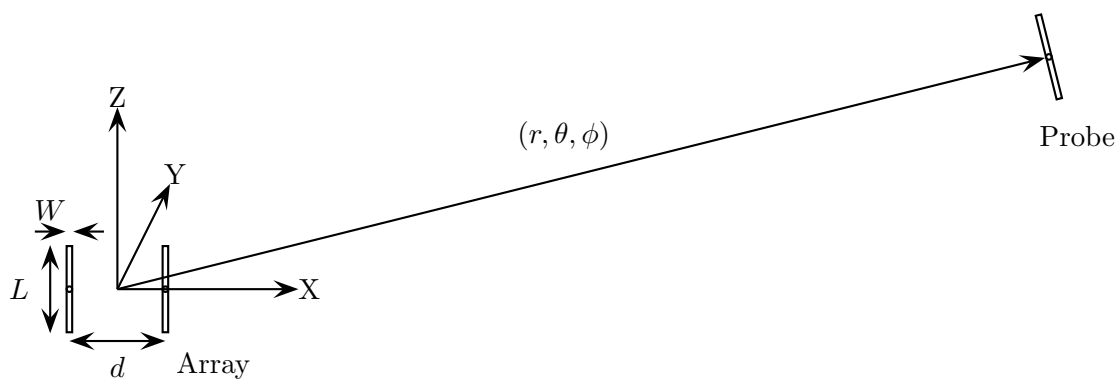


**Figure 4.4** Two element parallel dipole array and a dipole probe antenna. Dipole length,  $L = 50$  mm, diameter,  $W = 0.1$  mm, separation distance,  $d = 50$  mm, variable probe position  $(r, \theta, \phi)$ , frequency  $f = 3$  GHz.

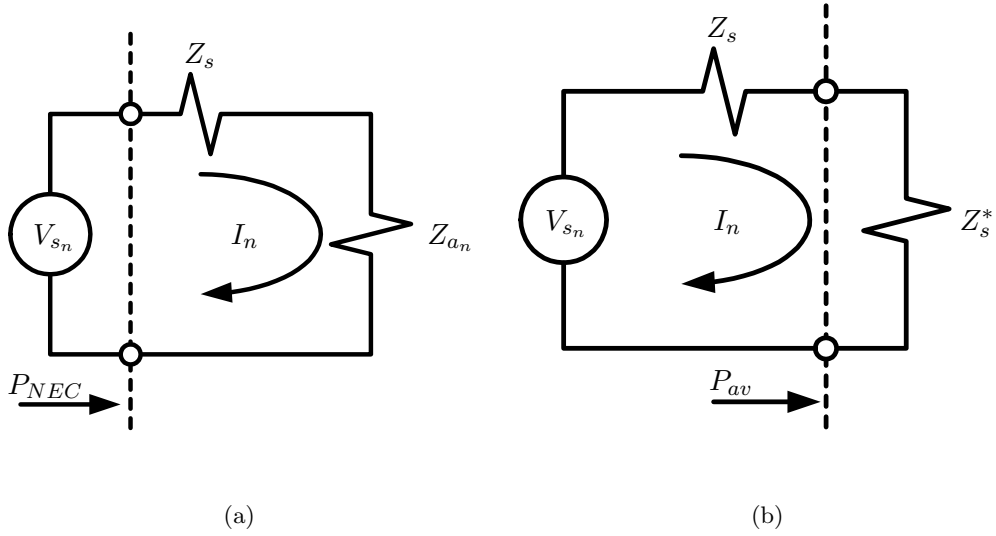


**Figure 4.5** Equivalent circuits for an element in the two dipole array of Fig. 4.4. (a) Equivalent circuit used for the computation of gain pattern in the NEC4 simulation. (b) Equivalent circuit used to determine the available power from the source in the computation of realized gain pattern.

parameter analysis using the source voltages and the feed point currents output from NEC4 simulation.

In the direct method, the gain pattern of two element array without probe antenna is evaluated using NEC4. The array elements are loaded with  $50\ \Omega$  lumped loads at the feed points to simulate the transmitter source impedances. Since NEC4 computes gain patterns assuming that the loads are part of the antenna elements as shown in Fig. 4.5(a), the gain output from the NEC4 simulations includes the power lost in these loads. We are interested in the realized gain of the array where these loads are included in the computation as part of the sources. The input power used in the gain computation is incorrect for our need. Thus, the gain pattern from NEC4 simulation must be re-normalized with available power from the voltage sources to determine the proper realized gain pattern.

The power input to the array which is used in the NEC4 gain pattern computation,  $P_{NEC4}$ , is determined from the source voltages  $\{V_{s_n}\}$  and the feed point currents,  $\{I_n\}$ , using [68]

$$P_{NEC4} = \frac{1}{2} \sum_{n=1}^2 \text{Re}(V_{s_n} I_n^*). \quad (4.69)$$

The total power available from the sources,  $P_{av}$ , is used in an array realized gain computation as defined in (4.48). The available power from a voltage source is determined when the load is conjugate matched to the source impedance as shown in Fig. 4.5(b), giving

$$P_{av} = \frac{1}{2} \sum_{n=1}^2 \left| \frac{V_{s_n}}{2} \right| \operatorname{Re}(Z_{s_n}) \quad (4.70)$$

where  $\{V_{s_n}\}$  are the source voltages and  $\{Z_s\}$  are the source impedances. The realized gain pattern,  $G_R$  is determined from the gain pattern output from NEC,  $G_{NEC4}$ , using

$$G_R(\theta, \phi) = G_{NEC4}(\theta, \phi) \frac{P_{NEC4}}{P_{av}}. \quad (4.71)$$

The realized gain pattern computed using the direct method is the expected pattern of the array in far-field region.

In the indirect method, the scattering matrix of the array and the probe antenna is determined from the NEC4 simulation output of the feed point currents. The array elements and the probe antenna are loaded with  $50 \Omega$  lumped impedances at the feed points to simulate the source impedances for the transmitters and the load impedance for the receiver similar to the simulation used in the direct method. An array element or the probe antenna is excited one at a time with a voltage source to determine the feed point currents. Then, the source voltage and the feed point currents are used to determine the  $3 \times 3$  array S-matrix. When  $n$ -th port of the array and probe network is excited with a voltage source,  $V_{s_n}$ , the diagonal component of the S-matrix is determined from the definition of S-parameters [63] using the feed point currents and the source impedance giving

$$S_{nn} = \frac{V_{s_n} - 2I_n Z_s}{V_{s_n}}, \quad (4.72)$$

while the off-diagonal components of the S-matrix are determined using

$$S_{mn} = \frac{-2I_m Z_s}{V_{s_n}}. \quad (4.73)$$

Finally, the S-parameter matrix of the array and the probe determined using (4.72) and (4.73) is used to compute the array realized gain pattern using (4.54).

### 4.3.1 Sum Pattern Example

The realized gain pattern of the two-element dipole array was computed using the direct and indirect methods discussed in the previous section. Figure 4.6 shows a comparison

of realized gain patterns of the dipole array between direct and indirect methods for  $E_\phi$  polarization in the  $\theta = 90^\circ$  plane at 3 GHz. The array elements are fed by independent sources with internal source impedances of  $50\ \Omega$ , and excited uniformly with incident waves

$$a_{t_1} = a_{t_2} = 1\angle 0^\circ \quad (4.74)$$

for the sum pattern in the broadside direction. The solid curve in the plot represents the array realized gain pattern which was determined by the indirect method using S-parameter network expression (4.54). The S-parameters necessary for the network analysis were computed from the NEC4 simulation of the array elements with a dipole probe antenna which was located at the probe distance of  $r = 10\ \lambda$  from the array center, and rotated around the array from  $\phi = -180^\circ$  to  $180^\circ$  in  $\theta = 90^\circ$  plane.

The dashed curve in Fig. 4.6 represents the realized gain pattern of the array without

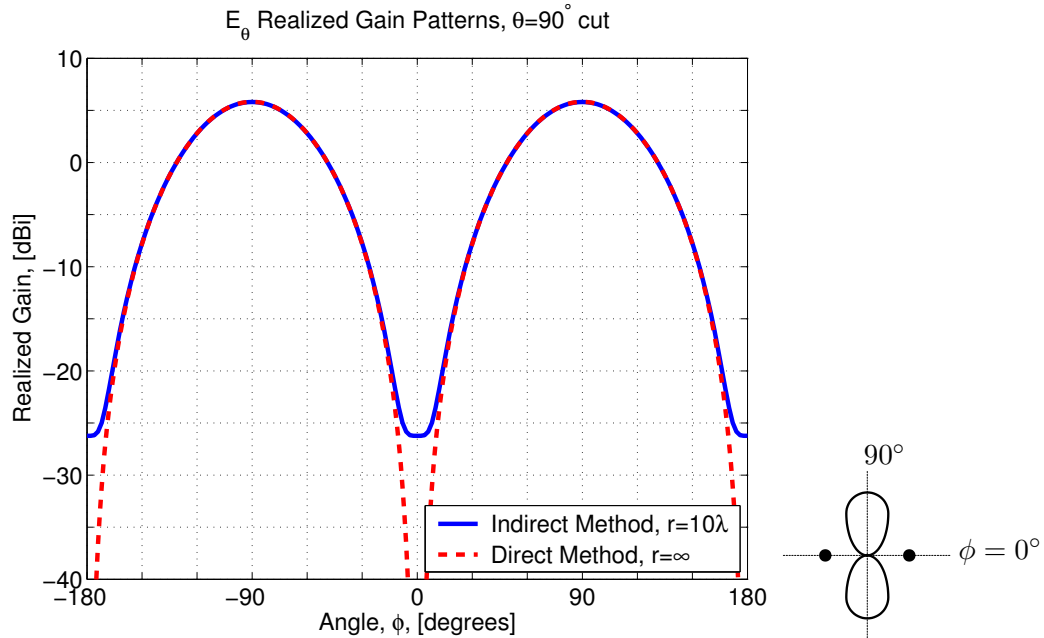
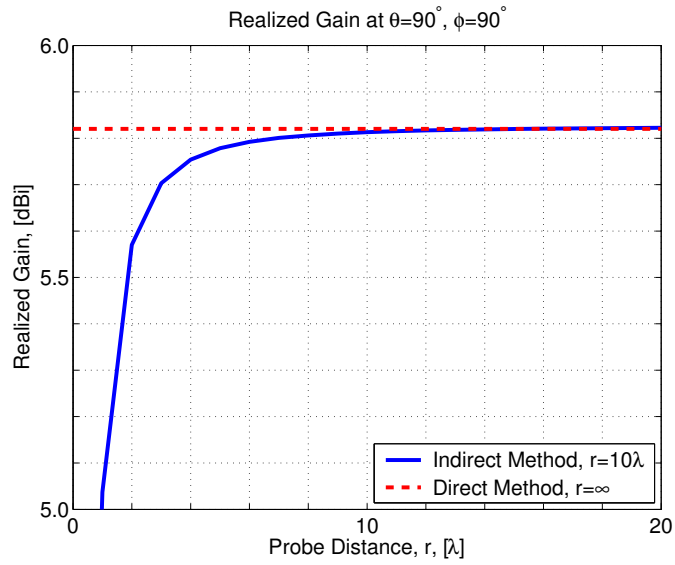


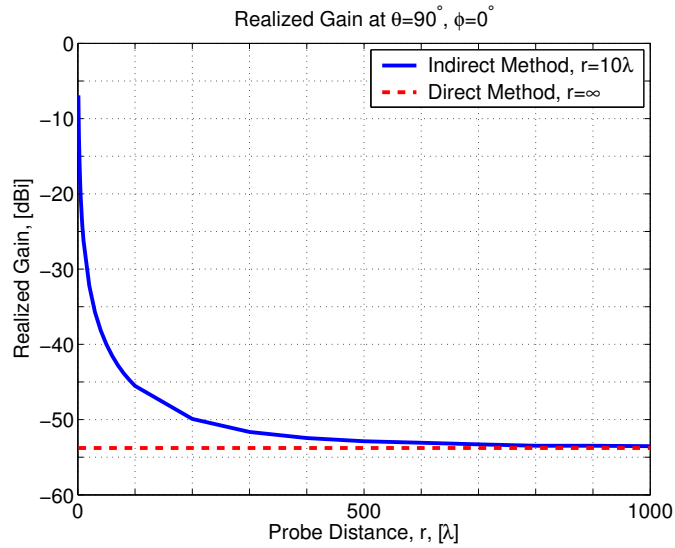
**Figure 4.6** Realized-gain patterns ( $E_\theta$  polarization) in  $\theta = 90^\circ$  plane for an array of two half-wave dipoles of Fig. 4.4 spaced half wavelength apart and parallel to the z-axis. The geometry is shown in the inset. The solid-curve pattern was computed using the indirect method based on the S-parameter network analysis using (4.54) for a half wavelength dipole probe at  $r = 10\ \lambda$  (Solid curve). The dashed-curve pattern was computed using the direct method from NEC4 gain pattern which is normalized using (4.71)

the probe antenna computed with the direct method from the NEC4 simulation gain pattern output using (4.71). The plot shows that the patterns agree very well over most of the pattern angles. However, the indirect method realized gain diverges considerably from the expect realized gain in the pattern nulls at  $\phi = 0^\circ$  and  $\phi = \pm 180^\circ$  for this particular array with the uniform excitation.

The effect of the selected probe distance,  $r$ , on the realized gain value was investigated for the indirect method using the S-parameter network network analysis. The realized gain value plots in  $\phi = 0^\circ$  and  $90^\circ$  directions in  $\theta = 90^\circ$  plane as a function of probe distance  $r$  is shown in Fig. 4.7. In the beam peak direction ( $\phi = 90^\circ$  in Fig. 4.6), the realized gain computed using the indirect method converges very quickly to the expect value computed using the direct method with less than 0.1 dB error when probe distance  $r$  is greater than  $4 \lambda$  as shown in Fig. 4.7(a). On the other hand, the convergence of the realized gain in the pattern null direction ( $\phi = 0^\circ$  in Fig. 4.6) is much slower as shown in Fig. 4.7(b). At the probe distance of  $r = 1000 \lambda$ , there is 0.4 dB difference in the realized gain values between the direct and the indirect methods. However, accurate calculation for deep nulls is often unnecessary and the probe distance can be small.



(a)



(b)

**Figure 4.7** Comparison of realized gain for the array of Fig. 4.6 in the  $E_\theta$  polarization as a function of probe antenna distance,  $r$ , between the indirect method using the S-parameter network analysis using (4.54) (solid curve), and the direct method from NEC4 gain pattern output normalized using (4.71) (dashed curve). (a)  $\theta = 90^\circ, \phi = 90^\circ$ . (In the beam peak region of Fig. 4.6) (b)  $\theta = 90^\circ, \phi = 0^\circ$  (In the pattern null region of Fig. 4.6).

### 4.3.2 Difference Pattern Example

A second example using a difference pattern was investigated because the deep broadside nulls revealed computational difficulties in the previous section. The computed realized gain patterns was simulated on the two half-wavelength element dipole array of Fig. 4.4 excited with uniform but opposite phase incident waves,

$$a_{t_1} = 1 \angle 0^\circ \quad a_{t_2} = 1 \angle 180^\circ. \quad (4.75)$$

With these excitation coefficients, the beam peaks and the pattern nulls will be in the end-fire directions ( $\phi = 0^\circ$  and  $\pm 180^\circ$ ) and the broadside directions ( $\phi = \pm 90^\circ$ ), respectively. These pattern peaks and pattern nulls are at the opposite locations from the sum pattern example in the previous section.

The same half-wavelength dipole probe antenna as the previous example was used to

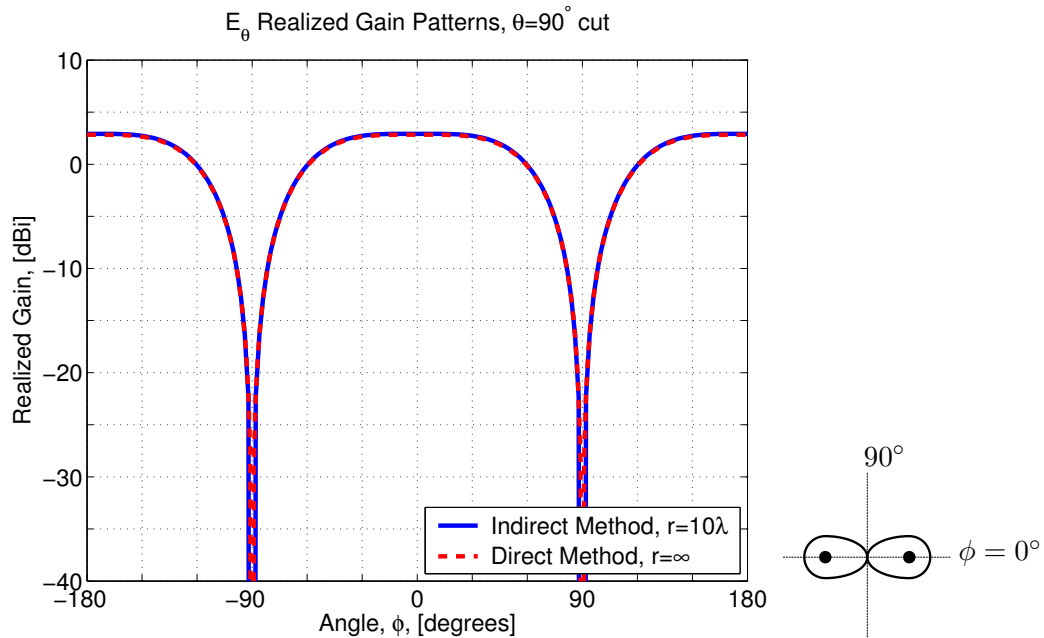


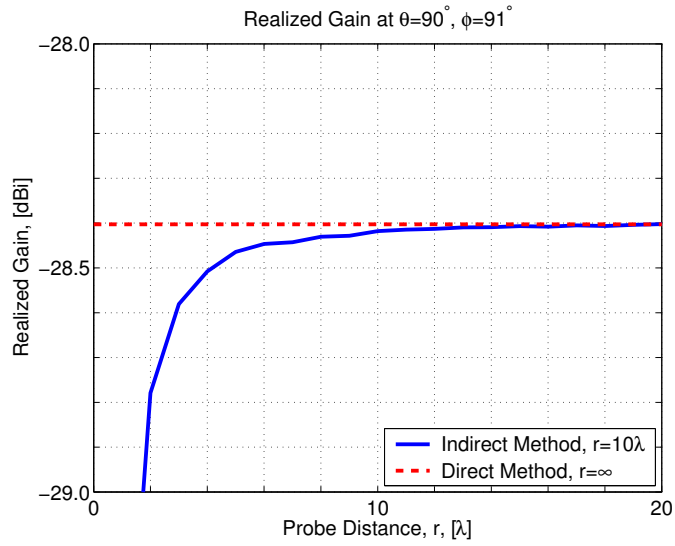
**Figure 4.8** Realized-gain patterns ( $E_\theta$  polarization) in  $\theta = 90^\circ$  plane for an array of two half-wave dipoles of Fig. 4.4 spaced a half wavelength apart and parallel to the z-axis. The geometry is shown in the inset. The solid-curve pattern was computed using the indirect method based on the S-parameter network analysis using (4.54) for a half wavelength dipole probe at  $r = 10 \lambda$  (Solid curve). The dashed-curve pattern was computed using the direct method from NEC4 gain pattern which is normalized using (4.71)

determine the realized gain pattern using the indirect method. The probe antenna was located at the distance of  $r = 10 \lambda$ , and rotated around the array from  $\phi = -180^\circ$  to  $180^\circ$  in  $\theta = 90^\circ$  plane. The S-parameter matrix necessary for the indirect method analysis was determined with the same procedure as before using (4.72) and (4.73).

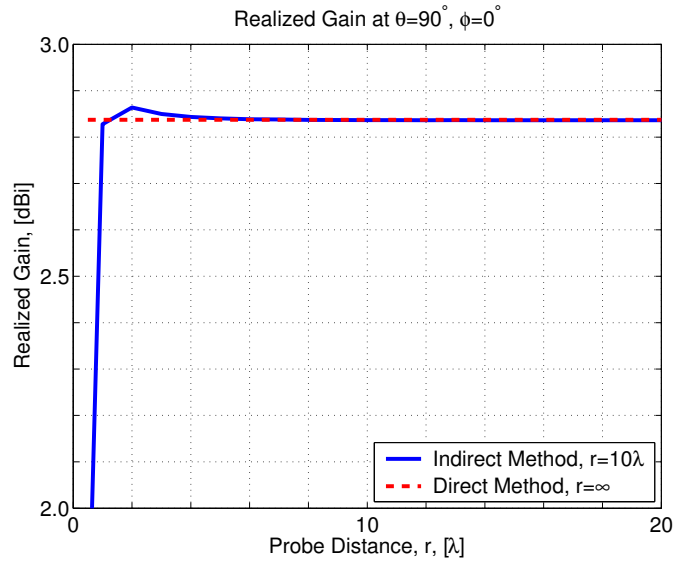
Figure 4.8 shows a comparison of the realized gain patterns for  $E_\theta$  polarization in  $\theta = 90^\circ$  plane computed using the direct and the indirect methods. The solid curve in the plot represents the computed array realized gain pattern which was determined using the indirect method, while the dashed curve represents the expected realized gain pattern computed using the direct method. Unlike the sum pattern of the previous section, the difference patterns between two methods compare very well in all directions.

The relationship between the probe distance from the array to the realized gain value was investigated. The realized gain plots in  $\phi = 0^\circ$  and  $90^\circ$  directions in  $\theta = 90^\circ$  plane as a function of probe distance,  $r$ , are shown in Fig. 4.9. Convergence of the realized gain computed using the indirect method to the values computed using the direct method occur very quickly in the beam peak and null directions. For the pattern null, there is less than 0.1 dB difference in the realized gain value for  $r \geq 4 \lambda$  as shown in Fig. 4.9(a). This contrast with the sum pattern case where the convergence required  $r \geq 1000 \lambda$ . In the pattern peak region, there is less than 0.1 dB error for  $r \geq 2 \lambda$ .

The sum and difference patterns of two presented examples are widely different pattern shapes that span those in common use, providing an excellent test of the computational methods. Based on the convergence of the realized gain values computed using the indirect method to the expected value for the direct method, we conclude that a probe distance of  $4 \lambda$  is sufficient for most cases. For accurate calculation of end-fire nulls, a greater probe distance is necessary.



(a)



(b)

**Figure 4.9** Comparison of array realized gain for the  $E_\theta$  polarization as a function of probe antenna distance,  $r$ , between the indirect method using the S-parameter network analysis using (4.54) (solid curve), and the direct method from NEC4 gain pattern output normalized using (4.71) (dashed curve). (a)  $\theta = 90^\circ$ ,  $\phi = 90^\circ$ . (In the beam peak region of Fig. 4.6) (b)  $\theta = 90^\circ$ ,  $\phi = 0^\circ$  (In the pattern null region of Fig. 4.6).

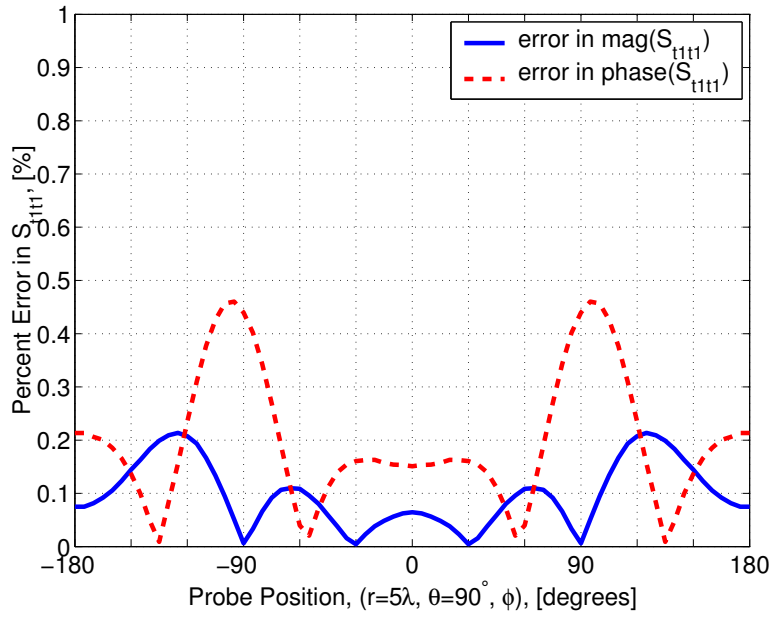
### 4.3.3 Verification of the assumption that S-parameters are probe position independent

In the derivation of network pattern analysis method, we assumed that the array element S-parameter matrix is independent of the probe antenna position,  $(r, \theta, \phi)$  as is implicit in (4.2) for sufficiently large probe distance  $r$ . To verify this assumption, the scattering parameters of the array elements were computed as the probe antenna is rotated around the two-element array of Fig. 4.4 from  $\phi = -180^\circ$  to  $180^\circ$ . To demonstrate that the coupling from the probe to the array causes only small deviation in the array S-parameters, a small probe distance of  $r = 5\lambda$  was selected. The plots in Fig. 4.10 show the percent error in the magnitudes and the phase of the dipole array S-parameters,  $S_{t_1 t_1}$  and  $S_{t_2 t_1}$  as a function of the probe antenna angular position. The error in S-parameters were computed using

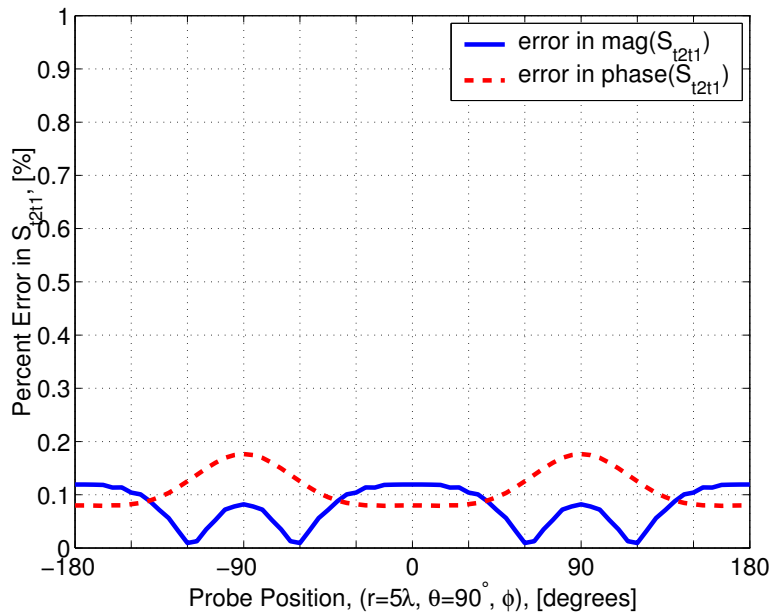
$$\delta m = \% \text{ Magnitude Error}(r, \theta, \phi) = \frac{|S_{tt}(r, \theta, \phi)| - |S_{tt}^o|}{|S_{tt}^o|} \times 100 \quad \text{for } r = 5\lambda, \theta = 90^\circ \quad (4.76a)$$

$$\delta ph = \% \text{ Phase Error}(r, \theta, \phi) = \frac{\angle S_{tt}(r, \theta, \phi) - \angle S_{tt}^o}{\angle S_{tt}^o} \times 100 \quad \text{for } r = 5\lambda, \theta = 90^\circ \quad (4.76b)$$

where  $S_{tt}^o$  is an S-parameter of the dipole array without the probe antenna. The plots show that the error in reflection term of the S-matrix,  $S_{t_1 t_1}$ , for the array with the probe antenna at distance  $r = 5 \lambda$  compared to the same S-parameter for the isolated array is less than 0.25% in magnitude and 0.5% in phase. Similarly, the coupling term of the S-matrix between two elements in the array,  $S_{t_2 t_1}$  has less than 0.15% and 0.2% error in the magnitude and the phase. We can conclude that the assumption that the scattering parameters are probe-position independent in (4.2) is valid for this two-element array case.



(a)



(b)

**Figure 4.10** Errors in the values of scattering parameters,  $S_{t_1 t_1}$  and  $S_{t_1 t_2}$ , for the two-element parallel dipole array of Fig.4.4 as a function of probe antenna position calculated using (4.76). The errors in the magnitude of S-parameters are shown in solid curves, and the errors in the phase of S-parameters are shown in dashed curves.

## 4.4 Summary

In this chapter, the scattering parameter network model for a single element antenna derived in Chapter 3 was extended to include  $N$  element array antenna. The model uses  $N + 2$  port S-matrix to describe the network where the two extra ports represent the radiation ports in two orthogonal polarization. A summary of the expressions derived in this chapter are shown in Table 4.1. These expressions are powerful tools for the analysis of antennas and antenna arrays because they allow seamless integration of impedance characteristics and the radiation pattern aspect of the antenna analysis and design. Some of the uses of the array network analysis concept will be demonstrated in the next two chapters.

This chapter also presented an analysis of two half-wavelength parallel dipole array using array network analysis. The analysis was conducted on a method of moment simulated data of two-element dipole array using NEC4. A sum and a difference patterns were computed using indirect method using array network analysis and direct method determined directly from NEC4 output. The results for both pattern cases for the indirect method converges with the results for the direct method providing a verification of the array network analysis method.

**Table 4.1** Summary of antenna parameters and their definition in terms of array network S-parameters.

Name	Variable	Definition	S-parameter Definition
Directivity	$D(\theta, \phi)$	$\frac{4\pi U(\theta, \phi)}{P_{rad}}$	(4.29) (4.27)
Gain	$G(\theta, \phi)$	$\frac{4\pi U(\theta, \phi)}{P_{in}}$	(4.40) (4.39)
Realized Gain	$G_R(\theta, \phi)$	$\frac{4\pi U(\theta, \phi)}{P_{av}}$	(4.52) (4.54)
Radiation Efficiency	$\epsilon_r$	$\frac{G}{D}$	(4.44) (4.43)
Impedance Mismatch	$q$	$\frac{G_R}{G}$	(4.56) (4.57)

## Chapter 5

# Impedance Matching of Array Antennas

This chapter presents an application of scattering parameter network models that were developed in the previous chapter for the analysis of antenna arrays. Specifically, we consider impedance matching of transmitter circuitry to the array elements. We investigate three configurations for source networks, and determine the source impedance matching solutions that can be implemented for these three networks. As an example, we apply the impedance matching to a three element strip dipole array, and analyze the bandwidth and radiation pattern of the array.

### 5.1 Impedance Matching Configurations and Strategies

Antenna arrays are used in RF systems to control radiation pattern shapes. Increasing the number of elements in an array can be utilized to increased the directivity and gain, or shape the radiation pattern. In addition, array pattern can be scanned in angular space through electronic control of the element excitation. These array pattern controls are nearly impossible to implement with a single antenna element.

Improvement of antenna gain is an important part of the antenna design process for some applications. The gain of a single element antenna is determined from the ratio of radiated power density to the input power from a matched source. We must have a priori

knowledge of the reflection coefficient or the antenna input impedance before the gain value can be determined.

It is also important to consider the realized gain of antennas in RF system design and analysis. Realized gain is the antenna gain including impedance mismatch effects; and thus, is reduced by the impedance mismatch loss between the antenna element and the source given by

$$G_R = qG \quad (5.1)$$

where the impedance mismatch factor,  $q$ , varies between 0 and 1. We can consider gain as the maximum achievable gain limit of an antenna, while realized gain is the actual gain value that the antenna can provide for a given RF system.

The gain of antenna arrays must be determined with matched source impedances. The process is not as simple as the single element antenna case since the active input impedances of array elements depend directly on the array mutual coupling and the element excitation. Impedance matching the array elements to the sources is especially important in high power transmitting arrays such as radar systems because severe mismatch can damage the transmitter circuits. The impedance mismatch factor for an antenna array was derived in Chapter 4 as

$$q = \frac{\mathbf{b}_s^\dagger \left[ \mathbf{I} - \mathbf{S}_{tt}^\dagger \mathbf{\Gamma}_{ss}^\dagger \right]^{-1} \left[ \mathbf{I} - \mathbf{S}_{tt}^\dagger \mathbf{S}_{tt} \right] \left[ \mathbf{I} - \mathbf{\Gamma}_{ss} \mathbf{S}_{tt} \right]^{-1} \mathbf{b}_s}{\mathbf{b}_s^\dagger \left[ \mathbf{I} - \mathbf{\Gamma}_{ss} \mathbf{\Gamma}_{ss}^\dagger \right]^{-1} \mathbf{b}_s} \quad (5.2)$$

where  $\mathbf{S}_{tt}$  and  $\mathbf{\Gamma}_{ss}$  represent the S-matrices of the array elements and source network, and  $\mathbf{b}_s$  represents the incident source waves. For a given array S-matrix we will determine the source network S-parameters required to minimize the mismatch, or equivalently maximize the mismatch factor.

Many ways exist to achieve impedance matching between the array elements and the source network. The solution depends on the source network architecture. Let us consider three types of source network configurations:

- Generalized source network.
- Individually matched sources.

- Individual sources with the same source impedance value.

The three source networks are illustrated in Fig. 5.1. We will analyze each source type in detail.

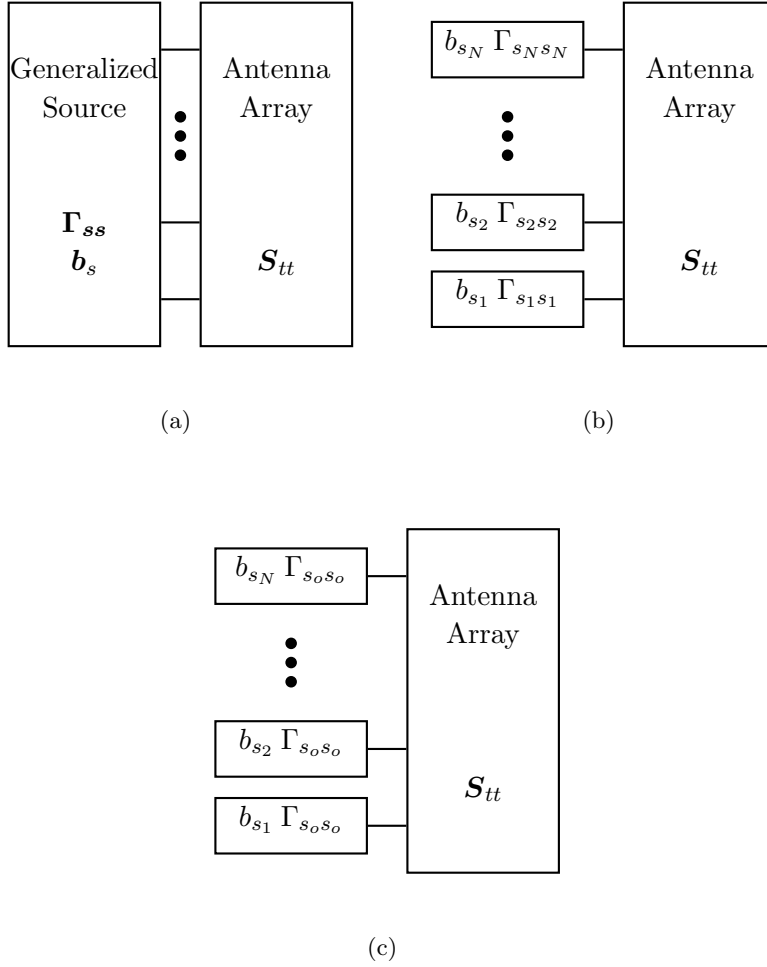


**Figure 5.1** Three types of source network configurations: (a) Generalized source with coupled transmitters,  $\Gamma_{ss}$  is a full S-matrix. (b) Individual sources. Each source circuit has an independent source impedance value. (c) Individual sources with the same source impedance.

### 5.1.1 Generalized Source Network

A generalized source network is a hypothetical circuit where the equivalent circuit consists of a set of  $N$  coupled transmitters. The coupled transmitters form a network which can be described by a scattering matrix,  $\mathbf{\Gamma}_{ss}$ , and an associated incident source wave vector,  $\mathbf{b}_s$  as shown in Fig. 5.1(a). Since  $N$  transmitters are coupled,  $\mathbf{\Gamma}_{ss}$  is a full  $N \times N$  matrix. The diagonal components of  $\mathbf{\Gamma}_{ss}$  represent the reflection coefficients of the transmitter circuits, while the off-diagonal components of  $\mathbf{\Gamma}_{ss}$  represent the coupling coefficients among the transmitters. Realizability of the network represented by  $\mathbf{\Gamma}_{ss}$  and  $\mathbf{b}_s$  using real electronic components is an important consideration. Though, the realizability falls outside the scope of this dissertation, we will show that  $\mathbf{\Gamma}_{ss}$  and  $\mathbf{b}_s$  represents an ideal solution that impedance matches the transmitter circuits to the array elements.

Many solutions for  $\mathbf{\Gamma}_{ss}$  exist that match the source impedances to the array element input impedances. When array elements are completely matched, the mismatch factor,  $q$ , becomes unity. In general, the solutions for  $\mathbf{\Gamma}_{ss}$  depend on the values of the source incident waves,  $\mathbf{b}_s$  because the active input impedances of the array elements depend on the array excitation. One of the solutions that provides complete impedance matching is given by

$$\mathbf{\Gamma}_{ss} = \mathbf{S}_{tt}^\dagger \quad (5.3)$$

where  $\mathbf{S}_{tt}$  is the scattering matrix of array elements and  $\dagger$  is Hermitian transpose operator. This solution is a multi-port network equivalence to the familiar conjugate matching of a source to a load [64]. When this condition is satisfied, the impedance mismatch factor becomes unity independent of the source excitations. This independence can be demonstrated by substituting (5.3) into (5.2), giving

$$q = \frac{\mathbf{b}_s^\dagger \left[ \mathbf{I} - \mathbf{S}_{tt}^\dagger \mathbf{S}_{tt} \right]^{-1} \left[ \mathbf{I} - \mathbf{S}_{tt}^\dagger \mathbf{S}_{tt} \right] \left[ \mathbf{I} - \mathbf{S}_{tt}^\dagger \mathbf{S}_{tt} \right]^{-1} \mathbf{b}_s}{\mathbf{b}_s^\dagger \left[ \mathbf{I} - \mathbf{S}_{tt}^\dagger \mathbf{S}_{tt} \right]^{-1} \mathbf{b}_s} = 1. \quad (5.4)$$

Of course, if such a source network with a scattering matrix  $\mathbf{S}_{tt}^\dagger$  can be synthesized, gain and realized gain patterns will be equal for any excitation coefficients.

We can utilize the Hermitian transpose impedance matching to determine the array gain without knowing the feed network specification. This is especially useful in array gain

measurements. In some cases, antenna engineers must design array antennas without a complete specification for the feed network. When the array element S-matrix,  $\mathbf{S}_{tt}$ , and the element pattern S-matrix,  $\mathbf{S}_{pt}(\theta, \phi)$ , are known, the gain of the antenna array can be determined for a given set of source excitation coefficients. This will be demonstrated in an example in Sec. 5.2.

### 5.1.2 Individually Matched Sources

The second type of source network consists of  $N$  individual transmitters that are each attached to the corresponding  $N$  elements in the array, as illustrated in Fig. 5.1(b). The impedance of the transmitters are adjusted individually for each array element to minimize the impedance mismatch. We assume that the transmitters are not coupled to each other and, thus, they are independent of each other. The source network scattering matrix,  $\mathbf{\Gamma}_{ss}$ , of independent transmitters is a diagonal matrix. The diagonal components in the matrix are determined by the reflection coefficients of the transmitters,

$$\Gamma_{s_n s_n} = \frac{Z_{s_n} - Z_o}{Z_{s_n} + Z_o^*} \quad (5.5)$$

where  $Z_{s_n}$  is the internal source impedance of transmitter  $n$  and  $Z_o$  is the reference impedance.

A solution for the source network that maximizes  $q$  is given by selecting the reflection coefficients of sources to be complex conjugates of the active-element reflection coefficients, giving

$$\Gamma_{s_n s_n} = S_{t_n}^* = \left( \frac{b_{t_n}}{a_{t_n}} \right)^* = \left( \frac{S_{t_n t_1} a_{t_1} + S_{t_n t_2} a_{t_2} + \cdots + S_{t_n t_N} a_{t_N}}{a_{t_n}} \right)^*. \quad (5.6)$$

Since each element in an array typically experiences a different amount of mutual coupling from other elements in the array, the active reflection coefficients will be different for each element. Thus, the required source impedance will be a different value for each element.

Since this solution is based on a conjugate matching of each element in the fully active array, the resulting array impedance mismatch factor is unity. Unlike the generalized source network, however, the required matching impedance values vary as the array excitation coefficients  $\{a_{t_n}\}$  are changed as seen in (5.6). If the source impedances are matched for a particular array excitation, the impedance mismatch will increase when the excitation is changed. For example, if the impedance matching is determined for a particular beam

direction, the mismatch will increase as the beam is scanned away from that direction.

### 5.1.3 Individual Sources with the Same Source Impedance

The third type of source network considered also assumes that the array is fed with individual transmitters similar to individually matched sources, but with the source impedances set to the same value,  $Z_{s_o}$ , for all array elements as illustrated in Fig. 5.1(c). The common impedance source model represents the most typical way phased array antennas are excited.

The source network for this case is also represented by a diagonal S-matrix. All of the diagonal elements in the matrix are set to an identical S-parameter, giving

$$\mathbf{\Gamma}_{ss} = \Gamma_{s_o s_o} \mathbf{I} \quad (5.7)$$

where  $\mathbf{I}$  is an identity matrix and  $\Gamma_{s_o s_o}$  is the reflection coefficient of a transmitter circuit. The source reflection coefficient is related to the source impedance,  $Z_{s_o}$ , by

$$\Gamma_{s_o s_o} = \frac{Z_{s_o} - Z_o}{Z_{s_o} + Z_o^*}. \quad (5.8)$$

There is no analytical solution for the impedance matching of sources to array elements using the common source impedance value method. In general, the impedance mismatch factor for this case is less than unity for arrays with finite mutual coupling. Thus, the realized gain of the array is less than the gain. An optimum value for the source impedance can be determined using a numerical technique. Maximizing the impedance mismatch factor,  $q$  by varying the source impedance,  $Z_{s_o}$  will result in the optimum solution for the maximum realized gain. In the numerical techniques, it is easier to implement a minimization process than a maximization process. Thus, we can minimize the inverse of the impedance mismatch factor,  $1/q$  by varying the source impedance  $Z_{s_o}$  to maximize the realized gain of the array pattern. Such minimization process is used in the example in the next section to determine the optimum source impedance value.

## 5.2 Example of Array Impedance Matching

In Section 5.1, we discussed three methods to implement the impedance matching of the source network to the array elements: generalized network of matched sources (Sec. 5.1.1), individually matched independent sources (Sec. 5.1.2), and independent sources with the same source impedance value (Sec. 5.1.3). As an example to illustrate these three array impedance matching types, we consider an array of three parallel strip dipoles printed on a dielectric substrate. The S-parameters and the active-element patterns of the array necessary for the network analysis derived in Chapter 4 is determined by numerical simulations using a commercial method of moments code IE3D by Zeland[69]. Then, various types of impedance matching derived in the previous section are applied. Array patterns under these matching conditions are computed using the network analysis, and the frequency bandwidth and the beam scan characteristics are determined.

### 5.2.1 Description of Three Element Strip Dipole Array

The geometry of the array used in the simulation is illustrated in Fig. 5.2. A three-element array is chosen because it is the smallest periodic array with different coupling conditions

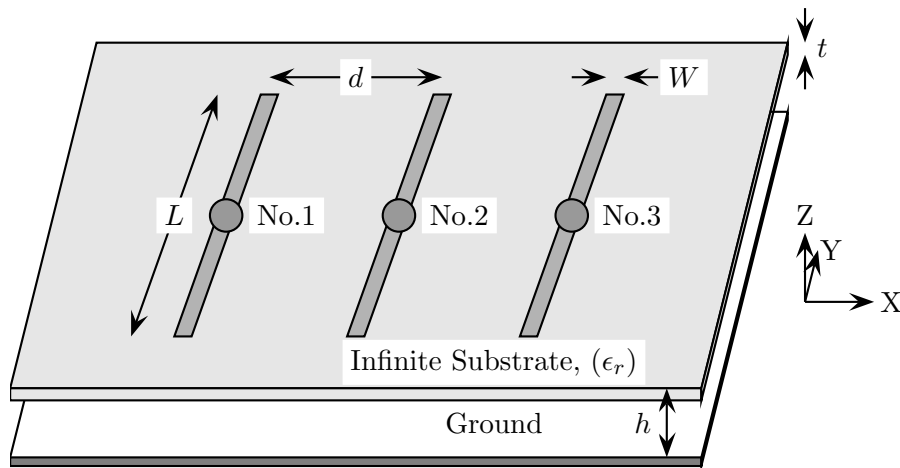


**Figure 5.2** Array of three-element parallel strip dipoles with the element length of  $L = 38$  mm and strip width of  $W = 2$  mm. The elements are printed on an infinite dielectric substrate with a finite thickness of  $t = 1$  mm and dielectric constant of  $\epsilon_r = 2.33$ . The substrate is suspended over an infinite ground plane at height of  $h = 20$  mm.

among the array elements. The center element of the array experiences a different mutual coupling environment than that for the outer two elements. The strip dipoles have length of  $L = 38$  mm, width of  $W = 2$  mm and inter-element spacing of  $d = 25$  mm. The elements are printed on an infinite dielectric substrate with a finite thickness of  $t = 1$  mm and relative permittivity of  $\epsilon_r = 2.33$ . The dielectric substrate is suspended over an infinite ground such that the top surface of the substrate is  $h = 20$  mm above the ground plane. The design frequency is 3 GHz where the element spacing is  $d = \lambda/4$  and the element length is  $L = 0.38\lambda$  where  $\lambda$  is free-space wavelength. A small inter-element spacing ( $1/4 \lambda$  at 3 GHz) is chosen to increase the mutual coupling for easy observation of the effects. The element length is chosen such that a single strip dipole printed on the same substrate as the array is resonant at 3 GHz. The design and the analysis of the single strip dipole is discussed in the following section.

### 5.2.2 Single Element Characteristics

Radiation patterns of an ideal array without mutual coupling effects are determined from an array element pattern and array factor using pattern multiplication as discussed in Sec. 2.1.2. When mutual coupling effects are small, array antenna radiation pattern can be estimated well using pattern multiplication. However, the three-element strip dipole array considered in this example has large mutual coupling among elements. We will demonstrate that the individual element analysis is not adequate to predict the performance of the antenna array with high mutual coupling.

The geometry of a single strip dipole element printed on an infinite substrate is shown in Fig. 5.3. The strip dipole has length of  $L = 38$  mm and width of  $W = 2$  mm. The infinite substrate for the single strip dipole is the same as the three element array with thickness of  $t = 1$  mm and dielectric constant of  $\epsilon_r = 2.33$ . The substrate is suspended over an infinite ground plane at height of  $h = 20$  mm. We will designate the radiation pattern and the input impedance of the single strip dipole printed on this substrate as the isolated element pattern and the isolated element impedance. It is noted that the term *isolated* does not represent the strip dipole in free space. In an isolated element analysis, only the unexcited array elements are removed from the simulation. The dielectric substrate and the ground

plane are included in the analysis.

A single strip dipole element printed on a substrate was simulated using IE3D from Zeland [69] to determine the S-parameter and the radiation pattern. The simulated dipole S-parameter as a function of frequency is shown in Fig. 5.4. All of the scattering parameters

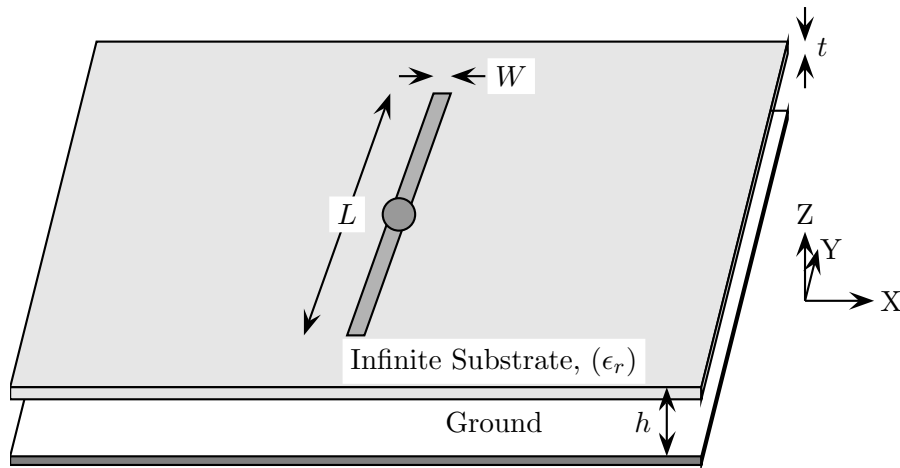


**Figure 5.3** A single strip dipole with the element length of  $L = 38$  mm and strip width of  $W = 2$  mm. The element is printed on a infinite dielectric substrate with a finite thickness of  $t = 1$  mm and dielectric constant of  $\epsilon_r = 2.33$ . The substrate is suspended over an infinite ground plane at height of  $h = 20$  mm.

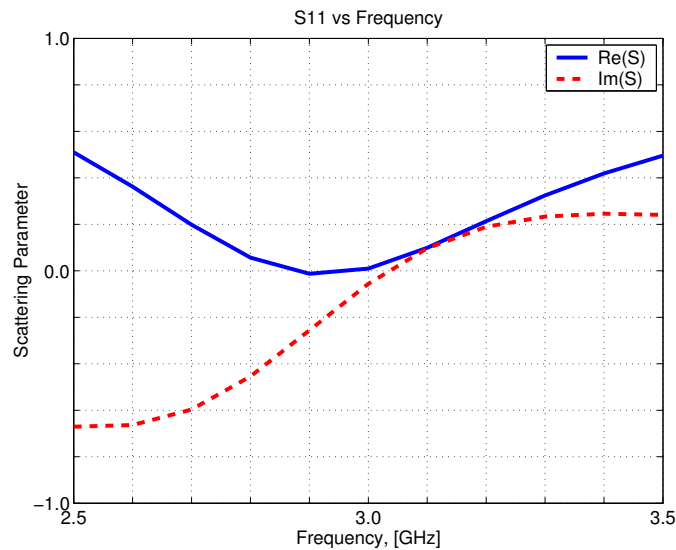


**Figure 5.4** Scattering parameter as a function of frequency for a single strip dipole with dimensions in Fig. 5.3 simulated by IE3D [69].

presented in this example are referenced to  $Z_o = 50 \Omega$ . The zero crossing of the imaginary part of the S-parameter near 3 GHz, and nearly zero value for the real part of the S-parameter at the same frequency indicates that the antenna is resonant near 3 GHz, with the input impedance of approximately  $50 \Omega$ .

From the simulated S-parameter of the dipole, we can compute the input impedance and the impedance bandwidth. The input impedance of an antenna element is determined from its S-parameter using [63]

$$Z_t = \frac{Z_o^* + Z_o S}{1 - S} \quad (5.9)$$

where  $Z_o$  is a complex valued reference impedance for the S-parameter. When the reference impedance is real valued, (5.9) simplifies to more familiar form,

$$Z_t = Z_o \frac{1 + S}{1 - S}. \quad (5.10)$$

The S-parameter value computed using IE3D (See Fig. 5.4 at 3 GHz) is

$$S = 0.0097 - j0.0559. \quad (5.11)$$

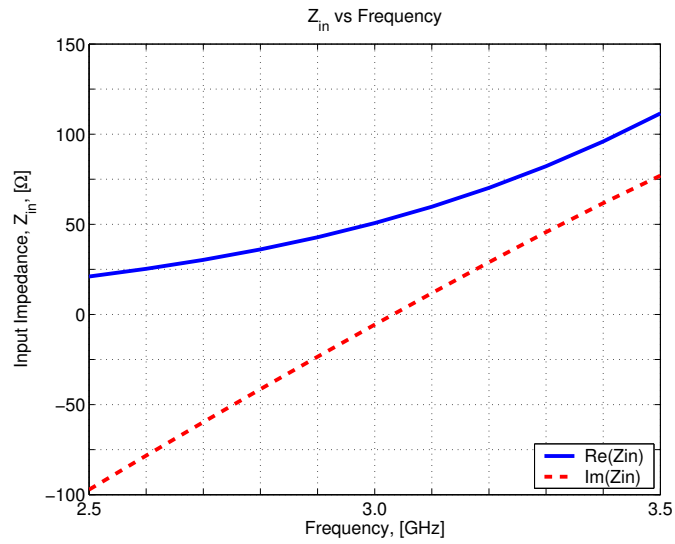
Substituting (5.11) into (5.10) yields the input impedance of the single element,

$$Z_t = 50 \frac{1 + S}{1 - S} = 50.7 - 5.67 \Omega. \quad (5.12)$$

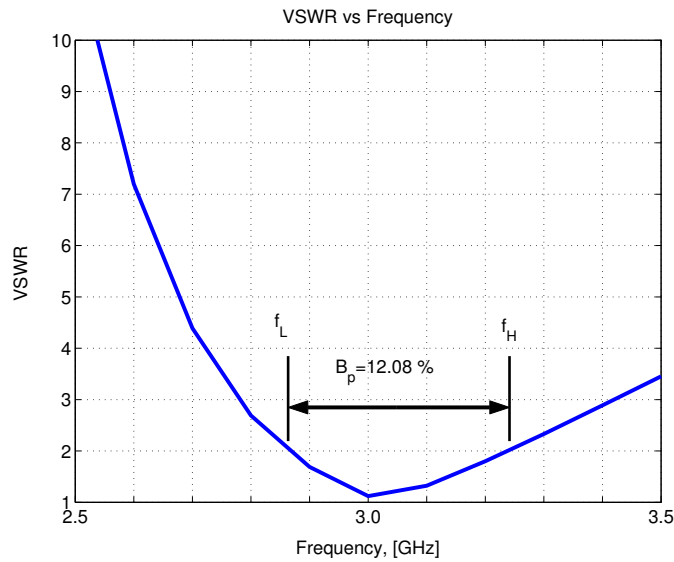
The isolated element input impedance as a function of frequency computed using (5.10) is shown in Fig. 5.5(a). As expected, the computed input impedance curve indicates that the isolated strip dipole is resonant near 3 GHz where the reactive component of the input impedance is zero.

The frequency bandwidth of an antenna element can be defined in many ways. One of the popular definitions of the bandwidth is based on the input impedance of the antenna element. We define the bandwidth to be the continuous band of frequencies where the voltage standing wave ratio (VSWR) of the antenna element is less than or equal to 2. The VSWR is defined in terms of a reference impedance value. If we assume that this referencing impedance for the VSWR is equal to the reference impedance,  $Z_o$ , used in the definition of S-parameters, then VSWR of an antenna element can be determined from its S-parameter using

$$\text{VSWR} = \frac{1 + |S|}{1 - |S|} \quad (5.13)$$



(a)



(b)

**Figure 5.5** Input impedance and VSWR computed using IE3D [69] of a single isolated strip dipole with the dimensions in Fig. 5.2. (a) Input impedance of the strip dipole as a function of frequency computed from S-parameter using (5.10), (b) VSWR as a function of frequency computed from S-parameter using (5.13).

The bandwidth as a percent of the center frequency,  $B_p$  is

$$B_p = \frac{f_U - f_L}{f_C} \times 100\%. \quad (5.14)$$

where the center frequency is given by

$$f_C = \frac{f_L + f_U}{2} \quad (5.15)$$

and  $f_U$  and  $f_L$  are the upper and the lower frequencies of operation for which  $\text{VSWR} \leq 2$ . Figure 5.5(b) shows the VSWR curve of the isolated strip dipole element as a function of frequency computed using (5.13). From the VSWR curve, we determine the lower and the upper cutoff frequencies are  $f_L = 2.87$  GHz and  $f_U = 3.24$  GHz, respectively. Then, using (5.14) and (5.15) the percent bandwidth of the isolated dipole is computed as 12.1%.

The directivity, the gain, and the realized gain patterns of the isolated strip dipole were also computed using IE3D simulations. The gain pattern of the isolated strip dipole element at 3 GHz for  $E_\theta$  polarization in  $\phi = 0^\circ$  plane is shown in Fig. 5.6. The comparison of the directivity, the gain and the realized gain patterns show that they are very close to each other, indicating nearly 100% radiation efficiency and nearly unity mismatch factor

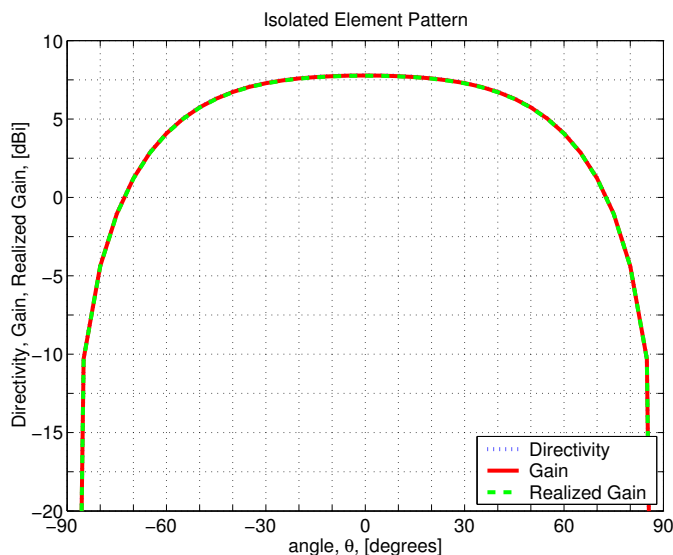


**Figure 5.6** Directivity, gain, and realized gain patterns of the isolated strip dipole depicted in Fig. 5.2 at 3 GHz for  $E_\theta$  polarization in  $\phi = 0^\circ$  plane simulated using IE3D [69].

( $q \approx 1$ ). The antenna performance parameters for the isolated strip dipole element from the simulated results are summarized in Table 5.1.

**Table 5.1** A summary of electrical performance of the isolated strip dipole of the same dimension as one element in Fig. 5.2 printed on an infinite dielectric substrate over an infinite ground plane simulated using IE3D.

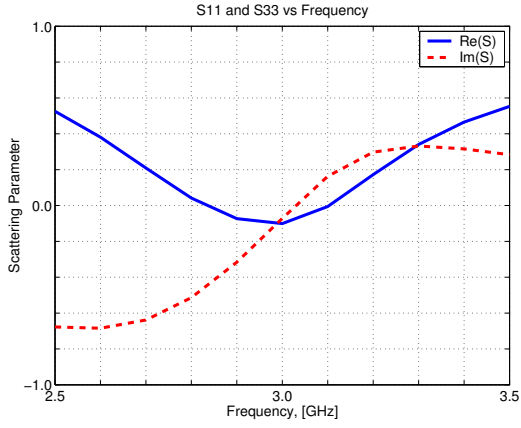
Description	Symbol	Performance
Broadside directivity	$D(0,0)$	7.80 dB
Broadside gain	$G(0,0)$	7.78 dB
Broadside realized Gain	$G_R(0,0)$	7.76 dB
Radiation efficiency	$e_r$	99.4%
Impedance mismatch factor	$q$	99.7%
S-parameter at 3 GHz	$S$	$0.0097 - j0.0559$
Input impedance at 3 GHz	$Z_t$	$50.7 - j5.67 \Omega$
Lower cutoff frequency at VSWR=2	$f_L$	2.87 GHz
Upper cutoff frequency at VSWR=2	$f_U$	3.24 GHz
Center frequency	$f_C$	3.05 GHz
Bandwidth	$B_p$	12.1%

### 5.2.3 Array Scattering Parameters and Active-Element Patterns

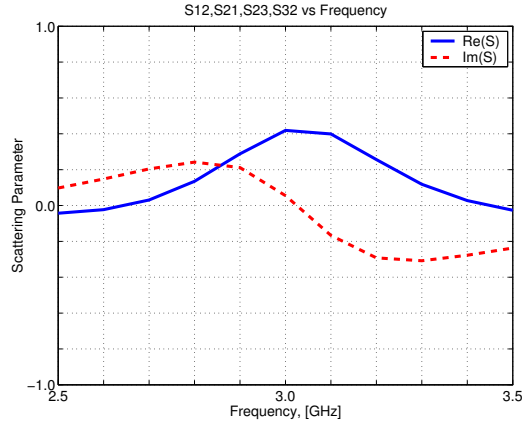
The scattering parameters and active-element patterns were also determined for the array of Fig. 5.2 using IE3D [69] simulations. The simulated scattering parameters of the array,  $S_{tt}$ , are shown in Fig. 5.7 as a function of frequency. The values of the S-parameters of the array at 3 GHz are

$$S_{tt} = \begin{bmatrix} -0.101 - j0.072 & 0.419 + j0.055 & -0.067 - j0.210 \\ 0.419 + j0.055 & -0.292 - j0.108 & 0.419 + j0.055 \\ -0.067 - j0.210 & 0.419 + j0.055 & -0.101 - j0.071 \end{bmatrix}. \quad (5.16)$$

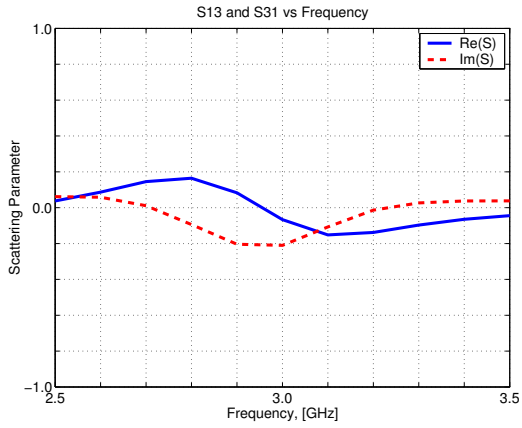
These S-parameter values correspond to  $20 \log_{10}(|0.419 + j0.055|) = -7.5$  dB of coupling between the center element to the outer two elements ( $S_{t_1 t_2}$ ,  $S_{t_3 t_2}$ ) and  $20 \log_{10}(|-0.067 -$



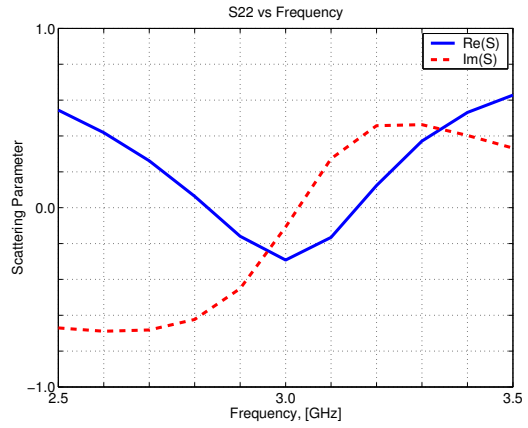
(a)



(b)



(c)



(d)

**Figure 5.7** Scattering parameters computed with IE3D [69] as a function of frequency of three-element parallel strip dipole array of Fig. 5.2 printed on a suspended infinite substrate. (a)  $S_{t_1 t_1}$  and  $S_{t_3 t_3}$  (b)  $S_{t_1 t_2}$ ,  $S_{t_2 t_1}$ ,  $S_{t_2 t_3}$  and  $S_{t_3 t_2}$ , (c)  $S_{t_1 t_3}$  and  $S_{t_3 t_1}$ , (d)  $S_{t_2 t_2}$

$j0.210|) = -13.1$  dB of coupling between two outer elements ( $S_{t_1t_3}$ ). Also, it is apparent in the S-parameter plots that the self terms of the S-parameters of the outer elements,  $S_{t_1t_1}$  and  $S_{t_3t_3}$ , in Fig. 5.7(a) and of the center element,  $S_{t_2t_2}$ , in Fig. 5.7(d) are quite different from the single isolated strip dipole S-parameter in Fig. 5.4(a) due to mutual coupling.

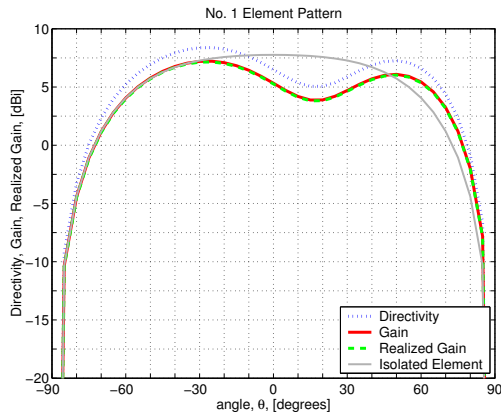
The directivity, the gain, and the realized gain of the active-element patterns from the simulated results for all elements are shown in Fig. 5.8. These element patterns are determined when one element is excited and all other elements are terminated with the reference impedance of  $50\ \Omega$  using IE3D [69]. The radiation patterns are computed at 3 GHz for  $E_\theta$  polarization in  $\phi = 0^\circ$  plane. As expected, the active-element patterns differ from each other due mutual coupling. Also, note that the patterns for elements 1 and 3 are mirror images of each other because of the symmetry in the array geometry.

The gain pattern of a single isolated element printed on the substrate is also overlaid in the plots for comparison. The active-element pattern shapes in Fig. 5.8 differ significantly from that of the single strip dipole pattern. These differences in the active-element patterns are primarily caused by the radiation from the currents on the unexcited elements induced by the mutual coupling.

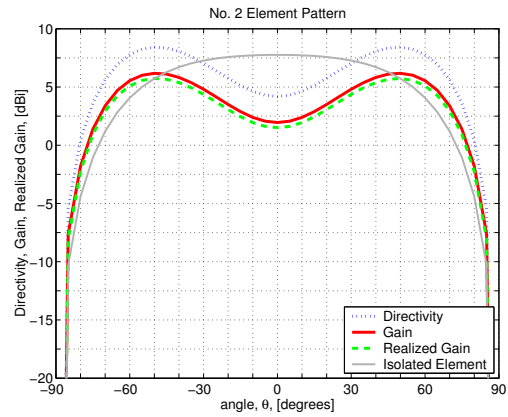
Unlike the isolated element pattern which exhibit low losses in the radiation efficiency and the impedance mismatch factor (see Table 5.1), the active-element patterns have significant losses in these efficiencies, causing the directivity, the gain and the realized gain values to be different from each other as evident in Fig. 5.8 (also see Table 5.2). The losses in the efficiencies are the most severe for the center element (element No. 2).

A comparison of the directivity and the gain of the active-element pattern for element 2 in Fig. 5.8(b) shows more than 2 dB difference caused by a moderately low radiation efficiency of 59.7% as indicated in Table 5.2. The active-element patterns for the elements 1 and 3 also show similar losses in the radiation efficiencies ( $e_r = 76.6\%$ ). Low radiation efficiencies for the active-element patterns are caused by the coupled energies that are dissipated in the terminations on the unexcited elements when active-element patterns are determined. This loss mechanism can also be quantified using the scattering parameter model of the array.

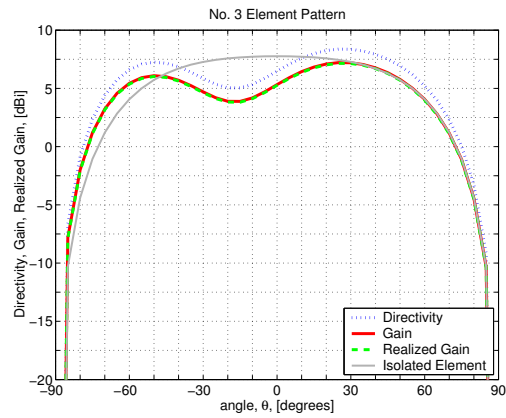
The active-element patterns in Fig. 5.8 are evaluated by exciting one element in the



(a)



(b)



(c)

**Figure 5.8** Directivity, gain and realized gain active-element patterns of the three element parallel strip dipoles of Fig. 5.2 printed on an infinite substrate computed by IE3D [69] simulations. The patterns are computed at 3 GHz when one element is excited and other two elements are terminated with  $50\ \Omega$  loads.

**Table 5.2** A summary of electrical performance of the strip dipole array of Fig. 5.2 at 3 GHz computed using IE3D [69] for the active-element pattern condition where one element is excited and all other elements in the array are terminated with reference impedance,  $Z_o$ .

Description	Symbol	Element Number		
		No. 1	No. 2	No. 3
Broadside directivity	$D(0,0)$	6.50 dB	4.19 dB	6.50 dB
Broadside gain	$G(0,0)$	5.33 dB	1.95 dB	5.33 dB
Broadside realized gain	$G_R(0,0)$	5.26 dB	1.50 dB	5.26 dB
Radiation efficiency	$e_r$	76.6%	59.7%	76.6%
Impedance mismatch factor	$q$	98.5%	90.3%	98.5%
active-element S-parameter	$S$	$-0.101 - j0.072$	$-0.292 - j0.108$	$-0.101 - j0.072$
active-element input impedance	$Z_t$	$40.5 - j5.91 \Omega$	$26.9 - j6.39 \Omega$	$40.5 - j5.91 \Omega$
Lower cutoff frequency at VSWR=2	$f_L$	2.90 GHz	2.99 GHz	2.90 GHz
Upper cutoff frequency at VSWR=2	$f_U$	3.19 GHz	3.11 GHz	3.19 GHz
Center frequency	$f_C$	3.04 GHz	3.05 GHz	3.04 GHz
Bandwidth	$B_p$	9.72%	3.85%	9.72%

array while terminating all other elements with the reference impedance,  $Z_o$ . In terms of S-parameter formulation, the active-element pattern of the center element is evaluated by exciting the array with the incident waves

$$\mathbf{a}_t = \begin{bmatrix} 0 \\ 1 \\ 0 \end{bmatrix}. \quad (5.17)$$

Using this excitation with (5.16) gives the reflected wave scattering parameter values from the array as

$$\mathbf{b}_t = \mathbf{S}_{tt} \mathbf{a}_t = \begin{bmatrix} 0.419 + j0.055 \\ -0.292 - j0.108 \\ 0.419 + j0.055 \end{bmatrix}. \quad (5.18)$$

From the incident waves (5.17) and the reflected waves (5.18) the power input to the array at the element 2 port is given by

$$P_{in_2} = a_{t_2}^* a_{t_2} - b_{t_2}^* b_{t_2} = 0.903 \quad (5.19)$$

while the powers at ports 1 and 3 are given by

$$P_{in_1} = a_{t_1}^* a_{t_1} - b_{t_1}^* b_{t_1} = -0.179 \quad (5.20a)$$

$$P_{in_3} = a_{t_3}^* a_{t_3} - b_{t_3}^* b_{t_3} = -0.179. \quad (5.20b)$$

The negative powers in (5.20) indicate that power flows out of the array network through ports 1 and 3 into the loads on these elements. The ratio of total power dissipated by elements 1 and 3 to the power input to element 2 is computed as

$$\frac{|P_{in_1} + P_{in_3}|}{P_{in_2}} \times 100\% = \frac{0.179 + 0.179}{0.903} \times 100\% = 39.5\%. \quad (5.21)$$

Thus, 39.5% of input power is dissipated in the terminations in the , or  $100\% - 39.5\% = 60.5\%$  of input power,  $P_{in_2}$ , is radiated or lost in the array elements as ohmic loss. We also note that the radiation efficiency for element 2 in active-element condition, from Table 5.2, is  $e_r = 59.7\%$ , indicating that 59.7% of the input power,  $P_{in_2}$ , is radiated. Comparing the power lost in the network with the radiation efficiency of the active-element pattern for the element 2, we conclude that  $60.5\% - 59.7\% = 0.8\%$  of the input power is dissipated in the array elements as ohmic loss due to finite conductivity of strip dipoles.

It is very important to note that the low radiation efficiencies in the active-element patterns of the array should not be used to infer the behavior of a fully excited array. When the array is fully excited with the sources with matched source impedances, all of the power flows into the array, rather than being dissipated in unexcited elements. This has been a source of confusion in some array evaluations.

A comparison of the gain and the realized gain of active-element patterns for the array show approximately 0.5 dB difference in their values, indicating some loss due to impedance mismatch. To investigate the impedance mismatch in the active-element excitation conditions, the active-element input impedance of the array is determined from the active-element S-parameter when one element in the array is excited and all other elements are terminated with the reference impedance. The active-element S-parameter for the element 2 is determined from the ratio of the incident and the reflect waves at port 2, giving

$$S_{t_2} = \frac{b_{t_2}}{a_{t_2}} = -0.292 - j0.108. \quad (5.22)$$

The active-element input impedance of element 2 is determined using (5.10) which yields

$$Z_{in_2} = 50 \frac{1 - S_{t_2}}{1 + S_{t_2}} = 26.9 - j6.39. \quad (5.23)$$

Thus, under the active-element pattern excitation conditions where one element is excited and all other elements are terminated with the reference impedance, the active-element input impedance deviates significantly from the reference impedance of  $50 \Omega$ , causing the impedance mismatch factor to decrease. The active-element input impedances for the other elements are summarized in Table 5.2.

The VSWR of the active-element input impedance is determined using a relation similar to (5.13) with the active-element S-parameter in (5.22) in place of isolated element S-parameter:

$$\text{VSWR}_{ae_n} = \frac{1 + |S_{t_n}|}{1 - |S_{t_n}|} \quad (5.24)$$

for element  $n$ . We denote this voltage standing wave ratio based on the active-element S-parameter as the *active-element VSWR*. Figure 5.10 shows the computed active-element VSWR curves as a function of frequency. Using these curves, the percent bandwidths of the active-element VSWR are determined using the procedure described in Sec. 5.2.2. The

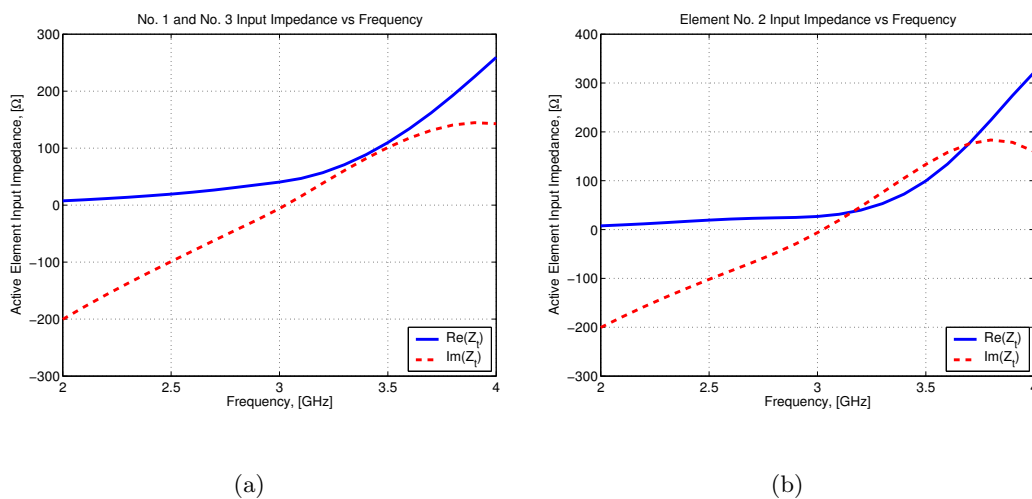


**Figure 5.9** Active-element input impedance as a function of frequency computed using IE3D for the three element array of Fig. 5.2 when one element in the array is excited and all other elements are terminated with reference impedance,  $Z_0$ . (a) Element No. 1 or No. 3 active, (b) Element No. 2 active.

center frequency of the operational bands,  $f_C$  for the active-element VSWR and the isolated element VSWR (see Tables 5.1 and 5.2) are essentially the same. The resulting percent bandwidths are quite different. The bandwidths of the active-element patterns are 9.72% for the element 1 and 3, and 3.85% for the element 2. These bandwidths are considerably lower than the bandwidth of the isolated strip dipole (12.1%). The reductions in the bandwidths of the active-element VSWRs are caused by the decrease in the impedance mismatch factor.

Similar to the reduction of the radiation efficiencies of the active-element patterns, the reduction in the impedance mismatch factors and reduction in the impedance bandwidths of the active-element patterns are not of immediate concern. This is because arrays are operated with all elements excited simultaneously. Array performances depend on the excitation of the array as well as the geometry and the configuration of the array as discussed in Chapter 4 and in Sec. 5.1. Unless the array application requires the operation similar to the active-element condition (a highly unusual situation), the low radiation efficiencies, low impedance mismatch factors, and low bandwidth associated with the active-element patterns can be ignored.

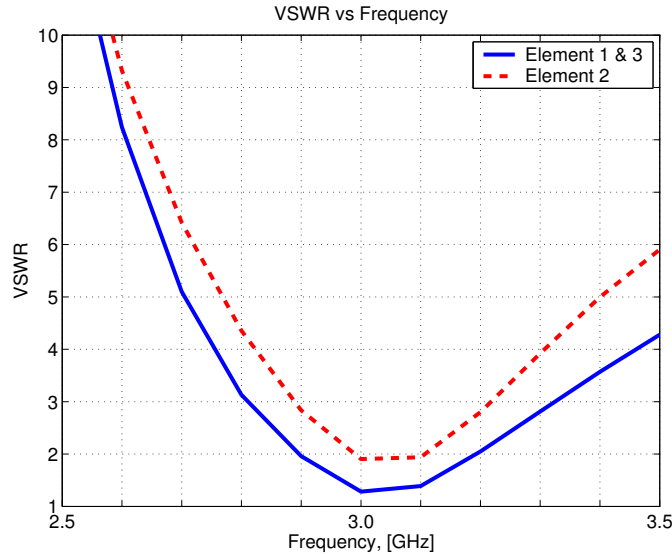


**Figure 5.10** Active-element VSWR for  $50\ \Omega$  impedance of the three element strip dipole array of Fig. 5.2 computed using IE3D. The VSWR was determined from the active-element S-parameter,  $S_{t_n}$ , when element  $n$  is excited and all other elements are terminated with reference impedance,  $Z_o$ .

## 5.2.4 Source Impedance Matching

In this section, we determine the source impedances that match the dipole array input impedances when the array is fully active. Six impedance matching cases are investigated for this example. The first case uses the generalized source matching discussed in Sec. 5.1.1. The second and the third cases use individually matched sources which was discussed in Sec. 5.1.2. Complex-valued source impedances are used in Case 2, and real valued source impedances are used in Case 3. The last three cases investigate the individually fed array with the same source impedance as discussed in Sec. 5.1.3. In Case 4, complex-valued source impedances are used while in Cases 5 real-valued source impedances are used. In Case 6,  $50\ \Omega$  source impedances are used as a reference.

**Table 5.3** Summary of impedance matching cases investigated for the three-element strip dipole array with the dimensions in Fig. 5.2 simulated by IE3D.

Case No.	Impedance Matching Method	Source Impedances	Figure	Section
1	Generalized Source Network	Complex-Valued	Fig. 5.1(a)	Sec. 5.2.4.1
2	Individually Matched Sources	Complex-Valued	Fig. 5.1(b)	Sec. 5.2.4.2
3	Individually Matched Sources	Real-Valued	Fig. 5.1(b)	Sec. 5.2.4.3
4	Sources with the Same Source Impedance	Complex-Valued	Fig. 5.1(c)	Sec. 5.2.4.4
5	Sources with the Same Source Impedance	Real-Valued	Fig. 5.1(c)	Sec. 5.2.4.5
6	Sources with $50\ \Omega$ Source Impedance	$50\ \Omega$	Fig. 5.1(c)	Sec. 5.2.4.6

For all six cases, the strip dipole array is fully excited with uniform incident waves,

$$\mathbf{a}_t = \begin{bmatrix} 1 \\ 1 \\ 1 \end{bmatrix} \quad (5.25)$$

as the desired element excitation coefficients at 3 GHz. Since the array incident waves are fixed, the directivity, the gain, and the radiation efficiency of the array are the same at the broadside for all six cases at this frequency because these values are independent of the source network S-matrix,  $\mathbf{\Gamma}_{ss}$  as shown in (4.27), (4.39) and (4.43).

**Table 5.4** A summary of broadside directivity, gain and radiation efficiency at 3 GHz for the fully active three element strip dipole array of Fig. 5.2 for the uniform incident waves.

Description	Variable	Performance
Directivity using (4.27)	$D(0, 0)$	9.63 dB
Gain using (4.39)	$G(0, 0)$	9.62 dB
Radiation Efficiency using (4.43)	$e_r$	99.9%

The input impedances of the fully active array, or *active input impedances*, depend on the array element S-parameters,  $\mathbf{S}_{tt}$  and array incident waves,  $\mathbf{a}_t$ . The waves reflected from the array elements are found using (5.16) with (5.25) to give

$$\mathbf{b}_t = \mathbf{S}_{tt}\mathbf{a}_t = \begin{bmatrix} 0.252 - j0.227 \\ 0.546 + j0.002 \\ 0.252 - j0.227 \end{bmatrix}. \quad (5.26)$$

The active S-parameter looking into an array element when the array is fully excited is given by

$$S_{t_n} = \frac{b_{t_n}}{a_{t_n}} \quad (5.27)$$

for the element  $n$ . Using (5.27) with (5.25), the active S-parameters for the array are

$$\mathbf{S}_t = \begin{bmatrix} 0.252 - j0.227 \\ 0.546 + j0.002 \\ 0.252 - j0.227 \end{bmatrix}. \quad (5.28)$$

The corresponding active input impedances of the uniformly excited array for a real-valued reference impedance  $Z_o$  is determined by

$$Z_{in_n} = Z_o \frac{1 + S_{t_n}}{1 - S_{t_n}}. \quad (5.29)$$

Substituting (5.28) into (5.29) yields

$$\mathbf{Z}_{in} = \begin{bmatrix} 72.4 - j37.2 \Omega \\ 170.4 - j1.02 \Omega \\ 72.4 + j37.2 \Omega \end{bmatrix} \quad (5.30)$$

for  $Z_o = 50 \Omega$ . The active input impedances of the uniformly excited array as a function of frequency computed using (5.29) are shown in Fig. 5.11. The active input impedances of the array in Fig. 5.11 are different from the input impedance of the isolated dipole in Fig. 5.5(a) due to mutual coupling effect.

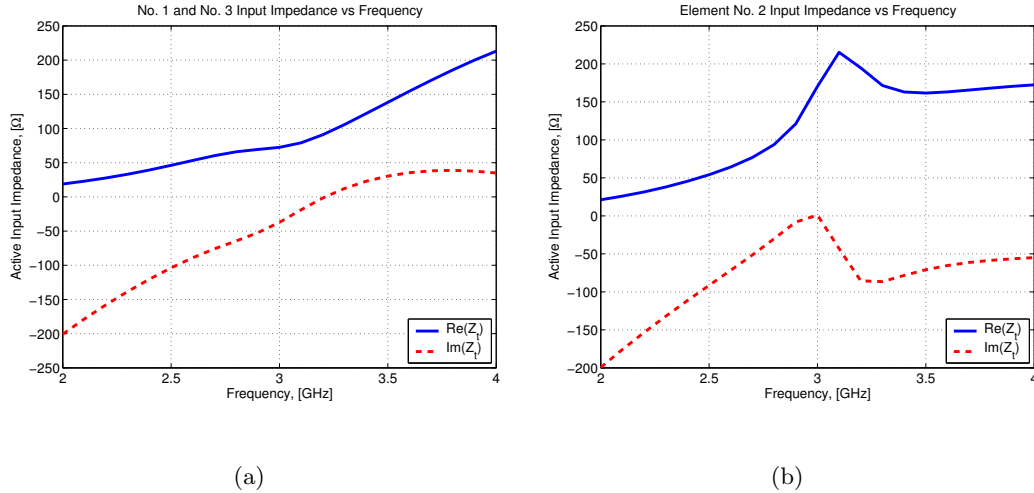


**Figure 5.11** Active input impedance as a function of frequency calculated using IE3D for the three element array of Fig. 5.2 when fully excited with identical excitations. (a) Element No. 1 and No. 3, (b) Element No. 2.

We now determine the source impedances to maximize the impedance mismatch factor. In all cases, the required source impedances, or source S-parameters are determined for given incident waves for the array at 3 GHz using one of the three source structures discussed in Sec. 5.1. The source incident waves,  $\mathbf{b}_s$ , are determined from the array incident waves,  $\mathbf{a}_t$

and the source S-parameters,  $\mathbf{\Gamma}_{ss}$  using (4.53). Then, the impedance mismatch factor,  $q$  is computed from the source S-parameter and the source incident waves using (4.57). The results for the six matching cases at 3 GHz are tabulated in Table 5.5 in Sec. 5.2.4.7.

#### 5.2.4.1 Case 1: Generalized Source Network

The impedance matching in Case 1 in Table 5.3 uses generalized source network discussed in Sec. 5.1.1. A generalized source network is a hypothetical circuit where the equivalent circuit consists of a set of  $N$  coupled transmitters. The coupled transmitters form a network which can be described by a full scattering matrix,  $\mathbf{\Gamma}_{ss}$ , and an associated incident source wave vector,  $\mathbf{b}_s$  as shown in Fig. 5.1(a). The required source network S-matrix for Case 1 is determined from the array element S-matrix by substituting (5.16) into (5.3) which gives

$$\mathbf{\Gamma}_{ss} = \mathbf{S}_{tt}^\dagger = \begin{bmatrix} -0.101 + j0.072 & 0.419 - j0.055 & -0.067 + j0.210 \\ 0.419 - j0.055 & -0.292 + j0.108 & 0.419 - j0.055 \\ -0.067 + j0.210 & 0.419 - j0.055 & -0.101 + j0.071 \end{bmatrix}. \quad (5.31)$$

The generalized source network is used as a reference for an exact impedance matching of the sources to the array elements. This source network S-matrix results in a 100% impedance mismatch factor ( $q = 1$ ) for the array for any source incident waves at 3 GHz as discussed Sec. 5.1.1 and shown in Table 5.5. The realized gain which relates to the gain of the array by (5.1) becomes identical to the gain of the array, resulting  $G_R = 9.62$  dB for the uniform incident waves excitation. (See Table 5.5).

#### 5.2.4.2 Case 2: Complex-Valued Individually Matched Sources

The impedance matching in Case 2 in Table 5.3 uses the individually matched sources discussed in Sec. 5.1.2. In this case,  $N$  individual uncoupled transmitters are attached to corresponding  $N$  elements in the array, as shown in Fig. 5.1(b). The internal source impedances of these transmitters are complex-valued and different from each other. These uncoupled and independent sources are represented by a diagonal S-matrix of the form

$$\mathbf{\Gamma}_{ss} = \begin{bmatrix} \Gamma_{s_1s_1} & 0 & 0 \\ 0 & \Gamma_{s_2s_2} & 0 \\ 0 & 0 & \Gamma_{s_3s_3} \end{bmatrix}. \quad (5.32)$$

The S-matrix of the required source network for Case 2 is determined from the complex conjugate of the active S-parameters for the array,  $\mathbf{S}_t$ , given in (5.28). Thus, substituting (5.28) into (5.6) and (5.32) gives required S-matrix for the matched sources as

$$\mathbf{\Gamma}_{ss} = \begin{bmatrix} S_{t_1}^* & 0 & 0 \\ 0 & S_{t_2}^* & 0 \\ 0 & 0 & S_{t_3}^* \end{bmatrix} = \begin{bmatrix} 0.252 + j0.227 & 0 & 0 \\ 0 & 0.546 - j0.002 & 0 \\ 0 & 0 & 0.252 + j0.227 \end{bmatrix}. \quad (5.33)$$

The required source impedance values for the impedance matching are determined from the source S-matrix using

$$Z_{s_n} = 50 \frac{1 + \Gamma_{s_n s_n}}{1 - \Gamma_{s_n s_n}} \quad (5.34)$$

for the source  $n$  which gives

$$\mathbf{Z}_s = \begin{bmatrix} 72.4 + j37.2 \Omega \\ 170.4 + j1.02 \Omega \\ 72.4 + j37.2 \Omega \end{bmatrix}. \quad (5.35)$$

As expected, the required source impedance values in (5.35) are complex conjugates of the input impedances of the fully excited array in (5.30). The source impedances for elements 1 and 3 are identical because of the symmetry in the array geometry and the uniform excitation requirement in (5.25).

The impedance mismatch factor  $q$  for this source network is also 100% as discussed in Sec. 5.1.2. This can be shown by substituting (5.33), (5.25) and (5.16) into (4.57). Similar to Case 1, the realized gain is identical to the gain of the array, giving 9.62 dB for the broadside direction for the uniform excitation as shown in Table 5.5.

#### 5.2.4.3 Case 3: Real-Valued Individually Matched Sources

The impedance matching in Case 3 in Table 5.3 uses the individually matched sources similar to Case 2. The source network is implemented with  $N$  uncoupled and independent transmitters. Unlike Case 2, the source impedances of the transmitters are constrained to real positive values. The uncoupled and independent sources are represented by a diagonal

S-matrix

$$\mathbf{\Gamma}_{ss} = \begin{bmatrix} \Gamma_{s_1s_1} & 0 & 0 \\ 0 & \Gamma_{s_2s_2} & 0 \\ 0 & 0 & \Gamma_{s_3s_3} \end{bmatrix} \quad (5.36)$$

where  $\Gamma_{s_n s_n}$  are real and positive. The constraint in source impedance values is equivalent to the constraint on the source S-parameters to be real valued and in the range

$$-1 \leq \Gamma_{s_n s_n} \leq 1. \quad (5.37)$$

Thus, the transmitters in Case 3 have purely resistive source impedances.

Unlike Case 2, there is no analytical solution for Case 3 source network. The desired source impedances must be solved numerically by maximizing the impedance mismatch factor,  $q$ , by adjusting the source S-parameters,  $\{\Gamma_{s_n s_n}\}$ . Numerical routines are typically written for minimization of functional, rather than for maximization. Thus, the maximization of impedance mismatch factor is implemented numerically as a minimization of the inverse of  $q$ . A MATLAB code was written utilizing a MATLAB minimization library routine to find the minimum of  $q^{-1}$ . The resulting source S-matrix is

$$\mathbf{\Gamma}_{ss} = \begin{bmatrix} 0.238 & 0 & 0 \\ 0 & 0.546 & 0 \\ 0 & 0 & 0.238 \end{bmatrix} \quad (5.38)$$

and corresponding impedance mismatch factor is  $q = 95.7\%$ . The required source impedance values are determined from the source S-matrix by substituting (5.38) into (5.34) which gives

$$\mathbf{Z}_s = \begin{bmatrix} 81.4 \Omega \\ 170.4 \Omega \\ 81.4 \Omega \end{bmatrix}. \quad (5.39)$$

The broadside realized gain of the array pattern is determined from the gain of the array and the impedance mismatch factor,  $q$ , using (5.1) which results in  $G_R = 9.43$  dB as shown in Table 5.5.

#### 5.2.4.4 Case 4: Complex-Valued Sources with the Same Source Impedance

The impedance matching in Case 4 uses the individual uncoupled sources with the same source impedance value discussed in Sec. 5.1.3. The sources are represented by a diagonal

S-matrix with identical diagonal elements

$$\mathbf{\Gamma}_{ss} = \begin{bmatrix} \Gamma_{s_0s_0} & 0 & 0 \\ 0 & \Gamma_{s_0s_0} & 0 \\ 0 & 0 & \Gamma_{s_0s_0} \end{bmatrix} \quad (5.40)$$

where  $\Gamma_{s_0s_0}$  is a complex valued source reflection coefficient. Similar to Case 3, there is no analytical solution for Case 4 that matches the source network to the array. The source impedances must be determined numerically using the same procedure as in Case 3 by minimizing the inverse of the impedance mismatch factor, or  $q^{-1}$ . The resulting source S-matrix is

$$\mathbf{\Gamma}_{ss} = \begin{bmatrix} 0.338 + j0.146 & 0 & 0 \\ 0 & 0.338 + j0.146 & 0 \\ 0 & 0 & 0.338 + j0.146 \end{bmatrix}. \quad (5.41)$$

The corresponding impedance mismatch factor for Case 4 is  $q = 95.8\%$ . The required source impedance values are determined from the source S-matrix by substituting (5.41) into (5.34) which gives

$$\mathbf{Z}_s = \begin{bmatrix} 94.1 + j31.7\Omega \\ 94.1 + j31.7\Omega \\ 94.1 + j31.7\Omega \end{bmatrix}. \quad (5.42)$$

The broadside realized gain of the array pattern is determined from the gain of the array and the impedance mismatch factor,  $q$ , using (5.1) which results in  $G_R = 9.44$  dB as shown in Table 5.5.

#### 5.2.4.5 Case 5: Real-Valued Sources with the Same Source Impedance

The impedance matching in Case 5 which is similar to Case 4 uses the individually sources with the same source impedance value. Unlike Case 4, the source impedance is constrained to a real value similar to Case 3. The required source S-matrix is solved numerically using the procedure discussed in Sec. 5.2.4.3. The resulting source S-matrix is

$$\mathbf{\Gamma}_{ss} = \begin{bmatrix} 0.330 & 0 & 0 \\ 0 & 0.330 & 0 \\ 0 & 0 & 0.330 \end{bmatrix}. \quad (5.43)$$

The impedance mismatch factor for this case is  $q = 93.1\%$ . The required source impedance values are determined from the source S-matrix by substituting (5.43) into (5.34) which results in

$$\mathbf{Z}_s = \begin{bmatrix} 99.2 \Omega \\ 99.2 \Omega \\ 99.2 \Omega \end{bmatrix}. \quad (5.44)$$

The broadside realized gain of the array pattern is determined from the gain of the array and the impedance mismatch factor using (5.1) resulting in  $G_R = 9.31$  dB as indicated in Table 5.5.

#### 5.2.4.6 Case 6: 50 $\Omega$ Source Impedance

Case 6 is a specific condition of Case 5. Case 6 represents the array excitation with fixed 50  $\Omega$  sources. The source impedance of 50  $\Omega$  is chosen because the isolated element has approximately 50  $\Omega$  input resistance at resonance as discussed in Sec. 5.2.2. Often, this type of source network design that ignore the mutual coupling effect occur. Case 6 is used as a reference for a poor impedance matching condition.

The source S-matrix corresponding to 50  $\Omega$  source impedances is given by a zero matrix

$$\mathbf{\Gamma}_{ss} = \begin{bmatrix} 0 & 0 & 0 \\ 0 & 0 & 0 \\ 0 & 0 & 0 \end{bmatrix}. \quad (5.45)$$

The corresponding impedance mismatch factor which is computed by substituting (5.45), (5.25) and (5.16) into (5.2) results in  $q = 82.4\%$  and the realized gain of 8.78 dB as indicated in Table 5.5.

#### 5.2.4.7 Summary of Impedance Matching Results

Source impedances that are matched to the three element strip dipole array of Fig. 5.2 were determined using six different types of matching networks in Sections 5.2.4.1 to 5.2.4.6. The results are summarized in Table 5.5. The equations for the S-parameter matrices of the source networks are shown in the third column. The corresponding source impedances that can be computed from the source network S-matrices using (5.29) are listed in the

fourth column. The fifth column shows the source incident waves computed using (4.53). The last two columns show the impedance mismatch factor and the broadside realized gain computed at 3 GHz using (5.2) and (5.1).

The resulting impedance mismatch factors,  $q$ , vary between 100% for Cases 1 and 2, to 93.1% for Case 5, as shown in Table 5.5. The corresponding broadside realized gain for Case 5 is 9.31 dB. Approximately 0.3 dB of the incident power is reflected back to the sources. In comparison, the impedance mismatch factor for Case 6 is 82.4% and the realized gain is 8.78 dB. The results indicate that matching the array with real valued source impedances that have the same value for all elements (Case 5) is a reasonable compromise for the array efficiency and the simplicity of the implementation for this particular array structure.

**Table 5.5** Summary of impedance matching results for the uniform incident waves requirement,  $\mathbf{a}_t = [1 \ 1 \ 1]^T$  at 3 GHz for the three element strip dipole array depicted in Fig. 5.2.

Case No.	Impedance Matching	$\Gamma_{ss}$	$\mathbf{Z}_s$ from (5.29)	$\mathbf{b}_s$ from (4.53)	$q$ from (5.2)	$G_R(0,0)$ from (5.1)
1	Generalized Source Network, Sec. 5.2.4.1	(5.31)	N/A	$0.725 \angle -4.41^\circ$ $1.019 \angle 6.27^\circ$ $0.725 \angle -4.41^\circ$	100%	9.62 dB
2	Complex Valued Individually Matched Sources, Sec. 5.2.4.2	(5.33)	$72.4 + j37.2 \Omega$ $170.4 - j1.02 \Omega$ $72.4 + j37.2 \Omega$	$0.885 \angle 0.00^\circ$ $0.702 \angle 0.00^\circ$ $0.885 \angle 0.00^\circ$	100%	9.62 dB
3	Real Valued Individually Matched Sources, Sec. 5.2.4.3	(5.38)	$81.4 \Omega$ $170.4 \Omega$ $81.4 \Omega$	$0.941 \angle 3.30^\circ$ $0.702 \angle -0.09^\circ$ $0.941 \angle 3.30^\circ$	95.7%	9.43 dB
4	Complex Valued Sources with the Same Source Impedance, Sec. 5.2.4.4	(5.41)	$94.1 + j31.7 \Omega$ $94.1 + j31.7 \Omega$ $94.1 + j31.7 \Omega$	$0.883 \angle 2.60^\circ$ $0.820 \angle -5.61^\circ$ $0.883 \angle 2.60^\circ$	95.8%	9.44 dB
5	Real Valued Sources with the Same Source Impedance, Sec. 5.2.4.5	(5.43)	$99.2 \Omega$ $99.2 \Omega$ $99.2 \Omega$	$0.920 \angle 4.67^\circ$ $0.820 \angle -0.05^\circ$ $0.920 \angle 4.67^\circ$	93.1%	9.31 dB
6	$50 \Omega$ source impedance, Sec. 5.2.4.6	(5.45)	$50 \Omega$ $50 \Omega$ $50 \Omega$	$1.000 \angle 0.00^\circ$ $1.000 \angle 0.00^\circ$ $1.000 \angle 0.00^\circ$	82.4%	8.78 dB

## 5.2.5 Array Bandwidth for Broadside Beam

We investigated the bandwidths for each of the six impedance match cases of the previous section. The array impedance bandwidth was computed by keeping the required source impedances constant while varying frequency during computation with IE3D. The required source impedances are determined at 3 GHz using the procedures described in Sections 5.2.4.1 through 5.2.4.6. The resulting source impedances for six cases are listed in Table 5.5 in Sec. 5.2.4.7.

The frequency bandwidth of antenna can be defined in many ways. One of the popular definition of the bandwidth is based on the voltage standing wave ratio (VSWR) of antenna element. The bandwidth of the single isolated element, and the array elements in the active-element pattern environment for  $\text{VSWR} \leq 2$  were discussed in Sec. 5.2.2 and Sec. 5.2.3, respectively.

The bandwidth of fully excited array antenna can be evaluated in two ways. In the first method, the array bandwidth is evaluated by computing the array impedance mismatch factors using (5.2) for the frequency band between 2 GHz and 3 GHz while keeping the source S-parameters,  $\mathbf{\Gamma}_{ss}$  and the source incident waves,  $\mathbf{b}_s$ , constant. The impedance mismatch factor for a single antenna is related to the voltage standing wave ratio (VSWR) by [12]

$$\text{VSWR}_q = \frac{1 + \sqrt{1 - q}}{1 - \sqrt{1 - q}}. \quad (5.46)$$

where VSWR values of 2 and 3 correspond to  $q$  values of 88.9% and 75.0%. We can use the same relationship to compute the VSWR for the fully excited array. The voltage standing wave ratio based on the array impedance mismatch factor will be denoted by  $\text{VSWR}_q$ .

The second method to evaluate the frequency bandwidth of the array is based on the *active VSWR*,  $\text{VSWR}_a$ , of the array. The active VSWR is evaluated similar to active-element VSWR discussed in Sec. 5.2.3. First, the reflected waves from the array are evaluated over the frequency band using

$$\mathbf{b}_t = \mathbf{S}_{tt}\mathbf{a}_t \quad (5.47)$$

where the array incident waves are determined from the source incident waves using (4.13). Then, the active S-parameter of the fully excited array is determined using

$$S_{t_n} = \frac{b_{t_n}}{a_{t_n}} \quad (5.48)$$

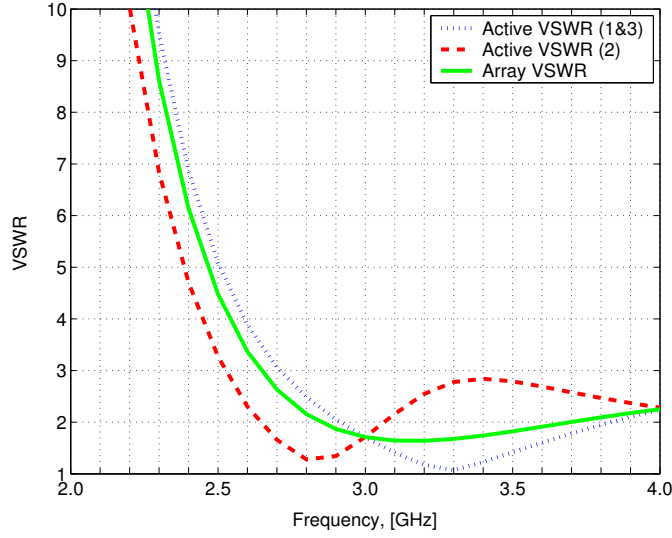


**Figure 5.12** VSWR as a function of frequency of fully excited array for Case 5 source impedance matching. The array VSWR based on impedance mismatch factor computed using (5.46)(solid curve). The active VSWR for elements 1 and 3 computed using (5.49), (dotted curve). The active VSWR for element 2 computed using (5.49), (dashed curve).

for element  $n$ . Similar to the active-element VSWR in (5.24), the active VSWR of fully excited array is computed from the active S-parameters of the array by

$$\text{VSWR}_{a_n} = \frac{1 + |S_{t_n}|}{1 - |S_{t_n}|} \quad (5.49)$$

for element  $n$ .

VSWR curves as a function of frequency of the fully excited strip dipole array computed using (5.46) and (5.49) for Case 5 impedance matching are shown in Fig. 5.12. The solid curve represents the VSWR as a function of frequency based on the impedance mismatch factor of fully excited array,  $\text{VSWR}_q$ , computed using (5.46). The dashed and dotted curves represent the active VSWR as a function of frequency,  $\text{VSWR}_{a_n}$  computed using (5.49) for elements 1 and 3, and for element 2, respectively. The upper and lower cutoff frequencies based on  $\text{VSWR} \leq 2$  were determined from the VSWR curves in Fig. 5.12, and listed in Table 5.6

The bandwidth based on the active VSWR for the outer elements in the array (elements 1 and 3), and the center element (element 2) are 27.2% and 14.6%, respectively. Also, the location of the pass bands are quite different between two VSWR curves. The bandwidths

**Table 5.6** A summary of the lower and the upper cutoff frequencies determined at VSWR=2 from Fig. 5.12 for the array VSWR based on  $q$  and for the active VSWR of fully excited three element strip dipole with Case 5 impedance matching. The percent bandwidths are computed using (5.14).

Description	Variable	Element Number			Array
		No. 1	No. 2	No. 3	
Lower cutoff frequency at VSWR=2	$f_L$	2.92 GHz	2.65 GHz	2.92 GHz	2.85 GHz
Upper cutoff frequency at VSWR=2	$f_U$	3.83 GHz	3.06 GHz	3.83 GHz	3.69 GHz
Center frequency	$f_C$	3.37 GHz	2.86 GHz	3.37 GHz	3.27 GHz
Bandwidth	$B_p$	27.20%	14.59%	27.20%	25.62%

and the pass band locations of the array VSWR based on  $q$  are also different from active VSWR. All of these VSWR curves are important in evaluating the array performance. The array VSWR based on  $q$  is directly related to the realized gain of the array radiation pattern. Thus, it is a useful figure to determine the overall efficiency of fully excited array. The active VSWR for each element can be used to identify a “hot spot” in the fully excited array. A large mismatch in one element in fully excited array may cause damages to a transmitter connected to the element.

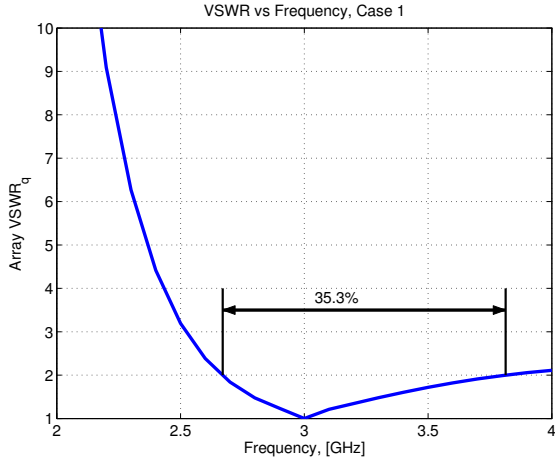
The array VSWR curves as a function of frequency based on the impedance mismatch factor computed using (5.46) are shown in Fig. 5.13 for six impedance matching cases. The sources impedances and source incident waves required for the six impedance matching cases were determined at 3 GHz using the procedures discussed in Sections 5.2.4.1 through 5.2.4.6. These source impedances and source incident waves were held constant as the frequency is varied to determine the array bandwidth. Percent bandwidths of the array were determined using (5.14) from the lower and upper cutoff frequencies where VSWR = 2. Table 5.7 summarizes the upper and lower cutoff frequencies, and computed percent bandwidth of fully excited array for the six impedance matching cases.

Several observations can be made from the plots. First, Case 1 has the widest bandwidth of 35% as compared to approximately 25% bandwidths for Cases 2 through 5. Further research is necessary to determine the reason for this extended bandwidth for Case 1. Second, matching the array elements with their isolated element input impedance may cause large mismatch as evident in Case 6. Yet, this type of error repeated in many array designs.

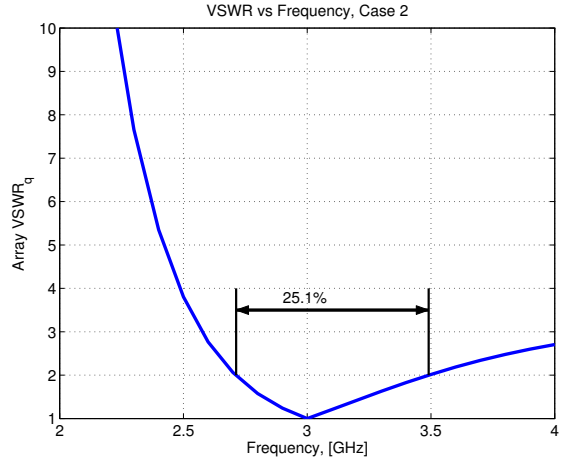
Third, comparison of Table 5.7 and Table 5.1 show that array bandwidth is much larger than the isolated strip dipole element bandwidth of 12.1% due to mutual coupling. Similar observation was made by Buxton[6]. Finally, comparison of Table 5.7 and 5.2 indicates that the active-element bandwidth (9% for the outer elements, and 4% for the center element) is not a predictor of the fully excited array bandwidth.

**Table 5.7** Summary of upper and lower cutoff frequencies determined for VSWR=2 for the curves in Fig. 5.12, and percent bandwidth computed using (5.14) for six impedance matching cases. The source impedances and source incident waves were determined at 3 GHz using the procedures discussed in Sections 5.2.4.1 through 5.2.4.6.

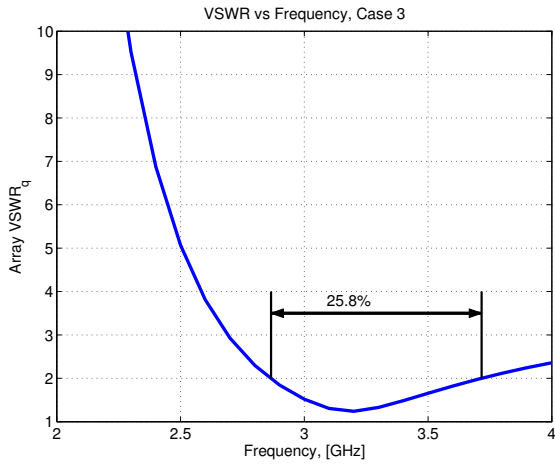
Case No.	Impedance Matching	Lower Cutoff Frequency, $f_L$	Upper Cutoff Frequency $f_U$	Center Frequency, $f_C$ , (5.15)	Percent Bandwidth, $B_p$ , (5.14)
1	Generalized Source Network, Sec. 5.2.4.1	2.67 GHz	3.81 GHz	3.24 GHz	35.3%
2	Complex Valued Individually Matched Sources, Sec. 5.2.4.2	2.71 GHz	3.49 GHz	3.10 GHz	25.1%
3	Real Valued Individually Matched Sources, Sec. 5.2.4.3	2.87 GHz	3.72 GHz	3.29 GHz	25.8%
4	Complex Valued Sources with the Same Source Impedance, Sec. 5.2.4.4	2.69 GHz	3.51 GHz	3.10 GHz	26.4%
5	Real Valued Sources with the Same Source Impedance, Sec. 5.2.4.5	2.85 GHz	3.69 GHz	3.27 GHz	25.62%
6	50 $\Omega$ source impedance, Sec. 5.2.4.6	N/A	N/A	N/A	0.00%



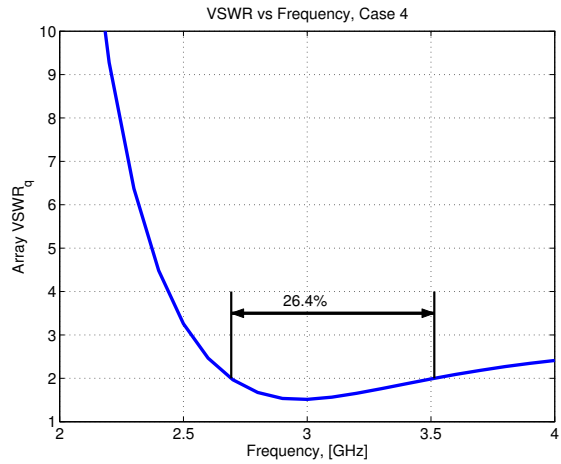
(a) Case 1



(b) Case 2



(c) Case 3



(d) Case 4

**Figure 5.13** Array  $VSWR_q$  as a function of frequency based on the impedance mismatch factor for fully excited array computed using (5.46) for the six matching cases. The required source impedances and source incident waves are computed at 3 GHz using procedures discussed in Sections 5.2.4.1 to 5.2.4.6, and used as the constants as the frequency is varied. The bandwidth is determined for  $VSWR_q \leq 2$ .

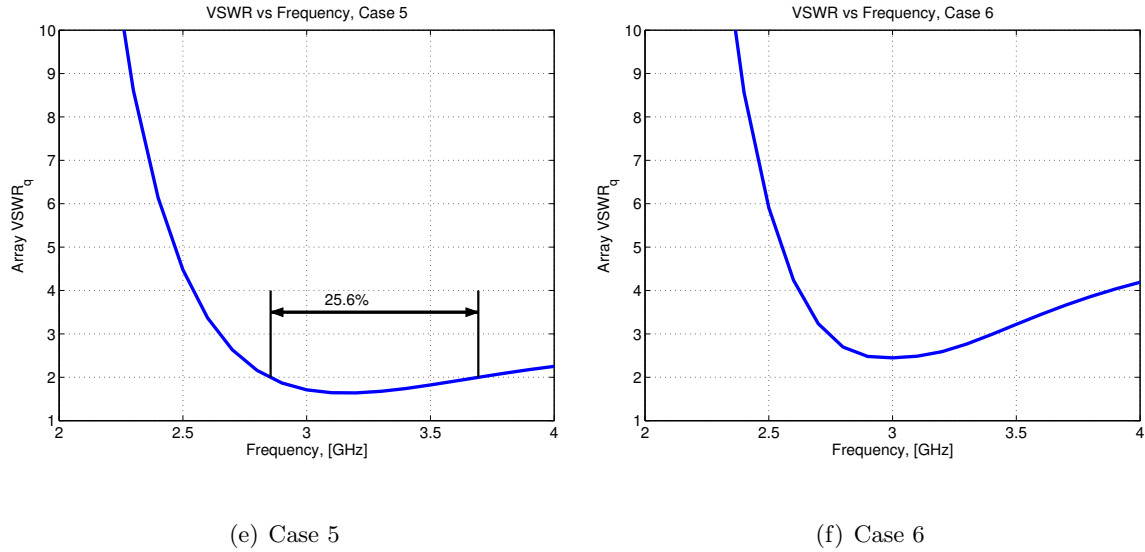


**Figure 5.13** Array  $VSWR_q$  as a function of frequency based on the impedance mismatch factor for fully excited array computed using (5.46) for the six matching cases. The required source impedances and source incident waves are computed at 3 GHz using procedures discussed in Sections 5.2.4.1 to 5.2.4.6, and used as the constants as the frequency is varied. The bandwidth is determined for  $VSWR_q \leq 2$ . (Cont.)

### 5.3 Summary

This chapter discussed the source impedance matching to the array input impedances. Three configurations of source matching were presented in Sections 5.1.1 through 5.1.3: generalized source network, individually matched sources and individual source with the same impedance value.

As an example of source impedance matching, six different cases of source impedances were considered. The first case uses the generalized source matching discussed in Sec. 5.1.1. The second and the third cases use individually matched sources which was discussed in Sec. 5.1.2. Complex-valued source impedances are used in Case 2, and real-valued source impedances are used in Case 3. The last three cases investigate the individually fed array with the same source impedance as discussed in Sec. 5.1.3. In Case 4, complex-valued source impedances are used while in Cases 5 real-valued source impedances are used. In Case 6,  $50\ \Omega$  source impedances are used as a reference.

The three-element array of strip dipoles printed on a substrate of Fig. 5.2 was simulated using IE3D for the evaluation of impedance matching. The results indicate that Cases 1 through 5 offers adequate impedance matching, which results in 35% bandwidth for Case 1 and 25% bandwidth for Cases 2 to 5 as shown in Table 5.7. These bandwidth are considerably wider than the bandwidth of single isolated strip dipole element (12%) indicating that mutual coupling can be utilized to increase that bandwidth of fully excited array. The results also indicate that the array can be matched to sources with identical real-valued source impedances (Case 5) with similar bandwidth characteristics as the more complex impedance matching (Cases 2 to 4).

## Chapter 6

# Analysis of Foursquare Array

## Antenna

This chapter presents results from an experimental investigation of a  $3 \times 3$  Foursquare array test article. The Foursquare antenna element, patented by Nealy [60] in 1999, offers several advantages, including wide bandwidth, low-profile geometry, similar E-plane and H-plane beam width, nearly equal radiation pattern over the bandwidth and dual linear polarization. The Foursquare antenna consists of four radiating squares printed on a dielectric substrate and positioned above a ground plane. Opposing squares are balanced-fed with equal amplitude but opposite phase. The Foursquare is similar to a crossed dipole antenna in polarization characteristics, and the dual orthogonal linear polarizations provided by the Foursquare can be processed to produce any desired orthogonal polarization states.

The square shape of Foursquare element leads naturally to a very closely packed array geometry. Analysis of a closely packed Foursquare array requires special care because of high mutual coupling that exists in the array due to close proximity of the elements. Radiation patterns and impedance characteristics of Foursquare array elements are significantly different from those for a single isolated Foursquare element. In addition, radiation patterns and impedance characteristics of a fully excited Foursquare array also differs from when an element in the array is excited. The feed to array element interaction also becomes a important consideration for the design of array hardware. Thus, the Foursquare array

must be analyzed including all of the mutual coupling effects using techniques such as the S-parameter based network model developed in Chapter 4.

This chapter presents an experimental validation of the S-parameter, network-model based, array analysis method of Chapter 4 using array element radiation patterns and S-parameter measurements of a  $3 \times 3$  Foursquare array. First, a description of array hardware is given along with their construction details. Then, the setup for S-parameter measurements and for radiation pattern measurements are described. The array network model is validated by comparing the indirect measurement results for active element patterns and fully excited array patterns with the directly measured results. Finally, the S-parameter network model is applied to evaluate impedance bandwidth of the Foursquare array fed with ideal hybrids as baluns.

## 6.1 Description of Array Hardware

The geometry of a  $3 \times 3$  Foursquare array test article is illustrated in Fig. 6.1, and the parameter values are summarized in Table 6.1. The Foursquare array hardware was constructed by Harris Corporation for their internal research, and tested at the Virginia Tech Antenna Lab (VTAG) anechoic chamber for measurement of S-parameter and radiation pattern measurements. The Foursquare element geometry is designed for a center frequency of 3 GHz with operational bandwidth of approximately 55%. The array elements are printed on a 31 mil thick RT/duroid 5870 with relative permittivity of  $\epsilon_r = 2.33 \pm 0.02$  and loss tangent of  $\tan \delta = 0.0012$  [70]. A second layer of dielectric substrate of the same material is glued under the first substrate to increase the overall thickness,  $t_d$ , to approximately 62 mils. The substrate is supported by a layer of foam over a ground plane such that the top of the substrate is  $h = 500$  mils above a  $12 \times 12$  inch aluminum ground plane. The Foursquare elements are in a uniform square grid with a cell length of  $C = 1513$  mils. The length along each side of the Foursquare element is  $L = 1478$  mils. The dimension of the element was chosen such that a single Foursquare over the same ground plane operates at 3 GHz as the center frequency with approximately 50 percent bandwidth [6].

**Table 6.1** Dimensions of the  $3 \times 3$  Foursquare hardware test article array of Fig. 6.1, given both in mils and in mm.

Parameter	Symbol	Sizes [mm]	Sizes [mils]
Substrate Thickness	$t_s$	1.57	62
Element height above ground plane	$h$	12.7	500
Side length of Foursquare	$L$	37.5	1478
Side length, including distance between elements	$C$	38.4	1513
Spacing between squares	$W$	0.51	20
Feed positions distance	$F'$	2.18	86
Relative dielectric constant	$\epsilon_r$	2.33	2.33

The dots in Fig. 6.1 show the locations of the coaxial feed points. The pair of squares used for vertical polarization in the Fig. 6.1 are fed with pairs of 086 semi-rigid coaxial

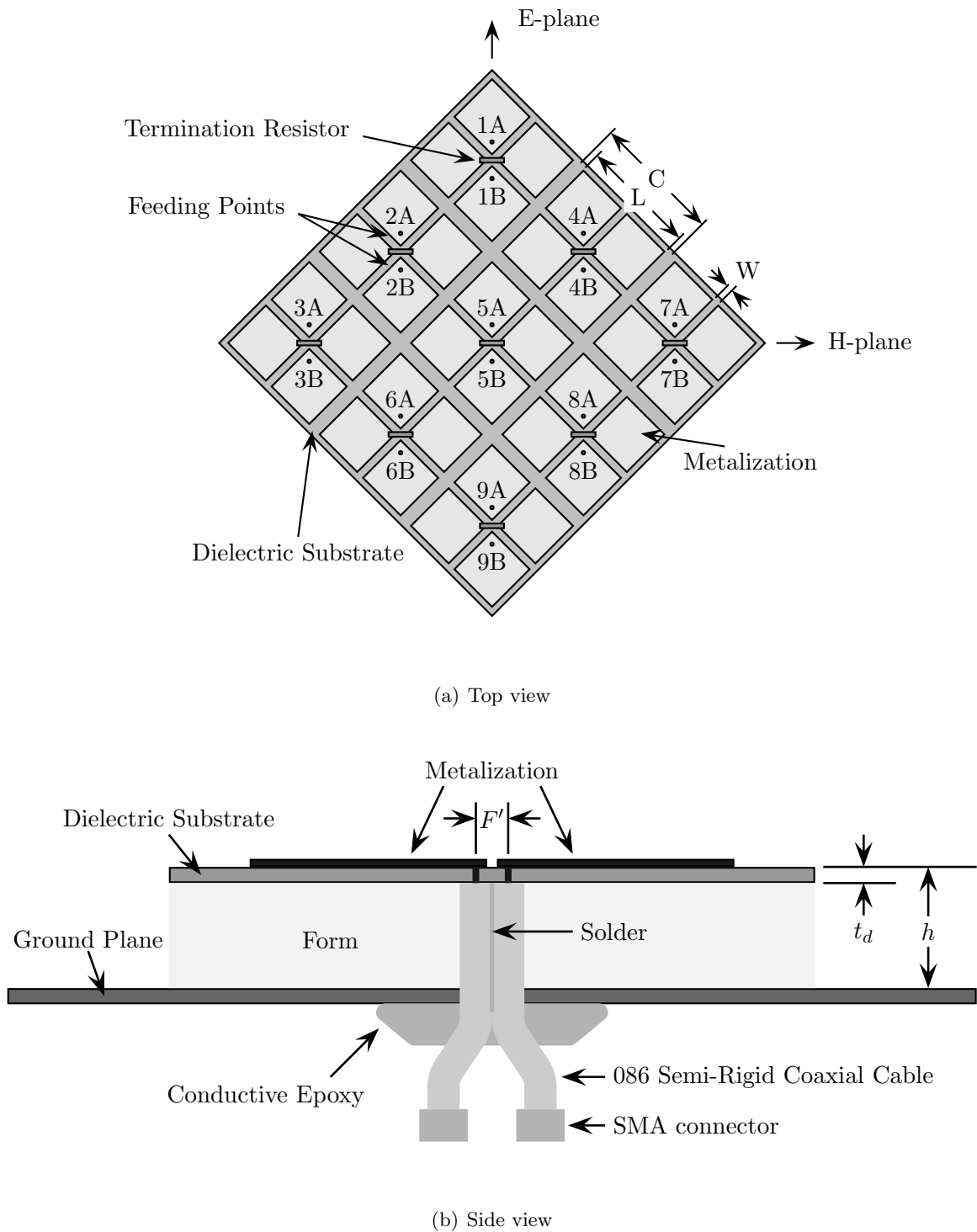


**Figure 6.1** Geometry of hardware test model  $3 \times 3$  array of Foursquare elements: (a) Top view. (b) Side view of one element. The array dimensions are summarized in Table 6.1

cables. The squares for horizontal polarization are not fed with coaxial cables. Instead, they are terminated with  $100\ \Omega$  chip resistors in 0402 packages at their feed points. Thus, the array is configured to operate in a single linear polarization (vertical polarization in Fig. 6.1). The outer shields of the coaxial cables between the dielectric substrate and the ground plane are soldered to keep them in the common ground for the balanced feeding. Conductive epoxy putty is used between the coaxial cable outer shields and the ground plane for good electrical connection as shown in Fig. 6.1. The array elements are numbered from 1 through 9, and each coaxial port for an element is identified with a letter either A or B. Overall, there are 18 coaxial ports on the array, and thus, the array is treated as a 18-port device in this experiment.

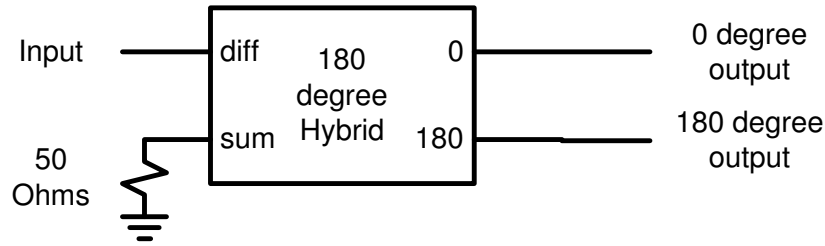
The array hardware is fed in one of two ways. To determine active-element patterns, an array element is balance fed using a 180 degree broadband hybrid as a balun while terminating all other array elements with  $50\ \Omega$  terminations. Secondly, to determine fully excited array radiation patterns, the array elements are fed with a feed network consisting of two 8-way broadband power dividers and a 180 degree broad band hybrid. The power dividers and the hybrid used for the active-element pattern and for the array pattern are manufactured by Electromagnetic Technologies, Inc [71] and their electrical specifications which are reproduced from manufacturer’s data sheet, are shown in Tables 6.2 and 6.3. The power dividers and the hybrid are connected with United Microwave Products Microflex 150 coaxial cable sets. A configuration of the feed network used for the array experiment is illustrated in Fig. 6.2. The combination of two power dividers and a hybrid allow excitation of up to 8 array elements with equal amplitudes and 180 deg phase shifts in balanced mode excitation.

**Table 6.2** Electrical specifications for ETI P8D118-8 broadband 8-way power divider.

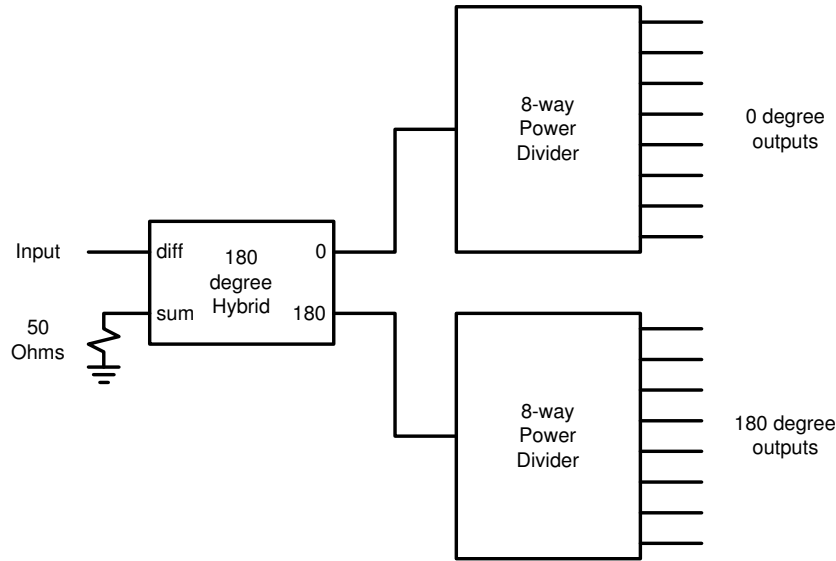
Frequency Range (GHz)	1.0-18.0
VSWR Input and Output Max.	1.70:1, 1.70:1
Insertion Loss Max. (dB)	3.5
Isolation (dB)	> 16 (1-8 GHz), > 18 (8-18 GHz)
Amplitude Balance (dB)	1.8
Phase Balance (deg)	10

**Table 6.3** Electrical specifications for ETI HY118-180 broadband 180 degree hybrid.

Frequency Range (GHz)	1.0-18.0
Amplitude Imbalance (dB)	$\pm 0.6$
Phase Imbalance (deg)	$\pm 14.0$
Isolation Min. (dB)	15.0
VSWR Max.	1.70:1
Insertion Loss Max (dB)	2.0



(a) Active-Element Pattern Feed Configuration



(b) Fully Excited Array Feed Configuration

**Figure 6.2** A block diagram of feed network configuration using two 8-way power dividers and one 180 degree hybrid.

## 6.2 Measurement Setup

Network analysis of the test article array requires three matrices: S-matrix for the array,  $S_{tt}$ , S-matrix for the source network,  $\Gamma_{ss}$ , and the array element pattern matrix,  $S_{pt}(\theta, \phi)$ .

The array elements and source network S-matrices are measured directly using a network analyzer. The element pattern matrix can be determined directly from S-parameter measurements between the array elements and a probe antenna, or from radiation pattern measurements of element patterns. In this experiment,  $\mathbf{S}_{pt}$  are determined from the far-field pattern measurements using a near-field scanner.

### 6.2.1 S-parameter Measurements

All of the S-parameters in the experiment are measured using an Agilent 8510C vector network analyzer [72]. The 8510C is a two-port network analyzer which allows simultaneous measurements of 4 S-parameters,  $S_{11}$ ,  $S_{12}$ ,  $S_{21}$ , and  $S_{22}$  for a two-port device. However, many of the components used in the array experiment are multi-port devices with more than two ports. Thus, a multi-port network S-matrix must be determined from multiple 2-port measurements while terminating unused ports with  $50\ \Omega$  loads. Inexpensive  $50\ \Omega$  SMA loads were used in the experiment to terminate the array. The non-ideal terminations cause some mismatch at the terminated ports, resulting in some errors for the measured S-parameter values. The error introduced by the non-ideal terminations can be reduced by measuring the S-parameters of the loads and systematically applying the generalized scattering parameter re-normalization transforms [73].

In addition to having more than two ports, the power dividers and the hybrid for the feed network used in the experiment are equipped with connectors of the same sex. They cannot be directly measured using the network analyzer that is configured with a male and a female 3.5mm coaxial connectors for each measurement port. An adapter must be inserted into one of the measurement ports, and the effect of adapter must be eliminated during the calibration process. There are several calibration procedures used to eliminate the effects of the adapter from the measurements. The adapter removal method discussed in [72] was used to calibrate the network analyzer.

The adapter removal method requires two sets of full two-port calibrations of the network analyzer: one with the adapter attached to the first analyzer port, and the other with the adapter attached to the second analyzer port. Because the adapter used is a device in a cal-kit, its S-parameter is known. Thus, the effect of adapter can be “removed” or

subtracted from the two sets of calibration measurements, and a third calibration data can be computed for the analyzer without the adapter [72].

### 6.2.2 Foursquare Array S-parameters

The frequency response of the array hardware is characterized using scattering parameters, or S-parameters. Typically, baluns for balanced-fed antenna elements are included in the array circuit, so a  $3 \times 3$  array, or a nine-element array is characterized by  $9 \times 9$  S-matrix. The Foursquare test article used in the experiment does not include a balun for each element as shown in Fig. 6.1. Instead of including the baluns in the array hardware, they are included in the feed network (See Fig. 6.2). Thus, the array hardware was characterized without the balun. There are two feed ports for each Foursquare element in the 9-element test article, giving eighteen ports in total. Thus, the array hardware was measured as an 18-port device. The effects of baluns can be included in the pattern and the impedance analysis by measuring S-parameters of the balun separately from the array hardware, and applying network analysis techniques to compute the combined network S-parameters.

The  $18 \times 18$  S-matrix of the array are determined from multiple 2-port measurements while terminating unused ports with  $50 \Omega$  loads, as we discussed in Sec. 6.2.1. A total of 153 two-port measurements as listed in Table 6.4 are necessary to analyze the 18-port array hardware. We performed these 153 two-port measurements and the 18-port S-parameter matrix was constructed from these measurements.

**Table 6.4** The measurement plan for the 153 two-port measurements of the Foursquare article array of Fig. 6.1. The measurements that include port 5A of the center element are highlighted to illustrate that there are 17 reflection coefficient measurements for this port within the overall measured data sets.

1A - 1B	1B - 2A	2A - 3A	2B - 4B	3A - 6B	3B - 9A	4B - 7A	5B - 7A	6B - 9A
1A - 2A	1B - 2B	2A - 3B	2B - 5A	3A - 7A	3B - 9B	4B - 7B	5B - 7B	6B - 9B
1A - 2B	1B - 3A	2A - 4A	2B - 5B	3A - 7B	4A - 4B	4B - 8A	5B - 8A	7A - 7B
1A - 3A	1B - 3B	2A - 4B	2B - 6A	3A - 8A	4A - 5A	4B - 8B	5B - 8B	7A - 8A
1A - 3B	1B - 4A	2A - 5A	2B - 6B	3A - 8B	4A - 5B	4B - 9A	5B - 9A	7A - 8B
1A - 4A	1B - 4B	2A - 5B	2B - 7A	3A - 9A	4A - 6A	4B - 9B	5B - 9B	7A - 9A
1A - 4B	1B - 5A	2A - 6A	2B - 7B	3A - 9B	4A - 6B	5A - 5B	6A - 6B	7A - 9B
1A - 5A	1B - 5B	2A - 6B	2B - 8A	3B - 4A	4A - 7A	5A - 6A	6A - 7A	7B - 8A
1A - 5B	1B - 6A	2A - 7A	2B - 8B	3B - 4B	4A - 7B	5A - 6B	6A - 7B	7B - 8B
1A - 6A	1B - 6B	2A - 7B	2B - 9A	3B - 5A	4A - 8A	5A - 7A	6A - 8A	7B - 9A
1A - 6B	1B - 7A	2A - 8A	2B - 9B	3B - 5B	4A - 8B	5A - 7B	6A - 8B	7B - 9B
1A - 7A	1B - 7B	2A - 8B	3A - 3B	3B - 6A	4A - 9A	5A - 8A	6A - 9A	8A - 8B
1A - 7B	1B - 8A	2A - 9A	3A - 4A	3B - 6B	4A - 9B	5A - 8B	6A - 9B	8A - 9A
1A - 8A	1B - 8B	2A - 9B	3A - 4B	3B - 7A	4B - 5A	5A - 9A	6B - 7A	8A - 9B
1A - 8B	1B - 9A	2B - 3A	3A - 5A	3B - 7B	4B - 5B	5A - 9B	6B - 7B	8B - 9A
1A - 9A	1B - 9B	2B - 3B	3A - 5B	3B - 8A	4B - 6A	5B - 6A	6B - 8A	8B - 9B
1A - 9B	2A - 2B	2B - 4A	3A - 6A	3B - 8B	4B - 6B	5B - 6B	6B - 8B	9A - 9B

When the terminations used in the measurements are ideal, the measured 2-port S-parameters between port  $m$  and port  $n$ ,  $S_{t_n t_m}^{(2)}$ , are identical to the 18-port S-parameter, or

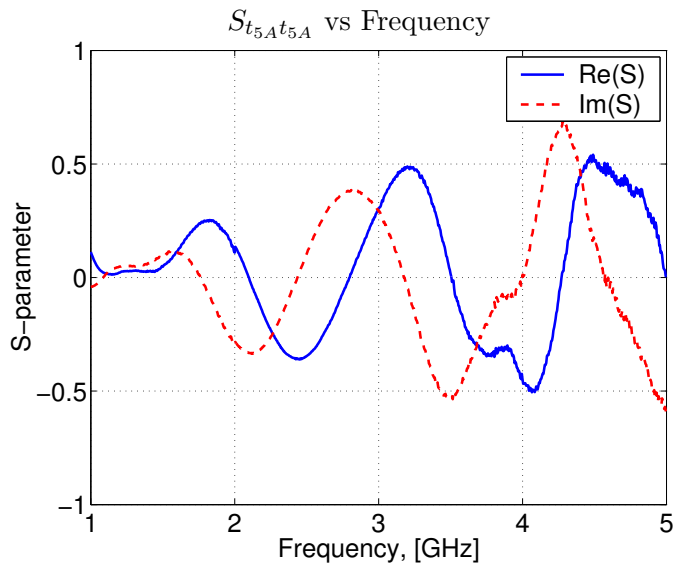
$$S_{t_n t_m}^{(2)} = S_{t_n t_m}, \text{ for ideal terminations.} \quad (6.1)$$

When the terminations used are not ideal, in general, the measured two-port S-parameter matrix is not equal to the 18-port S-parameter matrix, or

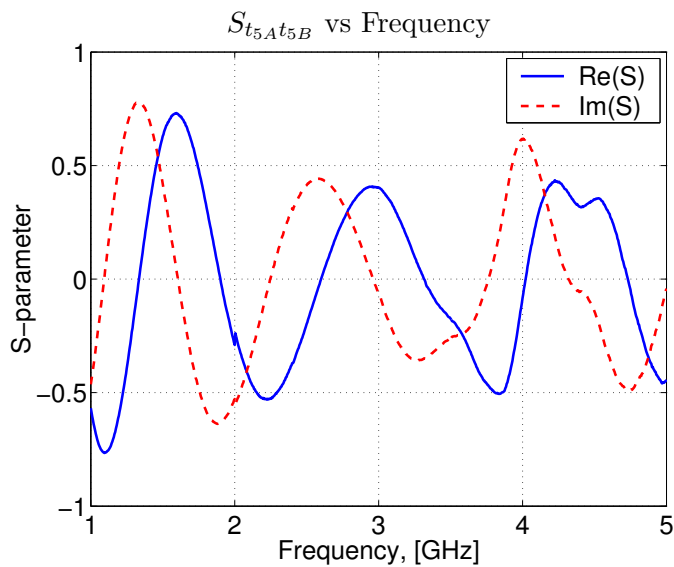
$$S_{t_n t_m}^{(2)} \neq S_{t_n t_m}, \text{ for non-ideal terminations.} \quad (6.2)$$

The error in S-parameters introduced by the non-ideal terminations can be reduced using a multi-port S-parameter measurement procedure developed by Tippet and Speciale [73]. We used their procedure to compute the complete 18-port S-parameter matrix. Representative samples of the 18-port S-parameters for  $S_{t_{5A} t_{5A}}$  and  $S_{t_{5A} t_{5B}}$  over 1 to 5 GHz are plotted in Fig. 6.3.

One of the consequences of multiple 2-port measurements is that the self-terms of the array S-matrix,  $\{S_{t_n t_n}\}$  are measured 17 times for each port. For example, there are 17



(a)  $S_{t_{5A}t_{5A}}$



(b)  $S_{t_{5A}t_{5B}}$

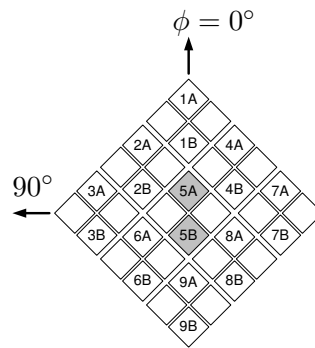


**Figure 6.3** Representative sample plots of measured S-parameters,  $S_{t_{5A}t_{5A}}$  and  $S_{t_{5A}t_{5B}}$ , as a function of frequency for the Foursquare array of Fig. 6.1. Solid curves represent the real components, and dashed curves represent the imaginary components.

two-port measurements that include port 5A that are highlighted in Table 6.4. Thus, the reflection term of the 2-port S-parameters for port 5A,  $S_{t_{5A}t_{5A}}$ , is measured seventeen times within the 153 two-port measurement sets. The redundant reflection coefficient measurements were used to assess the repeatability of the S-parameter measurements. The maximum variance in the magnitudes of the measured reflection S-parameters was computed as 0.8 percent of the average value, indicating a good stability during the measurements.

### 6.2.3 Radiation Pattern Measurements

The S-parameter network model based analysis developed in Chapter 4 requires array element radiation pattern information in addition to the scattering parameters of the array and feed network. The array patterns and active-element patterns of the Foursquare test article were measured in the Virginia Tech Antenna Group (VTAG) anechoic chamber using a near field scanner operating in the spherical scan mode. The S-parameters of the array elements were also measured with the array in the anechoic chamber to reduce the environmental effects.

A profile view of the VTAG tapered anechoic chamber is illustrated in Fig. 6.4. The anechoic chamber consists of three sections: a rectangular source section, a rectangular test section, and a tapered section connecting the source section and the test section. The source section of the chamber is still under construction, and therefore, it is currently left open.

A tapered anechoic chamber is usually operated in far-field mode by positioning the source antenna at the apex of the pyramidal taper and the antenna under test (AUT) in the test section. The taper from the source to the AUT reduces contribution of reflected energy illuminating the AUT by ensuring that the incidence angles to the absorbers remain high. In addition, the taper is designed such that any specular reflections that occur in the

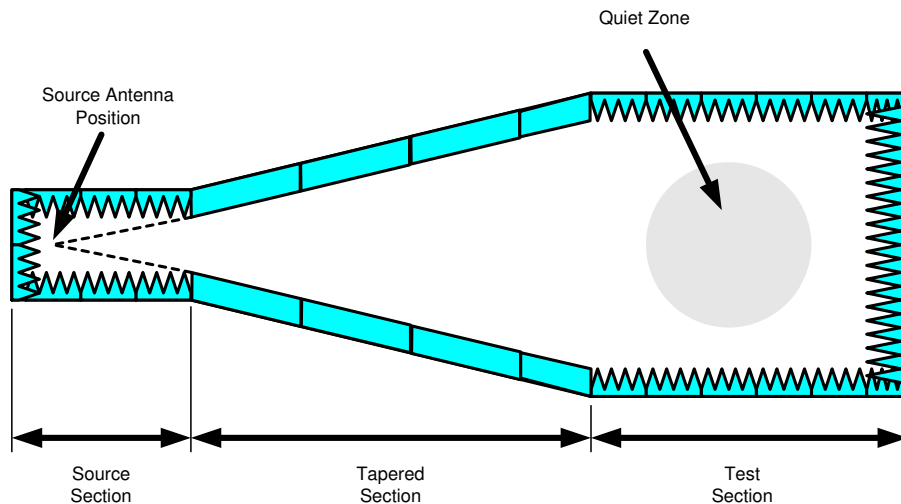


Figure 6.4 Illustration of VTAG anechoic chamber.

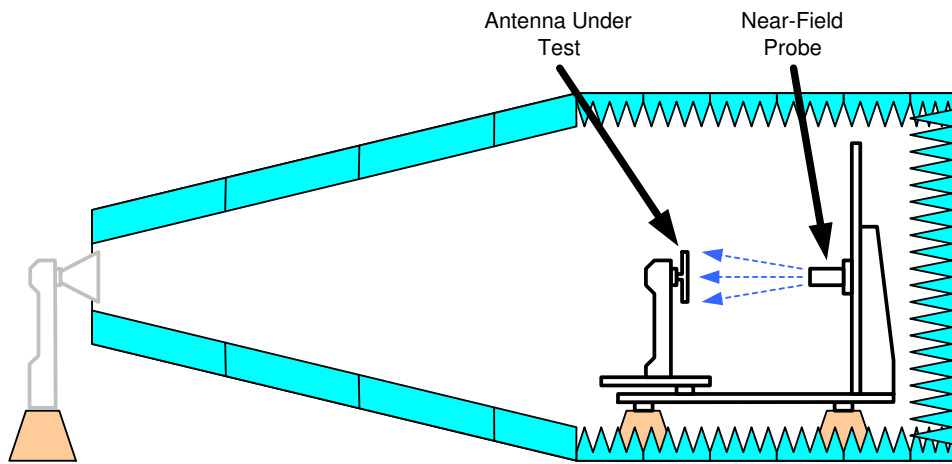
tapered section add in phase to create flat phase front in the quiet zone near the center of the test section.

The test section of the VTAG chamber is 11 feet square in cross section and 11.5 feet in length. The tapered section is 14.5 feet long and tapers from a 4 by 4 foot opening at the interface of source section and the tapered section. The tapered section and the test section of the chamber are lined with aluminum sheets beneath the absorber to improve the isolation of the chamber. The tapered section of the chamber is fitted with 12 inch thick wedge absorber panels. The top, bottom and side walls of the test section are fitted with 12 inch thick pyramidal absorber panels, and the back wall of the chamber is fitted with 18 inch thick pyramidal absorber panels.

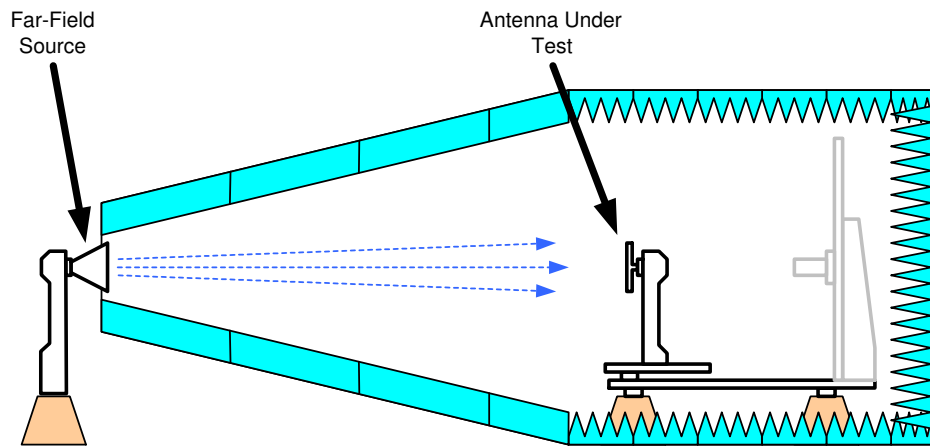
A near-field scanner, manufactured by ANTCOM [74], includes a 7+1 axis scanner that permits operation in either near-field or far-field modes using the same hardware and the software. In the near-field configuration, the antenna positioner in the test section points towards the back wall of the test section as illustrated in Fig. 6.5(a). The antenna positioner at the source section is covered with absorber during this configuration. The near-field pattern of the AUT is detected with a probe antenna mounted near the back wall. The ANTCOM system uses the network analyzer described in Sec. 6.2.1 as the transceiver which allows measurement of both amplitude and phase patterns. The complex near-field patterns are transformed to the corresponding complex far-field patterns using ANTCOM software [74].

In the far-field configuration, the AUT tower is rotated 180 degrees to face towards the source section as illustrated in Fig. 6.5(b). During this operation, the probe positioner is moved to the limits of travel and covered with absorber to reduce the unwanted scattering from it. The radiation from the source antenna is measured by the AUT to determine the far-field pattern directly. The measured far-field pattern is also complex valued since the same network analyzer as the near-field configuration is used as the transceiver.

The active-element patterns and the array radiation patterns were measured in the anechoic chamber using the spherical near-field measurement mode. The far-field patterns were computed from the near-field measurements using the ANTCOM [74] software. The gain patterns were determined using the gain comparison method [12] from the the near-



(a) Near-field configuration



(b) Far-field configuration

**Figure 6.5** Near-field and far-field measurement configurations used at VTAG chamber.

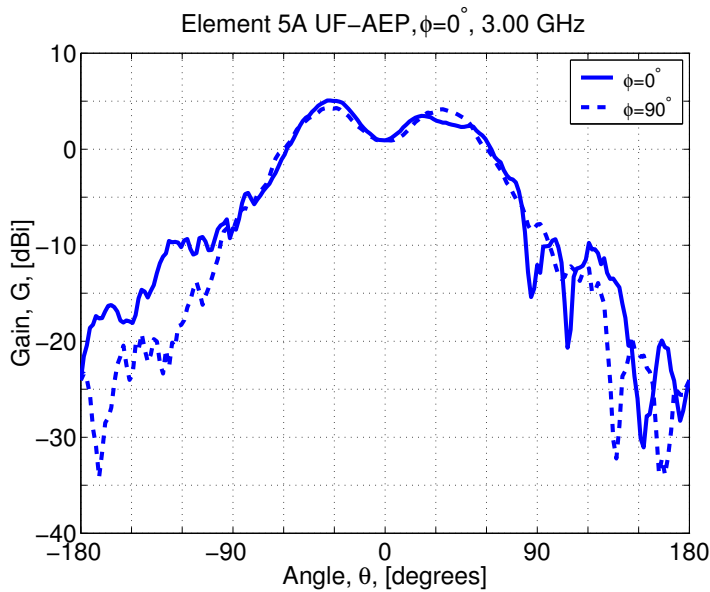
field measurements of standard gain horns. Since the ANTCOM near-field scanner control software uses the network analyzer as a transceiver without calibration, the ANTCOM computed gain represents the realized gain.

#### 6.2.4 Unbalanced-Fed Active-Element Pattern Measurements

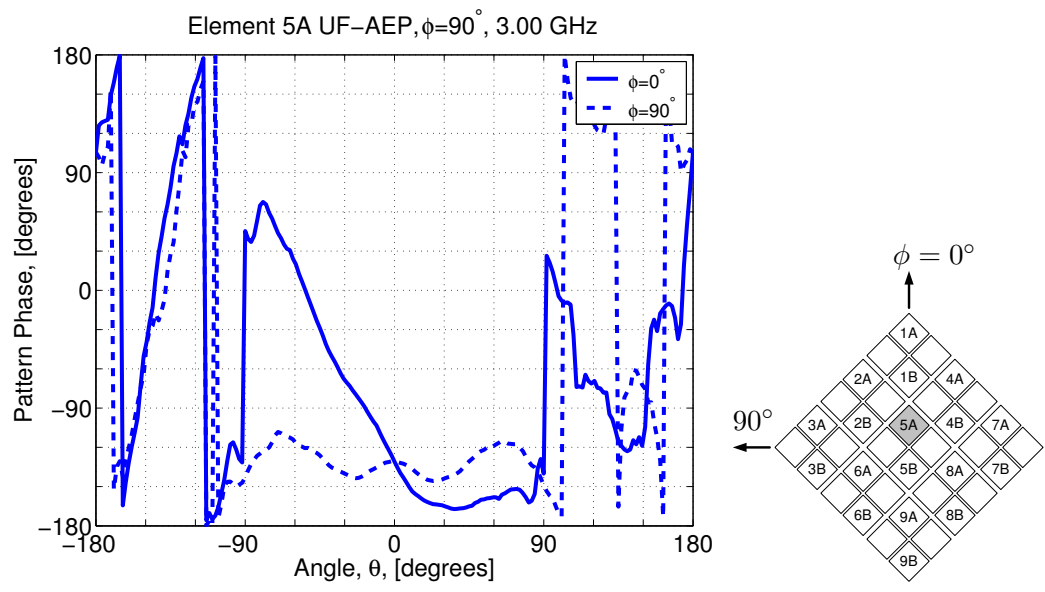
The  $3 \times 3$  Foursquare array was modeled as a 18-port device as described in Sec. 6.2.2. The active-element patterns of the array are also determined for each of these eighteen ports to be consistent with the array S-matrix. The active-element patterns are measured by exciting one of the eighteen ports in the array while terminating the other seventeen ports with  $50\Omega$  loads. Because only one half of a Foursquare element (i.e. one square in a Foursquare) was excited at a time, the measured patterns are for the elements with an unbalanced feed. We will denote these patterns as *unbalanced-fed active-element patterns*, (UF-AEP). On the other hand, the pattern of a balanced-fed array element (measured by exciting squares with equal amplitude and opposite phase) will be denoted by *active-element pattern*, AEP.

Figures 6.6 and 6.7 show the co-polarization component of unbalanced-fed active-element patterns of the elements 5A and 5B for the Foursquare array measured at 3 GHz. The patterns were determined from near-field measurements at Virginia Tech Antenna Group (VTAG) anechoic chamber and transforming to far-field patterns using ANTCOM[74] software. The measured amplitude and phase of unbalanced-fed active-element patterns for port 5A when all other ports are terminated with  $50\Omega$  loads are shown in Fig. 6.6, and the patterns for port 5B are shown in Fig. 6.7, respectively. As expected, the amplitude patterns in  $\phi = 90^\circ$  plane for both elements 5A and 5B show symmetry because of the symmetric geometry of the array with respect to the excited element. Although the the amplitude patterns in  $\phi = 0^\circ$  plane are asymmetric, they are mirror images of each other because elements 5A and 5B are positioned symmetrically about the center of the array in this plane.

The phase patterns in Figures 6.6 and 6.7 also have symmetry trends similar to the amplitude patterns with symmetry in  $\phi = 90^\circ$  plane and with mirror-imaged asymmetry in  $\phi = 0^\circ$  plane. We should note that there are approximately 180 degree offsets between phase patterns for the element 5A and the element 5B. These phase offsets occur due to the polarity reversal of the current flowing on the reversed elements. When used with a 180 degree hybrid, the results correctly add at 0 degree as expected.

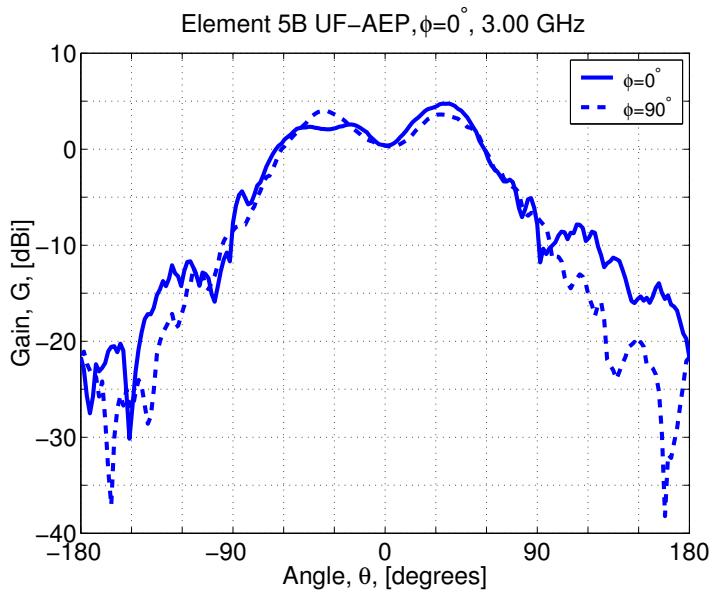


(a) Gain patterns amplitude for element 5A

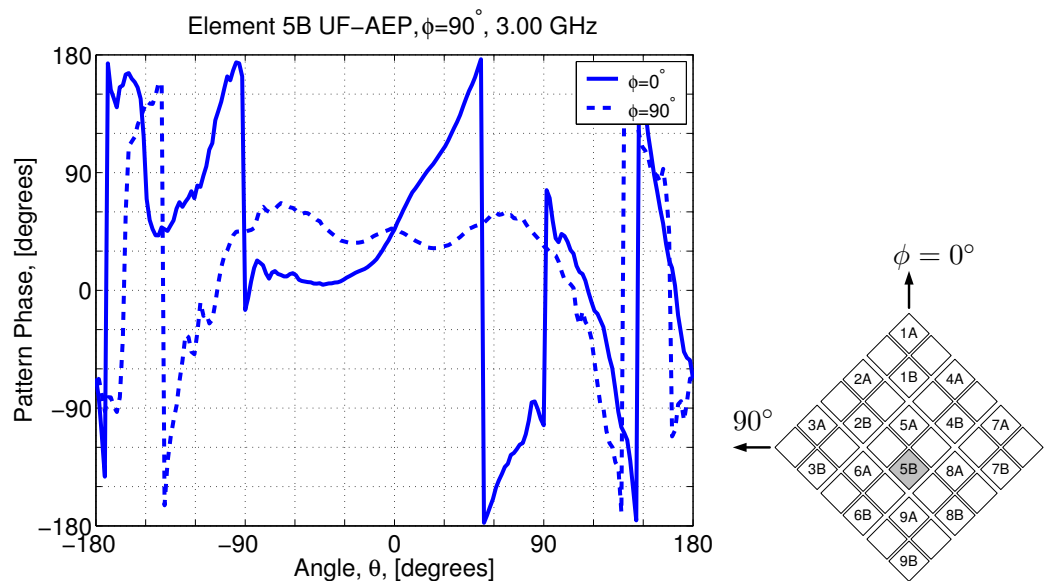


(b) Gain patterns phase for element 5A

**Figure 6.6** Measured amplitude and phase of co-polarization component of the unbalanced-fed active-element patterns (UF-AEP) at 3 GHz for element 5A of the Foursquare test array of Fig. 6.1. Solid curves represent a pattern in  $\phi = 0^\circ$  plane. Dashed curves represent a pattern in  $\phi = 90^\circ$  plane. These far-field quantities were determined from near-field measurements.



(a) Gain patterns amplitude for element 5B



(b) Gain patterns phase for element 5B

**Figure 6.7** Measured amplitudes and phases of co-polarization component of the unbalanced-fed active-element patterns (UF-AEP) at 3 GHz for element 5B of the Foursquare test array of Fig. 6.1. Solid curves represent patterns in  $\phi = 0^\circ$  plane. Dashed curves represent patterns in  $\phi = 90^\circ$  plane. These far-field quantities were determined from near-field measurements.

## 6.3 Measured Results

This section presents results from an experimental investigation of the  $3 \times 3$  Foursquare test array described in Sec. 6.1. This investigation serves two purposes: first, to experimentally validate the S-parameter network analysis technique developed in Chapter 4, and secondly, to demonstrate an application of S-parameter based analysis to the Foursquare array with a hypothetical feed network.

The investigation is conducted in three stages. First, the balanced-fed active-element patterns of the test article are computed using the array network analysis procedure developed in Chapter 4, with the measured S-parameters of the array elements and the measured unbalanced-fed active-element patterns. In Sec. 6.3.1, the computed balanced-fed active-element patterns are compared with the active-element patterns measured directly to validate the network analysis model as well as the measured data. Next, the array patterns of the Foursquare array fed with a broadband power divider corporate feed network are computed, and the results are compared to the patterns measured directly in the same configuration in Sec. 6.3.3. These two tests verify the S-parameter network analysis method, and validate the measured S-parameters of the array and their unbalanced-fed active-element patterns. The increased confidence in the analysis method and measured data allows us to evaluate the performance of the Foursquare array fed with a hypothetical feed network. The impedance bandwidths of the Foursquare array hardware fed with nine idealized broadband baluns is demonstrated in Sec. 6.3.4.

### 6.3.1 Comparison of Indirectly and Directly Measured Active-Element Patterns

In this section, we validate the S-parameter network model based analysis using experimental measurements. For the validation, we will determine active-element patterns (AEP) of the Foursquare array using two methods, and compare the results. An AEP is a radiation pattern of array antenna when one element in the array is excited and all other elements are terminated with  $50\ \Omega$  loads. A schematic of the array configuration for the measurement of the active-element pattern for element 5 of the Foursquare array is shown in Fig. 6.8. In one method, the active-element patterns are computed using the the array network analysis developed in Chapter 4 using the measured unbalanced-fed active-element patterns (UF-AEP) discussed in Sec. 6.2.4 and the S-parameter matrix of the array discussed in Sec. 6.2.2. We designate these computed active-element patterns based on measured data as *indirectly measured AEP*. The second method is to measure active-element patterns of the array directly by feeding an Foursquare element in the test article with a broadband hybrid as a balun, which will be designated as *directly measured AEP*. We will compare the indirectly measured active-element pattern with directly measured AEP of the same array

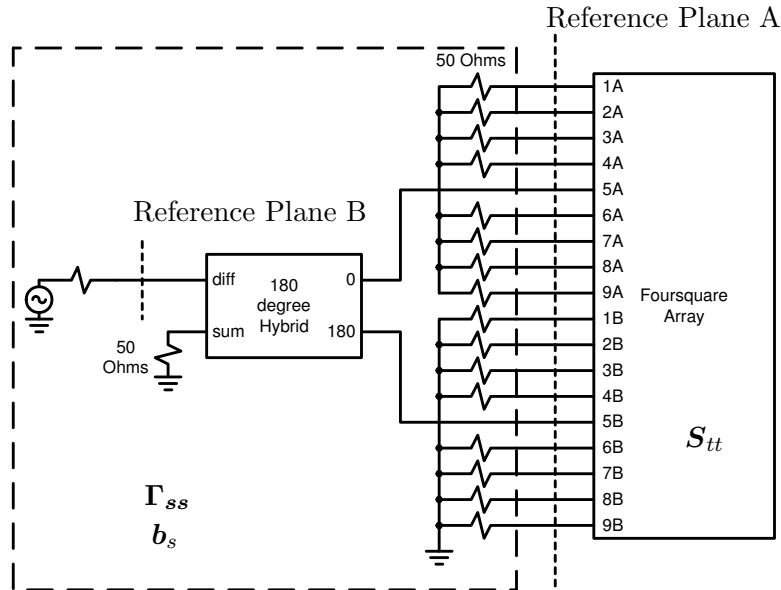


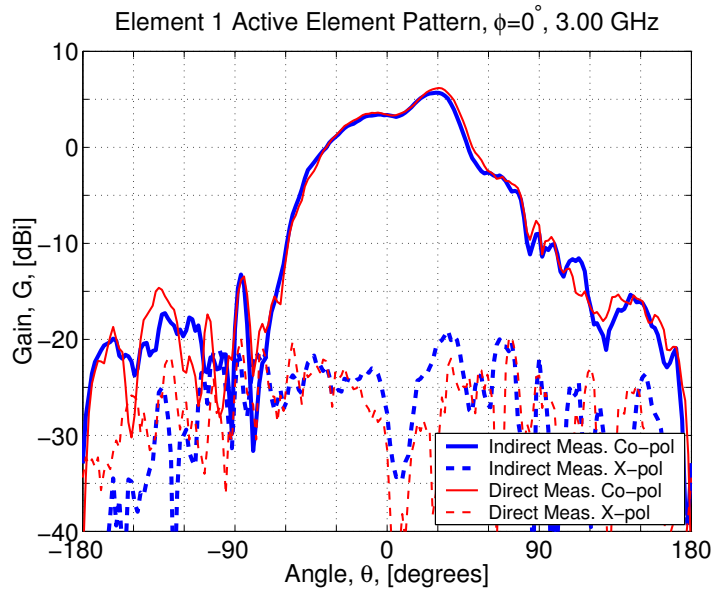
**Figure 6.8** Schematic of the array network configuration for measurement of active-element pattern of element 5 in the Foursquare array of Fig. 6.1.

to validate the S-parameter network based analysis method.

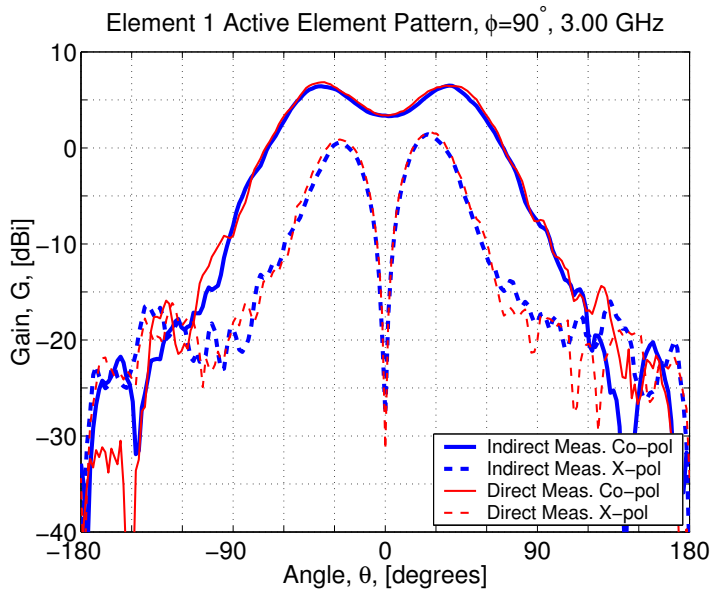
The unusual method for indirectly computing active-element patterns from two measured unbalanced-fed active-element patterns can be considered as an extension to the two-port impedance measurement method developed by Davis[75]. It allows us to choose various models for the balun to feed the antenna elements, and compute the balanced-fed antenna patterns based on the balun design. In this study, the balun consists of a broadband  $180^\circ$  hybrid described in Sec. 6.1. The measured S-parameters of the broadband hybrid are used in the computation. Then, the S-parameter network based analysis is applied to compute the gain pattern of active-elements using (4.66).

The indirectly measured active-element gain patterns in  $\phi = 0^\circ$  and  $90^\circ$  planes for the elements 1, 2, 3 and 5 of the  $3 \times 3$  array of Foursquares operated at 3 GHz are shown in Figures 6.9 through 6.12. In addition, the directly measured active-element patterns for the same array elements are overlayed in the plots. Note that the directly measured active-element pattern gain is referenced at the difference port of the  $180^\circ$  hybrid, as indicated by the reference plane B in Fig. 6.8. On the other hand, the gain plot of the indirectly measured AEP is referenced to the interface between array elements and the output of the hybrid as indicated by the reference plane A in the schematic. To make a meaningful comparison between indirectly measured and directly measured patterns, the gain must be referenced to the same reference position in the network. Since we are interested in the performance evaluation of the Foursquare elements independent of the balun design, the gain patterns will be compared referenced to plane A in Fig. 6.8. Thus, the insertion loss of the hybrid must be subtracted from the gain value of the directly measured AEP. A plot of the hybrid insertion loss measured for the frequency range between 1 to 5 GHz is shown in Fig. 6.13. The hybrid has approximately 0.7 dB of insertion loss at 3 GHz. The directly measured active-element pattern curves in Figures 6.9 through 6.12 are adjusted for the hybrid insertion loss.

The co-polarization component of the directly measured and the indirectly measured active-element patterns for the elements 1, 2, 3 and 5 in Figures 6.9 through 6.12 compare very well for both  $\phi = 0^\circ$  and  $\phi = 90^\circ$  plane cuts. Nearly all pattern features are faithfully reproduced. Deviations are typically less than 0.5 dB out to 10 dB down from the pattern



(a)  $\phi = 0^\circ$  cut



(b)  $\phi = 90^\circ$  cut

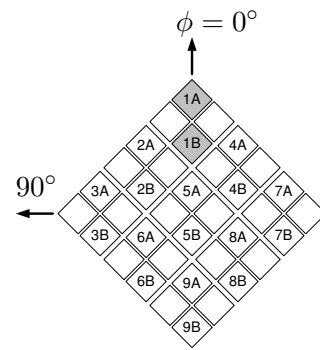
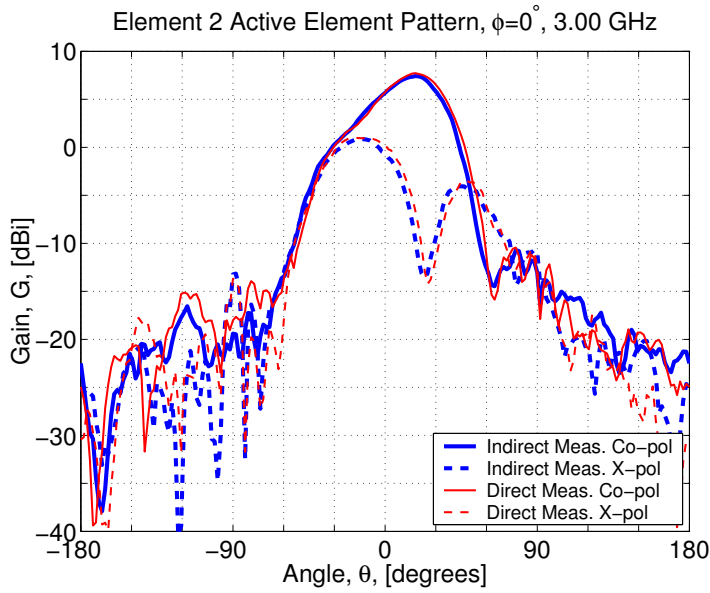
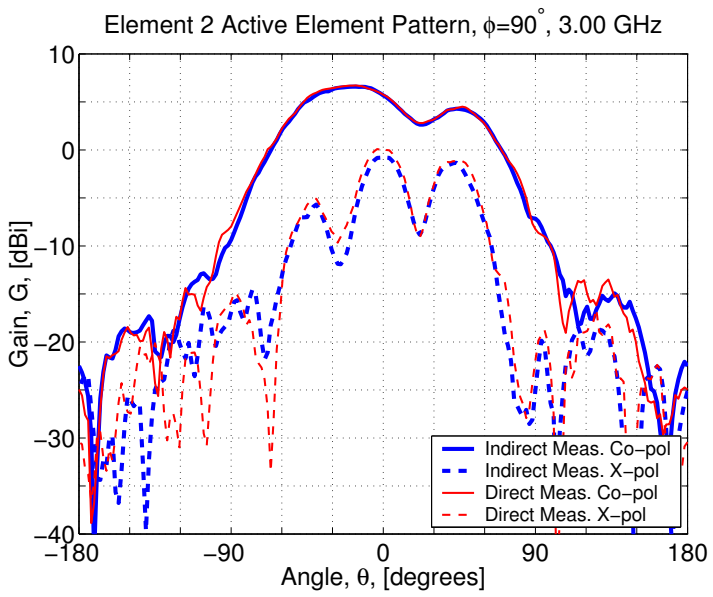


**Figure 6.9** Comparison of indirectly and directly measured active-element gain patterns for element 1 at 3 GHz in  $\phi = 0^\circ$  and  $90^\circ$  planes.



(a)  $\phi = 0^\circ$  cut



(b)  $\phi = 90^\circ$  cut

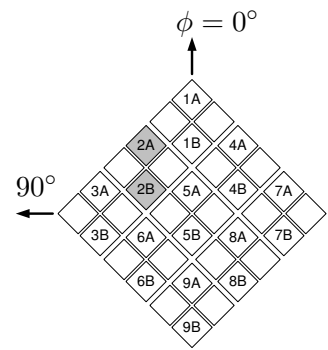
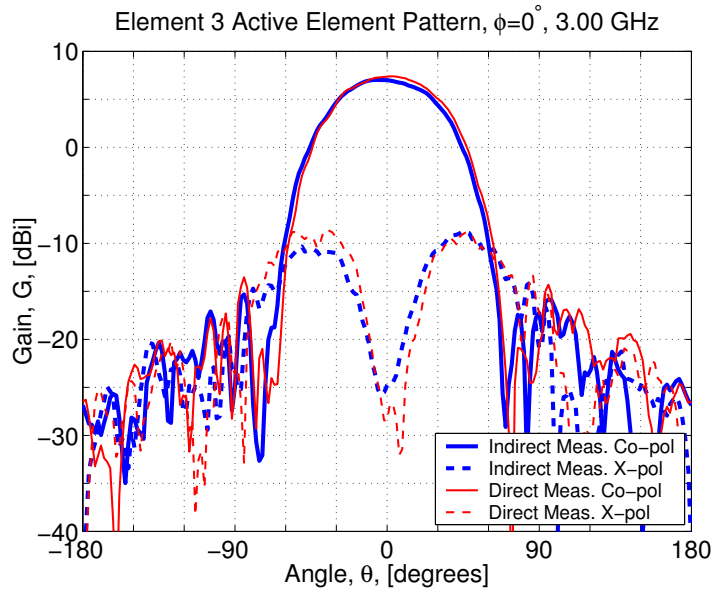
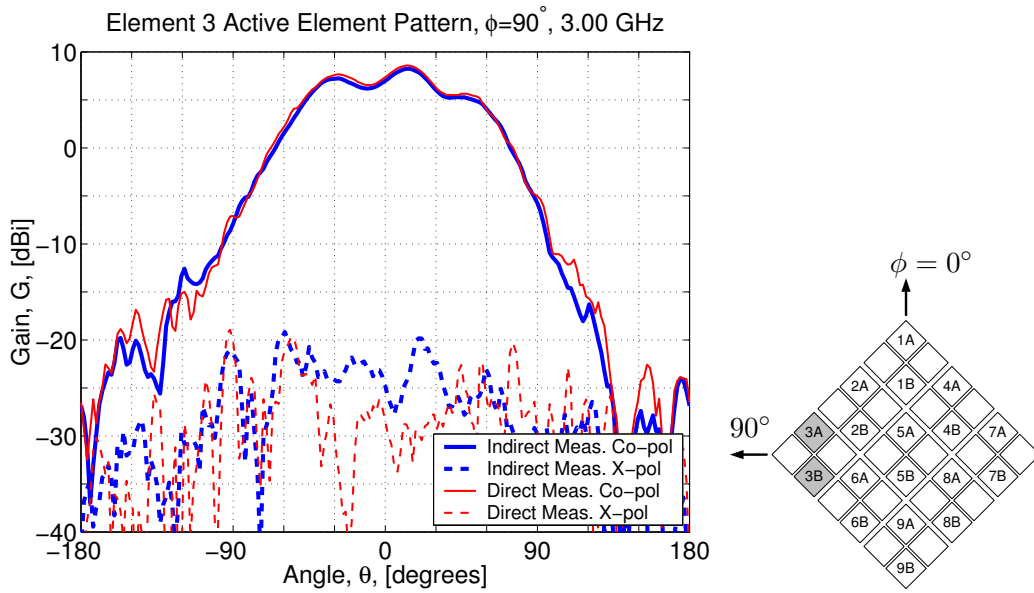


**Figure 6.10** Comparison of indirectly and directly measured active-element gain patterns for element 2 at 3 GHz in  $\phi = 0^\circ$  and  $90^\circ$  planes.

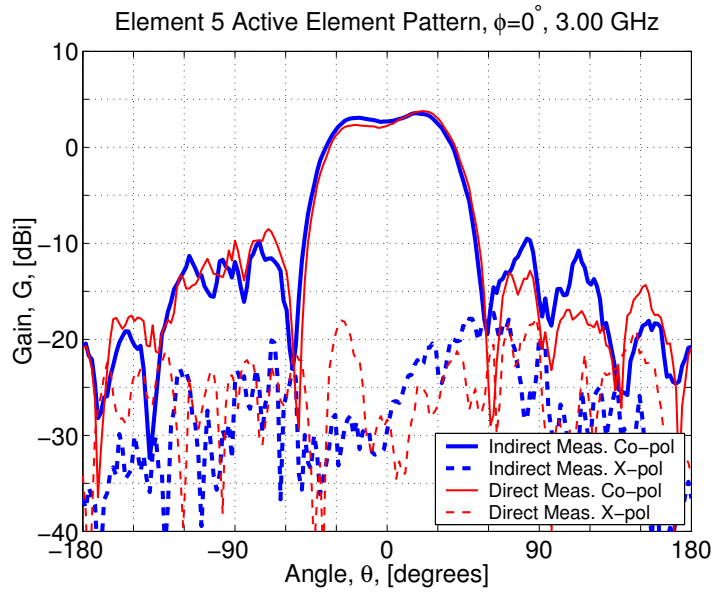


(a)  $\phi = 0^\circ$  cut

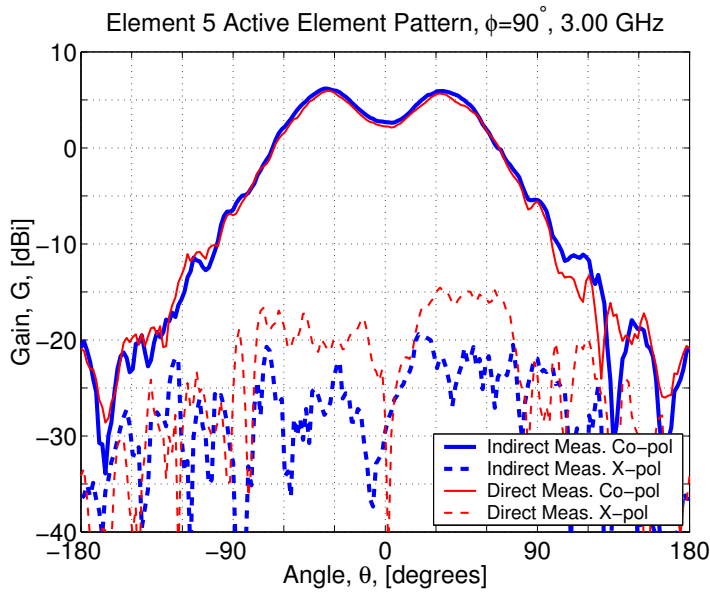


(b)  $\phi = 90^\circ$  cut

**Figure 6.11** Comparison of indirectly and directly measured active-element gain patterns for element 3 at 3 GHz in  $\phi = 0^\circ$  and  $90^\circ$  planes.



(a)  $\phi = 0^\circ$  cut



(b)  $\phi = 90^\circ$  cut

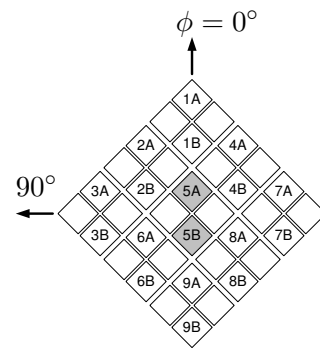


**Figure 6.12** Comparison of indirectly and directly measured active-element gain patterns for element 5 at 3 GHz in  $\phi = 0^\circ$  and  $90^\circ$  planes.

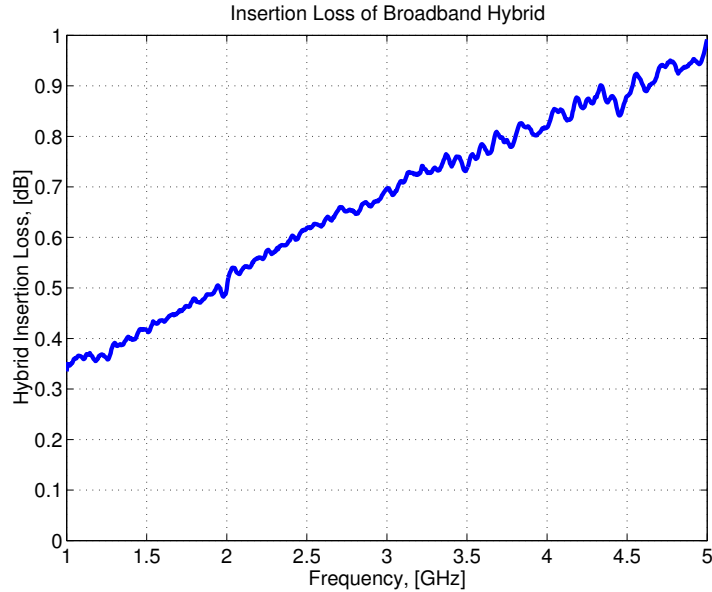


**Figure 6.13** Measured insertion loss as a function of frequency between 1 to 5 GHz of a 180 degree broadband hybrid that is configured as a broadband balun as shown in Fig. 6.2(a).

peak. The cross-polarization component of the active-element patterns also compare well when their values are close to the co-polarization component such as the cases for the elements 1 and 2 in  $\phi = 90^\circ$  plane and for the elements 2 and 3 in  $\phi = 0^\circ$  plane. As is typically the case for antenna measurements, the cross polarization patterns for the element 5 show less agreement than the co-polarization patterns.

Although comparison plots for all cases are not included in this dissertation, the directly measured and indirectly measured active-element patterns agree well for all nine Foursquare elements in the array at multiple frequencies. These results serve to validate the S-parameter network model based array analysis technique and to verify the accuracy of the measured data. The agreement also adds confidence that the directly measured results are accurate. We can confidently use the analysis technique and the measured data to evaluate the performance of the Foursquare array. In the next section, the active-element patterns of the Foursquare test array will be further evaluated.

### 6.3.2 Evaluation of Active-Element Patterns

In the previous section, we demonstrated the verification of the indirect method to compute active-element patterns of the Foursquare array using measured S-parameters and unbalanced-fed element patterns. This section presents further evaluation of active-element patterns of the Foursquare test array using the indirectly measured active-element patterns. Similar to the previous section, a broadband  $180^\circ$  hybrid was used as the balun to feed the elements. The unexcited array elements were terminated with  $50\ \Omega$  loads. Measured S-parameters of the broadband hybrid and  $50\ \Omega$  loads were used to form the feed network S-matrix to solve for the indirectly measured active-element patterns.

A composite plot of active-element patterns for all nine elements of the Foursquare array test article is shown in Fig. 6.14 for  $\phi = 0^\circ$  plane cuts and Fig. 6.15 for  $\phi = 90^\circ$  cuts. The active element patterns are similar to a dipole with a narrower pattern in the plane along the direction of the current flow in the element ( $\phi = 0^\circ$ , E-plane), and a broader pattern in the perpendicular plane ( $\phi = 90^\circ$ , H-plane). The active-element patterns of the Foursquare array show significant changes from element to element, signifying strong edge element effects. However, the element patterns also show symmetry for elements in a similar environment. For example, Elements 2, 4, 6 and 8 show very similar patterns for both co-polarization and cross-polarization patterns. Elements 1 and 9, and elements 3 and 7 also show the symmetry as expected. The results suggest that we may be able to reduce the number of active-element pattern measurements by utilizing symmetry in the array geometry.

The frequency variations of the active-element patterns for the center element (Element 5) of the Foursquare array were also evaluated. Figure 6.16 shows the results of indirectly measured active-element patterns of Element 5 in  $\phi = 0^\circ$  and  $\phi = 90^\circ$  plane cuts for frequencies between 2 to 4 GHz in 250 MHz steps. The plots show that the active-element patterns have a broadside ( $\theta = 0^\circ$ ) null in  $\phi = 0^\circ$  plane between 2.75 GHz to 3.0 GHz and in  $\phi = 90^\circ$  plane between 2.5 GHz to 3.5 GHz. Also, deep nulls are shown in  $\phi = 90^\circ$  plane at 3.75 GHz near  $\theta = \pm 30^\circ$ . These active-element pattern degradations were identified independently in experimental measurements and simulation studies conducted by Harris Corp. [76]. Also, FDTD simulation studies of a  $3 \times 3$  Foursquare array conducted by

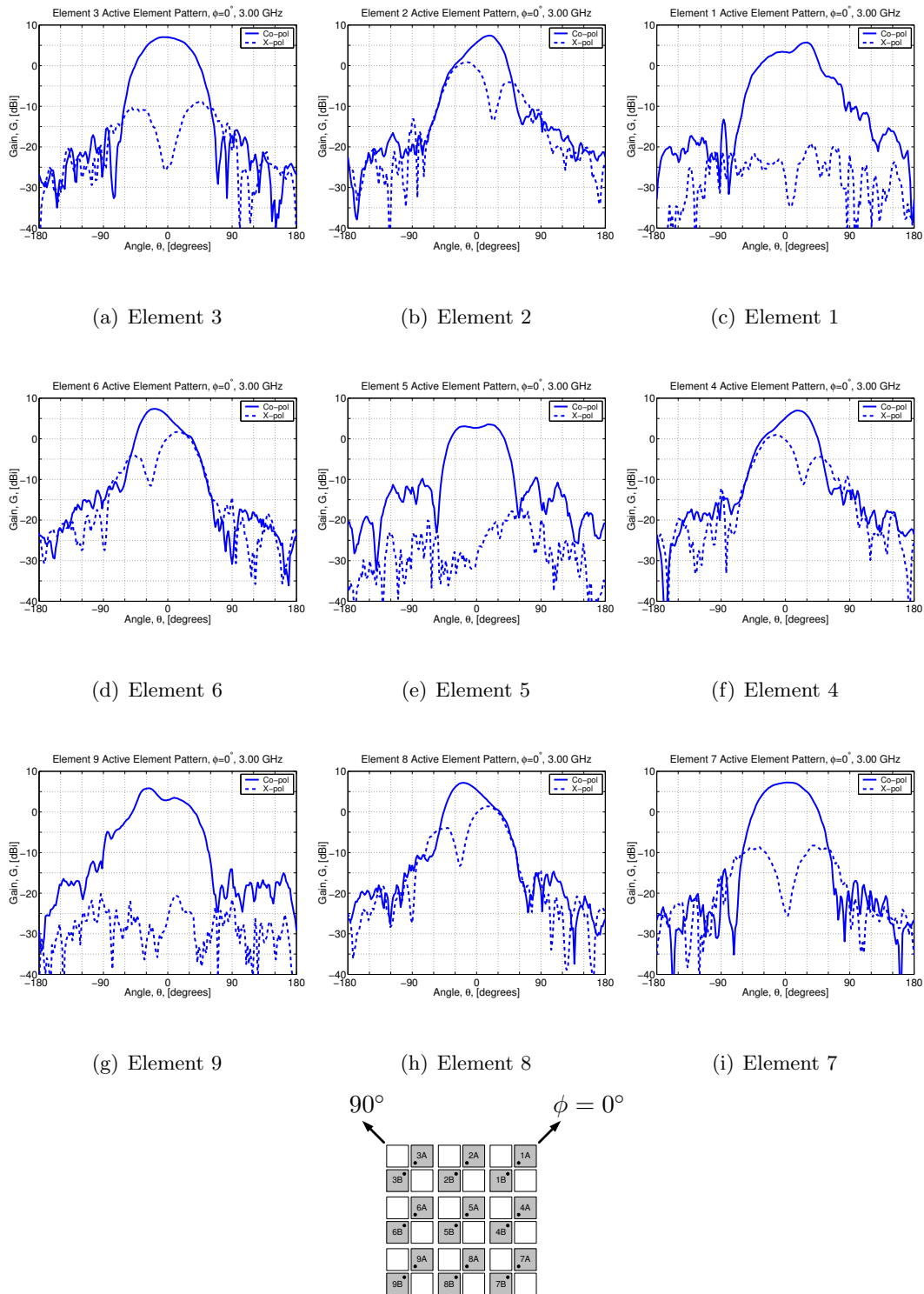


**Figure 6.14** Composite plots of indirectly measured active-element patterns of  $3 \times 3$  Foursquare array of Fig. 6.1 in  $\phi = 0^\circ$  plane at 3 GHz

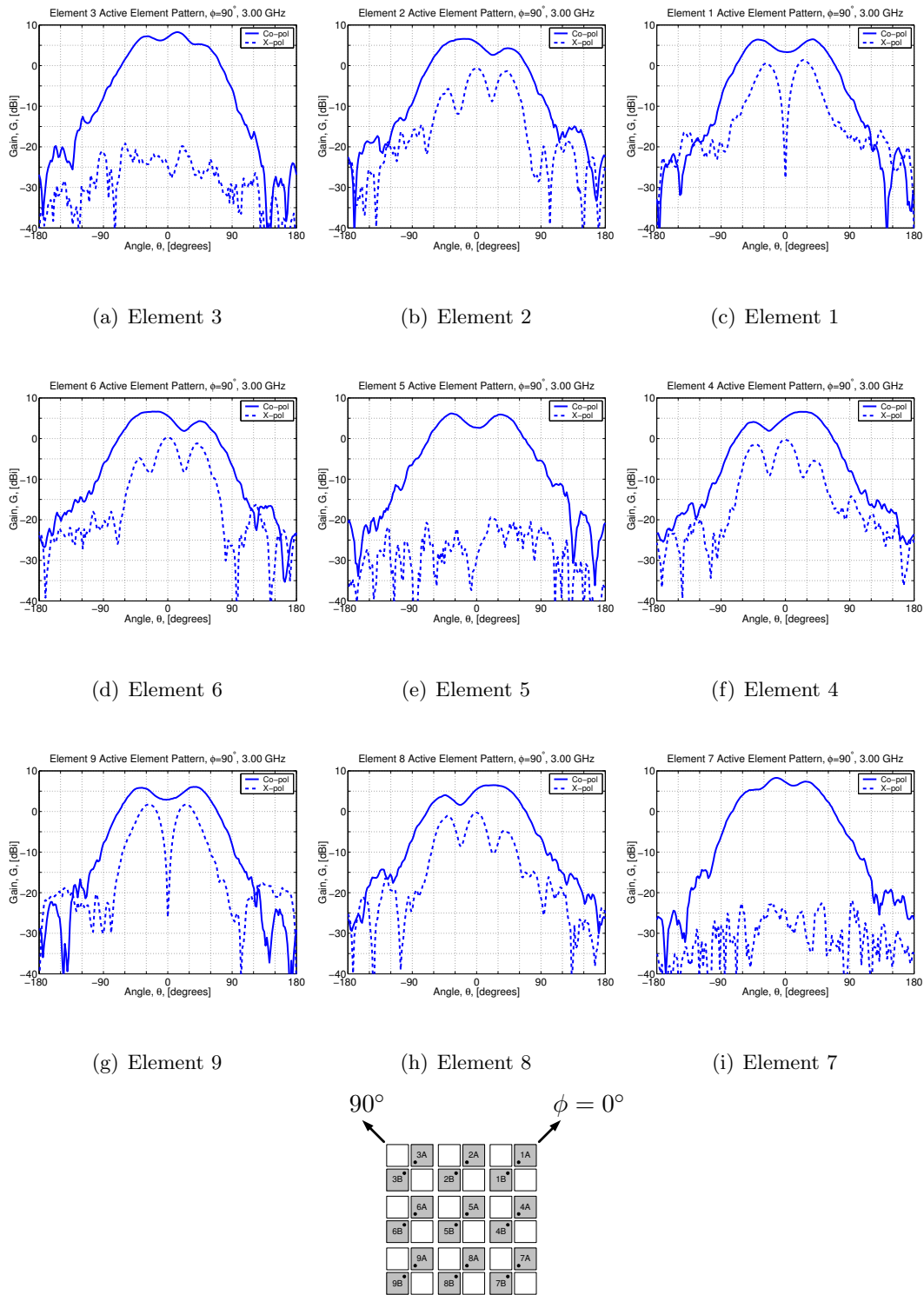
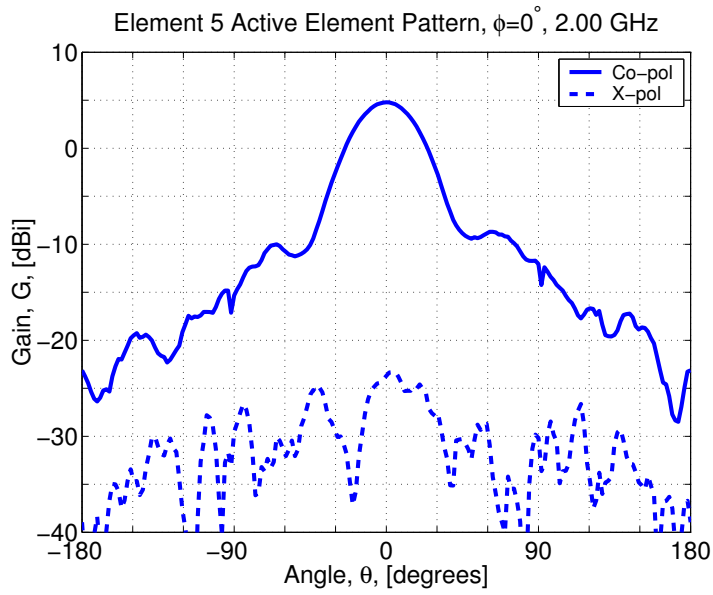
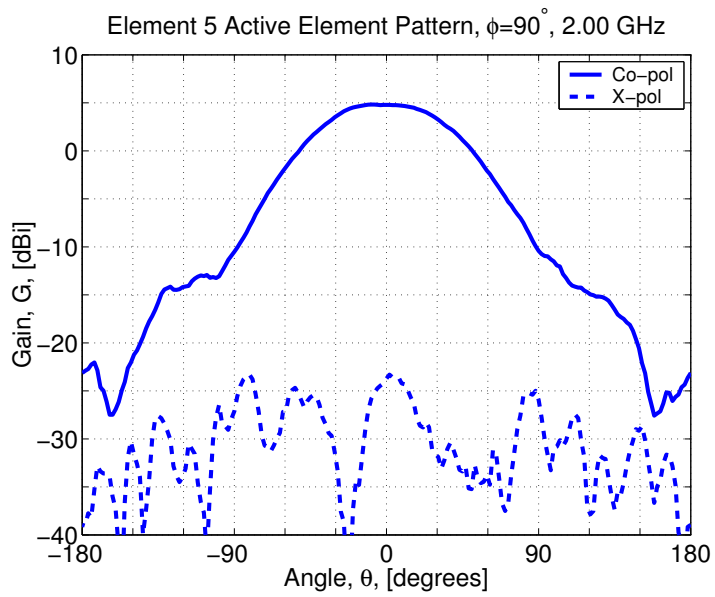


**Figure 6.15** Composite plots of indirectly measured active-element patterns of  $3 \times 3$  Foursquare array of Fig. 6.1 in  $\phi = 90^\circ$  plane at 3 GHz

Buxton [6] predicted similar pattern degradations.



(a) 2.0 GHz,  $\phi = 0^\circ$



(b) 2.0 GHz,  $\phi = 90^\circ$

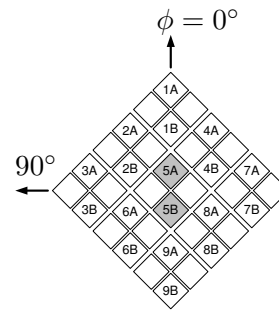
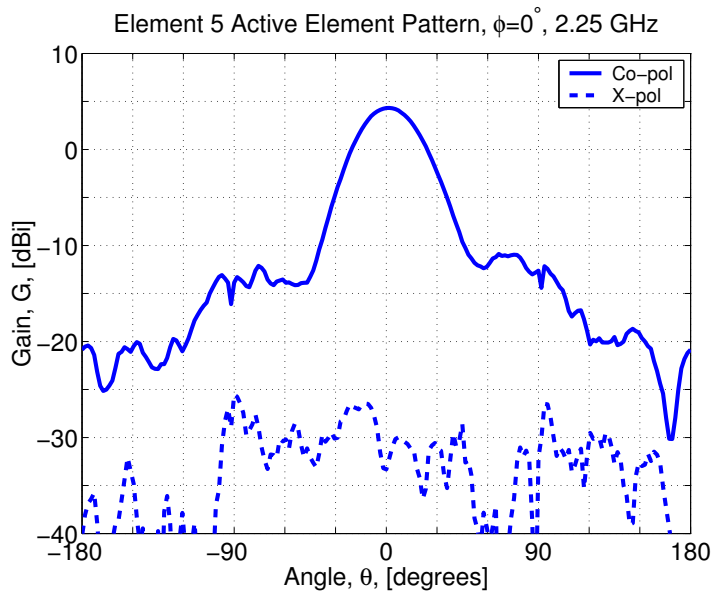
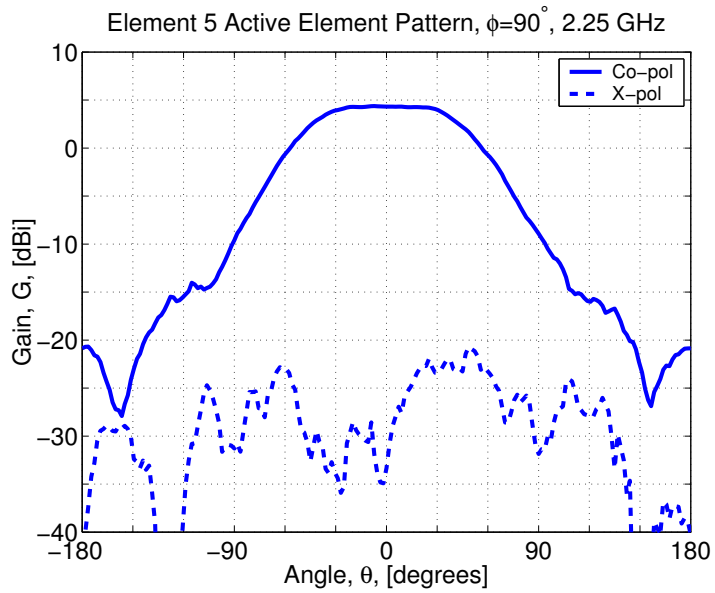


**Figure 6.16** Variations in the indirectly measured active-element patterns for the element 5 of  $3 \times 3$  Foursquare array of Fig. 6.1 in  $\phi = 0^\circ$  plane for the frequencies between 2 GHz to 4 GHz in 250 MHz steps.



(c) 2.25 GHz,  $\phi = 0^\circ$



(d) 2.25 GHz,  $\phi = 90^\circ$

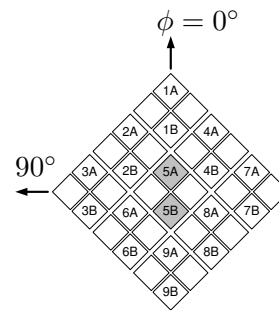
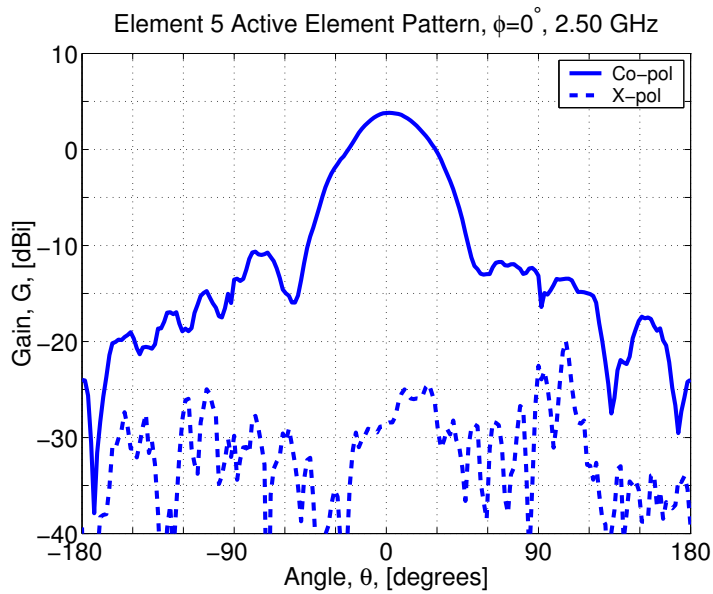
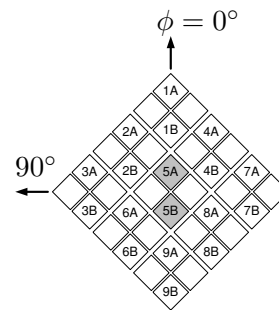
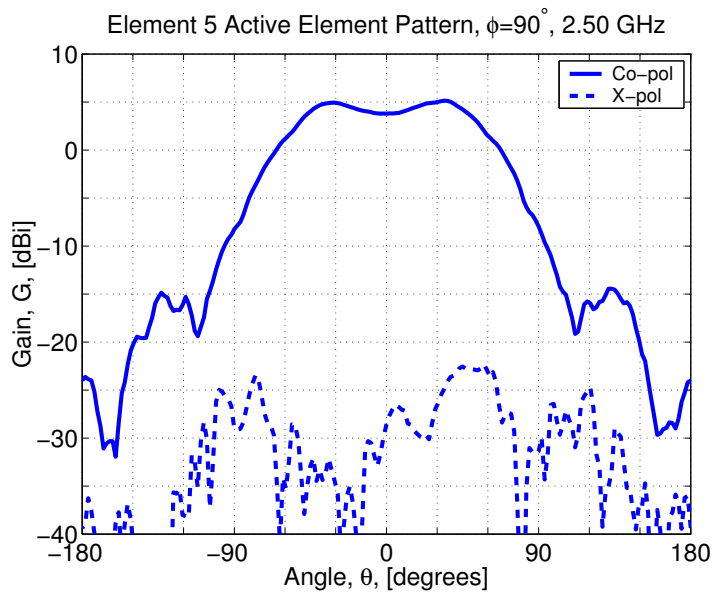


**Figure 6.16** Variations in the indirectly measured active-element patterns for the element 5 of  $3 \times 3$  Foursquare array of Fig. 6.1 in  $\phi = 0^\circ$  plane for the frequencies between 2 GHz to 4 GHz in 250 MHz steps. (Cont.)

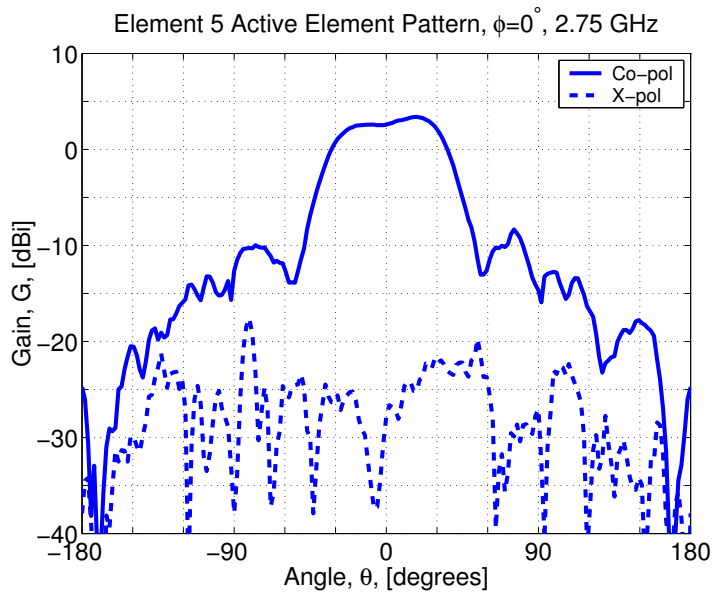


(e) 2.50 GHz,  $\phi = 0^\circ$

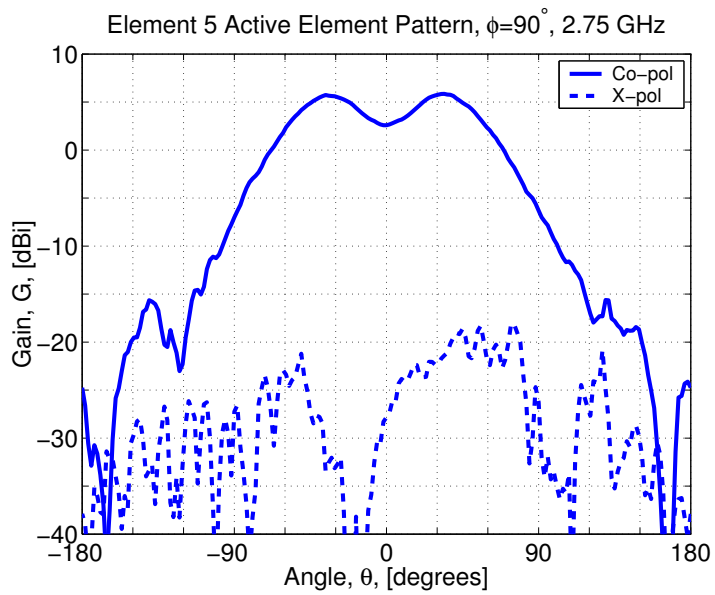


(f) 2.50 GHz,  $\phi = 90^\circ$

**Figure 6.16** Variations in the indirectly measured active-element patterns for the element 5 of  $3 \times 3$  Foursquare array of Fig. 6.1 in  $\phi = 0^\circ$  plane for the frequencies between 2 GHz to 4 GHz in 250 MHz steps. (Cont.)

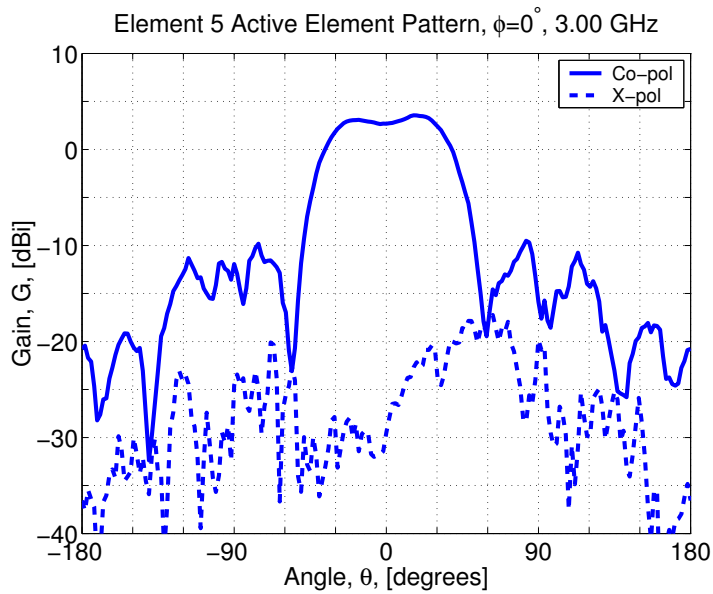


(g) 2.75 GHz,  $\phi = 0^\circ$

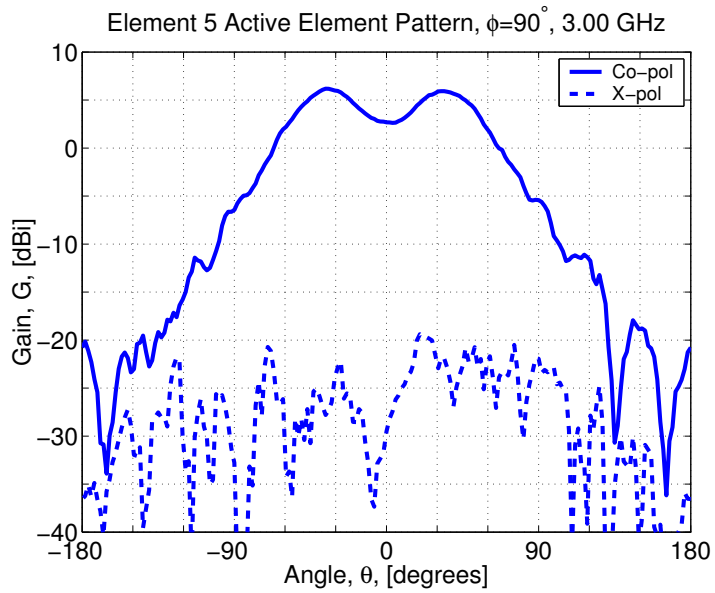


(h) 2.75 GHz,  $\phi = 90^\circ$

**Figure 6.16** Variations in the indirectly measured active-element patterns for the element 5 of  $3 \times 3$  Foursquare array of Fig. 6.1 in  $\phi = 0^\circ$  plane for the frequencies between 2 GHz to 4 GHz in 250 MHz steps. (Cont.)



(i) 3.00 GHz,  $\phi = 0^\circ$



(j) 3.00 GHz,  $\phi = 90^\circ$

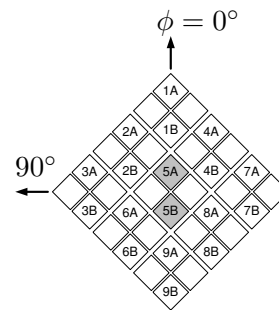
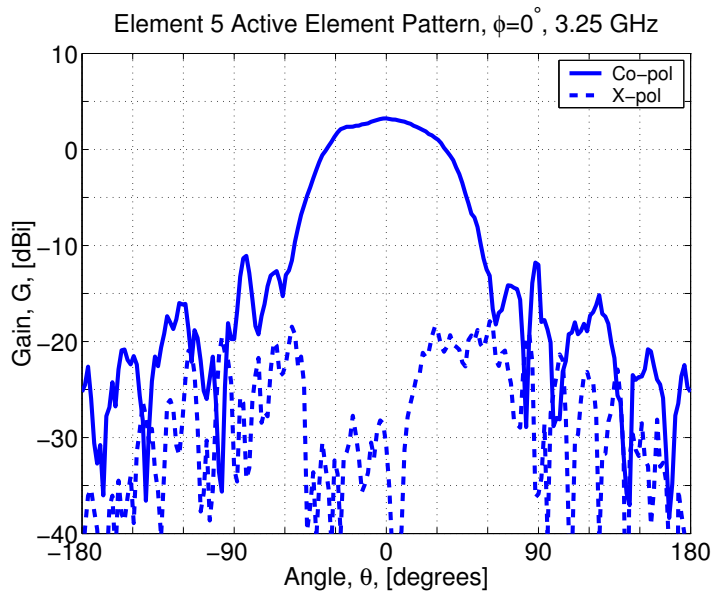
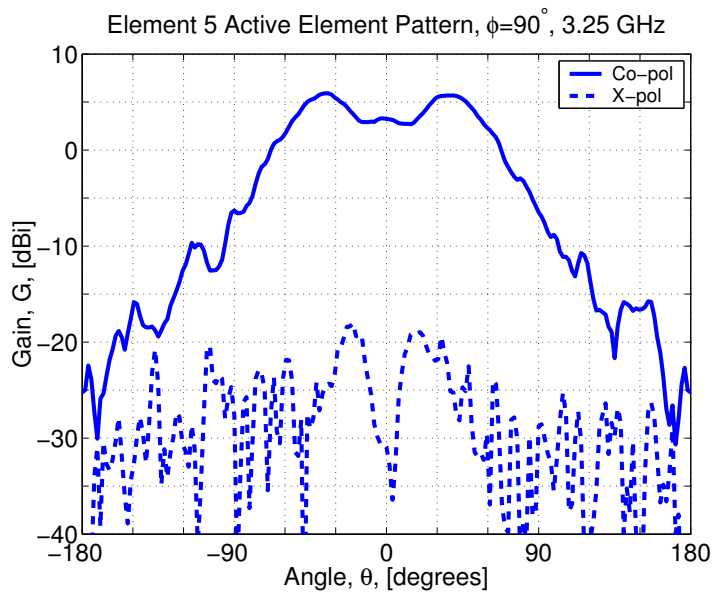


**Figure 6.16** Variations in the indirectly measured active-element patterns for the element 5 of  $3 \times 3$  Foursquare array of Fig. 6.1 in  $\phi = 0^\circ$  plane for the frequencies between 2 GHz to 4 GHz in 250 MHz steps. (Cont.)



(k) 3.25 GHz,  $\phi = 0^\circ$



(l) 3.25 GHz,  $\phi = 90^\circ$

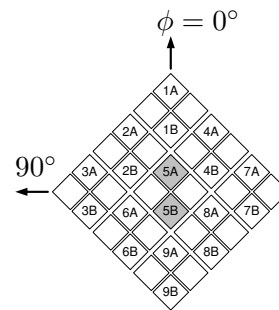
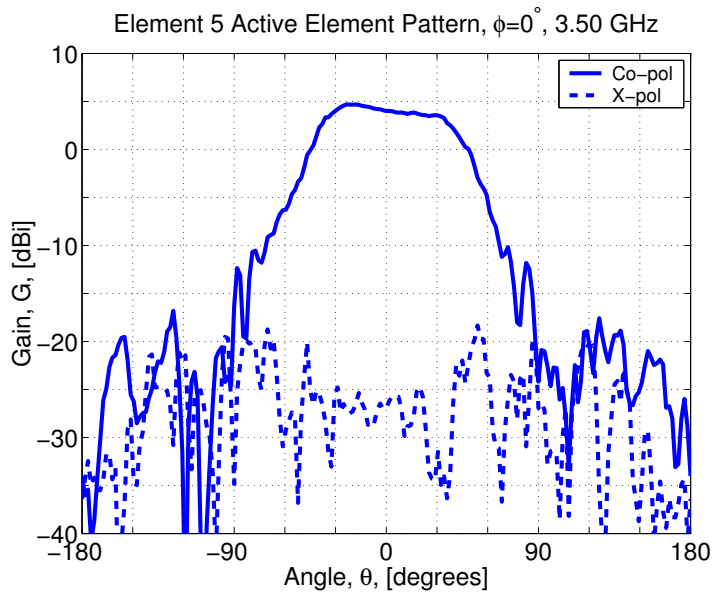
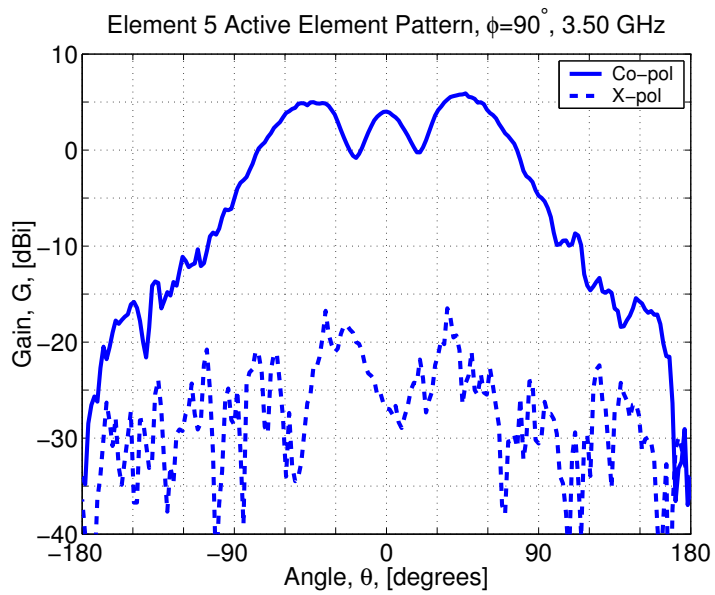


**Figure 6.16** Variations in the indirectly measured active-element patterns for the element 5 of  $3 \times 3$  Foursquare array of Fig. 6.1 in  $\phi = 0^\circ$  plane for the frequencies between 2 GHz to 4 GHz in 250 MHz steps. (Cont.)



(m) 3.5 GHz,  $\phi = 0^\circ$



(n) 3.5 GHz,  $\phi = 90^\circ$

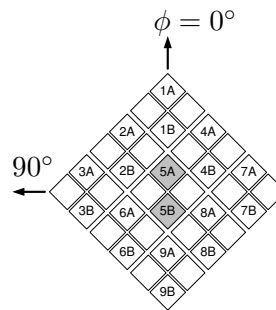
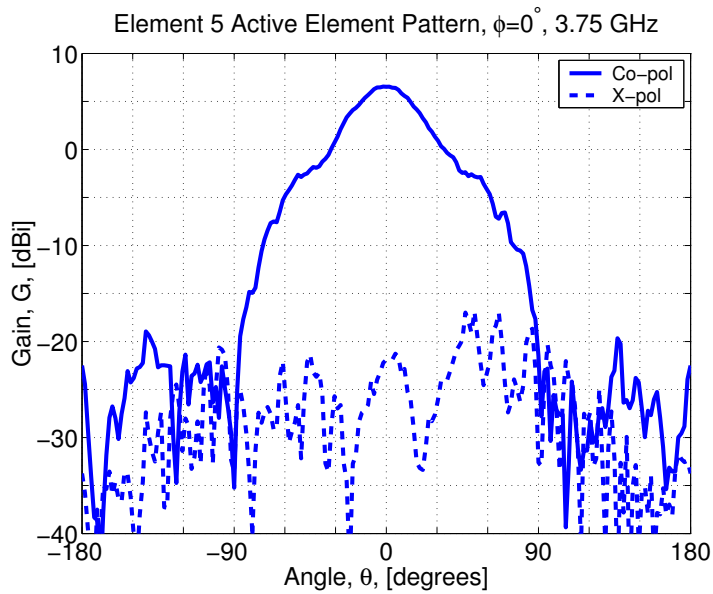
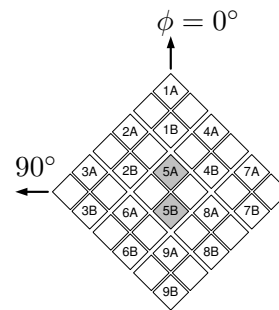
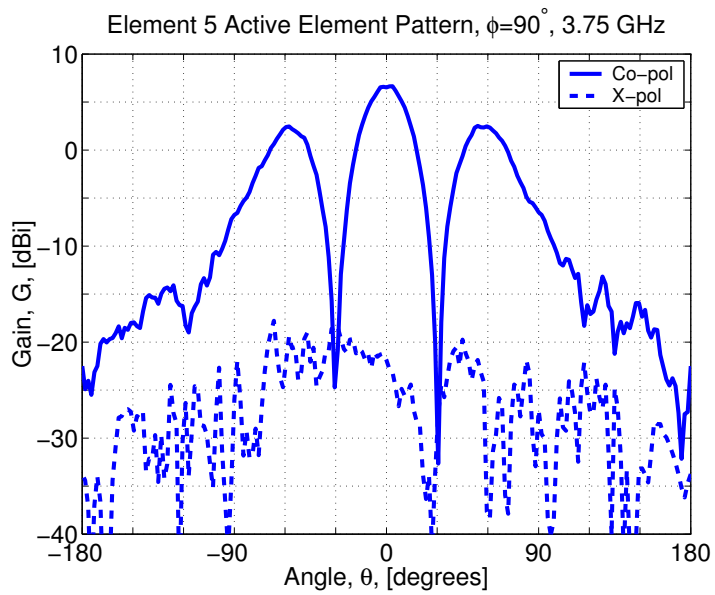


**Figure 6.16** Variations in the indirectly measured active-element patterns for the element 5 of  $3 \times 3$  Foursquare array of Fig. 6.1 in  $\phi = 0^\circ$  plane for the frequencies between 2 GHz to 4 GHz in 250 MHz steps. (Cont.)

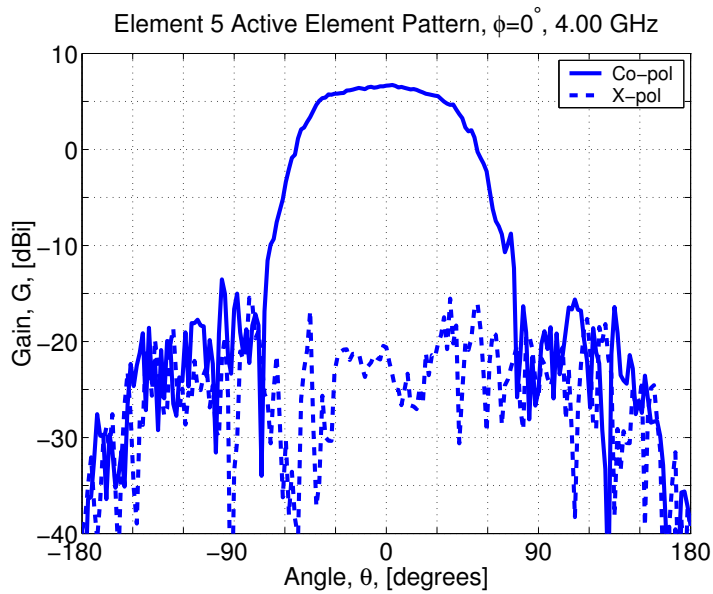


(o) 3.75 GHz,  $\phi = 0^\circ$

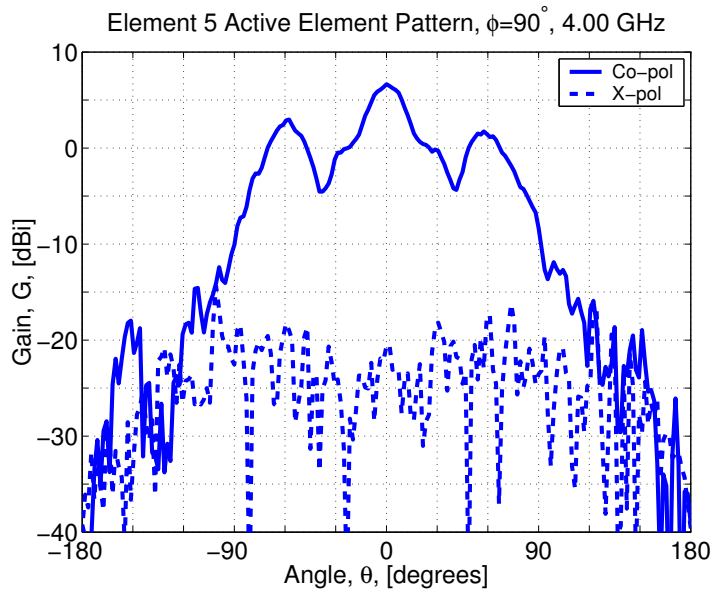


(p) 3.75 GHz,  $\phi = 90^\circ$

**Figure 6.16** Variations in the indirectly measured active-element patterns for the element 5 of  $3 \times 3$  Foursquare array of Fig. 6.1 in  $\phi = 0^\circ$  plane for the frequencies between 2 GHz to 4 GHz in 250 MHz steps. (Cont.)



(q) 4.0 GHz,  $\phi = 0^\circ$



(r) 4.0 GHz,  $\phi = 90^\circ$

**Figure 6.16** Variations in the indirectly measured active-element patterns for the element 5 of  $3 \times 3$  Foursquare array of Fig. 6.1 in  $\phi = 0^\circ$  plane for the frequencies between 2 GHz to 4 GHz in 250 MHz steps. (Cont.)

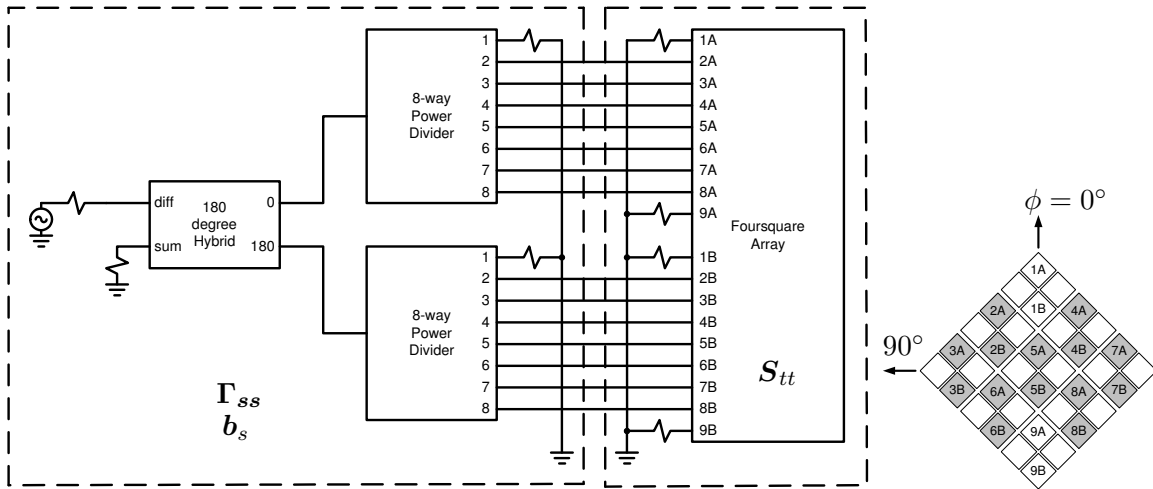
### 6.3.3 Comparison of Indirectly and Directly Measured Array Patterns

In Sec. 6.3.1, we demonstrated the validation of S-parameter network-based array analysis by comparing the indirectly measured active-element patterns (AEP) of  $3 \times 3$  Foursquare array with the directly measured active-element patterns. The indirectly measured active-element gain patterns were determined by (4.66) using measured unbalanced-fed active-element patterns and measured S-parameters of the array and the broadband  $180^\circ$  hybrid.

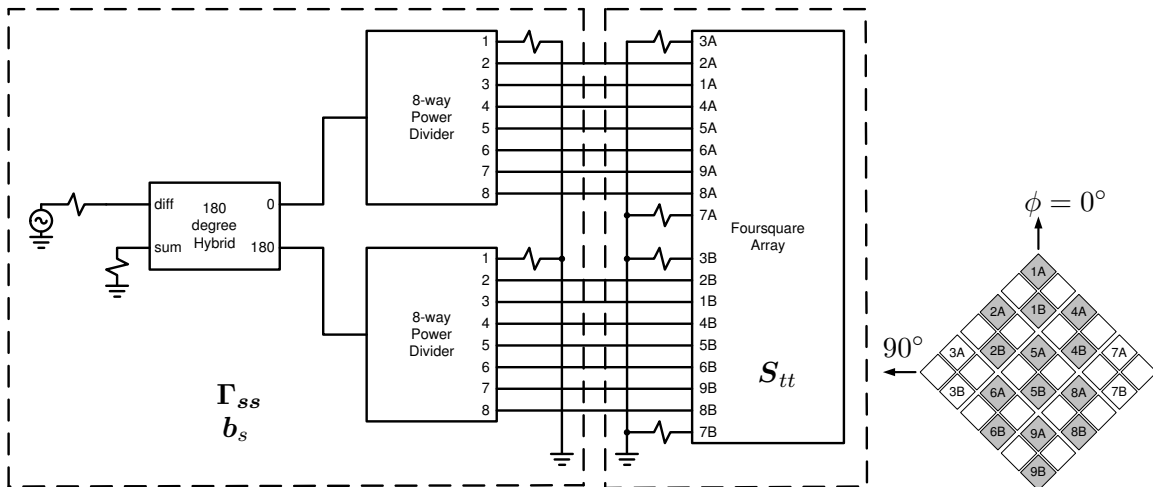
In this section, the validation of the S-parameter network-based array analysis is extended by comparing indirectly-measured, fully-excited Foursquare array with the directly-measured array patterns. Full excitation of the array would require a feed network with nine-way power divider. However, a nine-way power divider is not commercially available as a off-the-shelf component. For this study, a corporate feed, consisting of two broadband 8-way power dividers and a broadband  $180^\circ$  hybrid, is used to excite the array. Using this corporate feed, we can excite up to eight balanced-fed elements.

Figure 6.17 show schematics of the two array feed configurations used in the study. Using the power divider corporate feed, we excite seven out of nine elements in the array. The shaded elements in the illustrations of Foursquare array in Fig. 6.17 represent the excited elements. Thus, Elements 1 and 9 are unexcited and all other elements are fed with uniform excitation in Configuration 1. Similarly, Elements 3 and 7 are unexcited and all other elements are fed with uniform excitation in Configuration 2. The unexcited array elements are terminated with  $50\Omega$  loads as shown in the schematics. Configuration 1 creates the environment very similar to that for the H-plane of a fully excited array, and Configuration 2 for the E-plane of the fully excited array.

Figures 6.18 and 6.19 show the array radiation gain patterns of the Foursquare array in  $\phi = 0^\circ, 45^\circ, 90^\circ$  and  $135^\circ$  plane cuts measured at 3 GHz. Comparison of indirectly measured and directly measured array patterns show good match for both co-polarization and cross-polarization components for Configurations 1 and 2. Nearly all pattern features are reproduced. We should also note that peak gain values which are more difficult to match than relative pattern shapes, are predicted very well. Deviations in the gain values are typically less than 0.5 dB out to 15 dB down from the pattern peak. We also note that the  $45^\circ$  plane cut patterns are very similar as they should be due to symmetry. This



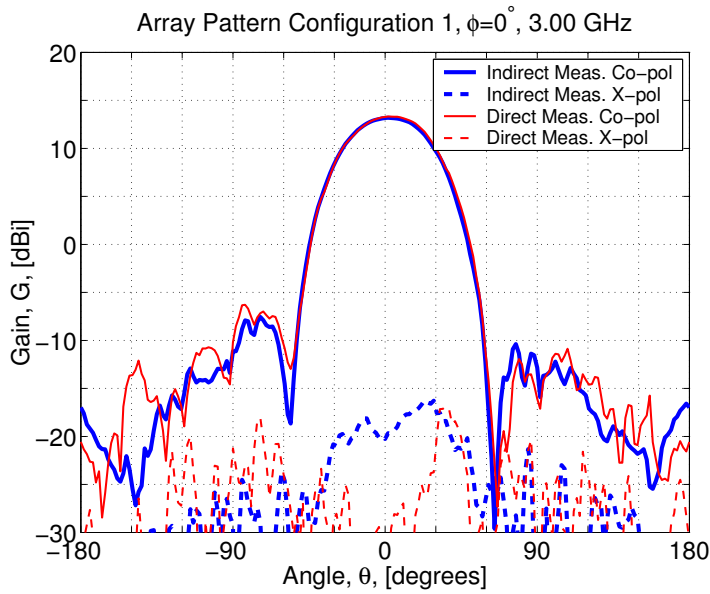
(a) Configuration 1



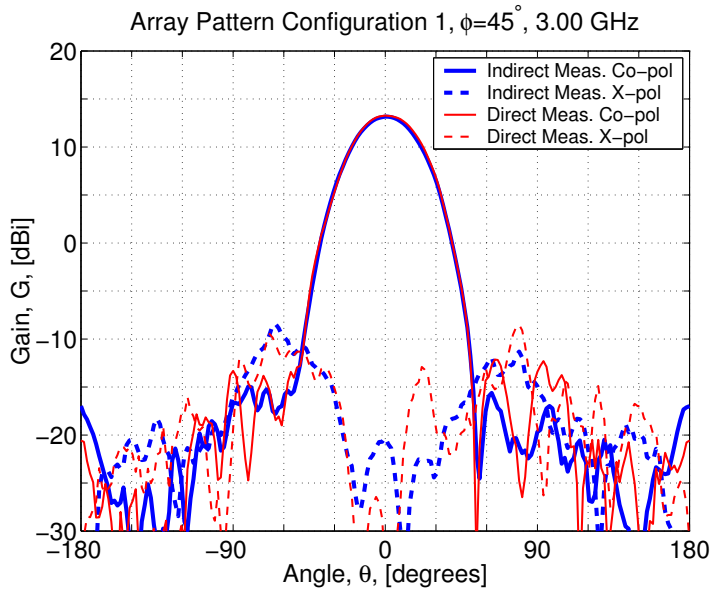
(b) Configuration 2

**Figure 6.17** Schematics of fully excited Foursquare array feed configurations using two broadband 1:8 power dividers and a broadband 180° hybrid. The shaded elements on the Foursquare array illustrations represent excited elements. (a) Configuration 1: elements 1 and 9 are unexcited, (b) Configuration 2: elements 3 and 7 are unexcited.

indicates that the fully excited array environment is being created.



(a)  $\phi = 0^\circ$  cut



(b)  $\phi = 45^\circ$  cut

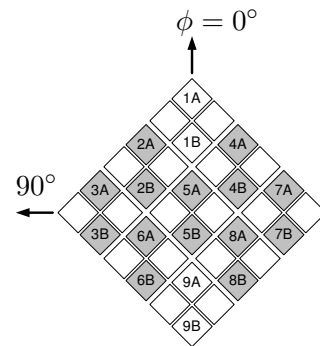
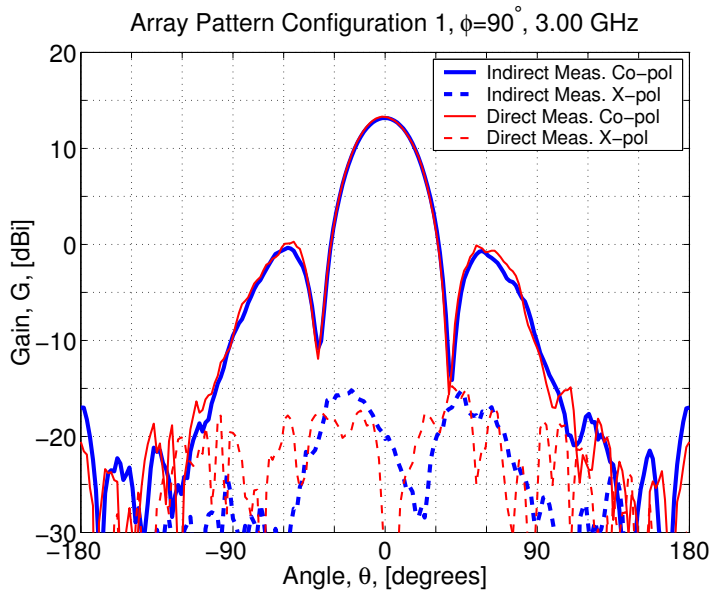
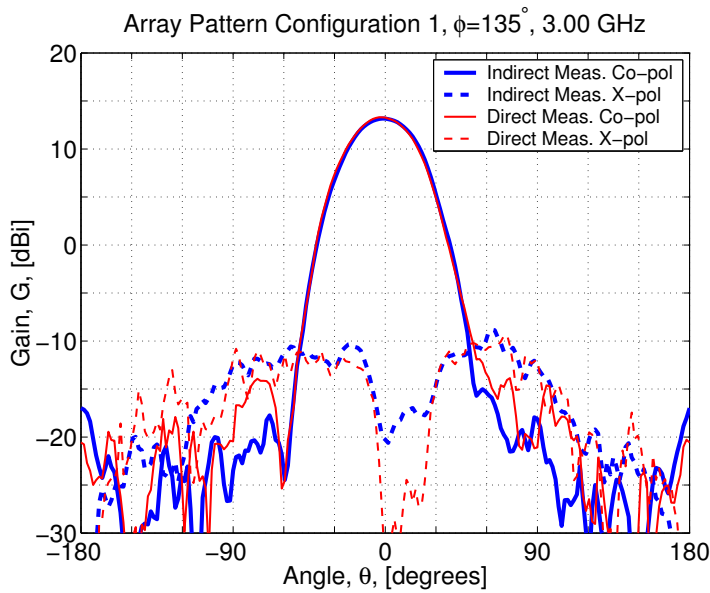


**Figure 6.18** Comparison of indirectly and directly measured co-pol and cross-pol patterns of the Foursquare array shown in Fig. 6.1 fed by broadband power dividers and a broadband  $180^\circ$  hybrid feed network in Configuration 1 shown Fig. 6.17(a).



(c)  $\phi = 90^\circ$  cut



(d)  $\phi = 135^\circ$  cut

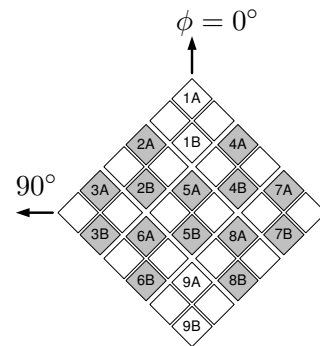
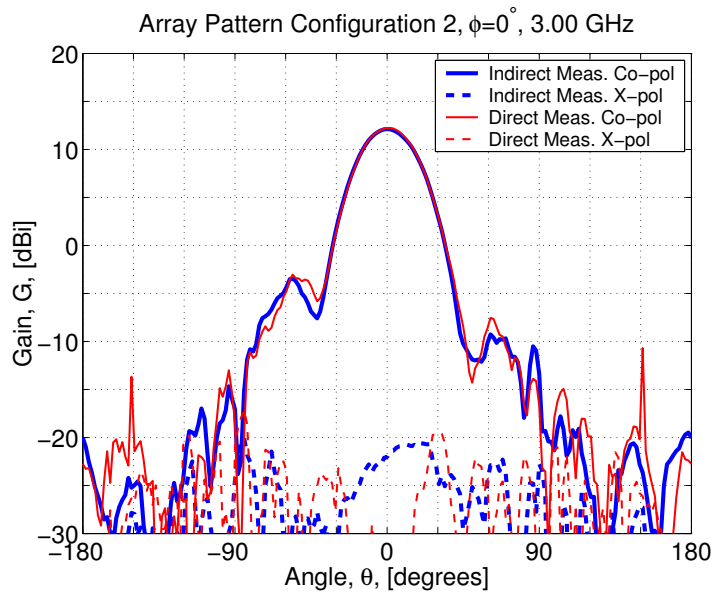
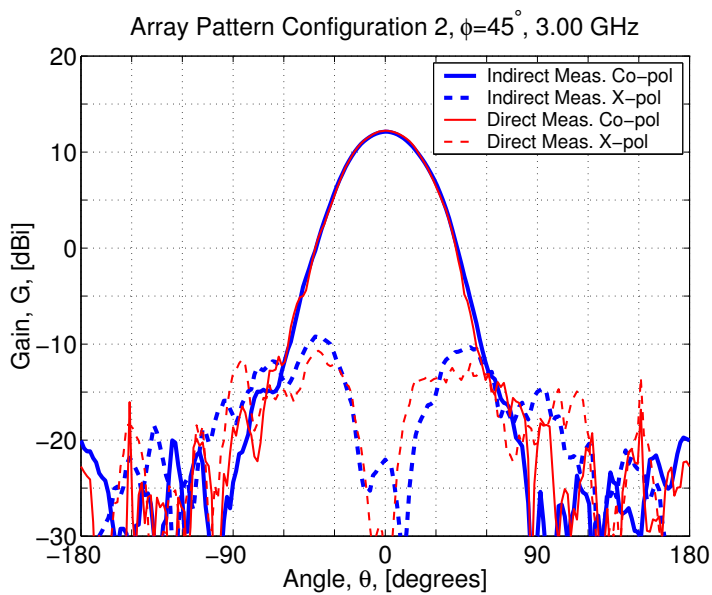


**Figure 6.18** Comparison of indirectly and directly measured co-pol and cross-pol patterns of the Foursquare array shown in Fig. 6.1 fed by broadband power dividers and a broadband  $180^\circ$  hybrid feed network in Configuration 1 shown Fig. 6.17(a). (Cont.)



(a)  $\phi = 0^\circ$  cut



(b)  $\phi = 45^\circ$  cut

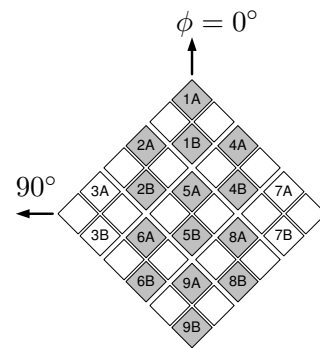
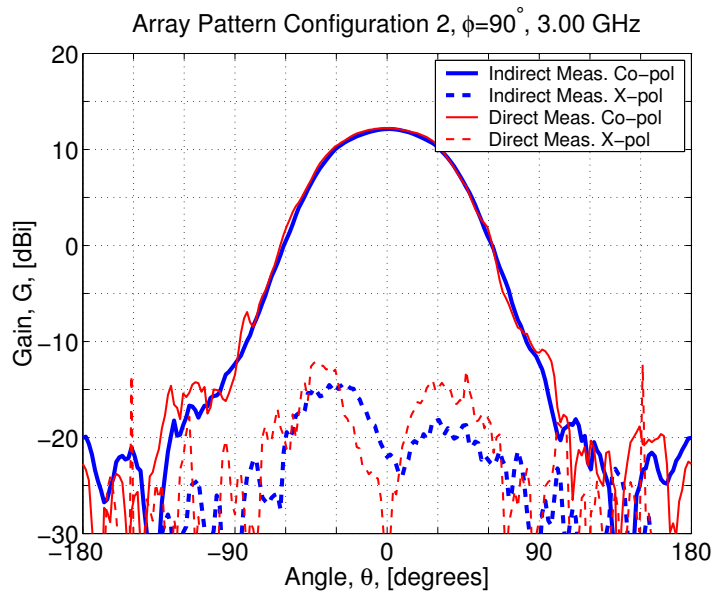
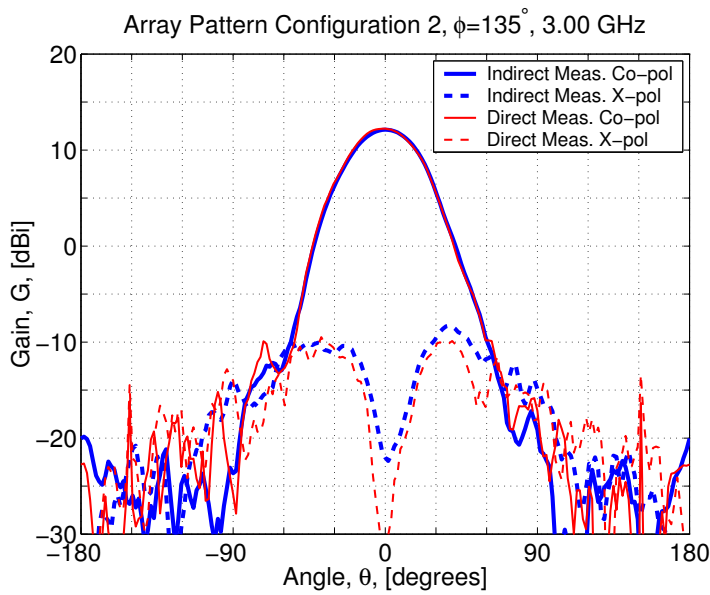


**Figure 6.19** Computed co-pol and cross-pol patterns of the Foursquare array shown in Fig. 6.1 fed by broadband power dividers and a broadband  $180^\circ$  hybrid feed network in Configuration 2 shown Fig. 6.17(b).



(c)  $\phi = 90^\circ$  cut



(d)  $\phi = 135^\circ$  cut

**Figure 6.19** Computed co-pol and cross-pol patterns of the Foursquare array shown in Fig. 6.1 fed by broadband power dividers and a broadband  $180^\circ$  hybrid feed network in Configuration 2 shown Fig. 6.17(b).

### 6.3.4 Analysis of Foursquare Array with Ideal Hybrid Feed

This section will demonstrate the use of S-parameter based network models for a hypothetical study of array systems with an idealized feed network configuration. When S-parameters of the array,  $\mathbf{S}_{tt}$ , and their element patterns,  $\mathbf{S}_{pt}(\theta, \phi)$ , are known, we can determine the fully-excited array pattern for given S-parameters of the feed network,  $\mathbf{\Gamma}_{ss}$ , and an incident wave vector induced by the sources,  $\mathbf{b}_s$ . The feed network S-parameters can be determined from measurements, such as the cases in Sec. 6.3.3, or it can be determined from a numerical model as it is demonstrated in this section.

As an example of a hypothetical array feed study, consider the  $3 \times 3$  Foursquare array of Fig. 6.1 fed with nine ideal 180 degree hybrids as broadband baluns. A schematic of the array with hybrids is shown in Fig. 6.20. A combined circuit of Foursquare elements and hybrids are treated as an array network in the model, and it is represented by a  $9 \times 9$  S-parameter matrix,  $\mathbf{S}_{tt}$  which is determined from the S-matrices of the Foursquare elements and the ideal hybrids. The S-parameter matrix of an ideal 180 degree hybrid,  $\mathbf{S}_H$ , is given by[77]

$$\mathbf{S}_H = \frac{-1i}{\sqrt{2}} \begin{bmatrix} 0 & 1 & -1 & 0 \\ 1 & 0 & 0 & 1 \\ -1 & 0 & 0 & 1 \\ 0 & 1 & 1 & 0 \end{bmatrix}. \quad (6.3)$$

where port numbers are defined in Fig. 6.21(a). For example,  $S_{H_{11}} = 0$  for the port 1 indicates a perfect match. When the sum port of the hybrid (Port 4) is terminated with an ideal  $50 \Omega$  load as shown in Fig. 6.21(b), (6.3) reduces to a  $3 \times 3$  S-matrix for an idealized balun,

$$\mathbf{S}_B = \frac{-1i}{\sqrt{2}} \begin{bmatrix} 0 & 1 & -1 \\ 1 & 0 & 0 \\ -1 & 0 & 0 \end{bmatrix}. \quad (6.4)$$

The combined S-matrix of the Foursquare array and nine idealized baluns was computed using standard network theory. Rather than computing the combined network S-parameters manually, we used ADS [78] which is a microwave CAE software developed by Agilent to compute the new S-matrix.

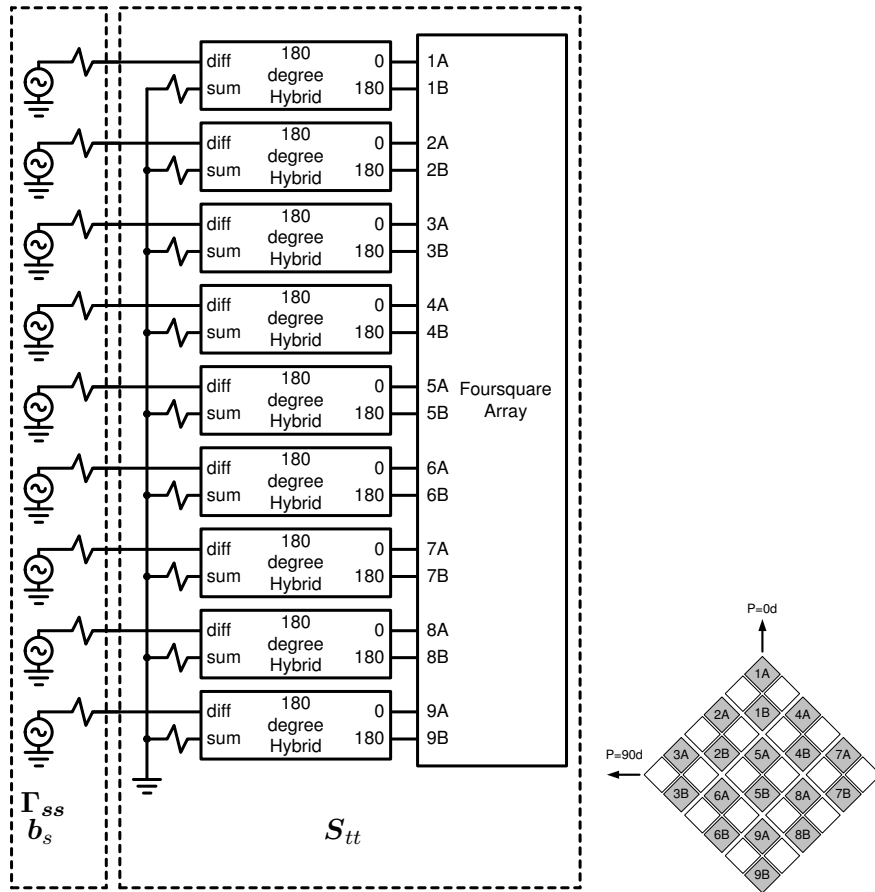


**Figure 6.20** Schematic of fully excited Foursquare array of Fig. 6.20 fed with nine ideal  $180^\circ$  hybrids and nine ideal voltage sources with  $50\ \Omega$  internal impedance. This model is used for numerical simulation to investigate the array impedance bandwidth.

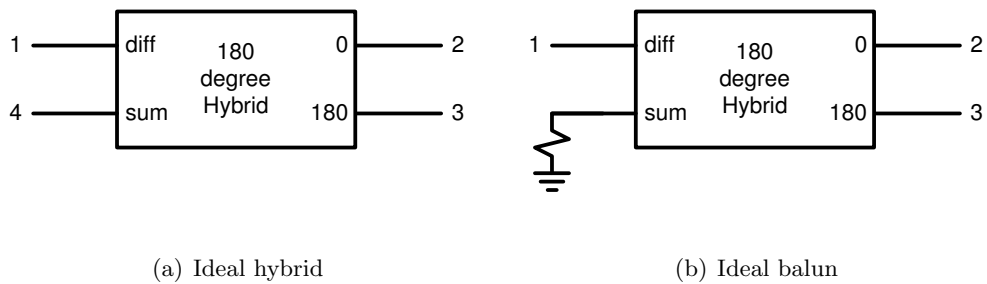


**Figure 6.21** Port number definitions for an ideal  $180^\circ$  hybrid and an ideal balun.

The array is assumed to be fed with nine independent Thevenin equivalent voltage sources with internal impedances of  $Z_S = 50 \Omega$  as indicated in the schematic in Fig. 6.20. Since the sources are independent of each other and they have  $50 \Omega$  internal impedances, the feed network S-parameter,  $\Gamma_{ss}$ , is a  $9 \times 9$  zero matrix. Also, we assume uniform excitation of the array elements, and thus, the impressed source wave vector is given by

$$\mathbf{b}_s = \left[ 1 \ 1 \ 1 \ 1 \ 1 \ 1 \ 1 \ 1 \ 1 \right]^\top \quad (6.5)$$

where  $\top$  is a matrix transpose operator.

We are interested in computing the impedance bandwidth of a uniformly excited Foursquare array. There are many ways to define the frequency bandwidth of an antenna. For this study, we use the conventional definition of bandwidth to be a range of frequencies where voltage standing wave ratio of the array is less than a reference value. Typically, maximum VSWR values of 2 or 3 are used to define an impedance bandwidth. Unlike a single antenna where voltage standing wave ratio (VSWR) is well defined, there are multiple ways to define VSWR of an array system. We will evaluate three types of voltages standing wave ratios: array VSWR, active VSWR, and active-element VSWR.

The first type of VSWR, the *array voltage standing wave ratio* ( $\text{VSWR}_q$ ) is computed from the impedance mismatch factor of the array using

$$\text{VSWR}_q = \frac{1 - \sqrt{1 - q}}{1 + \sqrt{1 - q}} \quad (6.6)$$

where the impedance mismatch factor,  $q$ , is computed for the fully excited array using (4.56). The array  $\text{VSWR}_q$  allows specification of the bandwidth based on the overall impedance matching of the array elements to the source impedances when the array is fully excited with  $\mathbf{b}_s$ . For this example we set  $\mathbf{b}_s$  to a uniform excitation of (6.5), however, the array VSWR analysis is not limited to the uniform excitation. It is possible that some of the array elements actually experience levels of impedance mismatches that differ from array  $q$  value, and thus, their individual impedance bandwidths can be different from the bandwidth based on  $q$ .

Unlike  $\text{VSWR}_q$ , the second and third types of voltage standing wave ratios are computed for each element in the array. The *active voltage standing wave ratio*,  $\text{VSWR}_a$  is

defined from the active S-parameter of an array element  $n$ ,  $S_{a_n}$ , when the array is fully excited with coefficients  $\mathbf{b}_s$  of (6.5). The active S-parameter is determined from the incident wave,  $a_{t_n}$ , and reflected wave,  $b_{t_n}$ , for the array element  $n$  using

$$S_{a_n} = \frac{b_{t_n}}{a_{t_n}}. \quad (6.7)$$

Using the array model developed in Chapter 4, incident and reflected wave vectors for the array elements are given by

$$\mathbf{a}_t = [\mathbf{I} - \mathbf{\Gamma}_{ss}\mathbf{S}_{tt}]^{-1} \mathbf{b}_s \quad (6.8)$$

and

$$\mathbf{b}_t = \mathbf{S}_{tt}\mathbf{a}_t. \quad (6.9)$$

Then, the active VSWR for element  $n$  is computed from the active S-parameter by

$$\text{VSWR}_{a_n} = \frac{1 + |S_{a_n}|}{1 - |S_{a_n}|}. \quad (6.10)$$

For the Foursquare test article fed by nine ideal  $180^\circ$  hybrids, the feed network S-parameter is a zero matrix,

$$\mathbf{\Gamma}_{ss} = \mathbf{0} \quad (6.11)$$

so, (6.8) and (6.9) simplify to

$$\mathbf{a}_t = \mathbf{b}_s \quad (6.12)$$

and

$$\mathbf{b}_t = \mathbf{S}_{tt}\mathbf{b}_s. \quad (6.13)$$

Using the excitation coefficients of a uniformly excited array as given by (6.5), the reflected wave at element  $n$  becomes

$$b_{t_n} = \sum_{j=1}^N S_{t_n t_j}. \quad (6.14)$$

Substituting (6.14) and (6.5) into (6.7) yields the active S-parameter for the element  $n$  as

$$S_{t_n} = \frac{b_{t_n}}{a_{t_n}} = \sum_{j=1}^N S_{t_n t_j}. \quad (6.15)$$

Finally, the active VSWR is obtained by substituting (6.15) into (6.10) giving

$$\text{VSWR}_{a_n} = \frac{1 + \left| \sum_{j=1}^N S_{t_n t_j} \right|}{1 - \left| \sum_{j=1}^N S_{t_n t_j} \right|} \quad (6.16)$$

The third type of VSWR, the *active-element voltage standing wave ratio* or  $\text{VSWR}_{ae}$  is also defined for each element in the array based on active S-parameters. Unlike the active VSWR, the active-element VSWR is determined when element  $n$  is excited, and all other elements in the array are terminated with  $50\ \Omega$  loads. Otherwise the analysis procedure is the same as the procedure for the active VSWR.

In the case of the Foursquare array fed with nine idealized baluns, the source excitation for active-element S-parameter computation is given by

$$b_{s_j} = \begin{cases} 1 & j = n \\ 0 & j \neq n \end{cases}. \quad (6.17)$$

Substituting (6.17) into (6.12) and (6.13) yield

$$a_{t_n} = 1 \quad (6.18)$$

and

$$b_{t_n} = S_{t_n t_n}. \quad (6.19)$$

Thus, the active-element S-parameter is given by

$$S_{t_n} = \frac{b_{t_n}}{a_{t_n}} = S_{t_n t_n}. \quad (6.20)$$

Finally, the active-element VSWR is determined from the active-element S-parameter by

$$\text{VSWR}_{ae_n} = \frac{1 + |S_{t_n t_n}|}{1 - |S_{t_n t_n}|}. \quad (6.21)$$

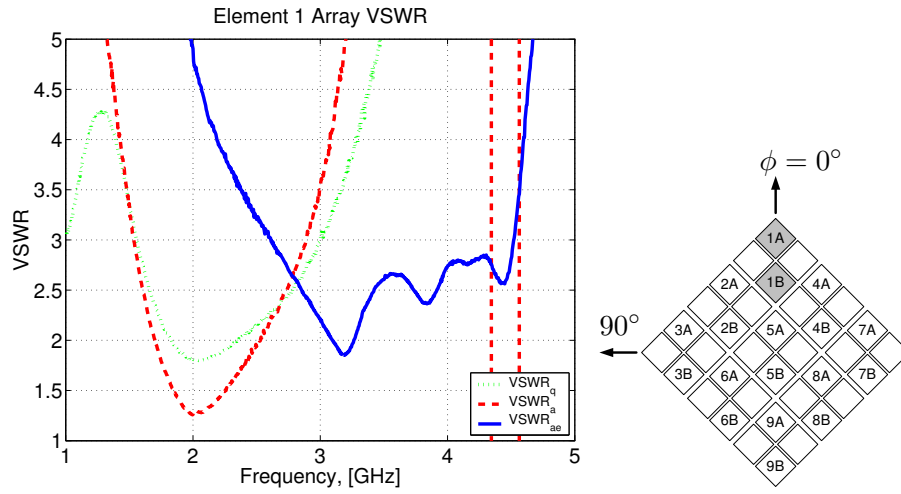
Figure 6.22 shows comparison plots of active-element voltage standing wave ratio,  $\text{VSWR}_{ae_n}$ , active voltage standing wave ratio,  $\text{VSWR}_{a_n}$ , and voltage standing wave ratio based on array impedance mismatch,  $\text{VSWR}_q$  as a function of frequencies between 1 to 5 GHz for Elements 1, 2, 3, and 5 of  $3 \times 3$  Foursquare test article shown in Fig. 6.1. Frequency

bandwidths that are determined from the voltage standing wave ratio plots in Fig. 6.22 for  $VSWR = 2$  and  $VSWR = 3$  are summarized in Table 6.5.

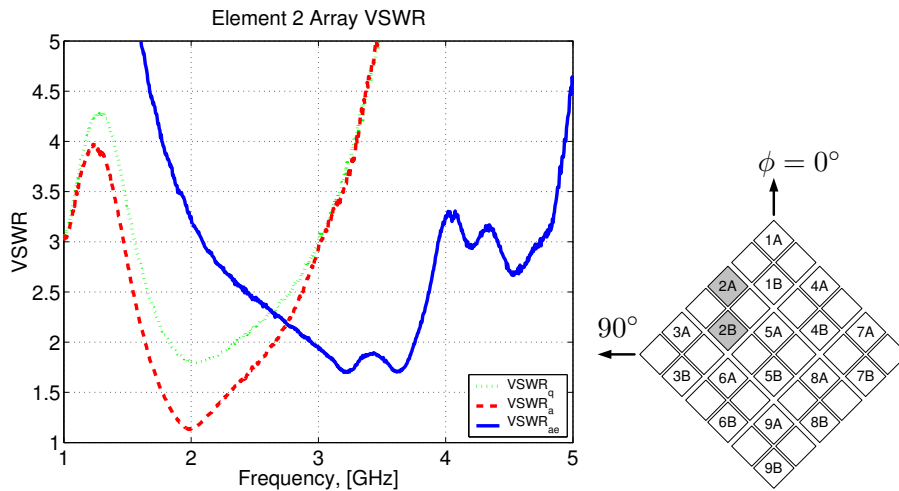
When one element in the array is excited and all other elements are terminated with  $50\ \Omega$  the impedance behavior of the array elements are represented by active-element voltage standing wave ratio of (6.21) and the calculated results are shown by the solid curves in Fig. 6.22. The minimum values for  $VSWR_{ae}$  can be considered as the resonance frequencies of the array elements and occur near 3.2 GHz, for Elements 1, 2, and 3. This frequency is close to the center of the operational bandwidth of the isolated Foursquare element of the same geometry as the array element. On the other hand, the minimum value for Element 5 active-element VSWR occur near 3.7 GHz, indicating that mutual coupling is affecting the resonance frequency of the center element in the array when one element is excited and all other elements are passively terminated.

The active VSWR of the Elements 1, 2, 3, and 5, when the array is uniformly excited, are plotted with dashed curves in Fig. 6.22. The minimum values of active  $VSWR_a$  occur at frequencies lower than the corresponding cases for the active-element  $VSWR_{ae}$ . For Elements 1 and 2, the minimum  $VSWR_a$  occur at 2 GHz, while for Elements 3 and 5, the minimum occur at 2.7 GHz and 1.7 GHz, respectively.

The overall VSWR of the array based on the impedance mismatch factor,  $q$ , of the array are plotted using dotted curves in Fig. 6.22. The minimum value of  $VSWR_q$  occurs at 2 GHz for the uniformly excited Foursquare array. The behavior of  $VSWR_q$  can be considered as an average of active  $VSWR_a$ . In this particular example, the position of minimum  $VSWR_q$  is dominated by the 2 GHz resonance frequency for 6 out of 9 elements in the array (Elements 1, 2, 4, 6, 8, and 9). If we consider one of the active-element patterns as a special case of fully excited array, we can conclude that the operational frequency bands of fully excited highly coupled array are highly dependent on the excitation coefficients of the array elements.

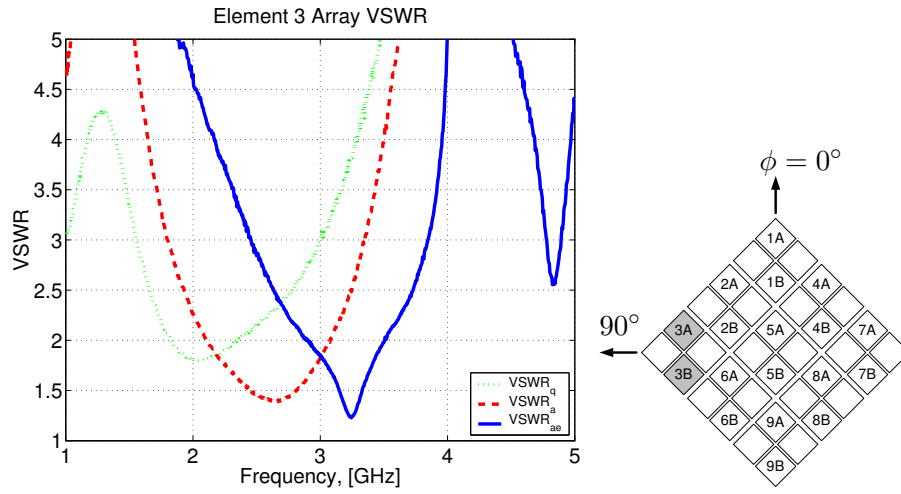


(a) Element 1

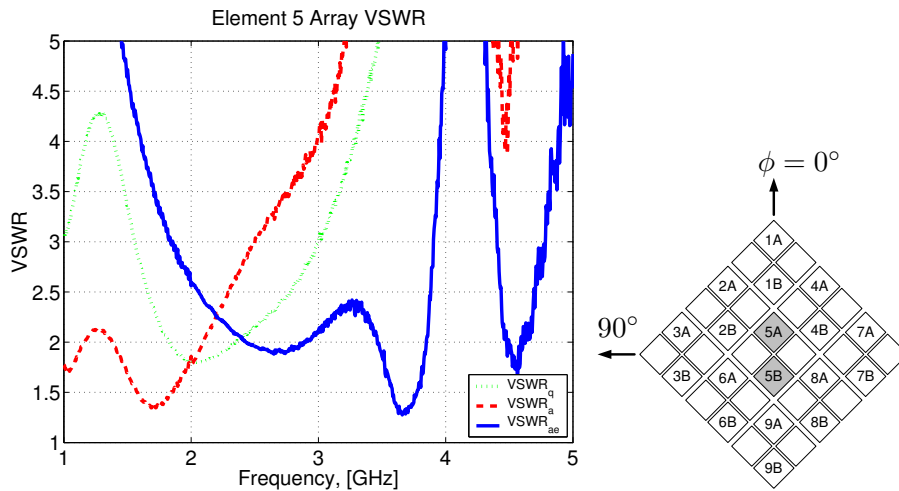


(b) Element 2

**Figure 6.22** Comparison of three voltage standing wave ratio (VSWR) as a function of frequency over a range between 1 to 5 GHz for Foursquare array of Fig. 6.1 fed with nine idealized baluns shown in Fig. 6.20. Solid curves are active-element  $VSWR_{ae}$  referenced to  $50\ \Omega$  computed using (6.21). Dashed curves are active  $VSWR_a$  referenced to  $50\ \Omega$  computed using (6.16). Dotted curves are array  $VSWR_q$  computed using (6.6).



(c) Element 3



(d) Element 5

**Figure 6.22** Comparison of three voltage standing wave ratio (VSWR) as a function of frequency over a range between 1 to 5 GHz for Foursquare array of Fig. 6.1 fed with nine idealized baluns shown in Fig. 6.20. Solid curves are active-element  $VSWR_{ae}$  referenced to  $50\ \Omega$  computed using (6.21). Dashed curves are active  $VSWR_a$  referenced to  $50\ \Omega$  computed using (6.16). Dotted curves are array  $VSWR_q$  computed using (6.6). (Cont.)

**Table 6.5** Summary of resonance frequencies,  $f_R$ , and impedance bandwidths,  $B_p$ , for  $3 \times 3$  Foursquare array of Fig. 6.1 computed based on three definitions of voltage standing wave ratio:  $\text{VSWR}_q$ ,  $\text{VSWR}_a$ , and  $\text{VSWR}_{ae}$ . The minimum values for VSWR are used to estimate the resonance frequencies,  $f_R$ , of the array and elements. The upper and lower cutoff frequencies which are determined from the plots in Fig. 6.22 are shown in columns  $f_U$  and  $f_L$ . The center frequencies,  $f_C$ , are determined by taking the average of  $f_U$  and  $f_L$  using (5.15). Impedance bandwidths,  $B_p$ , are determined using (5.14).

VSWR type	Elements	$f_R$ , GHz	VSWR = 2				VSWR = 3			
			$f_L$ , GHz	$f_U$ , GHz	$f_C$ , GHz	$B_p$ , %	$f_L$ , GHz	$f_U$ , GHz	$f_C$ , GHz	$B_p$ , %
$\text{VSWR}_{ae}$	1, 9	3.18	3.10	3.27	3.19	5.30	2.61	4.52	3.57	53.6
$\text{VSWR}_{ae}$	2, 4, 6, 8	3.20	2.95	3.76	3.33	24.1	2.09	3.94	3.02	61.4
$\text{VSWR}_{ae}$	3, 7	3.23	2.91	3.51	3.21	18.7	2.46	3.85	3.16	44.1
$\text{VSWR}_{ae}$	5	3.66	2.43	2.90	2.67	17.6	1.85	3.91	2.88	71.5
$\text{VSWR}_a$	1, 9	2.01	1.70	2.50	2.10	38.1	1.53	2.89	2.21	61.5
$\text{VSWR}_a$	2, 4, 6, 8	1.99	1.64	2.66	2.15	47.4	1.47	3.02	2.25	69.0
$\text{VSWR}_a$	3, 7	2.66	2.11	3.09	2.60	37.4	1.80	3.35	2.58	60.2
$\text{VSWR}_a$	5	1.71	1.39	2.10	1.75	40.7	< 1.00	2.50	–	–
$\text{VSWR}_q$	All	1.98	1.83	2.35	2.09	24.9	1.56	3.00	2.28	63.2

When array elements are not tightly coupled, the differences between array VSWR, active VSWR, and active-element VSWR become insignificant. As an example, consider a  $3 \times 3$  array of half-wavelength strip dipoles suspended over an infinite ground plane as illustrated in Fig. 6.23. The strip dipoles have element length of  $L = 48$  mm, and strip width of  $W = 2$  mm. The elements are suspended at height,  $h = 25$  mm, over an infinite ground plane. The dipoles are oriented similar to the Foursquare array, and are separated by element-to-element spacing of  $d = 75$  mm from each other. The array is designed to operate at center frequency of 3 GHz, ( $\lambda = 100$  mm). The strip dipole array was simulated using IE3D to compute S-parameters and active-element patterns for the array network analysis.

The array VSWR, active VSWR, and active-element VSWR of the strip dipole array are computed using the same procedures as described for the Foursquare array. Comparison of three types of VSWR for Elements 1, 2, 3, 5 of the strip dipole array is shown in Fig. 6.24. For all four elements, there are some differences between array VSWR, active VSWR, and active-element VSWR curves. However, these differences are much less significant than the results for the tightly coupled Foursquare array case.

The differences in the resonance frequencies and the bandwidths of the array depending on the definition of VSWR complicate the analysis and design of highly coupled arrays. A fully excited array bandwidth should be evaluated based on  $VSWR_q$  which represents the ratio of power accepted by the array to to the available power from sources. In test settings, it is easier to measure the active-element voltage standing wave ratio,  $VSWR_{ae}$ . As the dipole array example demonstrated, traditional arrays with small element mutual coupling can be predicted using active-element VSWR. In case of tightly coupled arrays, the operational band computed based on the active-element VSWR can be quite different from array VSWR. Thus, the bandwidth results based solely on the active-element VSWR can be significantly pessimistic. The actual array performance can be greatly improved over the element results by fully exciting the array.

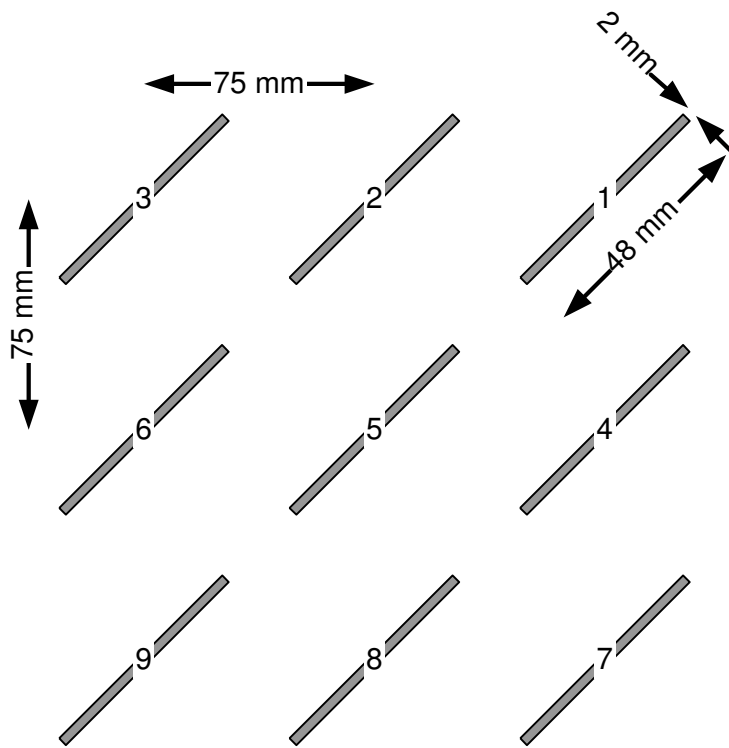
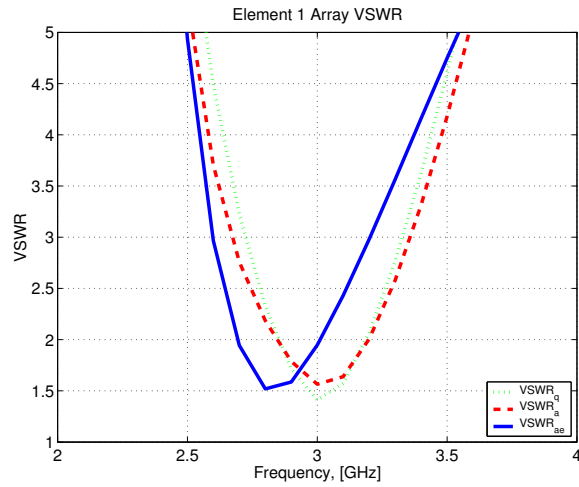
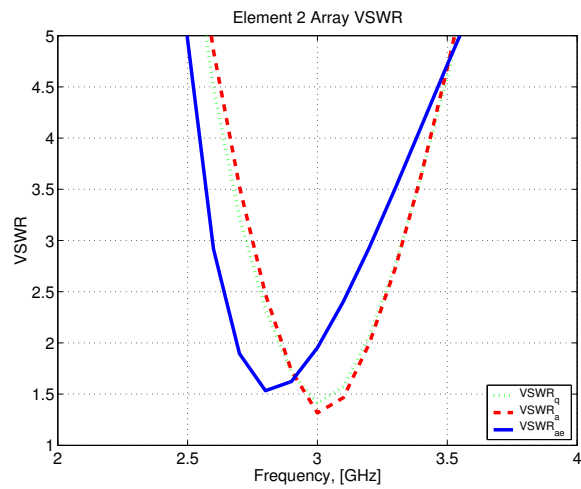


**Figure 6.23** Geometry of  $3 \times 3$  array of half-wavelength strip dipoles suspended over an infinite ground plane with strip length,  $L=48$  mm, strip width,  $W=2$  mm, and strip height over ground,  $h=25$  mm. The array is designed to operate at center frequency of 3 GHz, ( $\lambda = 100$  mm).

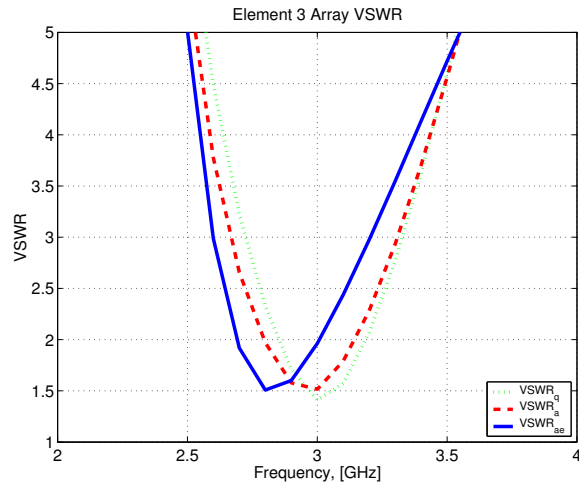


(a) Element 1

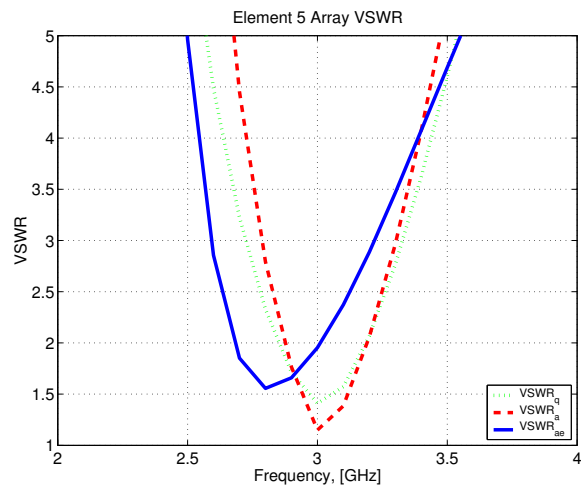


(b) Element 2

**Figure 6.24** Comparison of three voltage standing wave ratio (VSWR) as a function of frequency over a range between 2 to 4 GHz for a  $3 \times 3$  array of strip dipoles of Fig. 6.23 excited with uniform excitation. Solid curves are active-element  $VSWR_{ae}$  referenced to  $50 \Omega$  computed using (6.21). Dashed curves are active  $VSWR_a$  referenced to  $50 \Omega$  computed using (6.16). Dotted curves are array  $VSWR_q$  computed using (6.6).



(c) Element 3



(d) Element 5

**Figure 6.24** Comparison of three voltage standing wave ratio (VSWR) as a function of frequency over a range between 2 to 4 GHz for a  $3 \times 3$  array of strip dipoles of Fig. 6.23 excited with uniform excitation. Solid curves are active-element  $VSWR_{ae}$  referenced to  $50 \Omega$  computed using (6.21). Dashed curves are active  $VSWR_a$  referenced to  $50 \Omega$  computed using (6.16). Dotted curves are array  $VSWR_q$  computed using (6.6). (Cont.)

## 6.4 Summary

The experimental validation of the S-parameter, network-model, based array analysis was presented in this chapter. Indirectly measured active-element patterns and fully excited array patterns were computed based on the measured S-parameters of the  $3 \times 3$  array of Foursquare test article hardware, and S-parameters of broadband power divider corporate feed network, and unbalanced-fed active-element patterns of the array elements. The indirectly measured patterns were then compared with the directly measured active-element patterns and fully excited array patterns. Close matches in the indirectly and directly measured patterns confirms the validity of the S-parameter network based array analysis which includes all of the effects of mutual coupling in the array as well as the feed.

## Chapter 7

# Conclusions

A new scattering-parameter, network-model based, representation of array antenna was presented in this dissertation. Expressions for the directivity, gain, and realized gain patterns of array antennas were developed. An application of the network model for the analysis of a highly coupled wideband array was demonstrated in an experiment using a  $3 \times 3$  Foursquare array hardware. This chapter summarizes the important results of this dissertation, details the contributions presented, and proposes future work.

### 7.1 Summary

A review of previous work related to the analysis of array antennas was presented in Chapters 1 and 2. Reviews of traditional array analysis techniques using the ideal array analysis method, classical array analysis methods, and active-element pattern method were covered in Chapter 2. These conventional array analysis techniques are inadequate in predicting the array radiation patterns and impedance bandwidth of highly coupled arrays, providing motivations for the research presented.

Chapter 3 provided the development of a new scattering parameter model for a single antenna analysis. An ideal probe antenna with two ports for two orthogonal polarizations that is located on a spherical surface of constant radius  $r$  was used to detect the radiated field of the antenna under test (AUT). The test antenna port and the two probe antenna ports form a three port network, which were used to construct a 3-port scattering parameter

model for the test antenna. An extended S-parameters that include the position variables of the probe antenna which corresponds to the direction of the radiation  $(\theta, \phi, r)$  were introduced to complete the model. The power delivered to the probe ports when the test antenna is excited with a source was derived. Then, expressions for directivity, gain and realized gain of an antenna under test were developed from the ratio of delivered power to the available power from the source.

Chapter 4 extended the scattering parameter network model to include multiple antenna elements in antenna arrays. The model uses  $N + 2$  port S-matrix to describe an  $N$  element array and its radiation in two polarizations. Similar to the single antenna model, the delivered power expression from the test array to the probe antenna ports was derived. Then, expressions for the array directivity, gain and realized gain were developed using the delivered power. These expressions were utilized to show how source excitations and source impedances are included in the overall array radiation patterns.

The impedance matching of sources to the array was investigated in Chapter 5 using the scattering parameter network model developed in Chapter 4. Three types of source impedance matching configurations were examined: generalized source network, individually matched sources, and individual sources with the same source impedance value. The source impedance matching was applied to a numerically simulated three element strip dipole array to investigate the effects on the radiation pattern and bandwidth of the array. The results indicated that a common valued resistance value can be effectively utilized to match the sources to a coupled array structure.

Finally, the S-parameter network model was applied in the investigation of  $3 \times 3$  Foursquare array test article in Chapter 6. Indirectly measured active-element patterns and fully excited array patterns were constructed using the measured S-parameters of the array and feed network and the measured unbalanced-fed active-element patterns. The indirectly measured patterns were compared with the directly measured results. Close matches between indirectly measured and directly measured patterns with less than 0.5 dB difference in gain patterns provided an experimental verification of the S-parameter network based array analysis method.

## 7.2 Contributions

The major contribution of this dissertation is in the introduction and development of the scattering parameter network model to analyze antenna characteristics. The model developed is completely general and it can be applied to antennas and antenna arrays of any configurations. The model very clearly indicates how input impedance characteristics of antenna array and the feed network affect the radiation patterns of the array.

This dissertation also detailed other contributions. The application of the scattering parameter model was demonstrated for the analysis of a simulated highly coupled dipole array. The application of the network model was also demonstrated using the experimentally measured data of a Foursquare test article. Use of the impedance mismatch factor for the determination of fully excited array bandwidth was suggested. Also, the gain and realized gain radiation patterns, instead of normalized radiation patterns of a Foursquare array antenna were determined for the first time.

## 7.3 Recommendation for Future Work

The research presented in this dissertation may be extended in several ways. The examination and development of feed network design method for highly coupled wideband array which incorporate the array network model is the first extension to the work presented in this dissertation. Impedance matching of fully excited array to the sources using the matching conditions introduced in Chapter 5 must be integrated into the feed network synthesis. In particular, the realizability conditions for the generalized source network with S-matrix that is a hermitian transpose of the array S-matrix should be closely examined. Physical implementation of the generalized source may not be possible using the traditional feed network. However, an approximate implementation of the required feed network using the traditional feed hardware, of an exact implementation of the feed using a digital beam forming network may be possible.

Another extension to the work presented in this dissertation is in the development of the network models for an infinite array. As the number of elements in the array increases, the size of the scattering parameter matrices required to model the array becomes large. Con-

sequently, the time required to determine the necessary S-parameters of the array becomes impossibly large. In the limit, the array patterns and impedance characteristics of a large array become very similar to those for an equivalent infinite array. Thus, a S-parameter network description of an infinite array is a useful model in predicting the performance of a large array.

# References

- [1] M. Ghosh, X. Ouyang, and G. Dolmans, “On the use of multiple antennae for 802.11,” IEEE, Tech. Rep. IEEE 802.11-02/180r0, 2002.
- [2] A. Alastalo, S. Gray, and V. Vadde, “Performance of smart antennas and pcf,” IEEE, Tech. Rep. IEEE 802.11-00/269, 2000.
- [3] D. F. Kelley and W. L. Stutzman, “Array antenna pattern modeling methods that include mutual coupling effects,” *IEEE Trans. Antennas Propagat.*, vol. 41, no. 12, pp. 1625–1632, Dec. 1993.
- [4] D. M. Pozar, “The active element pattern,” *IEEE Trans. Antennas Propagat.*, vol. 42, no. 8, pp. 1176–1178, Aug. 1994.
- [5] J. James W. LaPean, “Analysis of infinite arrays of arbitrarily shaped planar radiating elements using a floquet mode based method of moments approach,” Ph.D. dissertation, Virginia Polytechnic Institute and State University, Blacksburg, VA, April 1996.
- [6] C. G. Buxton, “Design of a broadband array using the foursquare radiating element,” Ph.D. dissertation, Virginia Polytechnic Institute and State University, Blacksburg, VA, June 2001.
- [7] R. F. Harrington, *Field Computation by Moment Methods*. Piscataway, NJ: IEEE Press, 1993.
- [8] A. Chatterjee, L. C. Kempel, and J. L. Volakis, *Finite Element Method for Electromagnetics: Antennas, Microwave Circuits, and Scattering Applications*. Piscataway, NJ: IEEE Press, 1998.

- [9] A. Taflove, *Computational Electrodynamics: The Finite-Difference Time-Domain Method*, 2nd ed. Boston, MA: Artech House, 2000.
- [10] D. M. Pozar, S. Duffy, and N. Herscovici, "A comparison of commercial software packages for microstrip antenna analysis," in *Proc. 2000 IEEE Antennas Propagat. Soc. Int. Symp.*, vol. I, Salt Lake City, UT, 2000, pp. 152–155.
- [11] K. Takamizawa, N. P. Cummings, W. L. Stutzman, and W. A. Davis, "Comparative study of analysis techniques and measurement methods for a canonical microstrip antenna," in *Proc. 2000 USNC/URSI National Radio Science Meeting*, Salt Lake City, UT, July 2000, p. 77.
- [12] W. L. Stutzman and G. A. Thiele, *Antenna Theory and Design*, 2nd ed. New York: John Wiley and Sons, Inc., 1998.
- [13] P. S. Carter, "Circuit relations in radiating systems and applications to antenna problems," *Proc. IRE*, vol. 20, pp. 1004–1041, June 1932.
- [14] A. A. Oliner and R. G. Malech, "Mutual coupling in infinite array," in *Microwave Scanning Antennas*, R. C. Hansen, Ed. Los Altos, CA: Peninsula Publishing, 1985, vol. III, ch. 3, pp. 209–216.
- [15] K. M. Lee and R.-S. Chu, "Analysis of mutual coupling between a finite phased array of dipoles and its feed network," *IEEE Trans. Antennas Propagat.*, vol. 36, no. 12, pp. 1681–1699, Dec. 1988.
- [16] R. S. Smith, "Analysis and design of microstrip array antennas including mutual coupling," Master's thesis, Virginia Polytechnic Institute and State University, Blacksburg, VA 24061, 1986.
- [17] K. Takamizawa, "Array antenna synthesis including element and feed coupling," Master's thesis, Virginia Polytechnic Institute and State University, Blacksburg, VA 24061, 1988.
- [18] R. M. Barts and W. L. Stutzman, "A matrix description for arrays," Feb. 1991, unpublished note.

- [19] H. Steyskal and J. S. Herd, "Mutual coupling compensation in small array antennas," *IEEE Trans. Antennas Propagat.*, vol. 38, no. 12, pp. 1971–1975, Dec. 1990.
- [20] D. M. Pozar, "Analysis of finite phased array of printed dipoles," *IEEE Trans. Antennas Propagat.*, vol. AP-33, no. 10, pp. 1045–1053, Oct. 1985.
- [21] R. C. Hansen, *Phased Array Antennas*. New York: John Wiley and Sons, Inc., 1998.
- [22] P. W. Hannan, "The element-gain paradox for a phased-array antenna," *IEEE Trans. Antennas Propagat.*, vol. AP-12, no. 3, pp. 423–433, July 1964.
- [23] W. Wasylkiwskyj and W. K. Kahn, "Element patterns and active reflection coefficient in uniform phased arrays," *IEEE Trans. Antennas Propagat.*, vol. AP-22, no. 2, pp. 207–212, Mar. 1974.
- [24] J. L. Allen, "Gain and impedance variation in scanned dipole arrays," *IRE Trans. Antennas Propagat.*, vol. AP-10, no. 5, pp. 566–572, Sept. 1962.
- [25] H. A. Aumann, A. J. Fenn, and F. G. Willwerth, "Phase array antenna calibration and pattern prediction using mutual coupling measurements," *IEEE Trans. Antennas Propagat.*, vol. 37, no. 7, pp. 844–850, July 1989.
- [26] D. F. Kelley, "Analysis of phased array antenna radiation patterns including mutual coupling," Master's thesis, Virginia Polytechnic Institute and State University, Blacksburg, VA, November 1990.
- [27] R. F. Harrington, "Antenna excitation for maximum gain," *IEEE Trans. Antennas Propagat.*, vol. AP-13, no. 6, pp. 896–903, Nov. 1965.
- [28] W. K. Kahn and W. Wasylkiwskyj, "Coupling, radiation and scattering by antennas," in *Generalized Networks*, J. Fox, Ed., vol. XVI. New York: Polytechnic Press, New York, 1966, pp. 83–114.
- [29] A. C. Gately, Jr., D. J. R. Stock, and B. R. Cheo, "A network description for antenna problems," *Proc. IEEE*, vol. 56, no. 7, pp. 1181–1193, July 1968.

- [30] W. Wiesbeck and E. Heidrich, "Wide-Band multiport antenna characterization by polarimetric RCS measurements," *IEEE Trans. Antennas Propagat.*, vol. 46, no. 3, pp. 341–350, Mar. 1998.
- [31] K. Takamizawa, W. A. Davis, and W. L. Stutzman, "Novel techniques for analysis of array antennas," in *Proc. 2001 USNC/URSI National Radio Science Meeting*, Boston, MA, July 2001, p. 176.
- [32] J. E. Hansen, Ed., *Spherical Near-Field Antenna Measurements*, ser. IEE Electromagnetic Waves Series 26. London, UK: Peter Peregrinus, Ltd, 1988.
- [33] A. D. Yaghjian, "Efficient computation of antenna coupling and fields within the near-field region," *IEEE Trans. Antennas Propagat.*, vol. AP-30, no. 1, pp. 113–128, Jan. 1982.
- [34] E. D. Caswell and W. A. Davis, "Remote measurement of antenna input impedance," in *Proc. 1999 USNC/URSI National Radio Science Meeting*, Orland, FL, July 1999, p. ???
- [35] R. J. Mailloux, *Phased Array Antenna Handbook*. Boston: Artech House, 1994.
- [36] D. M. Pozar and D. H. Schaubert, "Scan blindness in infinite phased arrays of printed dipoles," *IEEE Trans. Antennas Propagat.*, vol. AP-32, no. 6, pp. 602–610, June 1984.
- [37] —, "Analysis of an infinite array of rectangular microstrip patches with idealized probe feeds," *IEEE Trans. Antennas Propagat.*, vol. AP-32, no. 10, pp. 1101–1107, Oct. 1984.
- [38] D. M. Pozar, "Analysis of an infinite phased array of aperture coupled microstrip patches," *IEEE Trans. Antennas Propagat.*, vol. 37, no. 4, pp. 418–425, Apr. 1989.
- [39] J. T. Aberle and D. M. Pozar, "Analysis of infinite arrays of one- and two-probe-fed circular patches," *IEEE Trans. Antennas Propagat.*, vol. 38, no. 4, pp. 421–432, Apr. 1990.

- [40] R.-S. Chu, "Analysis of an infinite phased array of dipole elements with ram coating on ground plane and covered with layered radome," *IEEE Trans. Antennas Propagat.*, vol. 39, no. 2, pp. 164–176, Feb. 1991.
- [41] K. M. Lee and R.-S. Chu, "Analysis of mutual coupling between an infinite phased array of horizontal dipoles and vertical wires," *IEEE Trans. Antennas Propagat.*, vol. 39, no. 5, pp. 591–599, May 1991.
- [42] D. M. Pozar, "Scanning characteristics of infinite arrays of printed antenna subarrays," *IEEE Trans. Antennas Propagat.*, vol. 40, no. 6, pp. 666–674, June 1992.
- [43] J. W. LaPean, W. L. Stutzman, and W. A. Davis, "A Computational Tool for Large Planar Phased Arrays - ASIA," in *1996 Antennas and Propagation Society International Symposium*, vol. 2, 1996, pp. 822–825.
- [44] W.-J. Tsay and D. M. Pozar, "Radiation and scattering from infinite periodic printed antennas with inhomogeneous media," *IEEE Trans. Antennas Propagat.*, vol. 46, no. 11, pp. 1641–1650, Nov. 1998.
- [45] A. K. Bhattacharyya, "Analysis of multilayer infinite periodic array structures with different periodicities and axes orientations," *IEEE Trans. Antennas Propagat.*, vol. 48, no. 3, pp. 357–369, Mar. 2000.
- [46] H. A. Wheeler, "The radiation resistance of an antenna in an infinite array or waveguide," *Proc. IRE*, vol. 36, pp. 478–488, Apr. 1948.
- [47] —, "Simple relations derived from a phased-array antenna made of an infinite current sheet," *IEEE Trans. Antennas Propagat.*, vol. AP-13, no. 4, pp. 506–514, July 1965.
- [48] D. M. Pozar, "General relations for a phased array of printed antennas derived from infinite current sheet," *IEEE Trans. Antennas Propagat.*, vol. AP-33, no. 5, pp. 498–504, May 1985.
- [49] W. L. Stutzman and C. G. Buxton, "Radiating elements for wideband phased arrays," *Microwave Journal*, pp. 130–141, Feb. 2000.

- [50] E. D. Caswell, "Design and analysis of star spiral with application to wideband arrays with variable element sizes," Ph.D. dissertation, Virginia Polytechnic Institute and State University, Blacksburg, VA, December 2001.
- [51] F. German, S. Sanzgeri, and D. Doyle, "Analysis of flared slot antennas for phased array applications," in *IEEE Antennas and Propagation Society International Symposium*, vol. 3, Ann Arbor, MI, June 1993, pp. 1600–1603.
- [52] D. H. Schaubert, J. A. Aas, M. E. Cooley, and N. E. Burris, "Moment method analysis of infinite stripline-fed tapered slot antenna arrays with a ground plane," *IEEE Trans. Antennas Propagat.*, vol. 42, no. 8, pp. 1161–1166, Aug. 1994.
- [53] E. Thiele and A. Taflove, "FDTD analysis of vivaldi flared horn antenna and arrays," *IEEE Trans. Antennas Propagat.*, vol. 42, no. 5, pp. 633–641, May 1994.
- [54] A. O. Boryssenko and D. H. Schaubert, "Single-polarized, dielectric-free, vivaldi tapered slot phased array: Performance prediction," in *IEEE Antennas and Propagation Society International Symposium*, Boston, MA, July 2001.
- [55] W. Mohuchy, P. A. Beyerle, and A. B. MacFarland, "4.5:1 bandwidth microstrip notch array measured performance," in *IEEE Antennas and Propagation Society International Symposium*, Boston, MA, July 2001.
- [56] Y. H. Choung, "Wideband double-slot cross-notch antenna," in *IEEE Antennas and Propagation Society International Symposium*, Boston, MA, July 2001.
- [57] N. Farahat, V. V. S. Prakash, and R. Mittra, "Analysis of a vivaldi array antenna using the conformal finite difference time domain (cfDTD) method," in *IEEE Antennas and Propagation Society International Symposium*, San Antonio, TX, July 2002, pp. 516–519.
- [58] M. Kragalott, W. R. Pickles, and M. S. Kluskens, "Design of a 5:1 bandwidth stripline notch array from FDTD analysis," *IEEE Trans. Antennas Propagat.*, vol. 48, no. 11, pp. 1733–1741, Nov. 2000.

- [59] W. L. Stutzman, "Wide bandwidth antenna array design," in *Proceedings of the IEEE Southeastern Regional Meeting*, Raleigh, NC, April 1985, pp. 92–96.
- [60] J. R. Nealy, "Foursquare antenna radiating element," U.S. Patent No. 5,926,137, July 20 1999, vTIP Ref. 96-056.
- [61] D. E. Kelley, "Relationship between active element patterns and mutual impedance matrices in phased array antennas," in *IEEE Antennas and Propagation Society International Symposium*, vol. I, San Antonio, TX, July 2002, p. 524.
- [62] W. L. Stutzman, *Polarization in Electromagnetic Systems*. Boston: Artech House, 1993.
- [63] K. Kurokawa, "Power waves and the scattering matrix," *IEEE Trans. Microwave Theory Tech.*, vol. 13, pp. 194–202, Mar. 1965.
- [64] T. T. Ha, *Solid-state Microwave Amplifier Design*. John Wiley and Sons, Inc., 1981.
- [65] *Agilent AN 154: S-parameter Design*, Agilent Technologies.
- [66] *IEEE Standard Definition of Terms for Antennas, IEEE Std. 145-1993*, IEEE, 1993.
- [67] A. C. Ludwig, "The definition of cross polarization," *IEEE Trans. Antennas Propagat.*, vol. AP-21, no. 1, pp. 116–119, Jan. 1973.
- [68] G. J. Burke, *Numerical Electromagnetics Code - NEC4, Method of Moments, Part I: User's Manual*, Lawrence Livermore National Laboratory, Jan. 1992.
- [69] *IE3D User's Manual, Release 7*, Zeland Software, Inc., Fremont, California, 1999.
- [70] Rogers Corporation, Microwave Materials Division, "RT/duroid 5870, 5880 Microwave Laminates," Product Data Sheet.
- [71] Electromagnetic Technology, Inc., "Eti technical data," <http://www.etionline.com>.
- [72] *8510C Network Analyzer System Operating and Programming Manual*, 2nd ed., Agilent Technologies, Santa Rosa, CA, Jan. 1994.

- [73] J. C. Tippet and R. A. Speciale, “A rigorous technique for measuring the scattering matrix of a multiport device with a 2-port network analyzer,” *IEEE Trans. Microwave Theory Tech.*, vol. MTT-30, no. 5, pp. 661–666, May 1982.
- [74] *Model NFH003 Near-Field Scanner Test System Technical Manual*, ANTCOM, Aug. 1999.
- [75] W. A. Davis, J. R. Nealy, G. F. Richardi, and W. L. Stutzman, “Techniques for the measurement of the impedance of wideband balanced antennas,” in *Proceedings of the Antenna Measurement Techniques Association Symposium*, Williamsburg, VA, Nov. 1995, pp. 60–63.
- [76] T. Durham, “Array analysis,” Harris Corp., Tech. Rep., Dec. 2000.
- [77] D. M. Pozar, *Microwave Engineering*. John Wiley and Sons, Inc., 1998.
- [78] *Advanced Design System 1.3, User’s Guide*, Agilent Technology, Nov. 1999.

## Appendix A

# Derivation of Equation (3.9)

Mason's rule [65] is a tool to determine a ratio of any two nodes in a network directly from a signal flow graph. To understand the Mason's rule, we need to define several terms associated with signal flow graphs.

Each port  $n$  of a network has two *nodes*,  $a_n$  and  $b_n$ . Node  $a_n$  represents a wave incident on the port  $n$ , while node  $b_n$  represents a wave reflected from port  $n$ . A *branch* represents a signal flow from a node to another node. Every branch has an associated S-parameter. A *path* is a product of branches between two nodes. The *first order loop* is defined as a product of all branches encountered in a path starting from a node and moving in the direction of signal flows back to the original node. A *second order loop* is a product of any two non-touching first order loops, and a *third order loop* is a product of any three non-touching first order loops.

The Mason's rule is defined as [65]

$$T = \frac{P_1[1 - \sum L(1)^{(1)} + \sum L(2)^{(1)} - \dots] + P_2[1 - \sum L(1)^{(2)} + \dots] \dots}{1 - \sum L(1) + \sum L(2) - \sum L(3) + \dots} \quad (\text{A.1})$$

where

$$T = \frac{b_m}{b_n} \quad (\text{A.2})$$

is the ratio of any two nodes in a signal flow graph.  $P_i$  are various path between two nodes of the interests. The term,  $\sum L(k)$ , in the denominator of (A.1) is a sum of all  $k$ -th order loops, and the term,  $\sum L(k)^i$ , in the numerator of (A.1) is a sum of all  $k$ -th order loops that do not touch the  $i$ -th path.

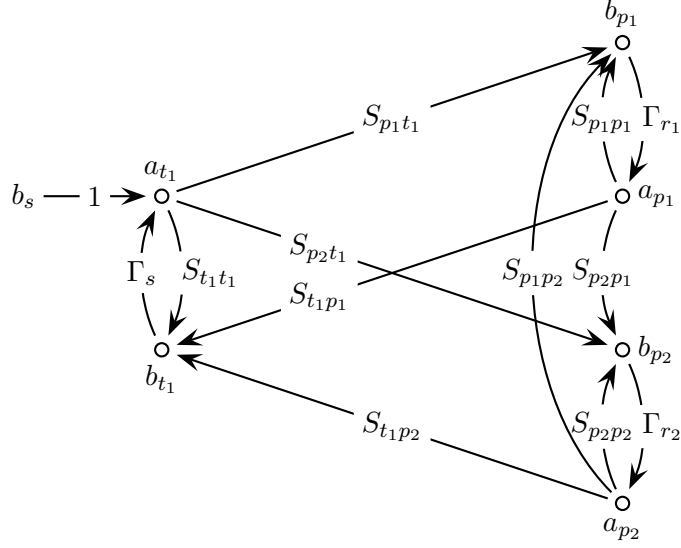


**Figure A.1** Signal flow diagram for an arbitrary test antenna and a probe antenna with two orthogonal polarization ports. Reproduced from Fig. 3.2.

The signal flow graph for the single element antenna network model from Fig. 3.2 in Chapter 3 is reproduced in Fig. A.1. We wish to determine the ratio of nodes  $b_{p1}$  and  $b_s$  in the signal flow graph. There are two paths between  $b_{p1}$  and  $b_s$

$$P_1 : S_{p1t1}(r, \theta, \phi) \quad (\text{A.3})$$

$$P_2 : S_{p2t1}(r, \theta, \phi)\Gamma_{r2}S_{p1p2} \quad (\text{A.4})$$

By the inspection of signal flow graph, we can identify that there are eight first order loops:

$$S_{t1t1}\Gamma_s \quad (\text{A.5})$$

$$S_{p1p1}\Gamma_{r1} \quad (\text{A.6})$$

$$S_{p2p2}\Gamma_{r2} \quad (\text{A.7})$$

$$S_{p1t1}(r, \theta, \phi)\Gamma_{r1}S_{t1p1}(r, \theta, \phi)\Gamma_s \quad (\text{A.8})$$

$$S_{p2t1}(r, \theta, \phi)\Gamma_{r2}S_{t1p2}(r, \theta, \phi)\Gamma_s \quad (\text{A.9})$$

$$S_{p1t1}(r, \theta, \phi)\Gamma_{r1}S_{p2p1}\Gamma_{r2}S_{t1p2}(r, \theta, \phi)\Gamma_s \quad (\text{A.10})$$

$$S_{p2t1}(r, \theta, \phi)\Gamma_{r2}S_{p1p2}\Gamma_{r1}S_{t1p1}(r, \theta, \phi)\Gamma_s \quad (\text{A.11})$$

$$S_{p1p2}\Gamma_{r1}S_{p2p1}\Gamma_{r2}. \quad (\text{A.12})$$

There are six second order loops which are

$$S_{t_1 t_1} \Gamma_s S_{p_1 p_1} \Gamma_{r_1} \quad (\text{A.13})$$

$$S_{t_1 t_1} \Gamma_s S_{p_2 p_2} \Gamma_{r_2} \quad (\text{A.14})$$

$$S_{p_1 p_1} \Gamma_{r_1} S_{p_2 p_2} \Gamma_{r_2} \quad (\text{A.15})$$

$$S_{p_1 t_1}(r, \theta, \phi) \Gamma_{r_1} S_{t_1 p_1}(r, \theta, \phi) \Gamma_s S_{p_2 p_2} \Gamma_{r_2} \quad (\text{A.16})$$

$$S_{p_2 t_1}(r, \theta, \phi) \Gamma_{r_2} S_{t_1 p_2}(r, \theta, \phi) \Gamma_s S_{p_1 p_1} \Gamma_{r_1} \quad (\text{A.17})$$

$$S_{p_1 p_2} \Gamma_{r_1} S_{p_2 p_1} \Gamma_{r_2} S_{t_1 t_1} \Gamma_s, \quad (\text{A.18})$$

and there is a third order loop which is

$$S_{t_1 t_1} \Gamma_s S_{p_1 p_1} \Gamma_{r_1} S_{p_2 p_2} \Gamma_{r_2}. \quad (\text{A.19})$$

Only one of the first order loop does not touch path  $P_1$  which is

$$S_{p_2 p_2} \Gamma_{r_2}. \quad (\text{A.20})$$

All of the first, the second, and the third order loops touch path  $P_2$ . Substituting (A.3) through (A.20) into (A.1) yields

$$\begin{aligned} \frac{b_{p_1}(r, \theta, \phi)}{b_s} = & \left\{ \left[ S_{p_1 t_1}(r, \theta, \phi) \{1 - S_{p_2 p_2} \Gamma_{r_2}\} + S_{p_2 t_1}(r, \theta, \phi) \Gamma_{r_2} S_{p_1 p_2} \right] \right\} / \\ & \left\{ 1 - \left[ S_{t_1 t_1} \Gamma_s + S_{p_1 p_1} \Gamma_{r_1} + S_{p_2 p_2} \Gamma_{r_2} + S_{p_1 t_1}(r, \theta, \phi) \Gamma_{r_1} S_{t_1 p_1}(r, \theta, \phi) \Gamma_s \right. \right. \\ & + S_{p_2 t_1}(r, \theta, \phi) \Gamma_{r_2} S_{t_1 p_2}(r, \theta, \phi) \Gamma_s + S_{p_1 t_1}(r, \theta, \phi) \Gamma_{r_1} S_{p_2 p_1} \Gamma_{r_2} S_{t_1 p_2}(r, \theta, \phi) \Gamma_s \\ & + S_{p_2 t_1}(r, \theta, \phi) \Gamma_{r_2} S_{p_1 p_2} \Gamma_{r_1} S_{t_1 p_1}(r, \theta, \phi) \Gamma_s + S_{p_1 p_2} \Gamma_{r_1} S_{p_2 p_1} \Gamma_{r_2} \left. \right] \\ & + \left[ S_{t_1 t_1} \Gamma_s S_{p_1 p_1} \Gamma_{r_1} + S_{t_1 t_1} \Gamma_s S_{p_2 p_2} \Gamma_{r_2} + S_{p_1 p_1} \Gamma_{r_1} S_{p_2 p_2} \Gamma_{r_2} \right. \\ & + S_{p_1 t_1}(r, \theta, \phi) \Gamma_{r_1} S_{t_1 p_1}(r, \theta, \phi) \Gamma_s S_{p_2 p_2} \Gamma_{r_2} + S_{p_2 t_1}(r, \theta, \phi) \Gamma_{r_2} S_{t_1 p_2}(r, \theta, \phi) \Gamma_s S_{p_1 p_1} \Gamma_{r_1} \\ & \left. + S_{p_1 p_2} \Gamma_{r_1} S_{p_2 p_1} \Gamma_{r_2} S_{t_1 t_1} \Gamma_s \right] - S_{t_1 t_1} \Gamma_s S_{p_1 p_1} \Gamma_{r_1} S_{p_2 p_2} \Gamma_{r_2} \left. \right\} \quad (\text{A.21}) \end{aligned}$$

which is equal to (3.9a). Derivation of (3.9b) takes the similar steps.

# Vita

Koichiro Takamizawa received a B.S. from Rensselaer Polytechnic Institute in 1985, and M.S. and Ph.D. from Virginia Polytechnic Institute and State University in 1988 and 2004. Prior to returning to Virginia Tech for his doctorate degree, he work as an engineer at Analogic Corp. in Peabody, MA and as a senior engineer at Furuno Diagnostics America, Inc. in Cary, NC designing medical digital ultrasound machines.